

AD-A046 702

EXPLORATORY DEVELOPMENT OF RAIN EROSION RESISTANT
INFRARED WINDOW MATERIALS(U) BELL AEROSPACE TEXTRON
BUFFALO N Y J V HACKWORTH ET AL MAY 77 AFML-TR-77-84

1/2

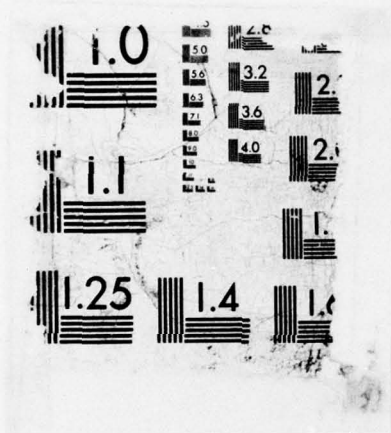
UNCLASSIFIED

F33615-76-C-5125

F/G 9/3

NL





AD A 0 46702

AFML-TR-77-84

EXPLORATORY DEVELOPMENT OF RAIN EROSION RESISTANT INFRARED
WINDOW MATERIALS

Bell Aerospace Textron
Post Office Box One
Buffalo, New York 14240

May 1977

TECHNICAL REPORT AFML-TR-77-84

Final Report for Period February 1976 - February 1977

Approved for public release; distribution unlimited.



AIR FORCE MATERIALS LABORATORY
AIR FORCE WRIGHT AERONAUTICAL LABORATORIES
AIR FORCE SYSTEMS COMMAND
WRIGHT-PATTERSON AIR FORCE BASE, OHIO 45433

AD NO. _____
DDC FILE COPY

NOTICE

When Government drawings, specifications, or other data are used for any purpose other than in connection with a definitely related Government procurement operation, the United States Government thereby incurs no responsibility nor any obligation whatsoever; and the fact that the government may have formulated, furnished, or in any way supplied the said drawings, specifications, or other data, is not to be regarded by implication or otherwise as in any manner licensing the holder or any other person or corporation, or conveying any rights or permission to manufacture, use, or sell any patented invention that may in any way be related thereto.

This report has been reviewed by the Information Office (ASD/OIP) and is releasable to the National Technical Information Service (NTIS). At NTIS, it will be releasable to the general public, including foreign nations.

This report covers a period from 16 February 1976 to 15 February 1977.

This technical report has been reviewed and is approved for publication.

T. L. Peterson
T. L. PETERSON
Project Monitor

FOR THE DIRECTOR

J. K. Sieron
J. K. SIERON, CHIEF
Elastomers and Coatings Branch
Nonmetallic Materials Division
Air Force Materials Laboratory

ADDITIONAL	
NTIS	White Section <input checked="" type="checkbox"/>
DOC	Ref Section <input type="checkbox"/>
UNANNOUNCED	<input type="checkbox"/>
JUSTIFICATION	
BY	
DISTRIBUTION/AVAILABILITY CODES	
Dist.	ATL. EMB. OR SPECIAL
A	

Copies of this report should not be returned unless return is required by security considerations, contractual obligations, or notice on a specific document.

SECURITY CLASSIFICATION OF THIS PAGE (When Data Entered)

DD FORM 1473 EDITION OF 1 NOV 65 IS OBSOLETE
1 JAN 73

SECURITY CLASSIFICATION OF THIS PAGE (When Data Entered)

LB

UNCLASSIFIED

SECURITY CLASSIFICATION OF THIS PAGE(When Data Entered)

20. ABSTRACT (Continued)

Erosion damage mechanisms were defined by detailed optical and electron microscopic analyses performed on the materials before and after exposure to the selected environments.

Single drop impact tests performed on zinc selenide, zinc sulfide, and gallium arsenide showed that each drop impact produced a ring fracture pattern characteristic of the material. Resistance to drop impact damage increased in the order zinc selenide, gallium arsenide, and zinc sulfide. The superior performance of zinc sulfide as compared to zinc selenide appeared to be related to the order of magnitude smaller grain size of zinc sulfide. Damage produced by overlapping drop impacts was essentially additive, at least for the first two or three drops impacting the same site. A zinc sulfide outer layer as thin as 0.25 mm protected zinc selenide from damage by impact of a 2.0 mm drop at 730 fps.

micrometers
Exposure of zinc sulfide at 730 fps to multiple drop impact in the rainfield showed transmittance loss at short wavelengths (0.5 to 2.1 μm) was linear with exposure time indicating a dependence on the extent of subsurface damage. At longer wavelengths (2.5 to 25 μm), there was an incubation period during which transmittance did not decrease. This incubation period was about one-half of the useful life of the window as defined by exposure time for 50% loss in transmittance. The end of the incubation period and the start of transmittance loss for the longer wavelengths were associated with the nucleation and lateral growth of surface pits.

A computer program was used to calculate, as a function of time and location, the stresses induced by a single water drop impact on zinc selenide, zinc sulfide, gallium arsenide, germanium, and polymethylmethacrylate. The predicted locations of the inner radii of the ring fracture annuli agreed with the experimental results indicating the analytical model provides a reasonable representation of the drop impact process.

UNCLASSIFIED

SECURITY CLASSIFICATION OF THIS PAGE(When Data Entered)

FOREWORD

This final report was prepared by J. Vaughn Hackworth and Lawrence H. Kocher of Bell Aerospace Textron, Buffalo, New York under Contract F33615-76-C-5125 with the Air Force Materials Laboratory, Wright-Patterson Air Force Base, Ohio. This contract was initiated under Project No. 7340 "Nonmetallic and Composite Materials", Task No. 734007, "Coatings for Energy Utilization, Control and Protective Functions".

This report covers research performed during the period February 1976 to February 1977.

TABLE OF CONTENTS

SECTION	PAGE
I. INTRODUCTION	1
II. EXPERIMENTAL INVESTIGATION OF RAIN EROSION OF INFRARED WINDOW MATERIALS	4
A. Description of Materials	4
B. Test Matrix	8
C. Single Drop Impact on Homogeneous Materials	10
1. Single Drop Generator	10
2. Impact at 730 Feet per Second	12
3. Impact at 1120 Feet per Second	38
D. Overlapping Drop Impact on Homogeneous Materials	42
E. Progress of Erosion in Rainfields	51
F. Protective Layers	79
G. Quasistatic Indentation Evaluations	94
III. THEORETICAL PREDICTION OF DYNAMIC STRESS	98
A. Description of Mathematical Model	98
B. Analysis of Single Drop Impacts	109
1. Homogeneous Materials	109
a. Description of Stress Predictions	109
b. Effect of Material Properties on Stress	122
c. Effect of Drop Size and Velocity on Stresses	128
2. Layered Systems	137
C. Comparison with Experimental Results	147
IV. CONCLUSIONS	158
A. Experimental Investigation	158
B. Theoretical Predictions	162
V. RECOMMENDATIONS	165
A. Experimental Investigation	165
B. Theoretical Predictions	166
VI. REFERENCES	168

LIST OF ILLUSTRATIONS

FIGURE		PAGE
1	Microstructure of Infrared Window Materials	6
2	Schematic of Single Liquid Drop Generator	11
3	Damage from Single Water Drop Impact at 730 fps	14
4	Electron Micrographs of Damage from 2.0 mm Diameter Single Water Drop Impact at 730 fps	17
5	Ring Fracture on Zinc Selenide Formed by Impact with 0.7 mm Diameter Drop at 730 fps. Reflected Light Except Where Noted	20
6	Ring Fracture on Zinc Selenide Formed by Impact with 2.0 mm Diameter Drop at 730 fps. Reflected Light Where Noted	23
7	Ring Fracture on Zinc Selenide Formed by Impact with 2.5 mm Diameter Drop at 730 fps. Reflected Light Except Where Noted	27
8	Electron Micrographs of Ring Fractures at Site of Impact of 0.7 mm Diameter Drop on Zinc Selenide	29
9	Electron Micrographs of Ring Fractures at Site of Impact of 2.5 mm Diameter Drop on Zinc Selenide	30
10	Electron Micrographs of Dislocation Etch Pits at Site of Impact of 2.0 mm Diameter Drop on Zinc Selenide	31
11	Ring Fracture on Zinc Sulfide Formed by Impact with 2.0 mm Diameter Drop at 730 fps	32
12	Electron Micrograph of Ring Fracture Cracks on Zinc Sulfide After Etching to Reveal Grain Boundaries	34
13	Ring Fractures on Gallium Arsenide Formed by Impact with 2.0 mm Diameter Drop at 730 fps	35
14	Electron Micrographs of Gallium Arsenide Specimen Etched After Impact by 2.0 mm Diameter Water Drop at 730 fps	36
15	Effects of Velocity on Damage from Single Water Drop Impact	40

LIST OF ILLUSTRATIONS

FIGURE		PAGE
16	Effect of Velocity on Extent of Chipping of Ring Fractures Formed on Zinc Selenide by Impact with 2.0 mm Diameter Drops. Reflected Light Except Where Noted	43
17	Electron Micrograph of Ring Fracture Crack Formed on Zinc Selenide by Impact with 2.0 mm Diameter Drop at 1120 fps	44
18	Overlapping Doublet Impact Sites on Zinc Selenide Impacted by Single Water Droplets at 730 fps	45
19	Overlapping Triplet Impact Sites on Zinc Selenide Impacted by Single Water Droplets at 730 fps	46
20	Closeup of Damage to Zinc Selenide in the Area of Overlapping Impact of Single Drops at 730 fps	48
21	Electron Micrographs of Overlap Regions of Doublet Impact Sites on Zinc Selenide Impacted by 2.0 mm Diameter Water Droplets at 730 fps	49
22	Overlapping Doublet Impact Sites on Zinc Sulfide and Gallium Arsenide Impacted by Single Water Drops at 730 fps	50
23	Electron Micrographs of Typical Cracks in the Overlap Region of Doublet Impact Sites on Gallium Arsenide Impacted by 2.0 mm Diameter Water Drops at 730 fps	52
24	Effects of Rain Erosion on Spectral Transmittance of Zinc Selenide between 0.5 and 2.1 Microns	54
25	Effects of Rain Erosion on Spectral Transmittance of Gallium Arsenide Between 0.5 and 2.1 Microns	55
26	Effects of Rain Erosion on Spectral Transmittance of Zinc Sulfide Between 0.5 and 2.1 Microns	56
27	Effects of Rain Erosion on Spectral Transmittance of Zinc Selenide Between 2.5 and 25 Microns	57
28	Effect of Rain Erosion on Spectral Transmittance of Gallium Arsenide Between 2.5 and 25 Microns	59

LIST OF ILLUSTRATIONS

FIGURE		PAGE
29	Effects of Rain Erosion on Spectral Transmittance of Zinc Sulfide Between 2.5 and 25 Microns	61
30	Surface Erosion of Zinc Selenide Exposed to Standard Rainfield (1 inch/hour, 1.8 mm Drops) at 730 fps	66
31	Surface Erosion of Gallium Arsenide Exposed to Standard Rainfield (1 inch/hour, 1.8 mm Drops) at 730 fps	67
32	Surface Erosion of Zinc Sulfide Exposed to Standard Rainfield (1 inch/hour, 1.8 mm Drops) at 730 fps	68
33	Progress of Damage at a Selected Site on Gallium Arsenide Exposed to Standard Rainfield (1 inch/hour, 1.8 mm Drops) at 730 fps	70
34	Progress of Damage at a Selected Site on Zinc Sulfide Exposed to Standard Rainfield (1 inch/hour, 1.8 mm Drops) at 730 fps	71
35	Subsurface Damage After Exposure to Standard Rainfield (1 inch/hour, 1.8 mm Drops) at 730 fps	74
36	Electron Micrographs of Typical Damage on Zinc Selenide Exposed for 20 Seconds to the Standard Rainfield (1 inch/hour, 1.8 mm Drops) at 730 fps	75
37	Electron Micrographs of Typical Damage on Gallium Arsenide Exposed to the Standard Rainfield (1 inch/hour, 1.8 mm Drops) at 730 fps	76
38	Electron Micrographs of Typical Damage on Zinc Sulfide Exposed to the Standard Rainfield (1 inch/hour, 1.8 mm Drops) at 730 fps	77
39	Sites of 2.0 mm Single Drop Impact at 730 fps on Zinc Sulfide Protective Layers Bonded to Zinc Selenide Substrate	82
40	Impact Site on Front Surface of 0.25 mm Thick Layer of Zinc Sulfide Bonded to Zinc Selenide. Surface Impacted by 2.0 mm Single Water Drops at 730 fps	83
41	Impact Site on Front Surface of 0.50 mm Thick Layer of Zinc Sulfide Bonded to Zinc Selenide. Surface Impacted by 2.0 mm Single Water Drops at 730 fps	84

LIST OF ILLUSTRATIONS

FIGURE		PAGE
42	Impact Site on Front Surface of 1.0 mm Thick Layer of Zinc Sulfide Bonded to Zinc Selenide Surface Impacted by 2.0 mm Single Water Drops at 730 fps	85
43	Overlapping Doublet Impact Sites on Front Surface of 0.25 mm Thick Layer of Zinc Sulfide Bonded to Zinc Selenide. Surface Impacted by 2.0 mm Single Water Drops at 730 fps	87
44	Electron Micrographs of Ring Fractures Formed by 2.0 mm Drop Impact at 730 fps on 0.25 mm Thick Zinc Sulfide Layer Bonded to Zinc Selenide	88
45	Electron Micrographs of Ring Fractures Formed by 2.0 mm Drop Impact at 730 fps on 0.50 mm Thick Zinc Sulfide Layer Bonded to Zinc Selenide	89
46	Electron Micrographs of Ring Fractures Formed by 2.0 mm Drop Impact at 730 fps on 1.0 mm Thick Zinc Sulfide Layer Bonded to Zinc Selenide	90
47	Overlapping Doublet Impact Sites on 0.25 mm Thick Layer of Zinc Sulfide (Same Sites as Figure 43) Viewed from the Back Surface After Removal of the Layer from the Zinc Selenide Substrates	92
48	Crack on Back Surface Near Impact Site on 0.25 mm Thick Layer of Zinc Sulfide Viewed from the Back Surface After Removal of the Layer from the Zinc Selenide Substrate	93
49	Typical Fractures Produced by Quasistatic Loads Applied by a 407 μm Diameter Al_2O_3 Sphere	95
50	Histograms of Fracture Loads and Fracture Diameters for Zinc Selenide Quasistatically Loaded with 407 μm Diameter Al_2O_3 Spheres	97
51	Perfectly Compressible Liquid Drop Impacting a Solid Surface	99
52	Wave Front Locations in A Semi-Infinite Median for Various Loaded Region Boundary Velocities	102
53	Lateral Outflow Angle as a Function of Time and Drop Size for Drop Velocities of 730 and 1120 ft/sec	104

LIST OF ILLUSTRATIONS

FIGURE		PAGE
54	Temporal Distribution of Principal Axial Stress (at $Z = 0.0005$ inches) for a 2.0 mm Water Drop Impacting ZnS at 730 ft/sec	110
55	Temporal Distribution of Principal Radial Stress (at $Z = 0.0005$ inches) for a 2.0 mm Water Drop Impacting ZnS at 730 ft/sec	111
56	Temporal Distribution of Axial Stress (at $Z = 0.0005$ inches) for a 2.0 mm Water Drop Impacting ZnS at 730 ft/sec	112
57	Temporal Distribution of Radial Stress (at $Z = 0.0005$ inches) for a 2.0 mm Water Drop Impacting ZnS at 730 ft/sec	113
58	Temporal Distribution of Shear Stress (at $Z = 0.0005$ inches) for a 2.0 mm Water Drop Impacting ZnS at 730 ft/sec	114
59	Temporal Distribution of Hoop Stress (at $Z = 0.0002$ in.) for 2.0 mm Water Drop Impacting ZnS at 730 ft/sec	116
60	Temporal Distribution of Principal Axial Stress (at $Z = 0.0002$) for a 2.0 mm Water Drop Impacting ZnS at 730 ft/sec	117
61	Temporal Distribution of Principal Radial Stress (at $Z = 0.0002$ in.) for a 2.0 mm Water Drop Impacting ZnS at 730 ft/sec	118
62	Temporal Distribution of Axial Stress (at $Z = 0.0002$ in.) for a 2.0 mm Water Drop Impacting ZnS at 730 ft/sec	119
63	Temporal Distribution of Radial Stress (at $Z = 0.0002$ in.) for a 2.0 mm Water Drop Impacting ZnS at 730 ft/sec	120
64	Temporal Distribution of Shear Stress (at $Z = 0.0002$ in.) for a 2.0 mm Water Drop Impacting ZnS at 730 ft/sec	121
65	Temporal Distribution of Radial Stress (at $Z = 0.0005$ in.) for a 2.0 mm Water Drop Impacting ZnSe at 730 ft/sec	123

LIST OF ILLUSTRATIONS

FIGURE		PAGE
66	Temporal Distribution of Radial Stress (at $Z = 0.0005$ in.) for a 2.0 mm Water Drop Impacting ZnS at 730 ft/sec	124
67	Temporal Distribution of Radial Stress (at $Z = 0.0005$ in.) for a 2.0 mm Water Drop Impacting GaAs at 730 ft/sec	125
68	Temporal Distribution of Radial Stress (at $Z = 0.0005$ in.) for a 2.0 mm Water Drop Impacting Ge at 730 ft/sec	126
69	Temporal Distribution of Radial Stress (at $Z = 0.0005$ in.) for a 2.0 mm Water Drop Impacting PMMA at 730 ft/sec	127
70	Temporal Distribution of Radial Stress (at $Z = 0.0002$ in.) for a 0.7 mm Water Drop Impacting ZnSe at 730 ft/sec	130
71	Temporal Distribution of Radial Stress (at $Z = 0.0002$ in.) for a 2.0 mm Water Drop Impacting ZnSe at 730 ft/sec	131
72	Temporal Distribution of Radial Stress (at $Z = 0.0002$ in.) for a 2.5 mm Water Drop Impacting ZnSe at 730 ft/sec	132
73	Temporal Distribution of Radial Stress (at $Z = 0.0002$ in. and $0.004 \leq R \leq 0.020$ in.) for 0.7 mm Water Drop Impacting ZnSe at 1120 ft/sec	133
74	Temporal Distribution of Radial Stress (at $Z = 0.0002$ in. and $0.004 \leq R \leq 0.020$ in.) for a 2.0 mm Water Drop Impacting ZnSe at 1120 ft/sec	134
75	Variation of Peak Radial Stress in ZnSe (at $Z = 0.0002$ and 0.0005 in.) with Drop Size and Impacting Velocity	136
76	Variation of Principal Axial Stress ($t = 0.2 \mu\text{sec}$) with Depth for a 2.0 mm Water Drop Impacting ZnS at 730 ft/sec	139
77	Variation of Principal Radial Stress ($t = 0.2 \mu\text{sec}$) with Depth for a 2.0 mm Water Drop Impacting ZnS at 730 ft/sec	140
78	Variation of Principal Hoop Stress (at $t = 0.2 \mu\text{sec}$) with Depth for a 2.0 mm Water Drop Impacting ZnS at 730 ft/sec	141

LIST OF ILLUSTRATIONS

FIGURE		PAGE
79	Variation of Axial Stress (at $t = 0.2 \mu\text{sec}$) with Depth for a 2.0 mm Water Drop Impacting ZnS at 730 ft/sec	142
80	Variation of Radial Stress (at $t = 0.2 \mu\text{sec}$) with Depth for a 2.0 mm Water Drop Impacting ZnS at 730 ft/sec	143
81	Variation of Shear Stress (at $t = 0.2 \mu\text{sec}$) with Depth for a 2.0 mm Water Drop Impacting ZnS at 730 ft/sec	144
82	Variation of Peak Principal Radial Stress (at $t = 0.1 \mu\text{sec}$) with Depth for a 2.0 mm Water Drop Impacting ZnSe at 730 ft/sec	146
83	Comparison of Ring Crack Fracture Radii to Theoretical Lateral Outflow Angle	150
84	Temporal Distribution of Radial Stress (at $Z=0.0002 \text{ in.}$ and $0.0004 \leq R \leq 0.020 \text{ in.}$) for a 0.7 mm Water Drop Impacting PMMA at 1120 ft/sec, with Pressure Pulse Limited to $0.096 \mu\text{sec}$ Duration	153
85	Temporal Distribution of Radial Stress (at $Z=0.0002 \text{ in.}$ and $0.004 \leq R \leq 0.020 \text{ in.}$) for a 2.0 mm Water Drop Impacting PMMA at 1120 ft/sec, with Pressure Pulse Limited to $0.275 \mu\text{sec}$ Duration	155
86	Temporal Distribution of Radial Stress (at $Z=0.0002 \text{ in.}$ and $0.024 \leq R \leq 0.040 \text{ in.}$) for a 2.0 mm Water Drop Impacting PMMA at 1120 ft/sec, with Pressure Pulse Limited to $0.275 \mu\text{sec}$ Duration	156

LIST OF TABLES

TABLE		PAGE
1	Experimental Test Matrix	9
2	Specimens Subjected to Single Water Drop Impact at 730 fps	13
3	Number of Impact Sites Obtained During One-Minute Exposure to Single Drop Impact At 1120 fps	39
4	Dimensions of Damage from Single 2.0 mm Water Drop Impact at 1120 fps	41
5	Loss in Transmittance Versus Exposure Time in Standard Rainfield (1 in./hr.) at 730 fps	65
6	Number of Impact Sites Obtained During Five-Minutes Exposure to Single Drop Impact at 730 fps	81
7	Water Drop Impact Pressures Predicted from One-Dimensional Shock Wave Relationship	106
8	Material Properties	108
9	Predicted Peak Radial Tensile Stresses for 2.0 mm Drop Impacting at 730 ft/sec	129
10	Predicted Peak Radial Tensile Stresses for 730 and 1120 ft/sec Water Drop Impact	148

I. INTRODUCTION

The leading materials being developed for infrared windows, for example, zinc selenide, zinc sulfide, and gallium arsenide, are all essentially brittle materials which are expected to be subject to serious degradation of transmittance when exposed to rainfields at moderate to high subsonic velocities. Development of infrared window materials with improved erosion resistance and development of techniques to protect the more susceptible materials would be greatly aided by knowledge of the mechanisms by which erosion is initiated and an understanding of the relationship between infrared transmission and erosion damage.

An evaluation of a zinc selenide and a zinc sulfide specimen exposed to a multiple drop rainfield in the AFML erosion facility has provided an initial indication of the severity of the erosion problem.⁽¹⁾ However, this evaluation was limited in its ability to delineate the erosion mechanisms because the specimens had been impacted by a large number of drops before they were examined. Also, the progress of erosion could not be followed since each specimen was exposed for a single, relatively long period of time.

The program described in this report was undertaken to investigate in detail the behavior of current infrared window materials when subjected to rain drop environment. The objectives of this program were to define the erosion mechanisms, to determine the interaction of erosion damage and infrared transmissibility, and to evaluate techniques for improving erosion resistance. The infrared window materials studied were zinc selenide, zinc sulfide, and gallium arsenide. Polymethylmethacrylate was also included as a standard material for characterizing the various rain drop environments.

A complete understanding of the erosion process requires the following: (1) defining the loads imparted to a surface by drop impact, (2) determining the dynamic stresses generated in

the material, and (3) establishing the response of the material to the dynamic stresses. These complex requirements dictated the use of a combined experimental/analytical approach for this investigation. This combined approach provides a logical framework to aid in the analysis of the experimental results, to guide in the selection of experimental variables, and to permit further refinement of the analytical models based on experimental data.

The experimental portion of this investigation concentrated on the following four areas:

1. The response of the materials to impact by a single water drop and the variation of this response with drop size (0.7 to 2.5 mm diameter) and impact velocity (730 and 1120 fps).
2. The accumulation of damage as single water drop impacts overlap sites of previous impact.
3. The behavior of erosion resistant protective layers (ZnS) on a less erosion resistant substrate (ZnSe).
4. The progress of erosion and loss of infrared transmittance during exposure to multiple drop rainfields at 730 fps.

Detailed optical and electron microscopic analyses were performed on the materials before and after exposure to water drop impact to characterize the erosion damage and to relate this damage to the significant features of the materials.

For the analytical portion of the program, a computer program was used to calculate the transient stresses induced in the selected infrared window materials by impact with a single water drop. This computer program calculates the four nonvanishing stress components, the principal normal stresses, and the principal shear stresses in cylindrical coordinates as a function of time. The stresses generated by single drop impact on zinc selenide, zinc sulfide, gallium arsenide, germanium and PMMA were calculated for drop sizes and impact velocities which corresponded

to those used for the single drop impact experiments. Approximations of stresses in a bilayered window configuration consisting of an outer layer of zinc sulfide on a zinc selenide substrate were also made using results calculated at various depths in homogeneous slabs of the individual materials. The calculated dynamic stress predictions in the window materials were then compared with the results from the microscopic analyses of the single drop impact sites to verify the validity of the analytical models.

II. EXPERIMENTAL INVESTIGATION OF RAIN EROSION OF INFRARED WINDOW MATERIALS

A. Description of Materials

The infrared transmitting materials selected for evaluation in this investigation are zinc selenide, zinc sulfide, and gallium arsenide. These predominantly covalent bonded semiconductors are representative of the materials currently being developed for infrared windows. The behavior of zinc selenide was investigated extensively to establish a data base to which the behavior of the other two materials could be compared at selected conditions of drop diameter and impact velocity. Polymethylmethacrylate (PMMA), Type G, was used as a standard target material to characterize the various water drop environments.

Zinc selenide and zinc sulfide, produced by the chemical vapor deposition (CVD) process, were procured as 0.375 in. thick blanks. Specimens 0.875 in. x 0.875 in. x 0.375 in. thick were cut from the blanks and optically polished on both sides by a vendor with considerable experience in the polishing of these two materials. The finish on the specimens had a scratch to dig ratio better than 60-40 and a flatness of 1 to 2 λ . These specimens were used to determine the behavior of homogeneous materials. A 0.125 in. thick CVD zinc sulfide blank was also procured for preparation of bilayered specimens. The zinc sulfide was bonded to 0.375 in. thick zinc selenide with lens cement and square specimens 0.875 in. x 0.875 in. were then cut from this bilayered blank. The zinc sulfide layers were ground and polished to give three sets of specimens with layer thicknesses of 0.25 mm, 0.50 mm, and 1.0 mm, respectively.

Arrangements were made through the Air Force Materials Laboratory for two specimens of gallium arsenide from one of their contractors. The material for these specimens was prepared by horizontal gradient freeze from the melt. The specimens, 0.875 in. x 1.50 in. x 0.375 in. thick, were provided in the

as-polished condition. The quality of the finish was not specified; however, it was obviously not as good as the finish on the zinc selenide and zinc sulfide specimens. Using Nomarski interference contrast to enhance the features, it was possible to see uniform surface scratches at 35X magnification. Long, deeper scratches were superimposed randomly on the uniform scratches.

Optical and electron microscopic examination of as-polished specimens of the three materials revealed nothing significant other than the presence of scratches on the gallium arsenide specimens described above. Specimens of each material were then chemically etched to reveal the microstructure. The etchant used for zinc selenide and zinc sulfide was a boiling solution of one part hydrofluoric acid (conc.) and one part water by volume. The etchant used for gallium arsenide was a room temperature solution of three parts nitric acid (conc.), one part hydrofluoric acid (48%) and four parts water by volume.

Figure 1 shows the grain structure of the zinc selenide and the zinc sulfide. The zinc selenide has a relatively large grain size with many grains containing twins: the zinc sulfide has an extremely fine grain size. The etched gallium arsenide specimen was found to be composed of five grains, two of which were quite large. The grain boundaries were essentially perpendicular to the 1.50 in. dimension on the specimen, although one grain did not extend completely across the specimen. Knoop microhardnesses (50 gm load) of the zinc selenide, zinc sulfide, and gallium arsenide were measured to be 100, 290, and 635, respectively.

Transmission electron microscopic examination of replicas from etched specimens showed that the grain boundaries of all three materials were narrow and free of any precipitates. The only significant feature found on any of the three materials was the presence of extremely small precipitates within the grains of the gallium arsenide as shown in Figure 1c.

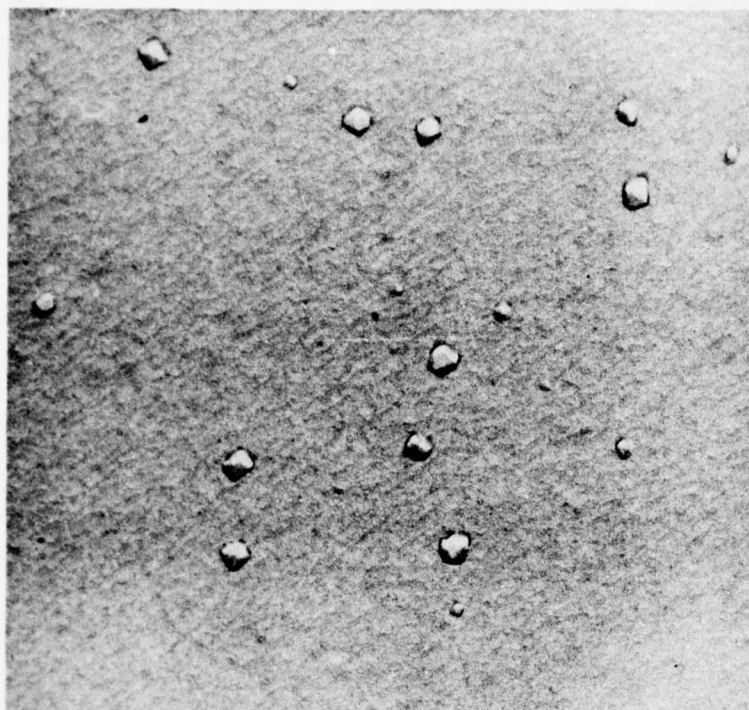


a. Grain Structure of Zinc Selenide, Mag. 135X

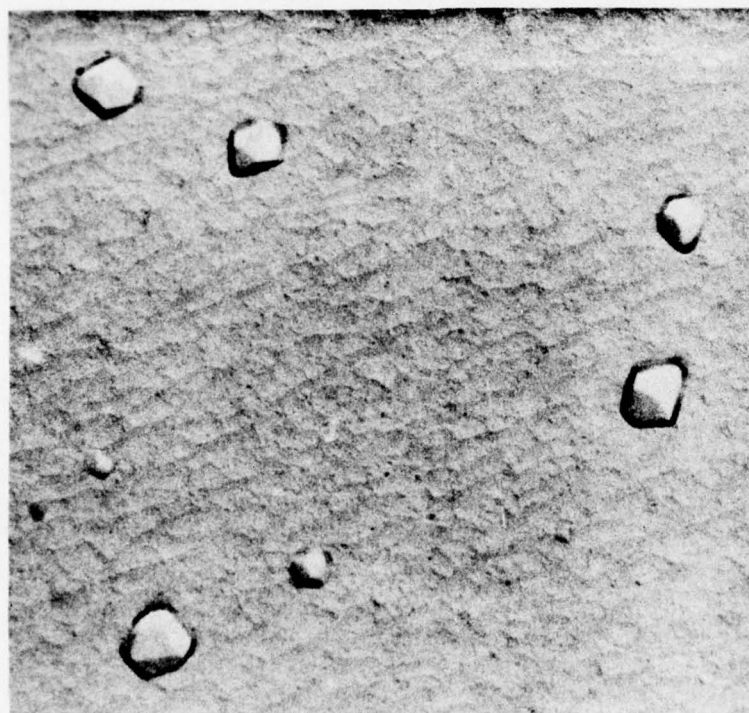


b. Grain Structure of Zinc Sulfide, Mag. 600X

Figure 1. Microstructure of Infrared Window Materials (Continued)



4500X



10,000X

c. Precipitates within the Grains of Gallium Arsenide

Figure 1. Microstructure of Infrared Window Materials (Concluded)

B. Test Matrix

The experimental test matrix used for the evaluation of the erosion behavior of zinc selenide, zinc sulfide, and gallium arsenide is presented in Table 1. Specimens of all three materials were obtained at various progressive stages of erosion created by the impact of a single drop, overlapping impacts from single drops, and multiple impacts from various exposure times in the rainfield of the AFML/Bell erosion facility. A constant velocity (730 fps) and a constant drop diameter (1.8 mm for the rainfield and 2.0 mm for the single drop generator) were used for this series of specimens. The 2.0 mm drop diameter for the single drop generator was as close to 1.8 mm as it was practical to obtain. Microscopic examination of these progressively eroded specimens provided the basis for identifying the erosion mechanisms. Infrared transmittance measurements after various exposure times in the rainfield provided an understanding of the relationship between erosion damage and transmission losses.

The effects of drop size on erosion mechanisms were investigated for zinc selenide at one velocity (730 fps) by means of single and overlapping drop impact. The effects of higher velocity (1120 fps) on erosion mechanisms were investigated for both zinc selenide and zinc sulfide by means of single drop impact at one drop size (2.0 mm diameter). In addition, the protective abilities of zinc sulfide outer layers of various thicknesses applied to zinc selenide substrates were evaluated for 2.0 mm diameter drops at 730 fps impact velocity. Microscopic examination served as the means of determining drop size and impact velocity effects and evaluating the performance of the bilayered specimens.

The following sections describe the results obtained from each series of experiments. Details of the experimental procedures and analyses of the specimens are also included in the pertinent section.

TABLE 1
EXPERIMENTAL TEST MATRIX

<u>Material</u>	<u>Impact Velocity (fps)</u>	<u>Single Drop Impact (Drop Dia. mm)</u>	<u>Overlapping Single Drop Impact (Drop Dia. mm)</u>	<u>Multiple Drop Impact in Rainfield</u>
ZnSe	730	0.7	0.7	-
ZnSe	730	2.0	2.0	1.8mm drop, 1 in./hr.
ZnSe	730	2.5	2.5	-
ZnSe	1120	2.0	-	-
ZnS	730	2.0	2.0	1.8mm drop, 1 in./hr.
ZnS	1120	2.0	-	-
GaAs	730	2.0	2.0	1.8mm drop, 1 in./hr.
ZnS Layer on ZnSe				
0.25 mm ZnS	730	2.0	2.0	-
0.50 mm ZnS	730	2.0	2.0	-
1.00 mm ZnS	730	2.0	2.0	-

C. Single Drop Impact on Homogeneous Materials

1. Single Drop Generator

A liquid drop generator as shown in the schematic diagram in Figure 2 was installed in the main chamber of the AFML/Bell erosion facility to permit the experimental investigation of the effects of single water drop impact on the selected infrared transmitting materials. Individual drops of water are generated by gravity feed at the tip of the hypodermic needle when the syringe barrel is open to atmospheric pressure via the first position of the two-way solenoid valve. The barrel of the syringe holds 50 ml of water. The size of the drop is governed by the bore of the hypodermic needle: the rate of drop formation is regulated by the length of the needle.

The second position of the two-way solenoid valve opens the system to the vacuum pump. Reduced pressure over the liquid then terminates the flow through the needle. The bleed valve serves to establish an adjustable pressure differential between the pressure in the reservoir and that in the main chamber of the erosion facility. This function serves the following two purposes: 1) instantaneous termination of flow of drops without drawing air into the reservoir and creating turbulent aeration of the liquid and 2) maintenance of the appropriate pressure differential in the system, even though the main chamber is being operated at reduced pressure.

One of the primary objectives of this program was to determine the effects of drop size on the response of the materials to impact. With the single drop generator, drops having preselected diameters in the range of 0.7 to 2.5 mm can be generated in a controlled and reproducible manner. A 23 gage hypodermic needle produces a 2.5 mm diameter drop, the largest size investigated. A 27 gage hypodermic needle, the smallest available, produces a 2.0 mm diameter drop. The 2.0 mm diameter drop was selected as representative of the drop size in the standard rainfield in the erosion facility. The 2.0 mm

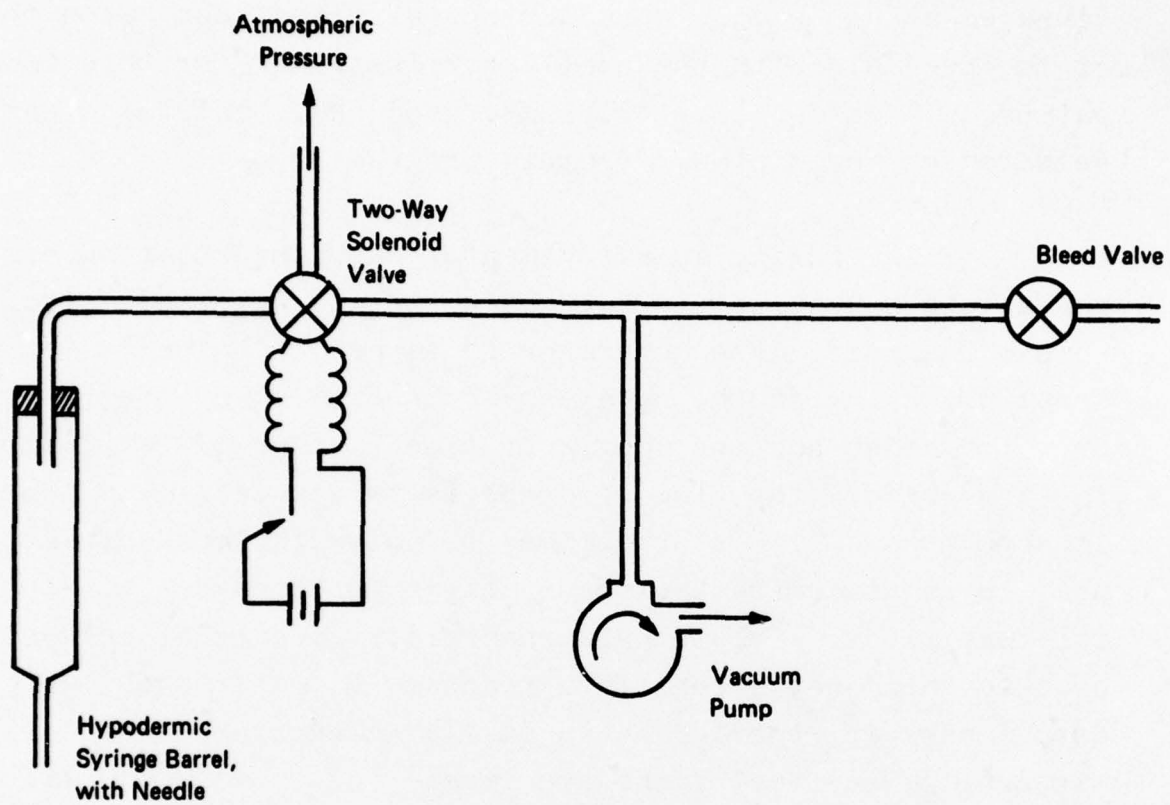


Figure 2. Schematic of Single Liquid Drop Generator

diameter drop is somewhat larger than the mean drop diameter of 1.8 mm in the rainfield; however, it was not practical to reduce the single drop diameter such a small amount below that generated by free fall from the needle. Drops with diameters less than 2.0 mm are produced by means of an oscillator which vibrates a thin needle in a horizontal plane just below the tip of the needle. With the oscillator installed for this investigation, 0.7 mm diameter drops are produced. This size was selected as the minimum for this program.

During an experimental run, the rotating arm with the attached specimen is brought up to the selected velocity before the water drop generator is turned on. The number of drops which impact the specimen is controlled by the rate of drop formation and the length of time (number of revolutions of the arm) before the flow of drops is terminated. The number of impacts versus time on specimens of polymethylmethacrylate was used to obtain correct exposure times for each set of experimental conditions. Polymethylmethacrylate is a relatively soft plastic which has a sensitive response to water drop impact: each drop impact is recorded as an easily recognizable annular depression on the surface of the specimen.

2. Impact at 730 Feet Per Second

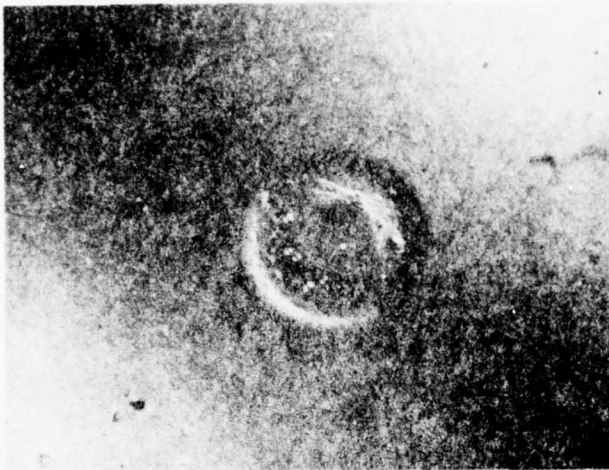
The infrared window materials subjected to single water drop impact at 730 fps are listed in Table 2 along with the drop diameters and the radii of the resultant ring fractures. Figure 3 shows micrographs at low magnification of typical impact sites created by 0.7, 2.0, and 2.5 mm diameter drops. The variations in intensity in these micrographs result from the Nomarski interference contrast which was used to enhance the appearance of the surface damage. Nomarski interference contrast is sensitive to surface height differences of 300\AA ($\approx \lambda/20$). The variations in light intensity produced by this technique are quite noticeable when low magnification objective lenses are used. Based on the micrographs in Figure 3, the ranking of the

TABLE 2
SPECIMENS SUBJECTED TO SINGLE
WATER DROP IMPACT AT 730 FPS

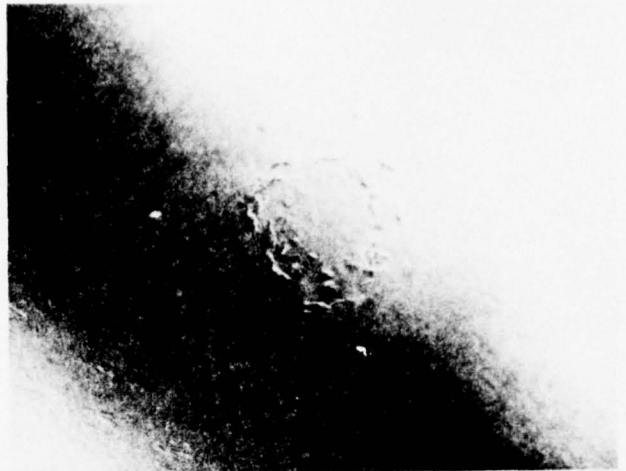
<u>Material</u>	<u>Drop Diameter (mm)</u>	<u>Ring Fracture Radii (mm)</u>	
		<u>Inner</u>	<u>Outer</u>
PMMA	0.7	.12 ^(a)	.30 ^(a)
ZnSe	"	.12	.30
PMMA	2.0	.22 ^(a)	.46 ^(a)
ZnSe	"	.18	.71 (.48) ^(b)
ZnS	"	.32	.41
GaAs	"	.36	.52
PMMA	2.5	.22 ^(a)	.52 ^(a)
ZnSe	"	.18	.83 (.48) ^(b)

(a) Radii of indented annulus.

(b) Major extent of cracking lies within the outer radius in parentheses.

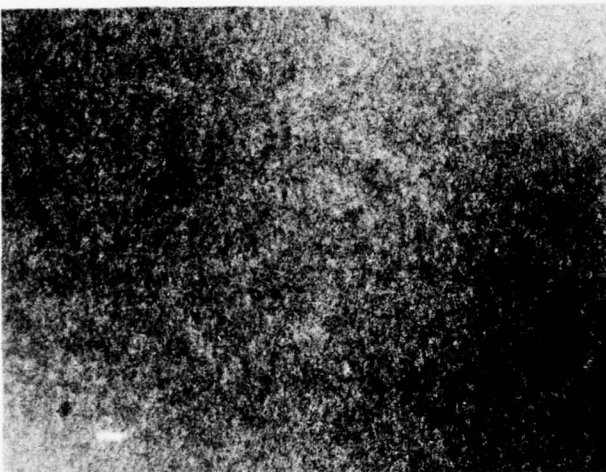


Polymethylmethacrylate

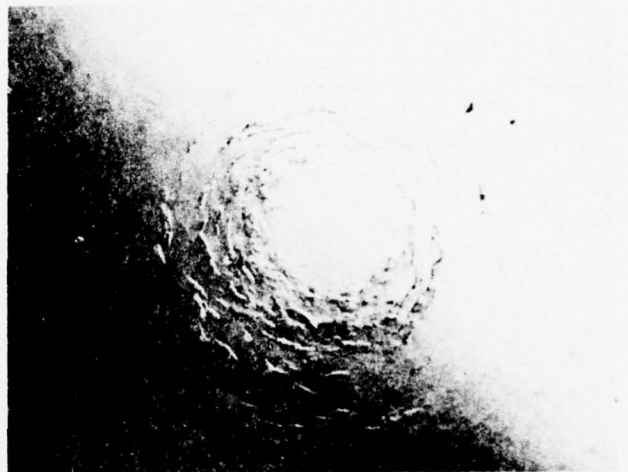


Zinc Selenide

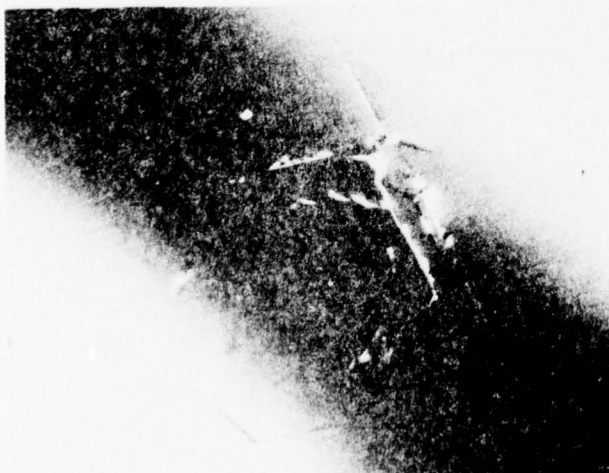
a. 0.7 mm Diameter Drop



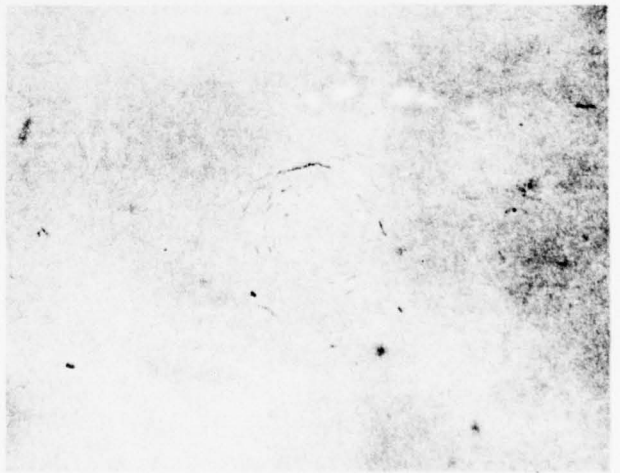
Polymethylmethacrylate



Zinc-Selenide



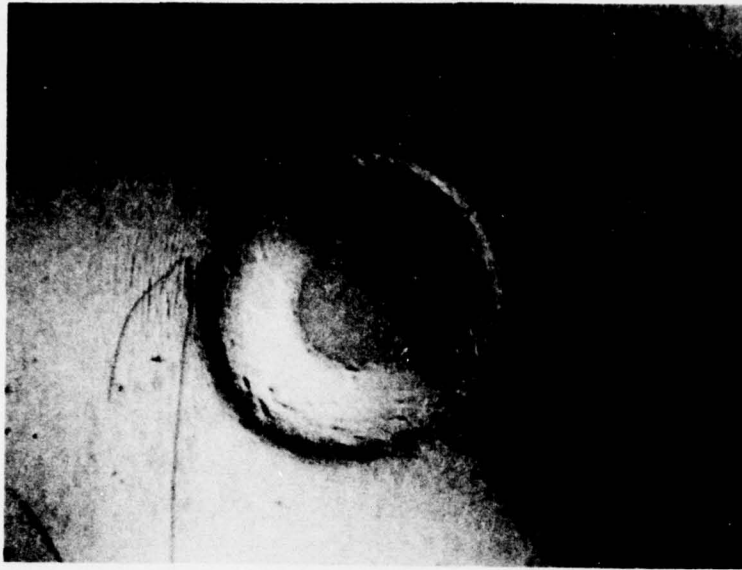
Gallium Arsenide



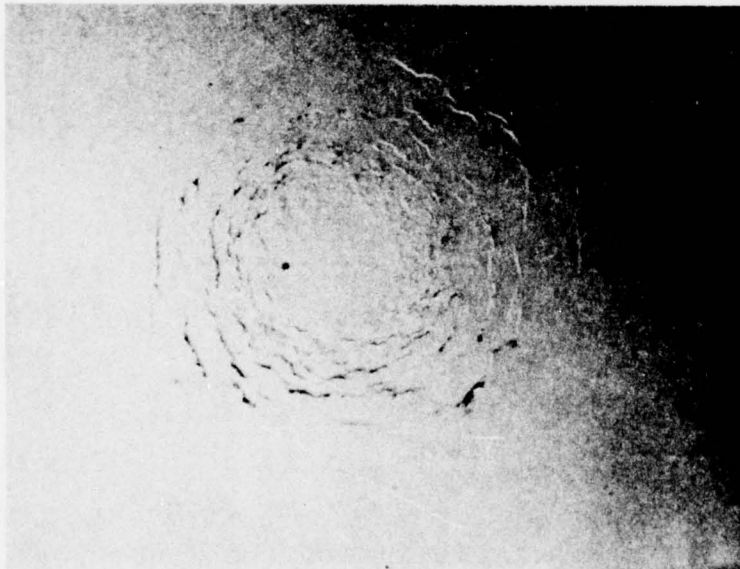
Zinc Sulfide

b. 2.0 mm Diameter Drop

Figure 3. Damage from Single Water Drop Impact at 730 fps. Mag. 40X (Continued)



Polymethylmethacrylate



Zinc Selenide

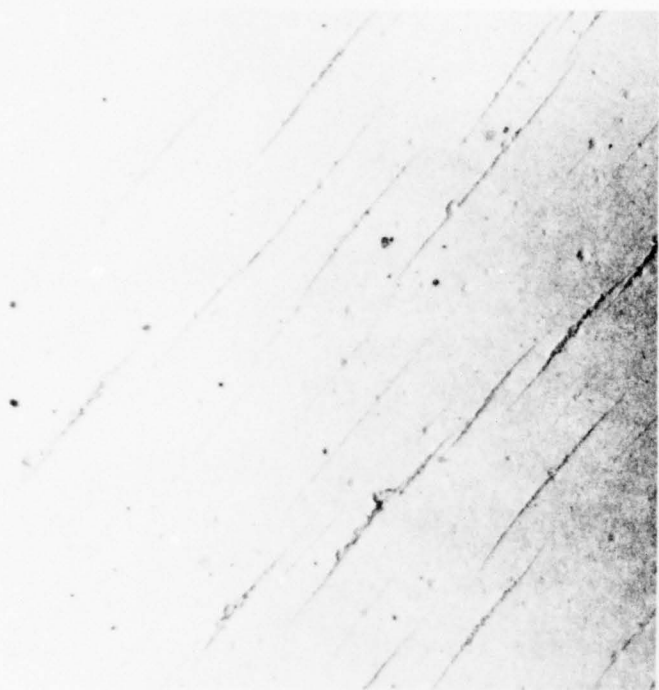
c. 2.5 mm Diameter Drop

**Figure 3. Damage from Single Water Drop Impact at 730 fps. Mag. 40X
(Concluded)**

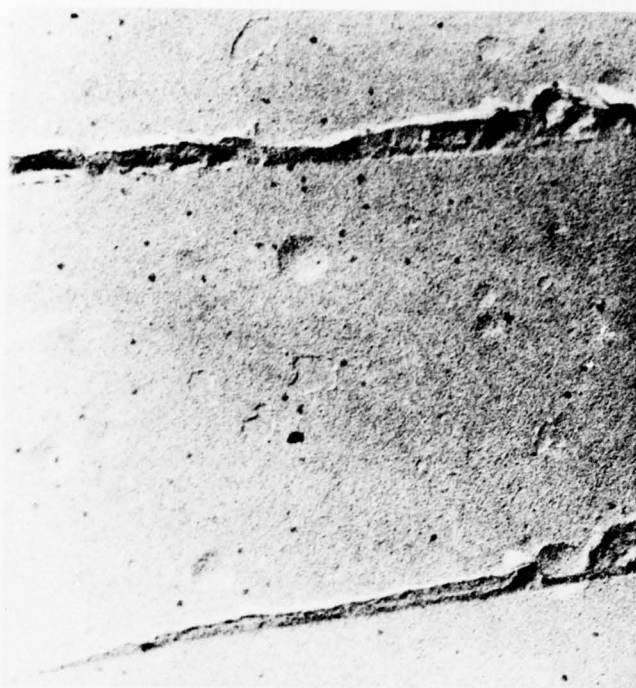
infrared window materials in order of increasing resistance to visible impact damage is zinc selenide, gallium arsenide, and zinc sulfide. The large grained gallium arsenide shows evidence of preferred crystallographic orientation of cleavage along {110} planes. The smaller grained zinc selenide and zinc sulfide show no obvious orientation of cleavage. The primary effect of drop diameter, evaluated with zinc selenide and polymethylmethacrylate, is to change the size of the damaged area. A 0.7 mm diameter drop appears to produce damage comparable to that of the larger drops, only over a smaller area.

Details of the damage from impact by 2.0 mm diameter drops are illustrated in the electron micrographs in Figure 4. What appear at low magnification to be cracks in the PMMA at the outside of the indented annulus are actually steps in the surface. These steps are quite evident at 20,000X magnification. Zinc selenide exhibits extensive surface cracking and spalling. This spalling always occurs on the side of the crack opposite the center of drop impact. Gallium arsenide also undergoes surface cracking and spalling, although not to the extent exhibited by zinc selenide. The surface cracks formed on zinc sulfide are very shallow, having a maximum depth of approximately $0.56\mu\text{m}$ based on the length of the shadow cast in the micrograph at 20,000X magnification. This crack depth is an order of magnitude less than that for zinc selenide or gallium arsenide. Zinc sulfide is obviously the most erosion resistant of the materials subjected to single drop impact at 730 fps. Electron micrographs of the fractures formed on zinc selenide by the impact of 0.7 and 2.5 mm diameter drops are not presented since the characteristics of the fractures were similar to those of the fractures formed by 2.0 mm diameter drops.

Following the initial optical and electron microscopic examinations, the impacted infrared window specimens were chemically etched to reveal the relationships between the ring fractures and the microstructures of the materials. The etchants, described in the Description of Materials Section,

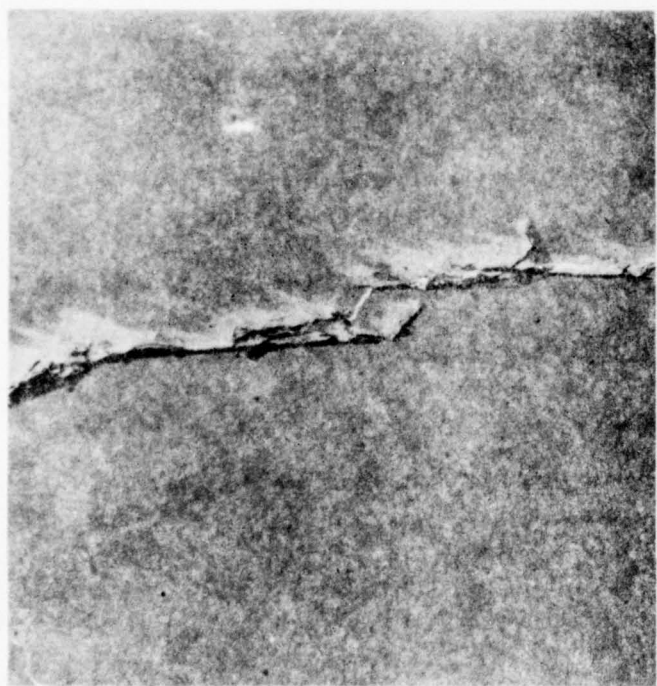


2,000X

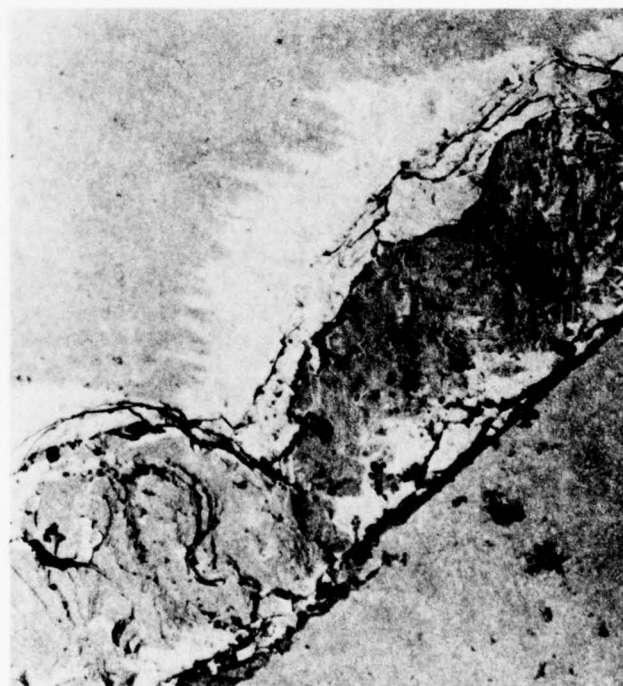


20,000X

a. Polymethylmethacrylate



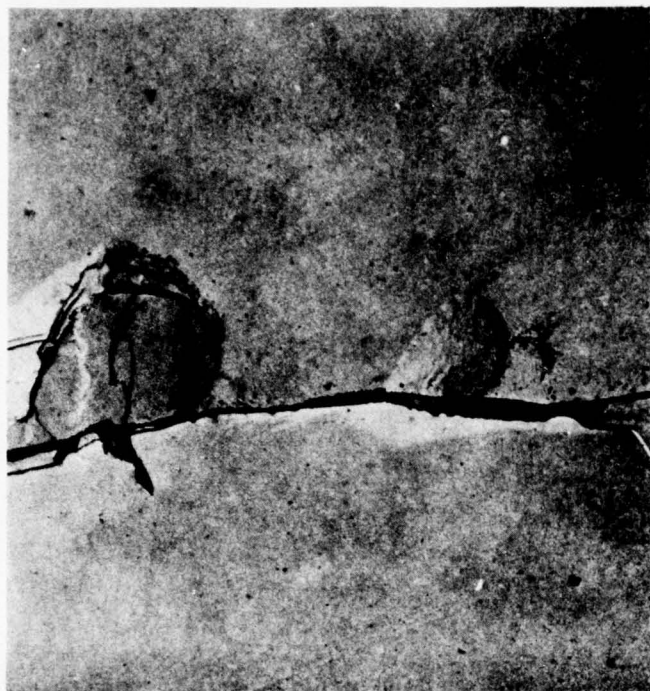
3,000X



3,000X

b. Zinc selenide

Figure 4. Electron Micrographs of Damage from 2.0 mm Diameter Single Water Drop Impact at 730 fps.
(Continued)

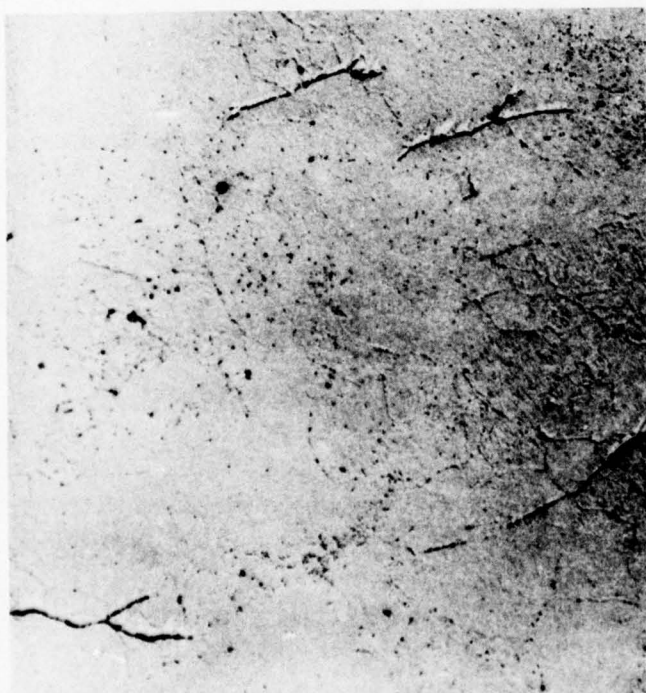


3,000X



3,000X

c. Gallium Arsenide



2,000X



20,000X

d. Zinc Sulfide

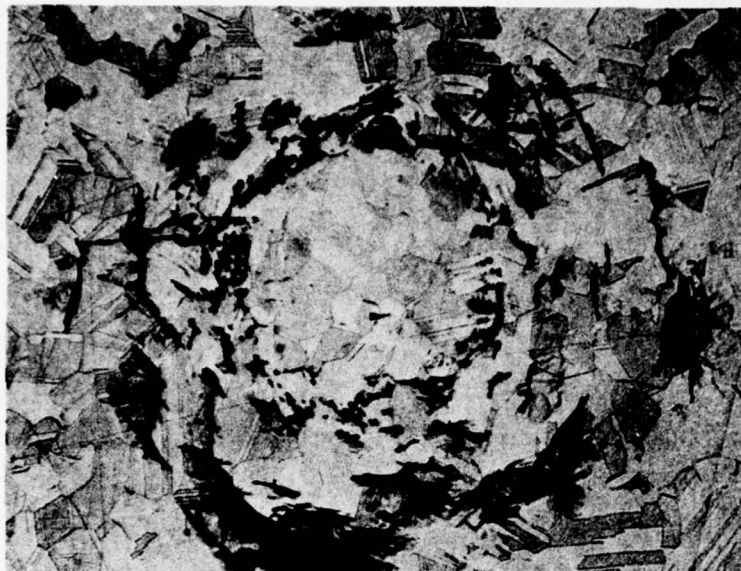
Figure 4. Electron Micrographs of Damage from 2.0 mm Diameter Single Water Drop Impact at 730 fps.
(Concluded)

were a boiling solution of hydrochloric acid in water for zinc selenide and zinc sulfide and a room temperature solution of nitric and hydrofluoric acids in water for gallium arsenide.

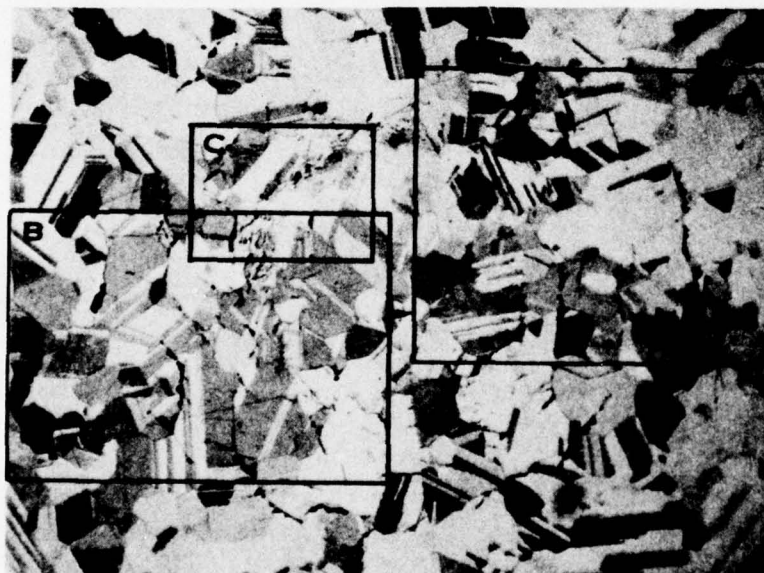
Optical micrographs, after etching, of a ring fracture formed on zinc selenide by impact with a 0.7 mm diameter water drop at 730 fps are presented in Figure 5. Transmitted light was used in Figure 5a to show the overall appearance of the fracture in relation to the grain structure. Transmitted light was found to be particularly useful in revealing surface fractures, as well as the location and extent of subsurface damage, on the optically transparent zinc selenide and zinc sulfide specimens. Subsurface damage as revealed by transmitted light would include both cracks which did not extend to the surface and surface cracks which changed direction to become more nearly parallel to the surface. Most of the loss in optical transmission in Figure 5a appears to be caused by the latter, i.e., surface cracks which change angle below the surface.

Figure 5b outlines three areas of interest which are shown at higher magnifications in Figures 5c, d and e. The predominantly transgranular nature of the fractures is quite apparent in Figure 5c; however, some intergranular cracking is evident near the inner radius of the ring fracture as shown in Figure 5d. Figure 5e shows what appear to be dislocation etch pits which are at the inner radius of the ring fracture and just inside the uncracked circular area around the center of impact.

Optical micrographs, after etching, of a ring fracture formed on zinc selenide by impact with a 2.0 mm diameter water drop at 730 fps are presented in Figure 6. Figure 6a shows the overall appearance of the impact site and Figure 6b identifies three areas with significant features which are shown at higher magnifications in Figures 6c, d, and e. Again, as was the case with the 0.7 mm diameter drop impact site, the fractures are predominantly transgranular (Figure 6c) with some intergranular fracture included near the inner radius (Figure 6d). Dislocation etch pits at the inner radius are shown in Figure 6e.

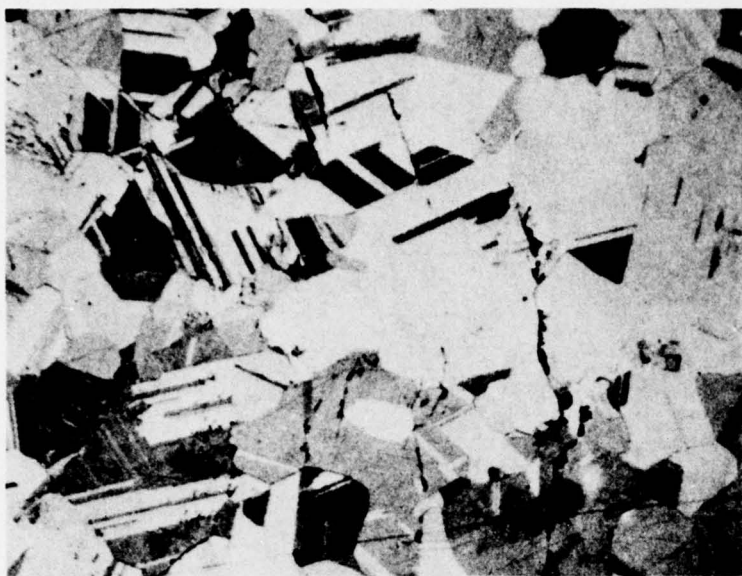


a. Overall Appearance, Transmitted Light. Mag. 135X



b. Overall Appearance. Mag. 135X

Figure 5. Ring Fracture on Zinc Selenide Formed by Impact with 0.7 mm Diameter Drop at 730 fps. Reflected Light Except Where Noted (Continued)

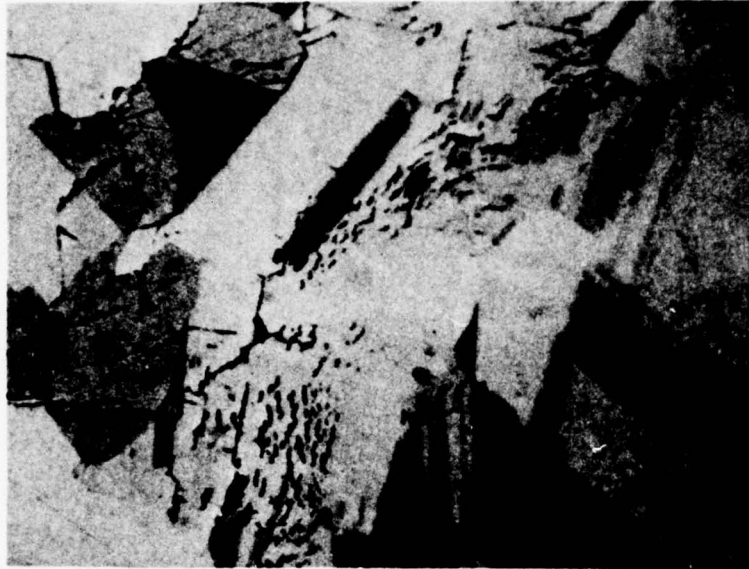


c. Transgranular Cracks in Area A. Mag. 250X



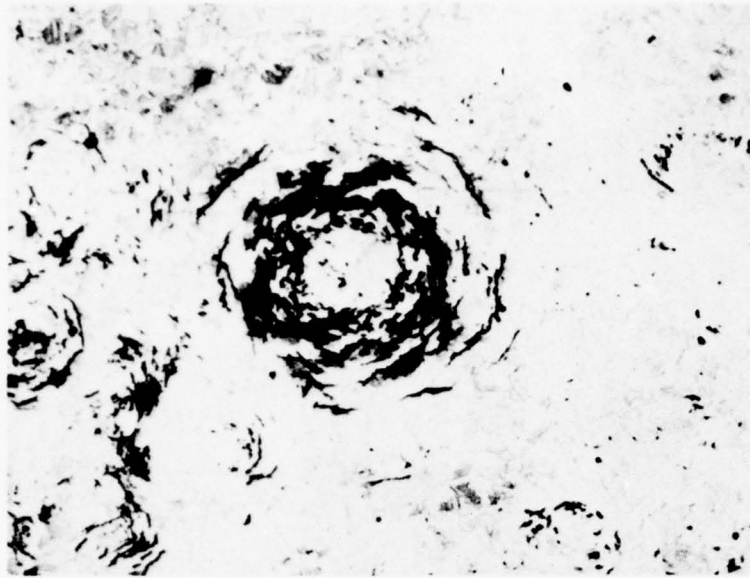
d. Evidence of Intergranular Cracks in Area B. Mag. 250X

Figure 5. Ring Fracture on Zinc Selenide Formed by Impact with 0.7 mm Diameter Drop at 730 fps. Reflected Light Except Where Noted (Continued)



e. Etch Pits at Inner Radius of Ring Fracture in Area C. Mag. 470X

Figure 5. Ring Fracture on Zinc Selenide Formed by Impact with 0.7 mm Diameter Drop at 730 fps. Reflected Light Except Where Noted (Concluded)



a. Overall Appearance, Transmitted Light. Mag. 30X



b. Appearance of Left Side. Mag. 135X

Figure 6. Ring Fracture on Zinc Selenide Formed by Impact with 2.0 mm Diameter Drop at 730 fps. Reflected Light Except Where Noted (Continued)



c. Transgranular Cracks in Area A. Mag. 250X



d. Evidence of Intergranular Cracks in Area B. Mag. 250X

Figure 6. Ring Fracture on Zinc Selenide Formed by Impact with 2.0 mm Diameter Drop at 730 fps. Reflected Light Except Where Noted (Continued)



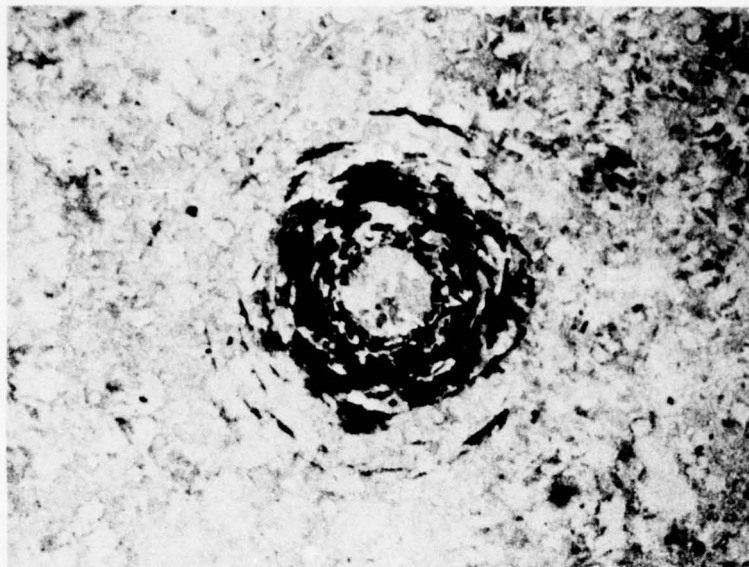
e. Etch Pits at Inner Radius of Ring Fracture in Area C. Mag. 470X

**Figure 6. Ring Fracture on Zinc Selenide Formed by Impact with 2.0 mm Diameter Drop
at 730 fps. Reflected Light Except Where Noted
(Concluded)**

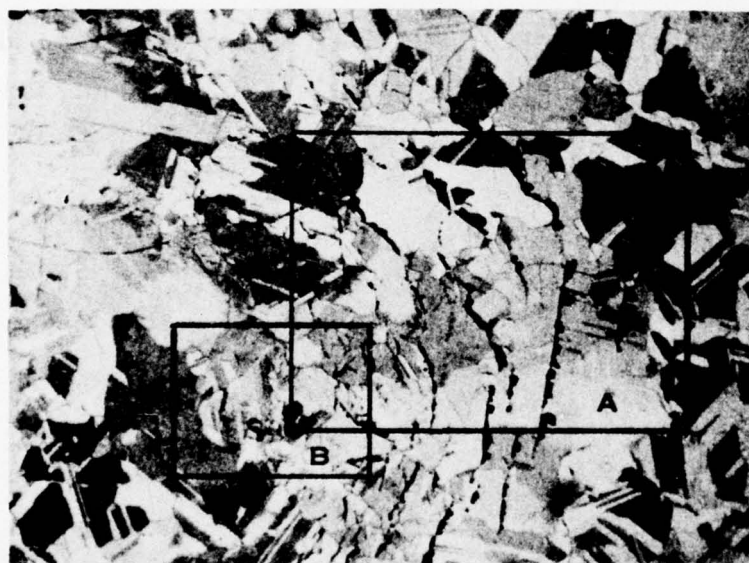
Micrographs, after etching, of a ring fracture formed on zinc selenide by impact with a 2.5 mm diameter water drop at 730 fps are presented in Figure 7. The fractures at both the outer and the inner radii appear to be transgranular (Figure 7c) with little or no evidence of intergranular fracture to the extent present in the impact sites formed by 0.7 and 2.0 mm diameter drops. Again, as was the case for the two smaller drop impact sites, extensive dislocation etch pits were found at the inner radius of the ring fracture (Figure 7d).

Electron micrographs of etched zinc selenide specimens showing various features of the ring fractures at higher magnifications are presented in Figures 8, 9 and 10. Both the intergranular and the transgranular natures of the cracks near the inner radius of the ring fracture formed by the impact of a 0.7 mm diameter drop are shown in Figure 8. Figure 9a shows a typical transgranular crack formed by the impact of a 2.5 mm diameter drop. This type of transgranular cracking is also common to the ring fractures formed by 0.7 and 2.0 mm diameter drops. Figure 9b reveals intergranular cracking within the ring fracture formed by the 2.5 mm diameter drop. At the lower magnifications obtained with optical microscopy (Figure 7), intergranular cracks could not be definitely identified. The intergranular crack in Figure 9b is obviously very narrow. Figure 10 shows dislocation etch pits found near the inner radius of the ring fracture formed by the impact of a 2.0 mm drop. The tetrahedral shape of the pits formed on grains oriented in the $\langle 111 \rangle$ direction is evident even though the specimen was over-etched. The etch pits found at ring fractures formed by 0.7 and 2.5 mm drops were similar to those shown in Figure 10.

Optical micrographs, after etching, of a ring fracture formed on zinc sulfide by impact with a 2.0 mm diameter water drop at 730 fps are presented in Figure 11. The overall appearance with transmitted light is shown in Figure 11a. The difference in subsurface damage caused by a single drop impact on zinc sulfide and zinc selenide is readily apparent when



a. Overall Appearance, Transmitted Light. Mag. 30X



b. Appearance of Right Side. Mag 135X

Figure 7. Ring Fracture on Zinc Selenide Formed by Impact with 2.5 mm Diameter Drop at 730 fps. Reflected Light Except Where Noted (Continued)



c. Transgranular Cracks in Area A. Mag. 250X

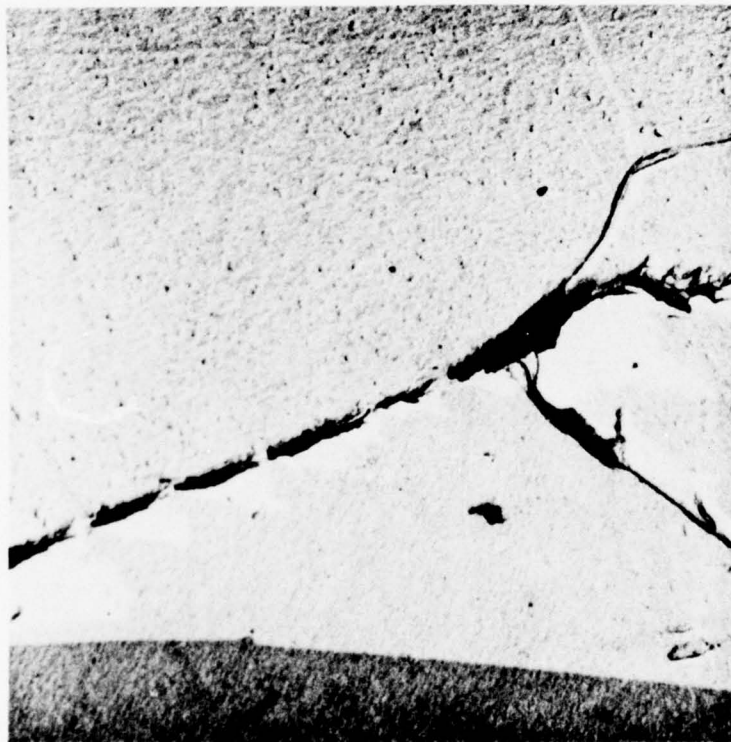


d. Etch Pits at Inner Radius of Ring Fracture in Area B. Mag. 470X

**Figure 7. Ring Fracture on Zinc Selenide Formed by Impact with 2.5 mm Diameter Drop
at 730 fps. Reflected Light Except Where Noted
(Concluded)**

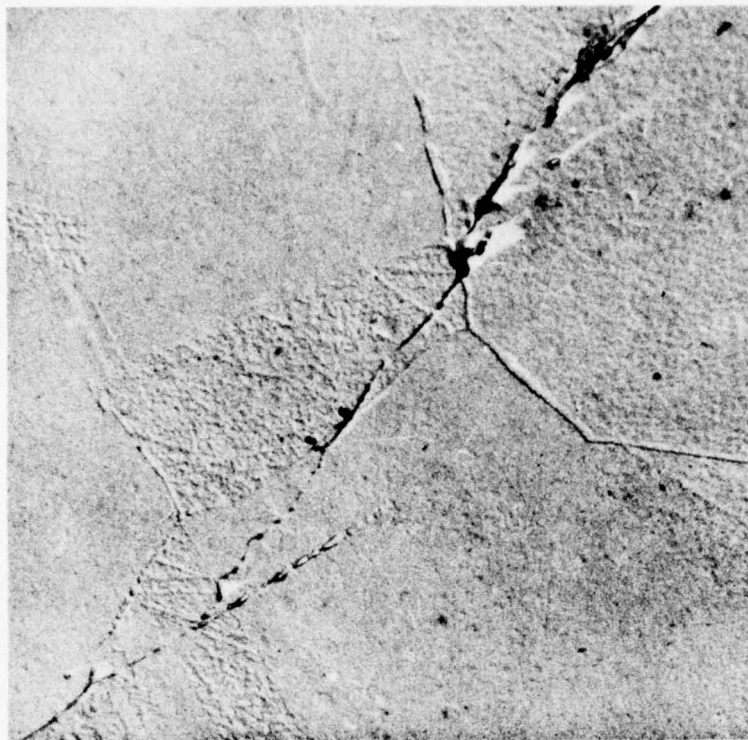


a. Cracking and Chipping at Grain Boundaries

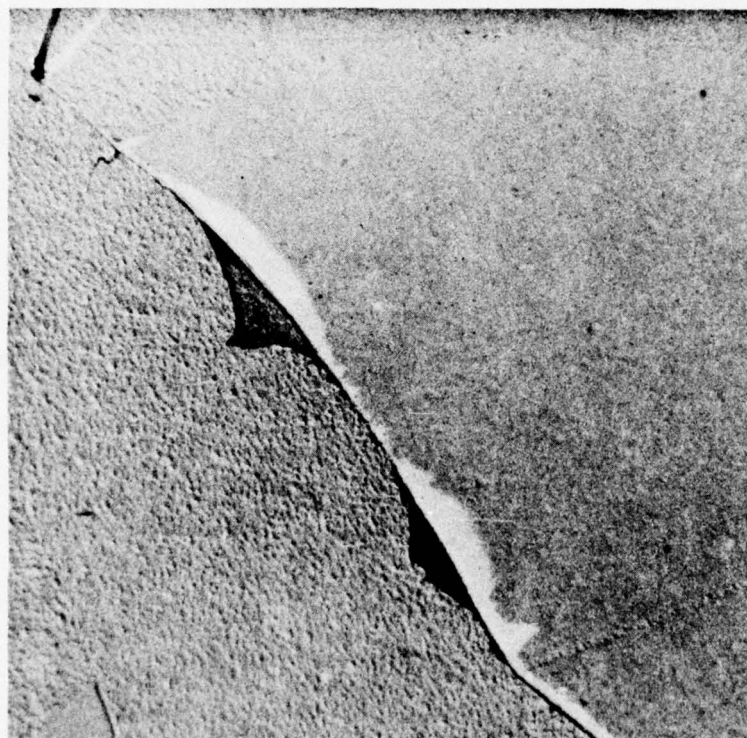


b. Mixed Intergranular and Transgranular Cracks

Figure 8. Electron Micrographs of Ring Fractures at Site of Impact of 0.7 mm Diameter Drop on Zinc Selenide. Mag. 2000X

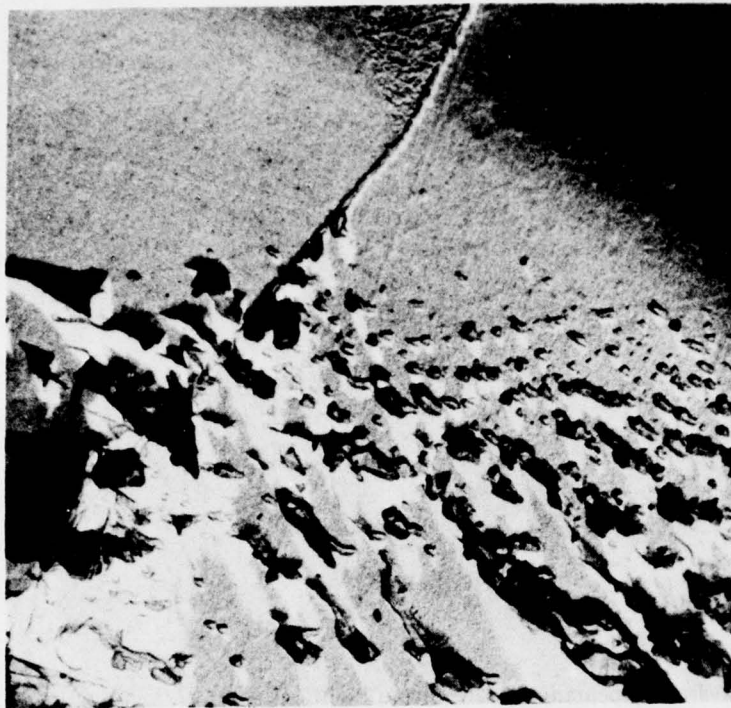


a. Transgranular Crack



b. Intergranular Crack

Figure 9. Electron Micrographs of Ring Fractures at Site of Impact of 2.5 mm Diameter Drop on Zinc Selenide. Mag. 2000X

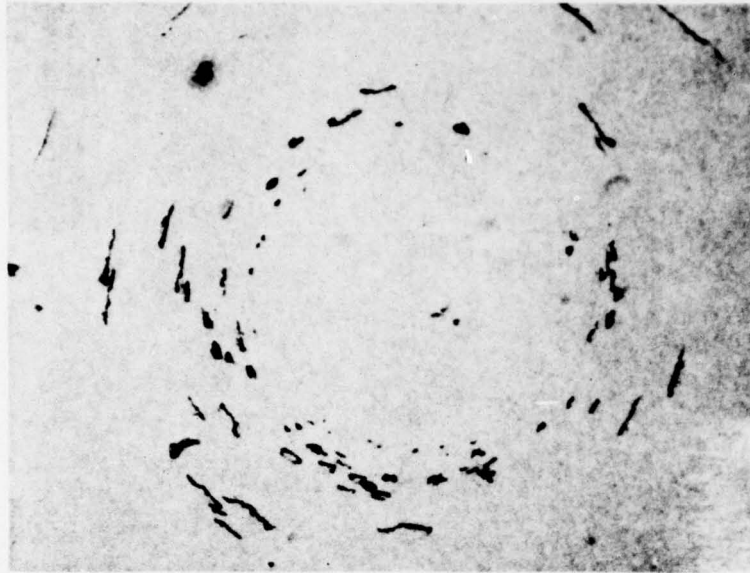


2000X

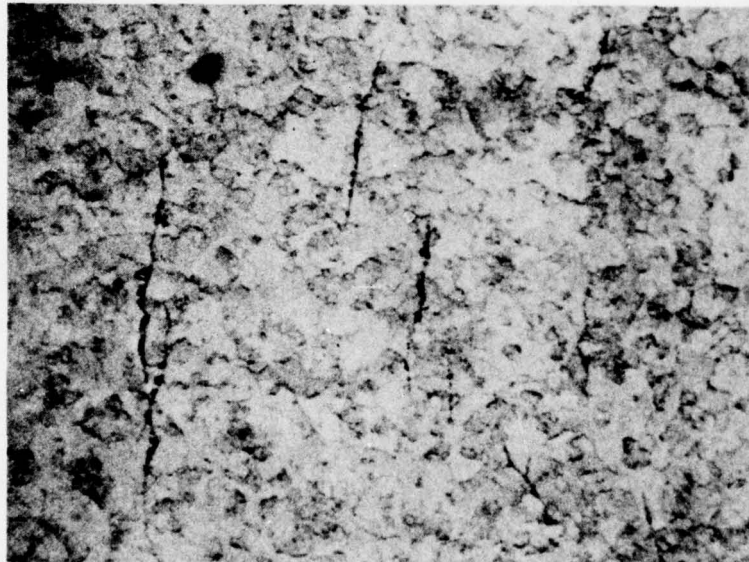


8000X

Figure 10. Electron Micrographs of Dislocation Etch Pits at Site of Impact of 2.0 mm Diameter Drop on Zinc Selenide



a. Overall Appearance, Transmitted Light. Mag. 135X



b. Transgranular Cracks on Left Side. Mag. 470X

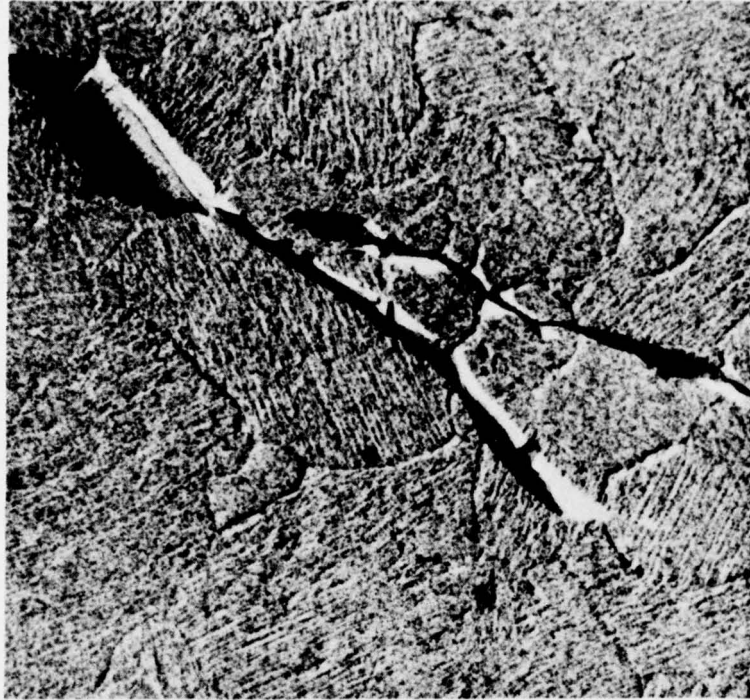
Figure 11. Ring Fracture on Zinc Sulfide Formed by Impact with 2.0 mm Diameter Drop at 730 fps.

Figure 11a is compared to Figure 6a. Unlike zinc selenide, zinc sulfide shows no significant loss in optical transmission except at the surface cracks, themselves. The closeup of a portion of the fractured area in Figure 11b shows the cracks are transgranular with no evidence of intergranular fracture. The electron micrograph in Figure 12 also illustrates the transgranular nature of the cracks. The electron microscopic examination revealed no evidence of intergranular failure or dislocation etch pits.

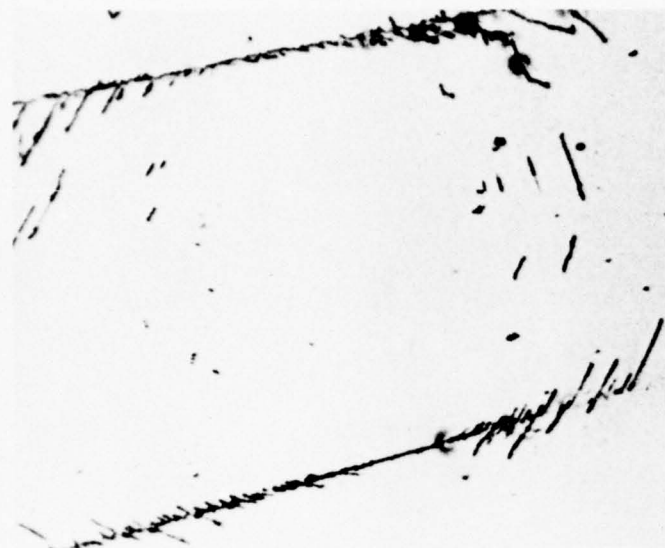
Optical micrographs, after etching, of ring fractures formed on gallium arsenide by impact with 2.0 mm diameter drops are presented in Figure 13. Pre-existing surface scratches serve as nucleation sites for damage as illustrated in Figure 13a. No evidence was found that damage is nucleated by grain boundaries. Figure 13b shows an impact site which straddles a grain boundary that remains undamaged; however, damage at pre-existing scratches is again apparent in this figure. Figure 13c shows an impact site at what appear to be twin boundaries; no interaction can be seen.

Electron micrographs of the gallium arsenide specimen which was etched after being impacted by 2.0 mm diameter drops are presented in Figure 14. Many of the cracks and chipped areas appear to be associated with precipitate particles within the grains such as were shown in Figure 1b. Particles can be seen at the bottom of several of the cracks in Figure 14. The primary ring fractures occur because the cleavage strength of the material is exceeded by the stresses generated by drop impact. However, a large amount of secondary cracking appears to be nucleated by stress concentrations at the precipitate particles.

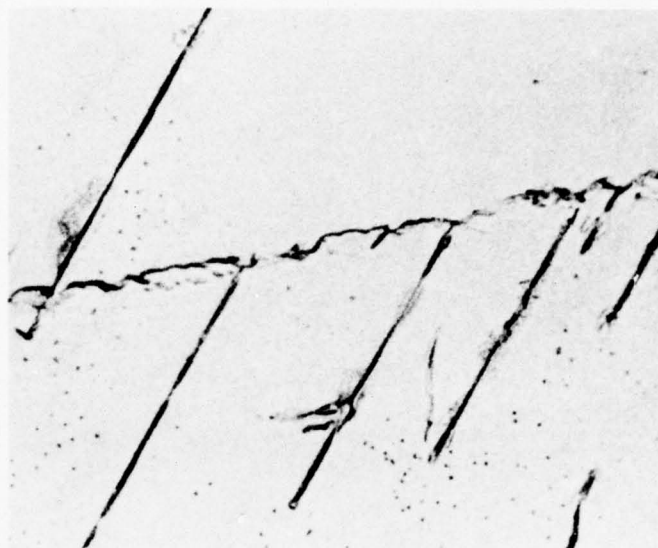
The detailed analyses of the single drop impacted specimens after etching revealed much information on the response of the three materials. Concerning the effects of drop size, the initial appraisal that the 0.7 mm diameter drop produced



**Figure 12. Electron Micrograph of Ring Fracture Cracks on Zinc Sulfide
After Etching to Reveal Grain Boundaries. Mag. 3400X**

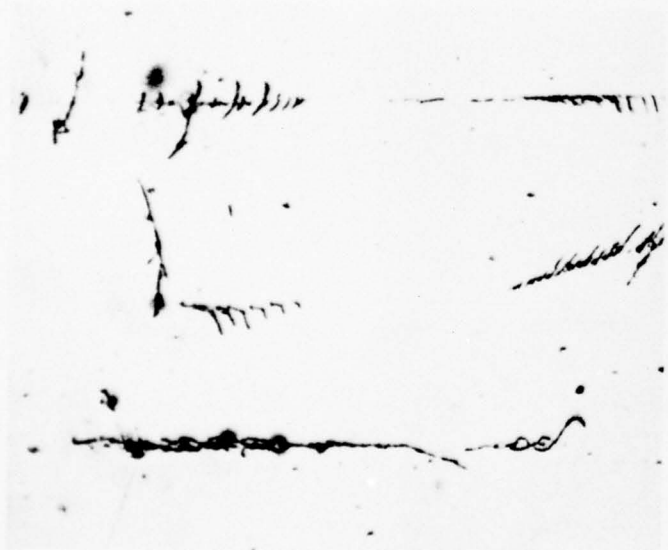


150X



560X

a. Impact Site at Scratches



135X

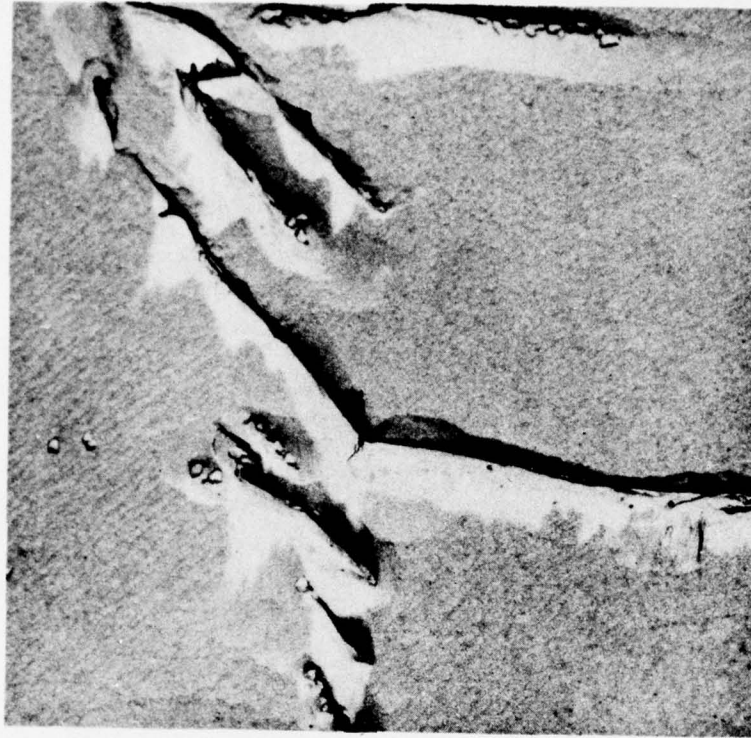
b. Impact Site at Grain Boundary



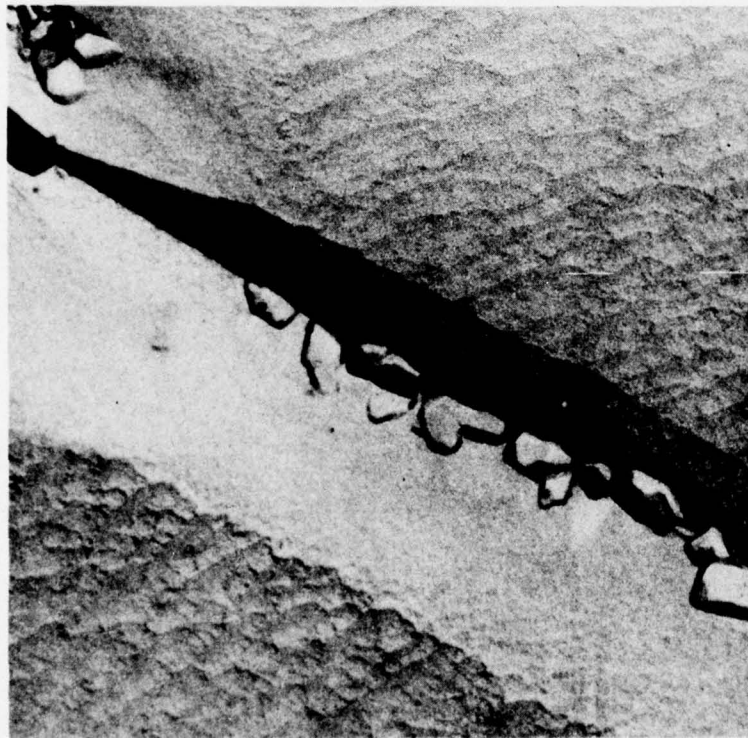
135X

c. Impact Site at Twins, Polarized Light

Figure 13. Ring Fractures on Gallium Arsenide Formed by Impact with 2.0 mm Diameter Drop at 730 fps



2000X



10,000X

Figure 14. Electron Micrographs of Gallium Arsenide Specimen Etched After Impact by 2.0 mm Diameter Water Drop at 730 fps

damage on zinc selenide comparable to that of the larger drops, only over a smaller area, was not completely correct. The predominance of transgranular cleavage, with intergranular cracking and etch pits near the inner ring fracture radii, is common to all impact sites on zinc selenide, regardless of drop diameter. However the extent of subsurface damage is significantly less for the impact site of a 0.7 mm diameter drop than for the impact site of a 2.0 or 2.5 mm diameter drop. This is apparent when Figure 5a is compared to Figures 6a and 7a.

Grains as large as 0.13 mm across are common in the zinc selenide specimens, while large grains in the zinc sulfide specimens are only 0.013 mm, an order of magnitude less. It is probable that the superior erosion resistance of zinc sulfide is related to the shallow depth of the cleavage cracks and the lack of subsurface damage. These, in turn, are related to the small grain size of the zinc sulfide. The small grains limit the depth of the cleavage cracks because they must traverse grain boundaries and undergo directional changes in neighboring grains at different orientations.

The examination by transmitted light of the single drop impact sites on the zinc selenide specimens leads to the theory that much of the subsurface damage consists of the intergranular extension of the surface cracks along grain boundaries which are approximately parallel to the specimen surface. Such evidence of subsurface crack extensions was not found at the impact sites on zinc sulfide. Additional evidence of the weaker grain boundaries in zinc selenide is the intergranular fractures apparent on the specimen surface near the inner ring fracture radii. No intergranular cracks were found at the impact sites on zinc sulfide.

On the basis of this analysis of the ring fractures formed by single drop impacts, it appears that the erosion resistance of zinc selenide can be improved by decreasing the grain size and increasing the strength of the grain boundaries. The

extent of subsurface damage at impact sites on gallium arsenide could not be ascertained because the specimens are opaque. It is apparent that the erosion is enhanced by the presence of surface scratches and subsurface precipitates. Elimination of these two defects should provide an improvement in erosion resistance for gallium arsenide.

3. Impact at 1120 Feet Per Second

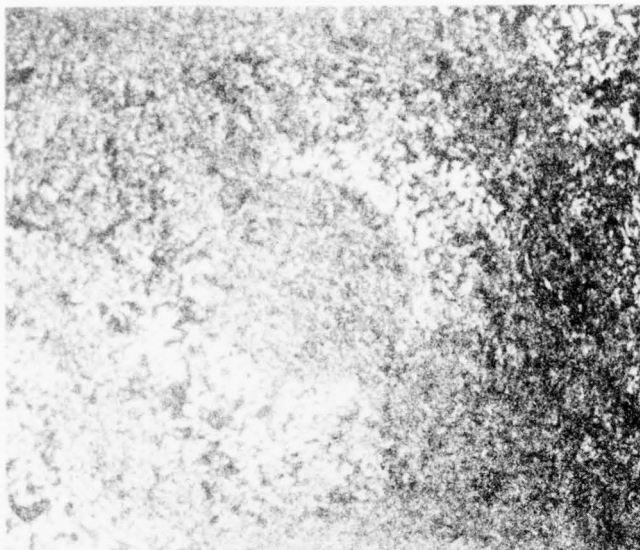
PMMA, zinc selenide, and zinc sulfide were subjected to impact by 2.0 mm diameter water drops at 1120 fps to investigate the effects of an increase in impact velocity upon the behavior of these materials. Prior to this series of experiments, the inside of the test facility was cleaned to reduce solid particle contamination. The drop formation rate of the single drop generator was also increased so that exposure time could be decreased to one minute from the nominal five minutes used for single drop impact experiments at 730 fps. The number of impact sites obtained on each specimen exposed to single drop impact at 1120 fps is listed in Table 3. No evidence of impact sites was found on the zinc sulfide specimen even though sites were readily apparent on the zinc selenide specimen tested before, and the PMMA specimen tested after.

Impact sites formed on PMMA and zinc selenide by 2.0 mm diameter drops at 1120 fps are compared to those formed at 730 fps in Figure 15. It is apparent from this figure that significant solid particle erosion occurred at 1120 fps in addition to the damage from the impact with the water drops. The shock wave formed at 1120 fps apparently stirred up solid particles (sand and glass beads) remaining in the facility from previous erosion tests. This solid particle erosion had been unnoticeable at the lower velocity of 730 fps used for single drop impact experiments up to this time. Dimensions of the damaged areas produced by drop impact at 1120 fps are listed in Table 4. The photographs in Figure 15 and the data in Table 4 show that the velocity had a much greater effect on the dimensions of the damaged area on PMMA than it did on zinc selenide.

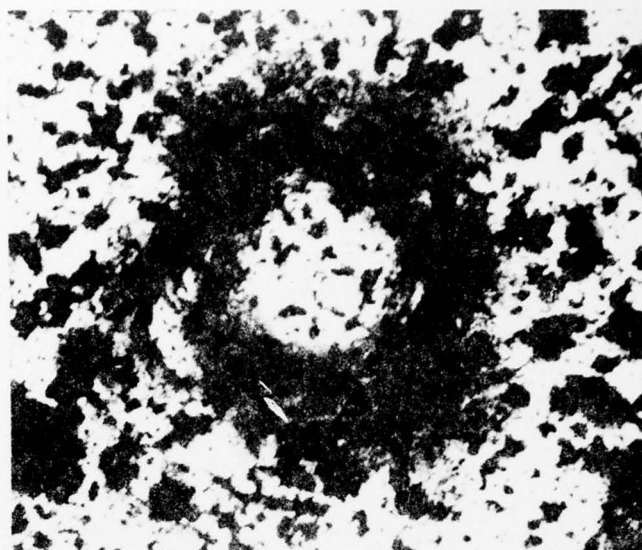
TABLE 3
 NUMBER OF IMPACT SITES OBTAINED DURING
 ONE-MINUTE EXPOSURE TO SINGLE DROP IMPACT AT 1120 fps

<u>Specimen</u> ^(a)	<u>Impact Sites After 1 Minute Exposure</u>
PMMA	19
ZnSe	16
ZnS	None Detectable
PMMA	9

(a) Specimens listed in order of exposure.

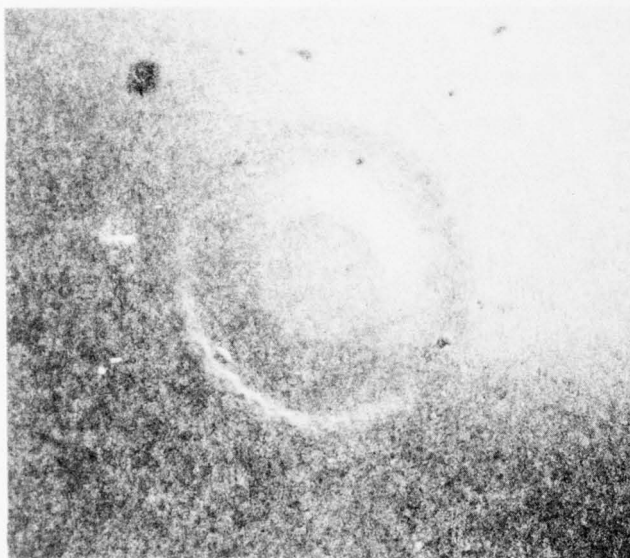


Polymethylmethacrylate

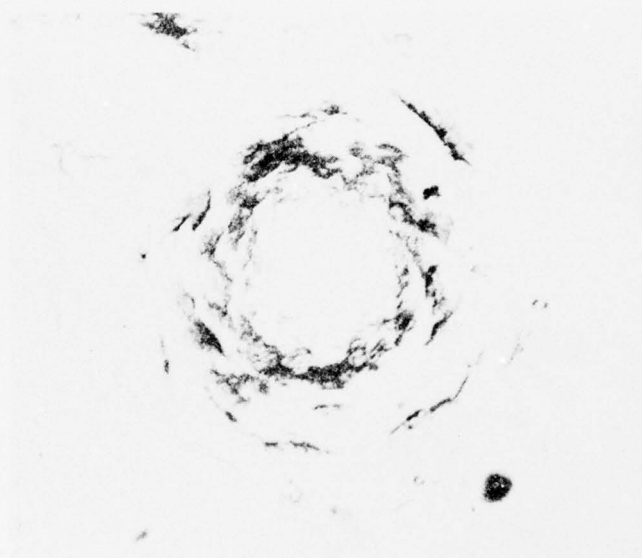


Zinc Selenide

a. 1120 fps Impact Velocity



Polymethylmethacrylate



Zinc Selenide

b. 730 fps Impact Velocity

Figure 15. Effects of Velocity on Damage from Single Water Drop Impact. Mag. 40X

TABLE 4
 DIMENSIONS OF DAMAGE FROM
 SINGLE 2.0 MM WATER DROP IMPACT AT 1120 FPS

<u>Material</u>	<u>Ring Fracture Radii, mm^(a)</u>	
	<u>Inner</u>	<u>Outer</u>
PMMA	.36	.99
"	.30	.86
"	.36	.91
"	.30	.99
"	.28	.71
"	<u>.36</u>	<u>.79</u>
	.33 Avg.	.88 Avg.
ZnSe	.20	.91 (.56) ^(b)
"	.22	1.12 (.64) ^(b)
"	.24	1.14 (.79) ^(b)
"	.18	1.04 (.51) ^(b)
"	<u>.22</u>	<u>.86 (.64)^(b)</u>
	.21 Avg.	1.01 (.63) ^(b) Avg.

- (a) Radii of indented annulus for PMMA.
 (b) Major extent of cracking lies with this radius.
 (c) Results from Table 2 for impact at 730 fps.

<u>Material</u>	<u>Inner Radii</u>	<u>Outer Radii</u>
PMMA	.22	.46
ZnSe	.18	.71 (.48)

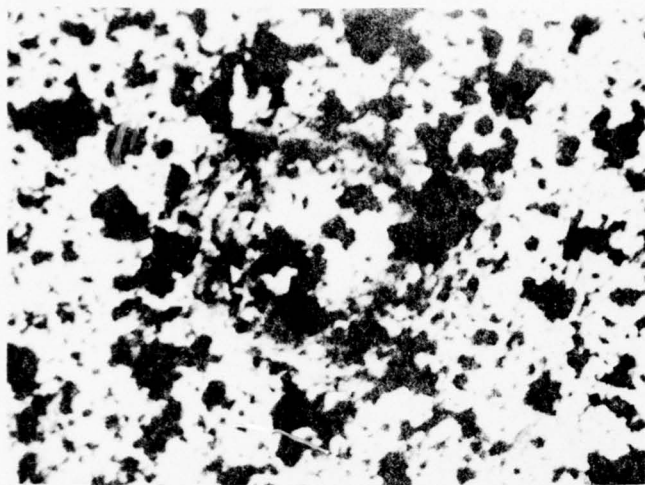
Figure 16a shows details of one of the ring fractures formed on zinc selenide at 1120 fps. This impact site has a large area of the ring fracture that is relatively free of solid particle erosion. For comparison, Figure 16b shows details of a ring fracture formed on zinc selenide at 730 fps. The extent of cracking and the chipping, at the outflow side of the cracks, is surprisingly similar for both impact velocities. An electron micrograph of a ring fracture crack formed on zinc selenide at 1120 fps is shown in Figure 17. Again, the crack is quite similar to those formed by impact at 730 fps (Figure 4b).

Increasing the impact velocity from 730 fps to 1120 fps did not affect the characteristics of the ring fractures on zinc selenide to the extent that was expected. Other than an increase in the areas of the ring fracture, the increase in impact velocity had little effect. The actual extent of damage within the ring fractures appeared to be comparable at both velocities.

D. Overlapping Drop Impact on Homogeneous Materials

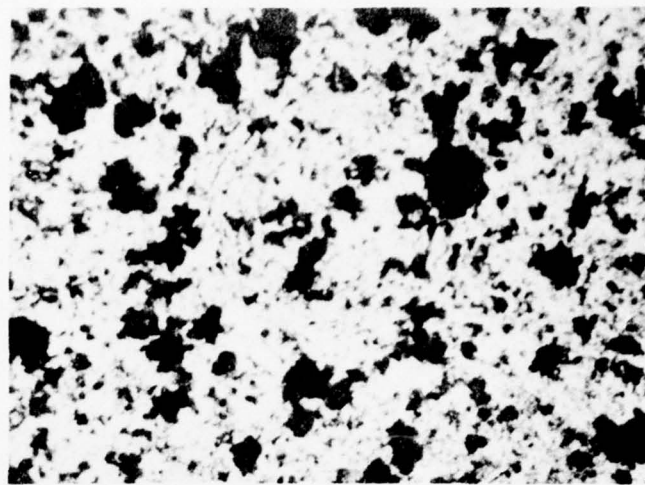
Specimens of zinc selenide, zinc sulfide, and gallium arsenide were subjected to overlapping impacts by 2.0 mm diameter single drops of water at 730 fps. Additional specimens of zinc selenide were impacted with drops of 0.7 and 2.5 mm diameter. These experiments were to determine how material damaged by a drop impact would respond to a subsequent impact at the same site and how this response would be affected by drop size. Knowledge of material behavior in this very early incubation stage is required for understanding the rain erosion process.

Optical micrographs of overlapping impact sites on zinc selenide generated by drops of 0.7, 2.0 and 2.5 mm diameter are presented in Figure 18. These micrographs are of doublet impact sites where the ring fracture from one drop is overlapped by the ring fracture from a second drop. Figure 19 shows triplet impact sites on zinc selenide for drops of 2.0 and 2.5 mm

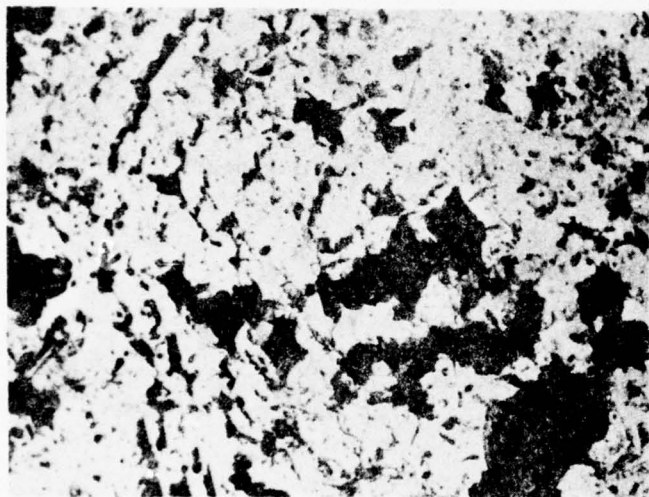


40X

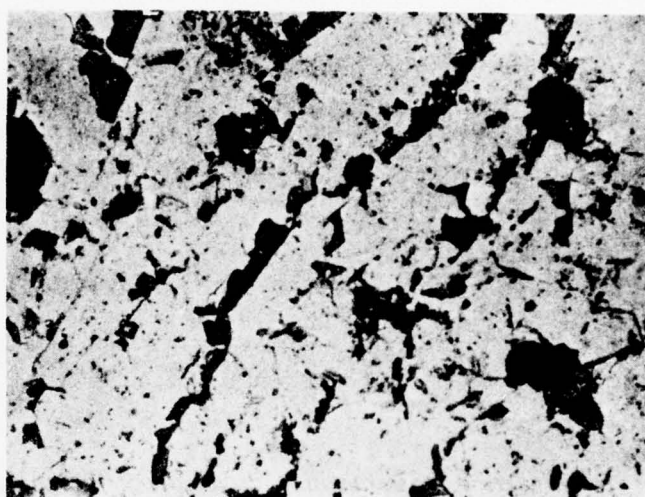
Transmitted Light



40X

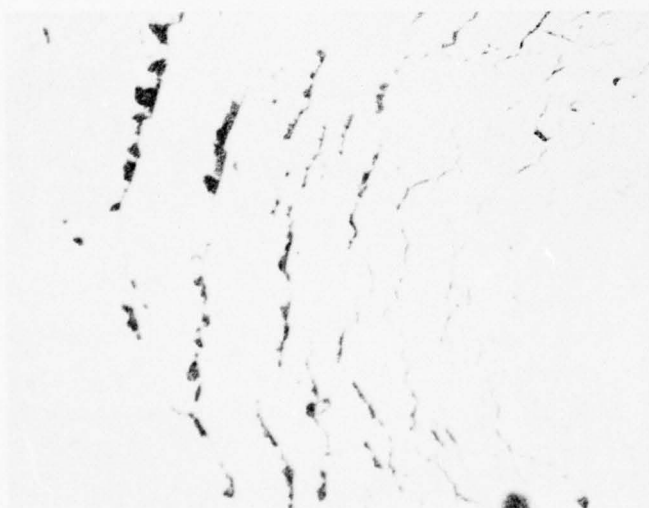


150X

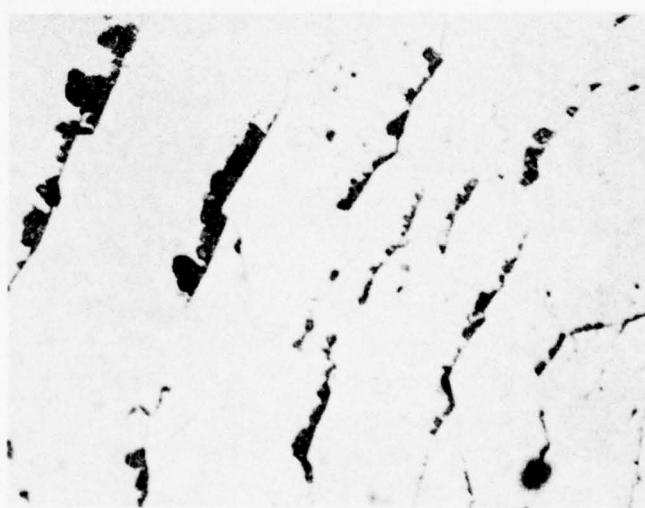


290X

a. 1120 fps Impact Velocity



150X



290X

b. 730 fps Impact Velocity

Figure 16. Effect of Velocity on Extent of Chipping of Ring Fractures Formed on Zinc Selenide by Impact with 2.0 mm Diameter Drops. Reflected Light Except Where Noted

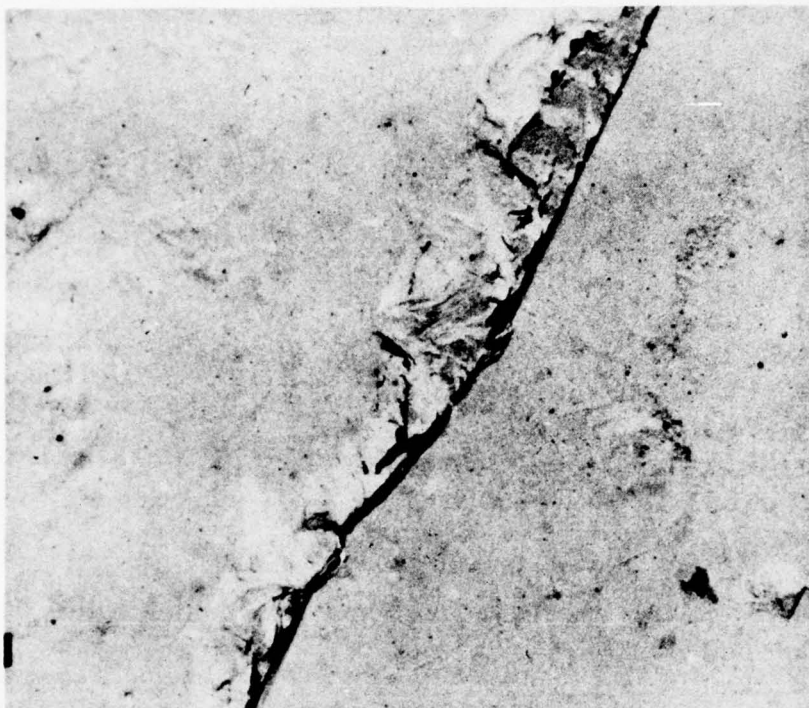
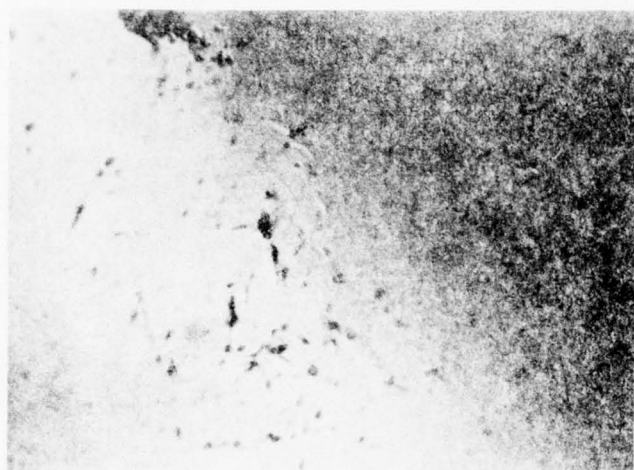
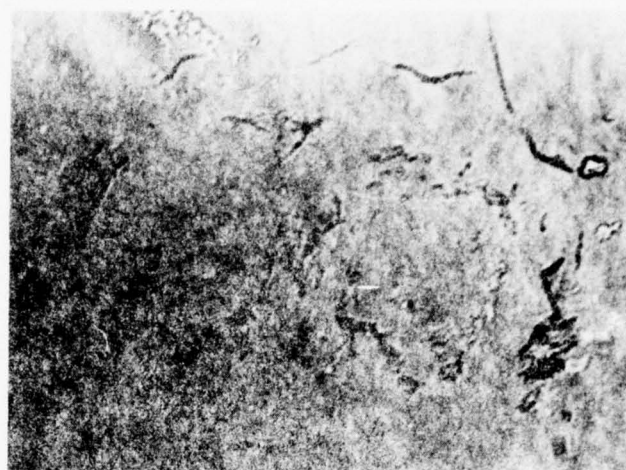


Figure 17. Electron Micrograph of Ring Fracture Crack Formed on Zinc Selenide by Impact with 2.0 mm Diameter Drop at 1120 fps. Mag. 3400X



45X

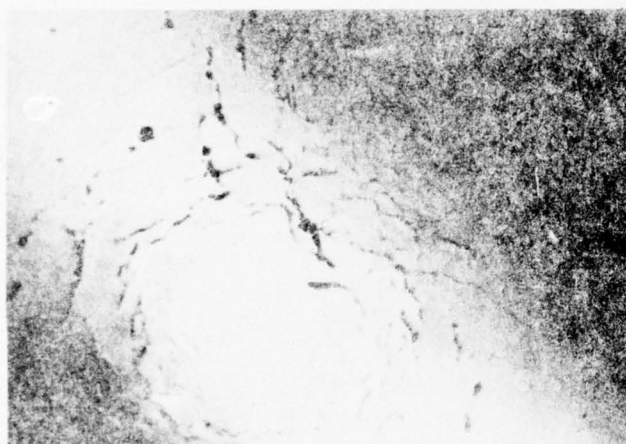
Reflected Light



Transmitted Light

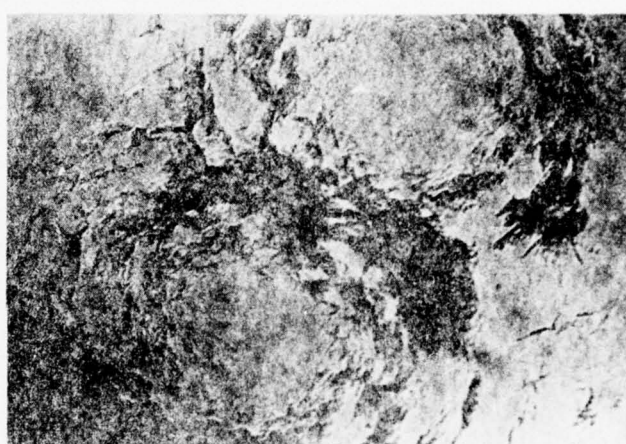
45X

a. 0.7 mm Drop Impact



30X

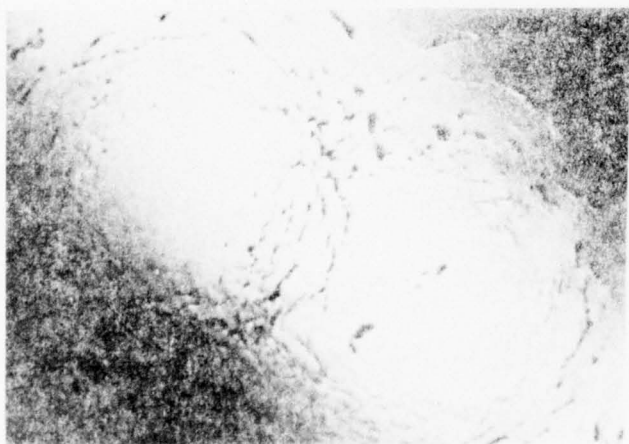
Reflected Light



Transmitted Light

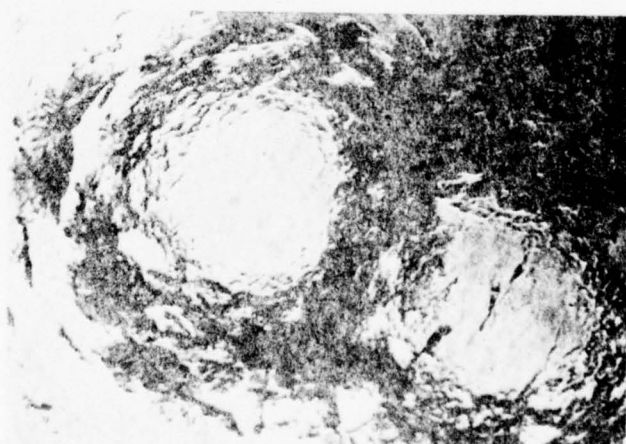
30X

b. 2.0 mm Drop Impact



30X

Reflected Light

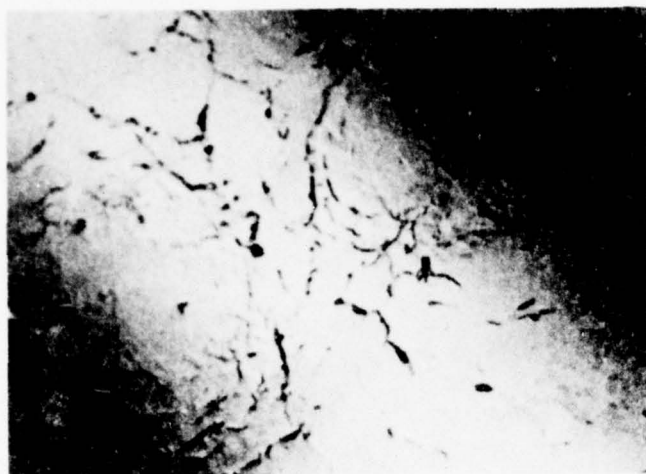


Transmitted Light

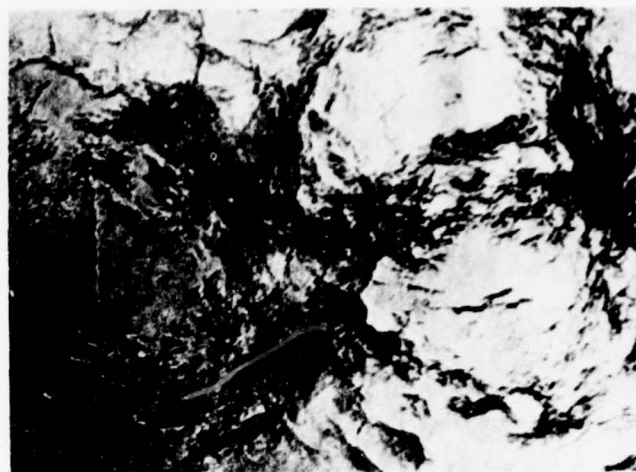
30X

c. 2.5 mm Drop Impact

Figure 18. Overlapping Doublet Impact Sites on Zinc Selenide Impacted by Single Water Droplets at 730 fps

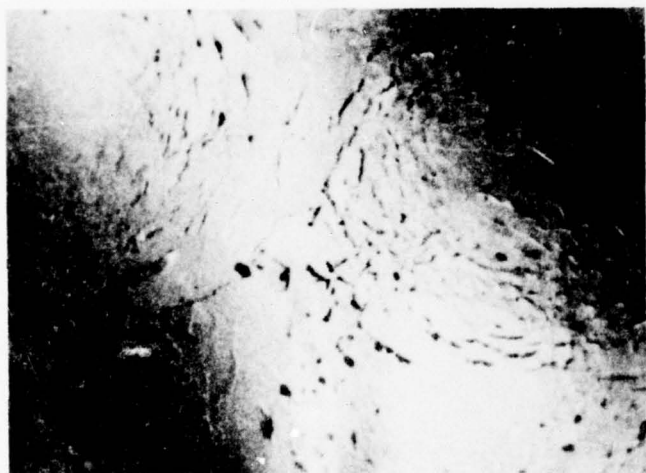


Reflected Light

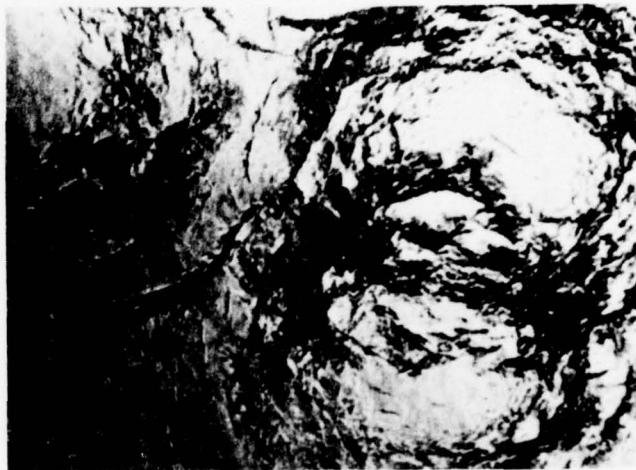


Transmitted Light

a. 2.0 mm Drop Impact



Reflected Light



Transmitted Light

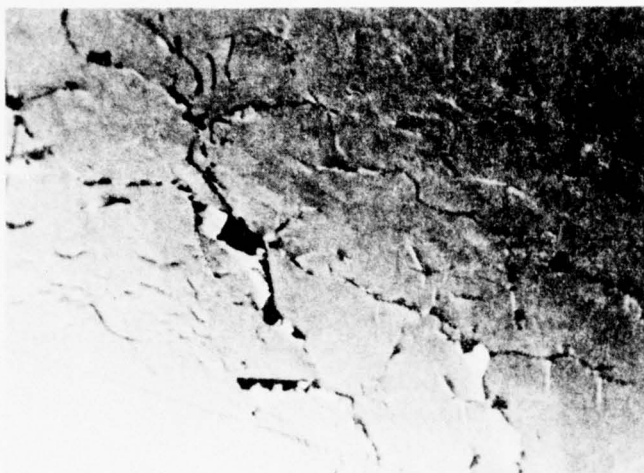
b. 2.5 mm Drop Impact

Figure 19. Overlapping Triplet Impact Sites on Zinc Selenide Impacted by Single Water Droplets at 730 fps. Mag. 30X

diameter. At a triplet impact site, a third drop has impacted at the region of overlapping of two previously formed ring fractures. Reflected light was used to reveal the surface cracking and transmitted light was used to reveal the extent of the subsurface damage. The transmitted light micrographs in Figures 18 and 19 show some increased loss in transmission in the areas of overlapping ring fractures, particularly for the 2.0 and 2.5 mm diameter drops. This loss results from the increased concentration of subsurface fractures in those areas which have been subjected to the effects of a second and third impact. It is apparent that the overlapping 0.7 mm diameter drops produce much less damage than do the overlapping 2.0 or 2.5 mm diameter drops.

Figure 20 contains higher magnification optical micrographs of the ring fracture overlap areas shown in Figures 18 and 19. These micrographs were made with reflected light to show surface damage. The second and third overlapping impacts do produce enhanced damage by chipping the edges of the fractures produced by the first impact; however, the surface damage, particularly for the case of the triplet impact sites, is not as extensive as might be expected. Figure 21a shows an electron micrograph of the intersection of ring cracks at a 2.0 mm diameter drop doublet impact site. There is surprisingly little interaction of the two ring fractures in this micrograph. Figure 21b is an electron micrograph illustrating the enhanced chipping caused by a second impact.

As was the case for zinc selenide, only slight enhancement of damage was found in the area of doublet impact sites on zinc sulfide and gallium arsenide. No triplet impact sites were present on either the zinc sulfide or the gallium arsenide specimen. Optical micrographs of doublet, 2.0 mm diameter drop impact sites on zinc sulfide and gallium arsenide are shown in Figure 22. The transmitted light micrograph in Figure 22a reveals a much lesser extent of subsurface damage in the overlapping region of the ring fractures for zinc sulfide than for zinc selenide (Figure 18b). Several attempts to examine in the

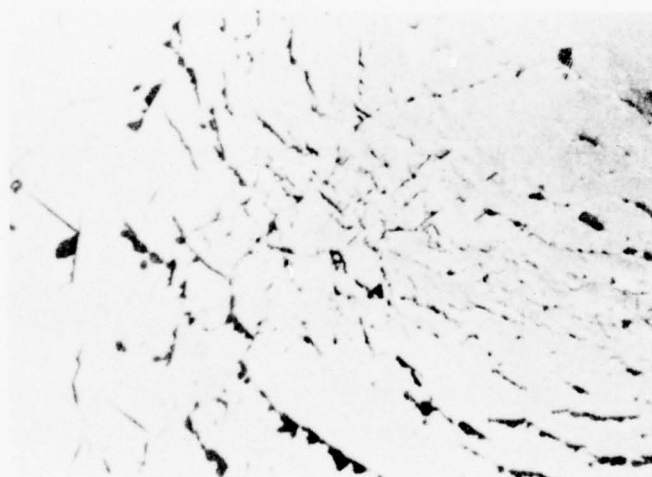


2.0 mm Drops



2.5 mm Drops

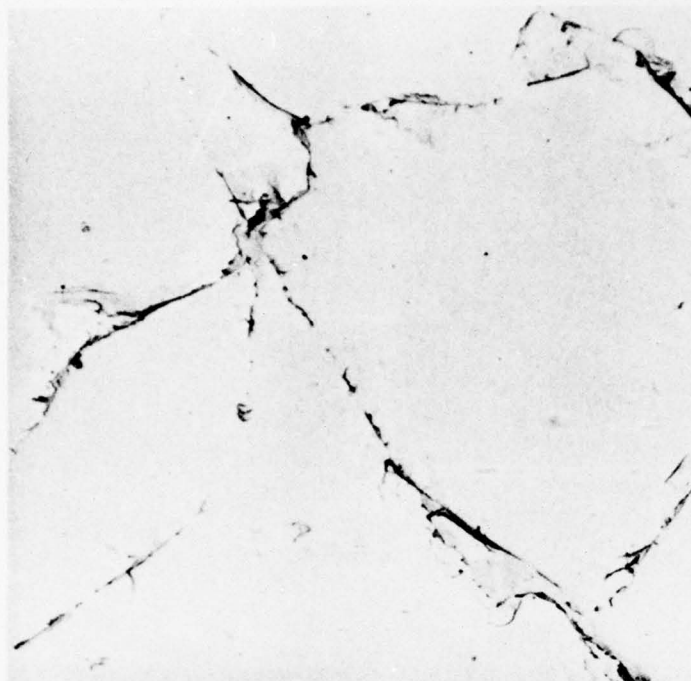
a. Doublet Impact Sites in Figure 1b and c.



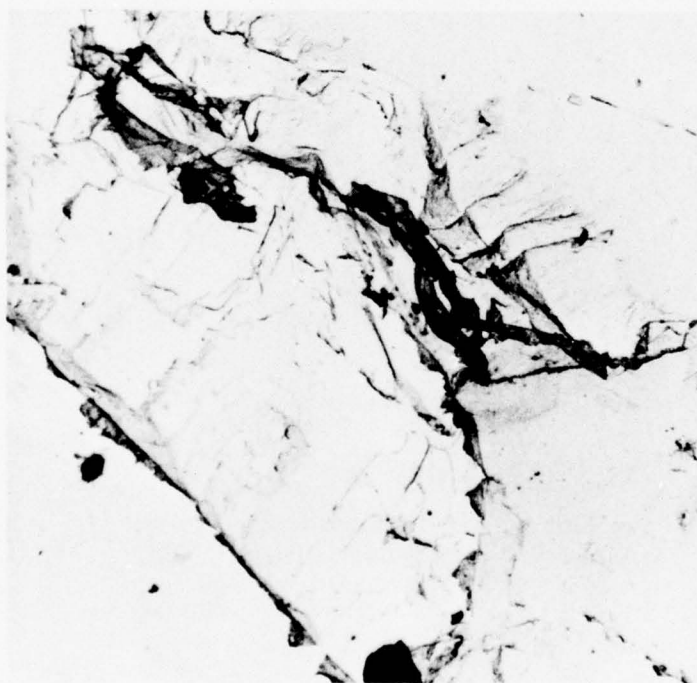
2.5 mm Drops

b. Triplet Impact Site in Figure 2b for 2.5 mm Drops

Figure 20. Closeup of Damage to Zinc Selenide in the Area of Overlapping Impact of Single Drops at 730 fps. Mag. 160X

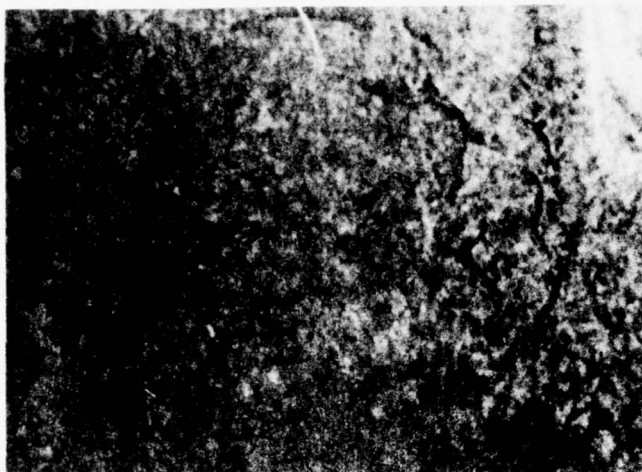


a. Intersecting Cracks Typical of Most of the Overlap Regions



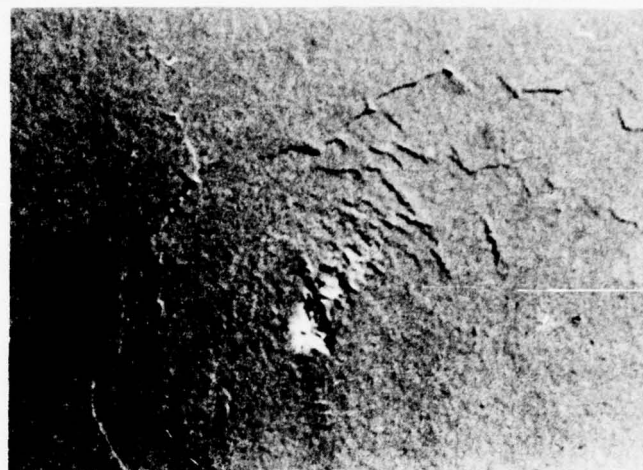
b. Enhanced Chipping

Figure 21. Electron Micrographs of Overlap Regions of Doublet Impact Sites on Zinc Selenide Impacted by 2.0 mm Diameter Water Droplets at 730 fps. Mag. 2000X



30X

Transmitted Light



Reflected Light

125X

a. Zinc Sulfide



30X

Reflected Light



Reflected Light

125X

b. Gallium Arsenide

Figure 22. Overlapping Doublet Impact Sites on Zinc Sulfide and Gallium Arsenide Impacted by Single Water Drops at 730 fps.

electron microscope replicas of doublet impact sites on zinc sulfide were unsuccessful. The electron micrographs of a doublet overlap region on gallium arsenide shown in Figure 23 corroborate the slight interaction of two impacts as shown at lower magnification in Figure 22b.

The examination of the overlapping impact sites on zinc selenide, zinc sulfide, and gallium arsenide revealed only a small amount of enhanced damage in the regions of overlapping ring fractures. This lack of enhanced damage was somewhat unexpected based on the results of an investigation by Adler⁽²⁾ of the erosion of glass specimens impacted with glass beads. Adler observed that pits were nucleated at triplet impact sites. He used this observation as the basis for establishing the pit nucleation criterion for a pit nucleation and growth model of erosion of brittle materials by raindrops and by solid particles. The experimental results from this program indicate that triplet water drop impacts do not nucleate a pit on the surface of zinc selenide. Although no triplet water drop impact sites were obtained on zinc sulfide and gallium arsenide, the results from the doublet impact sites make it appear unlikely that a third drop impact would nucleate a pit.

E. Progress of Erosion in Rainfields

Specimens of 3/8 inch thick zinc selenide, zinc sulfide, and gallium arsenide were exposed in the AFML/Bell erosion facility for short increments of time at 730 fps in the standard rainfield of 1.8 mm diameter drops falling at the rate of one inch per hour. This series of experiments was performed to study the progress of damage of infrared window materials in the multiple drop impact environment of the rainfield to relate the loss of transmittance to the type and extent of damage, and to correlate results with the overlapping single drop experiments. Before the tests, and after each increment of exposure, transmittance was measured over the wavelength range of 0.5 to 2.1 microns with a Cary Model 14 spectrophotometer and over the wavelength range of 2.5 to 25 microns with a Perkin Elmer Model 621

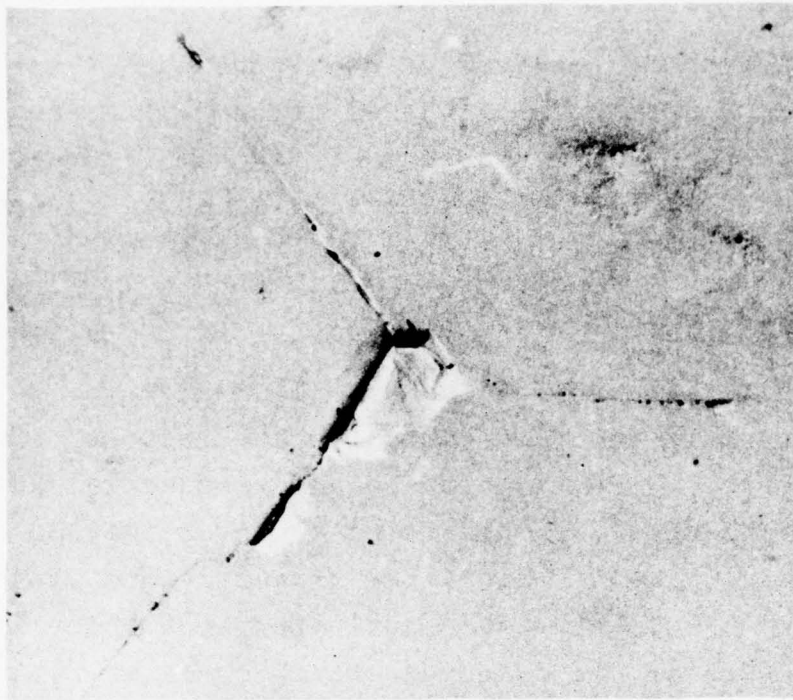


Figure 23. Electron Micrographs of Typical Cracks in the Overlap Regions of Doublet Impact Sites on Gallium Arsenide Impacted by 2.0 mm Diameter Water Drops at 730 fps. Mag. 3400X

spectrophotometer. The incremental exposures to the rainfield were continued until the transmittance decreased by approximately 50%, or the specimen broke. The cumulative exposure time increments for the three specimens were as follows:

ZnSe - 20 and 30 seconds,
GaAs - 20, 40 and 60 seconds,
ZnS - 20, 40, 80, 160, 240 and 320 seconds

The zinc selenide specimen had broken into two pieces after 30 seconds, but transmittance could still be measured. The gallium arsenide specimen was shattered after 60 seconds and transmittance could not be measured. The zinc sulfide specimen was still intact after 320 seconds.

The effects of rain erosion on transmittance between 0.5 and 2.1 microns for the three materials are shown in the curves in Figures 24, 25 and 26. The effects of rain erosion on transmittance between 2.5 and 25 microns for the three materials are shown by the curves in Figures 27, 28 and 29. Loss in transmittance versus exposure time is tabulated in Table 5 at the selected wavelengths of 2, 5, 7 and 10 microns to aid in interpretation of the results. It is obvious from the data in this table that zinc sulfide is the most erosion resistant of the three materials. In the near infrared range of 0.7 to 2.1 microns, the transmittance of all three materials is significantly reduced in the initial stage of erosion. This reduction is almost linear with exposure time. On the other hand, there appears to be an incubation period before significant loss of transmission occurs in the wavelength range of 2.5 to 12 microns. This incubation is particularly evident for zinc sulfide across the entire band and for gallium at the longer wavelength end of the band. Surface damage in the initial stage of erosion obviously has a greater effect on the shorter wavelengths.

Micrographs showing the progress of surface erosion are presented in Figures 30, 31 and 32 for zinc selenide, gallium arsenide and zinc sulfide, respectively. Large pits had

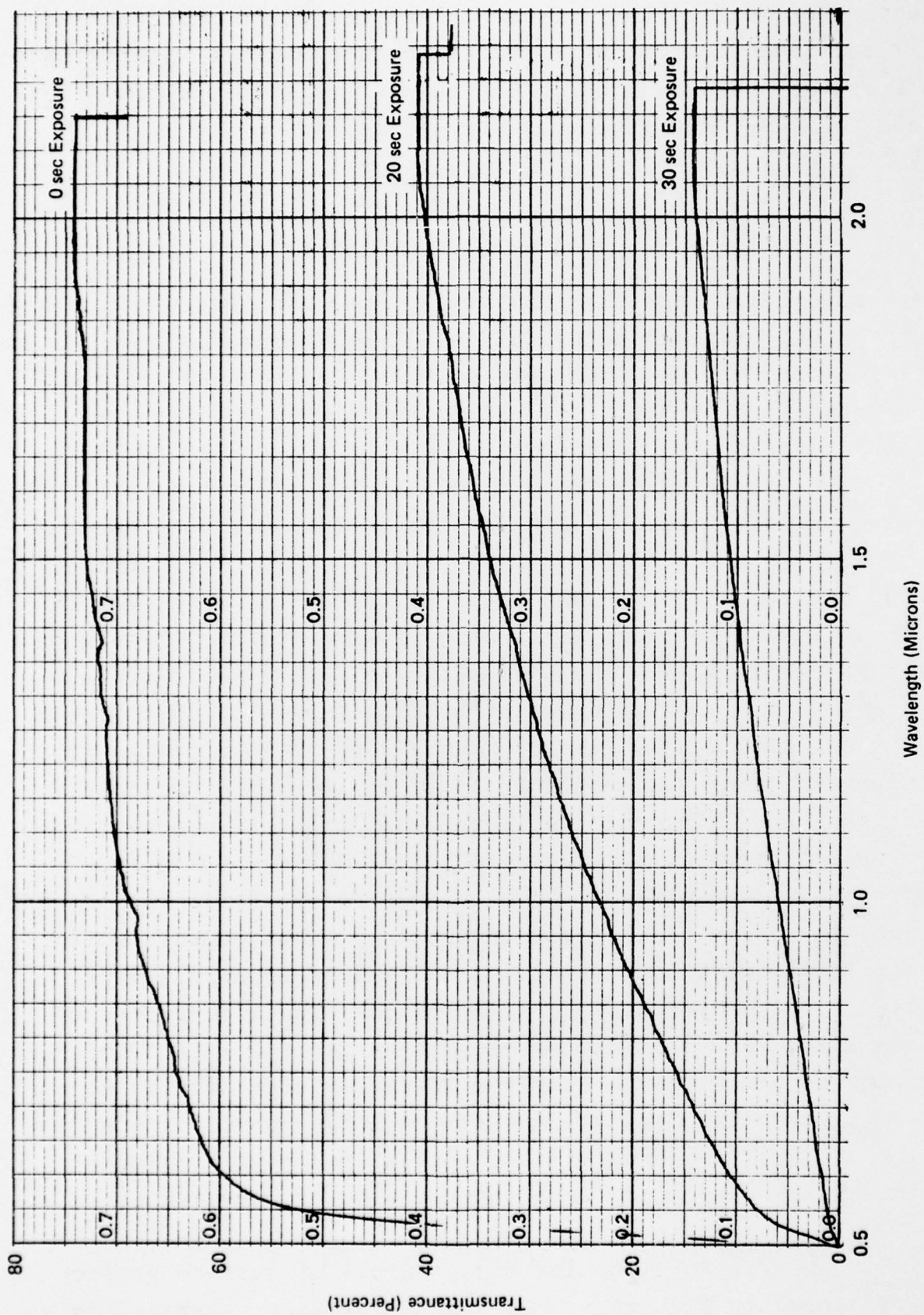


Figure 24. Effects of Rain Erosion on Spectral Transmittance of Zinc Selenide between 0.5 and 2.1 Microns

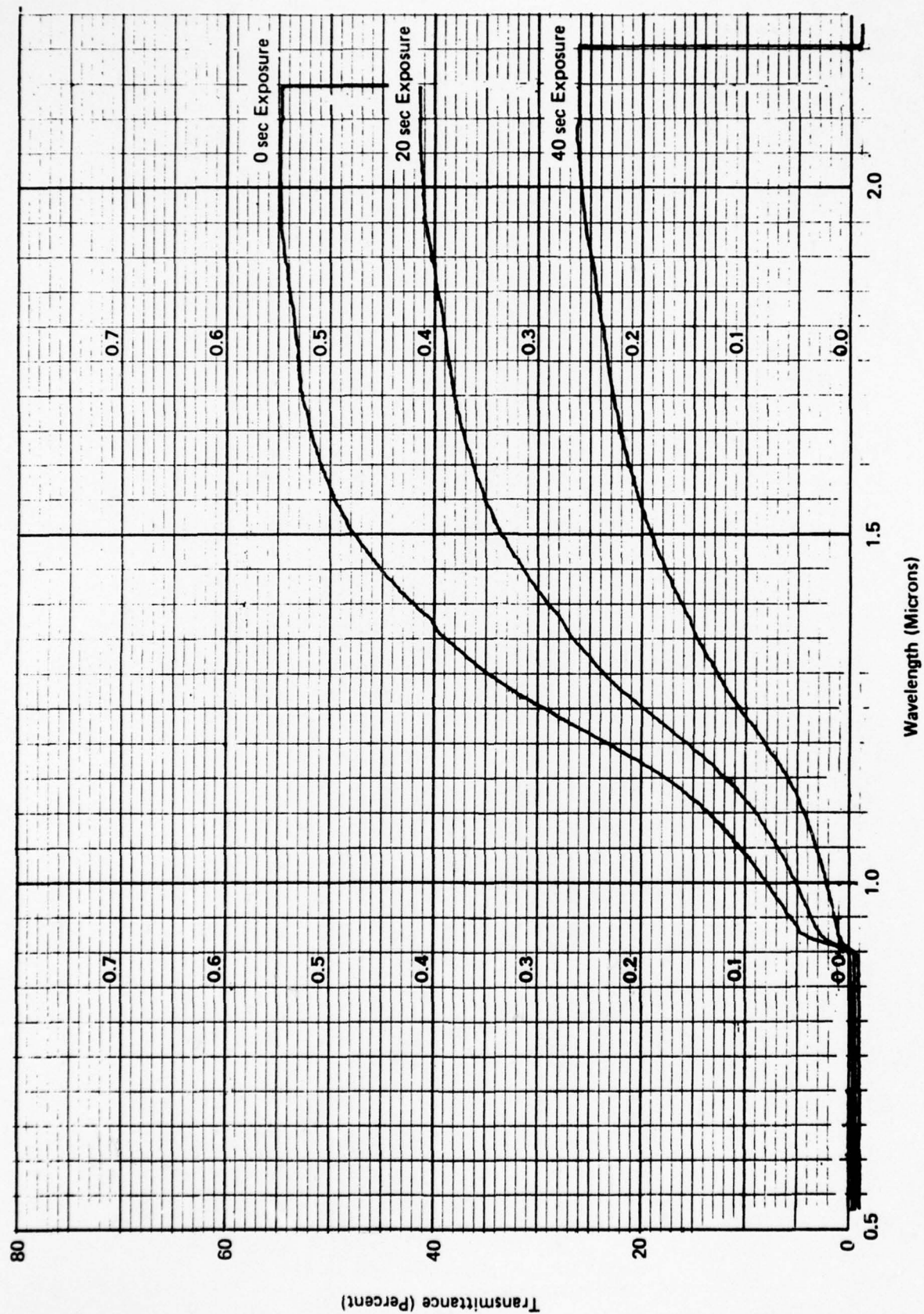


Figure 25. Effects of Rain Erosion on Spectral Transmittance of Gallium Arsenide between 0.5 and 2.1 Microns

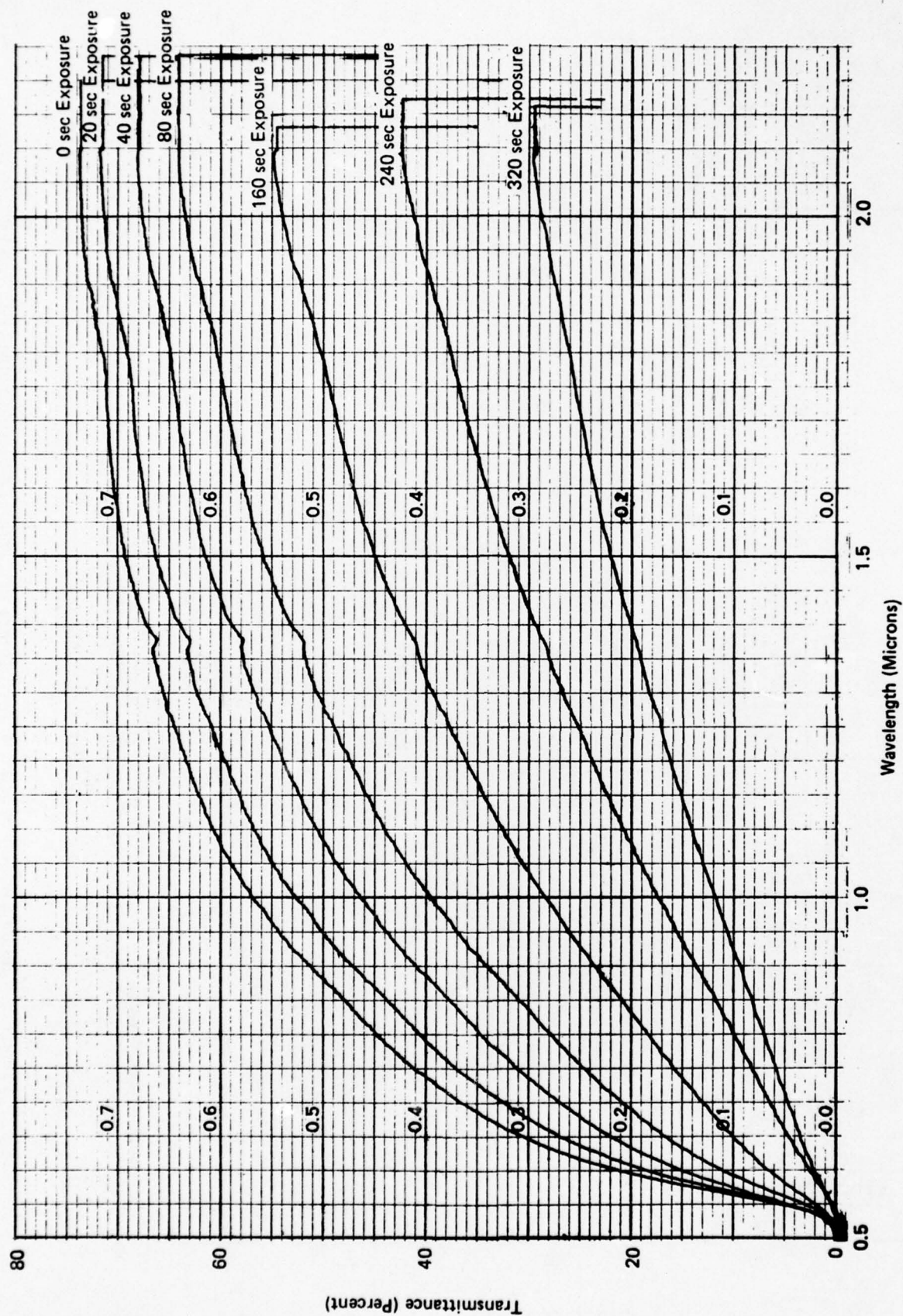
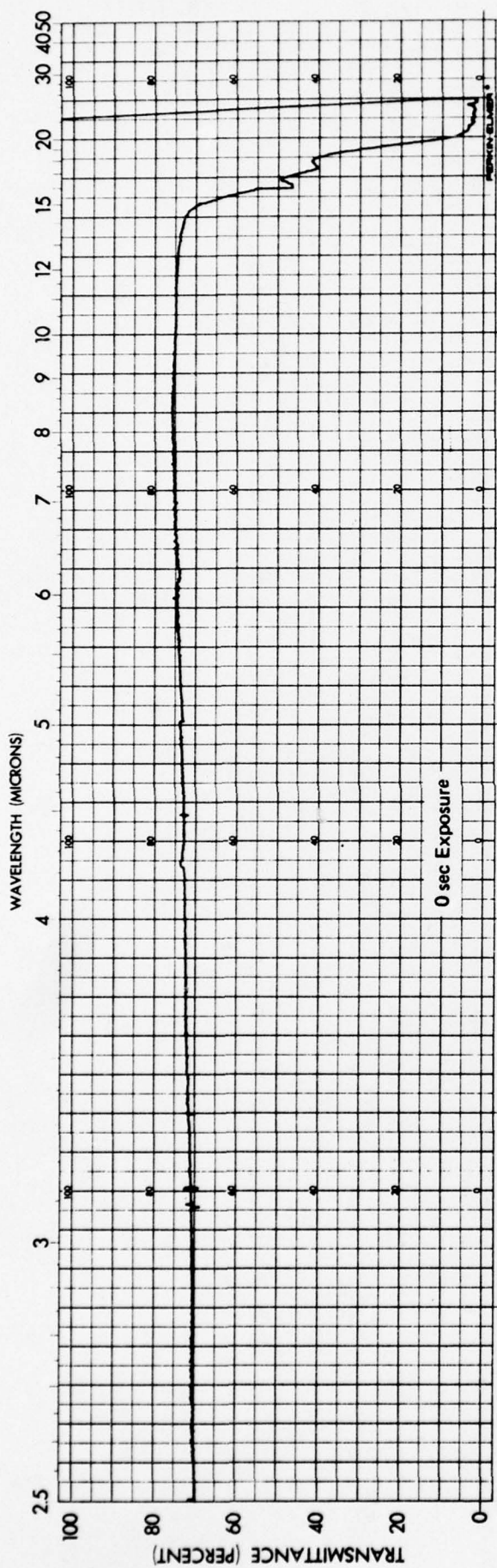


Figure 26. Effects of Rain Erosion on Spectral Transmittance of Zinc Sulfide between 0.5 and 2.1 Microns



57

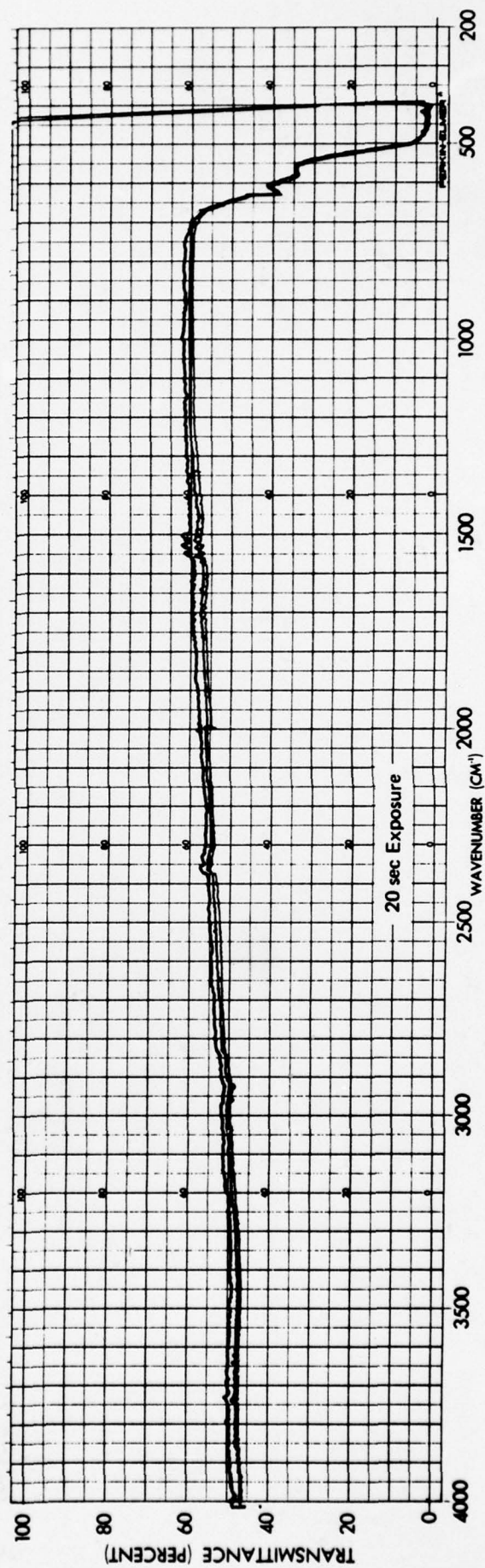


Figure 27. Effects of Rain Erosion on Spectral Transmittance of Zinc Selenide between 2.5 and 25 Microns (Continued)

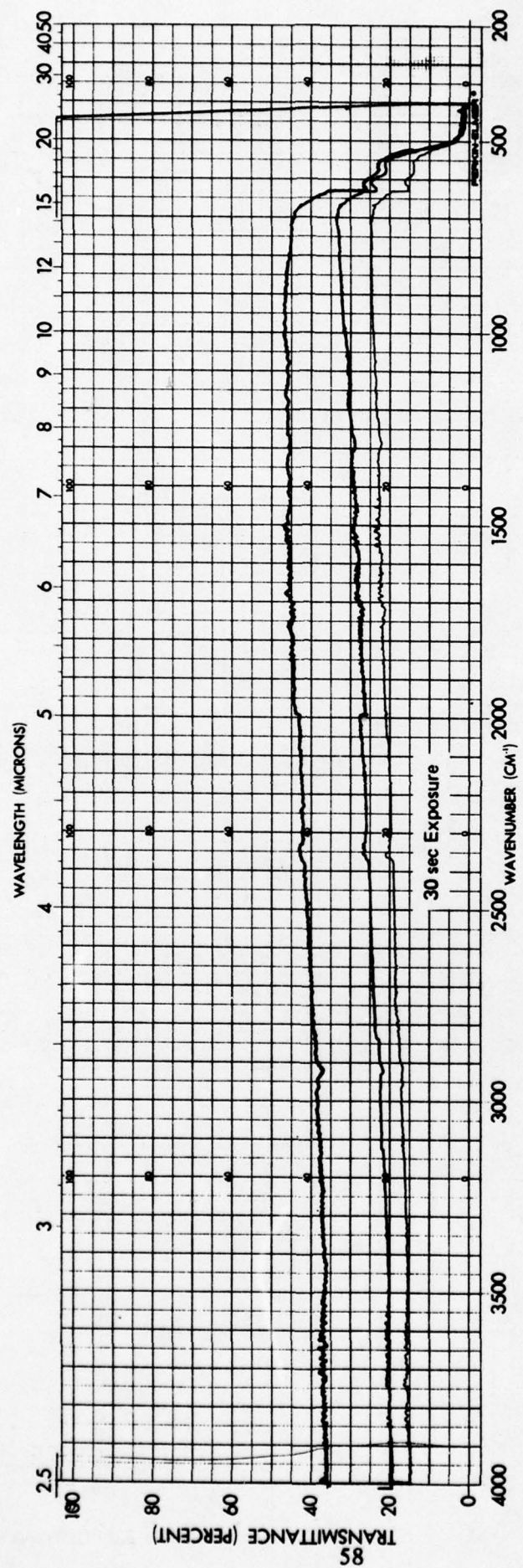
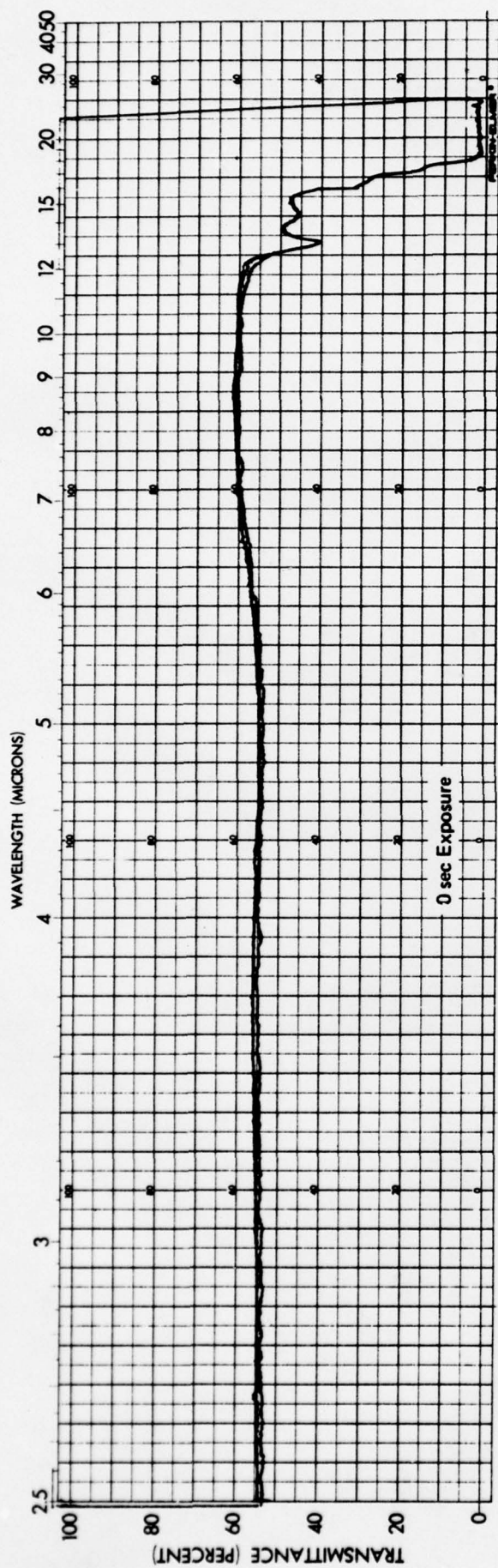


Figure 27. Effects of Rain Erosion on Spectral Transmittance of Zinc Selenide between 2.5 and 25 Microns (Concluded)



65

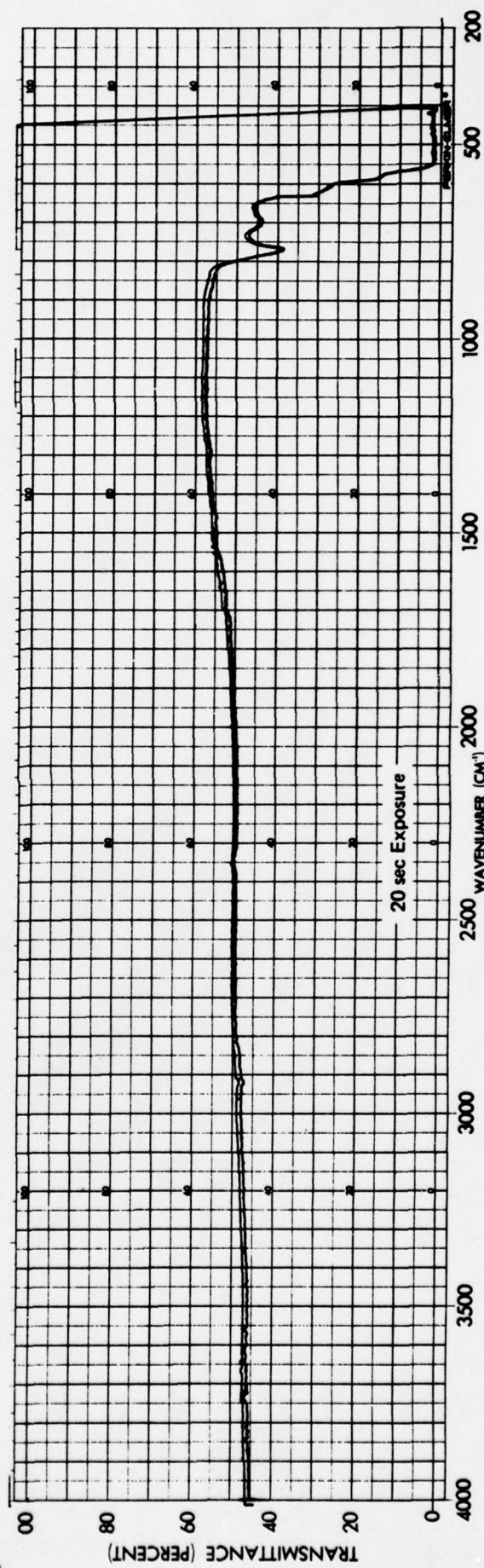


Figure 28. Effect of Rain Erosion on Spectral Transmittance of Gallium Arsenide between 2.5 and 25 Microns
(Continued)

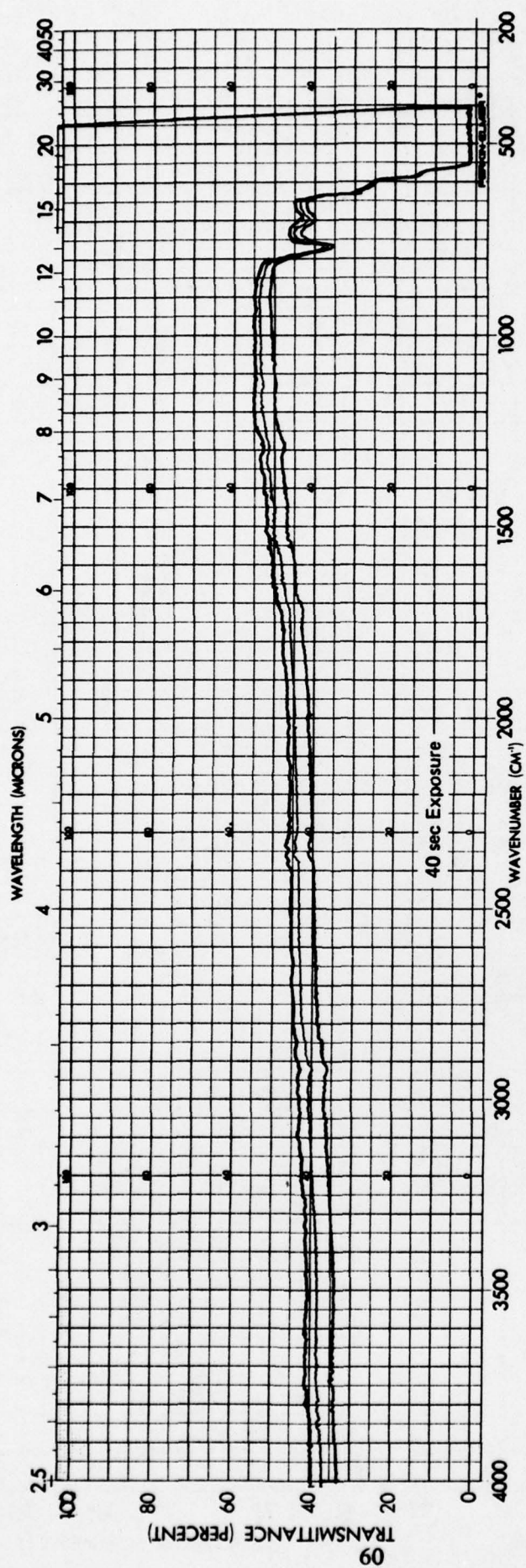
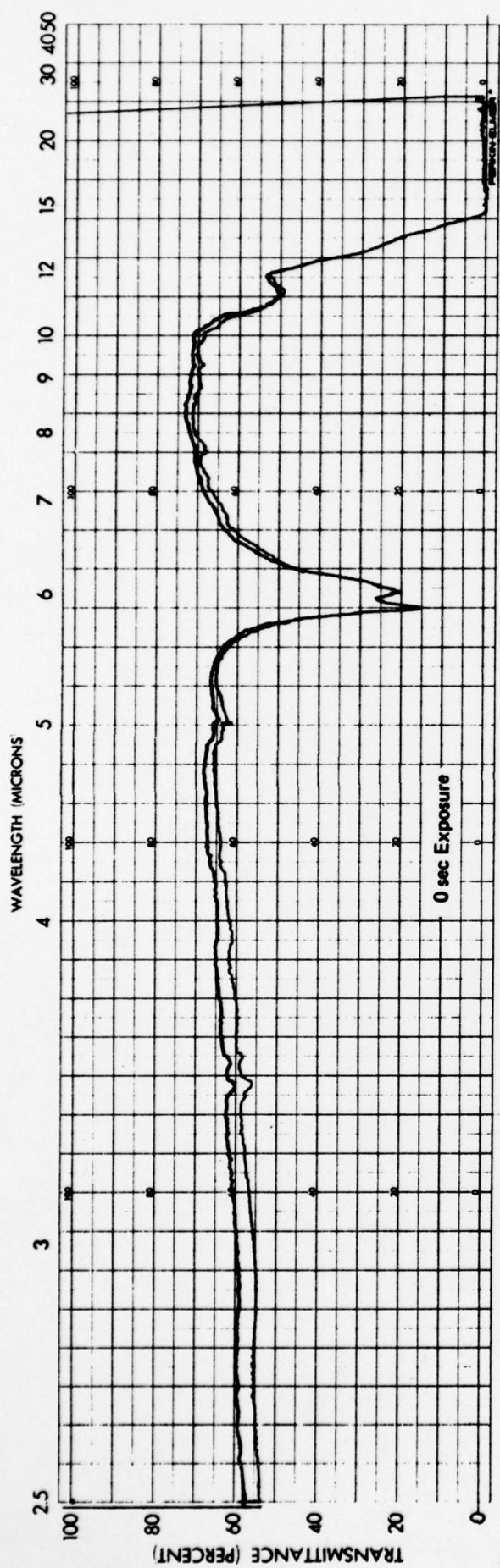


Figure 28. Effect of Rain Erosion on Spectral Transmittance of Gallium Arsenide between 2.5 and 25 Microns
(Concluded)



19

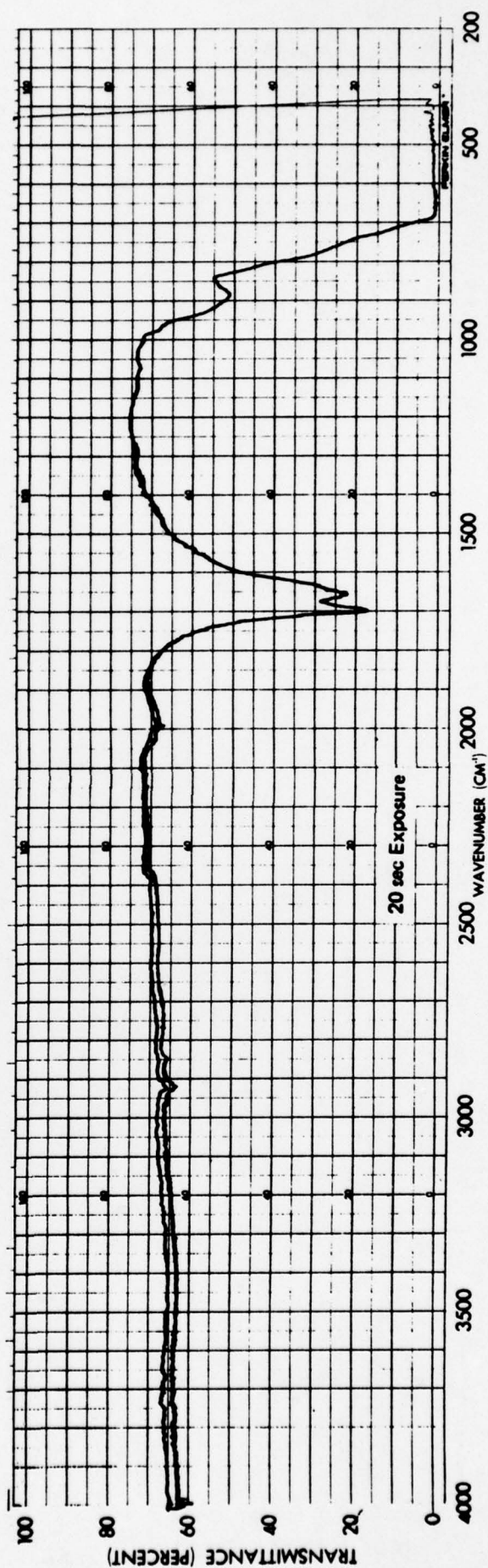
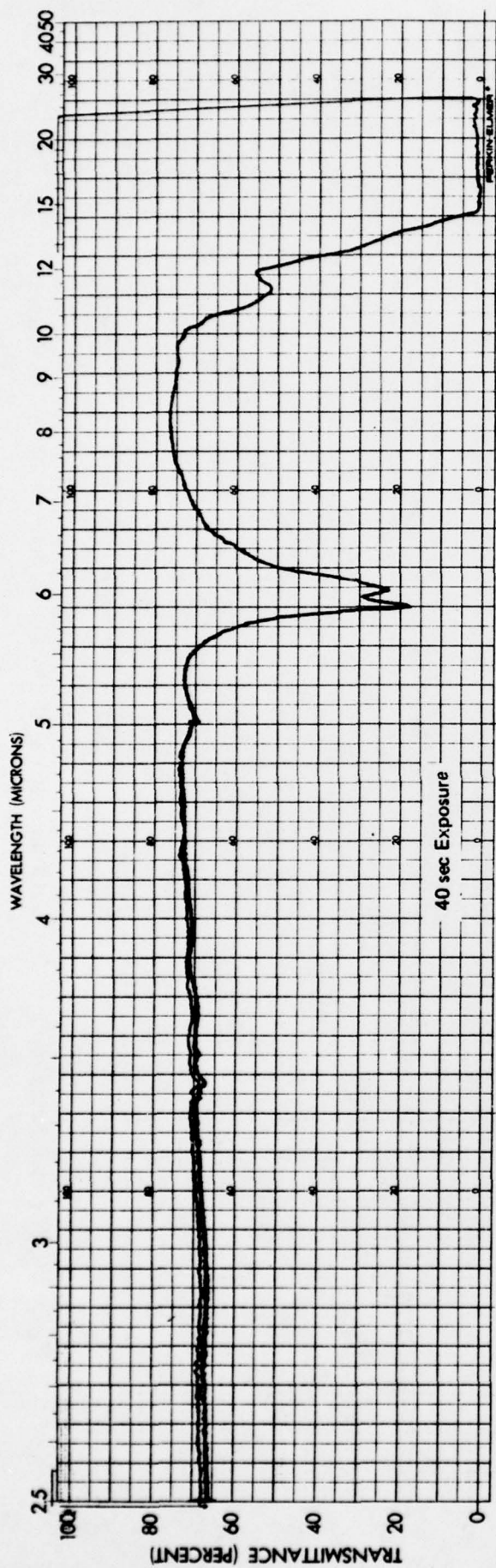


Figure 29. Effects of Rain Erosion on Spectral Transmittance of Zinc Sulfide between 2.5 and 25 Microns
(Continued)



29

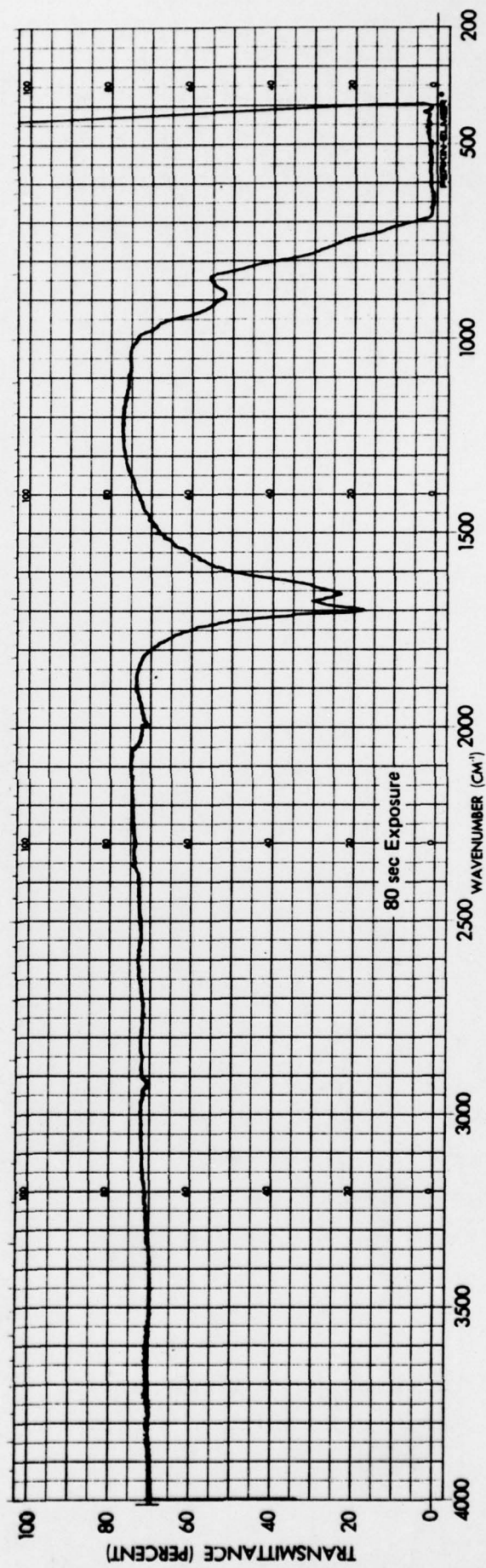
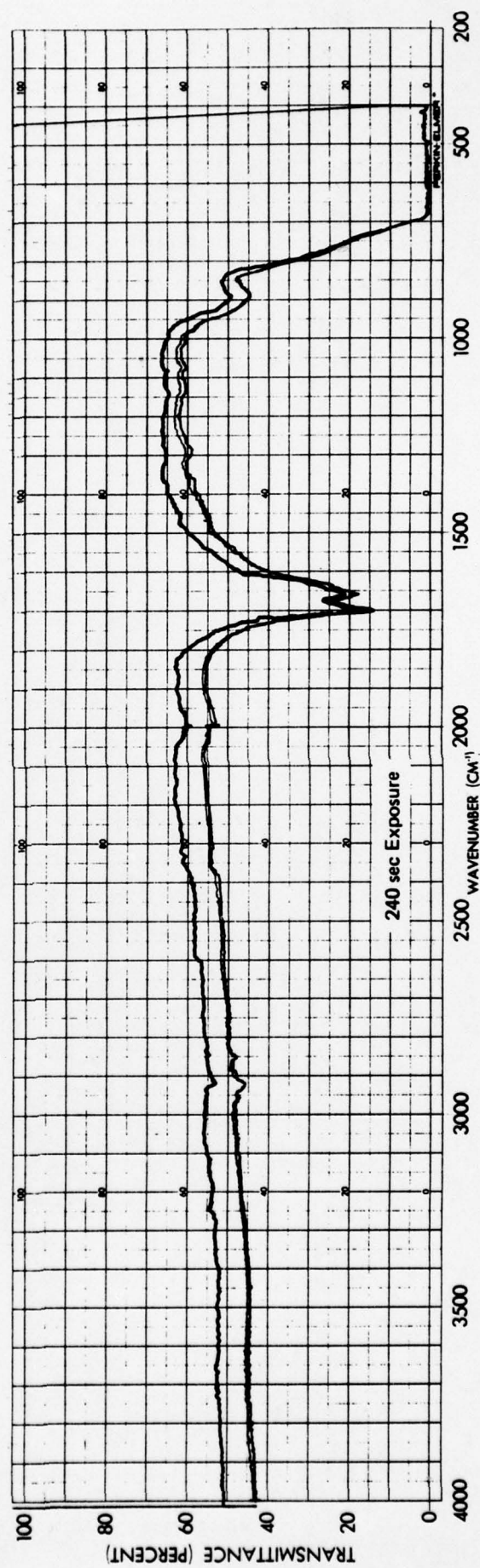
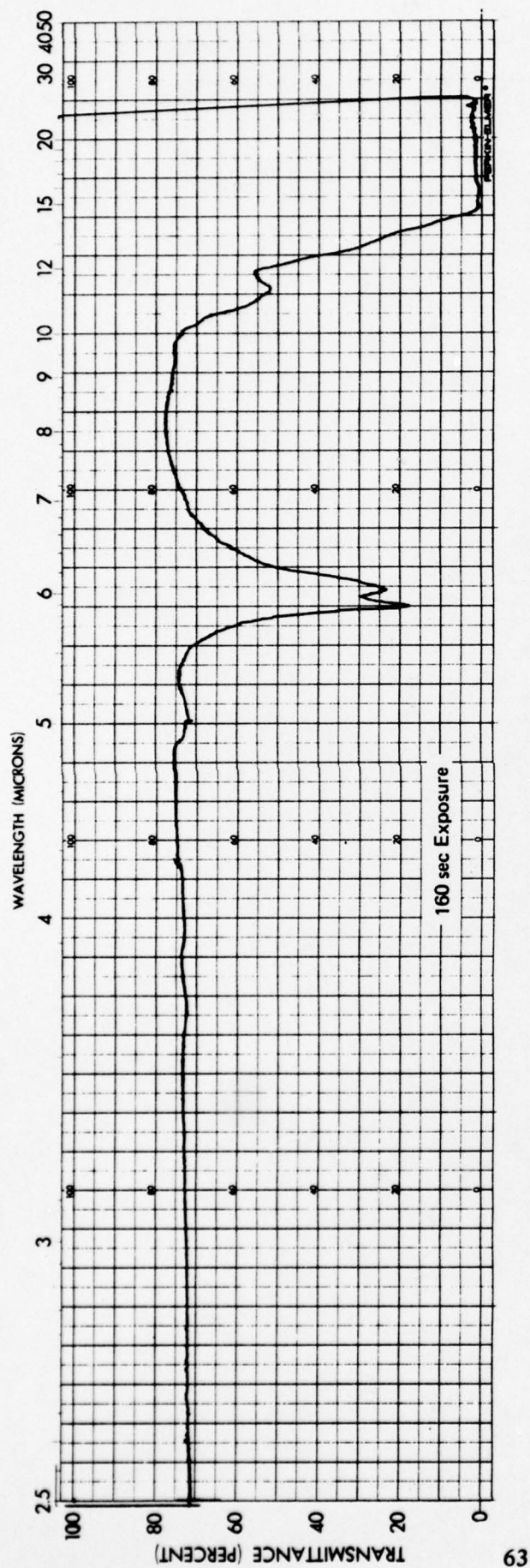


Figure 29. Effects of Rain Erosion on Spectral Transmittance of Zinc Sulfide between 2.5 and 25 Microns
(Continued)



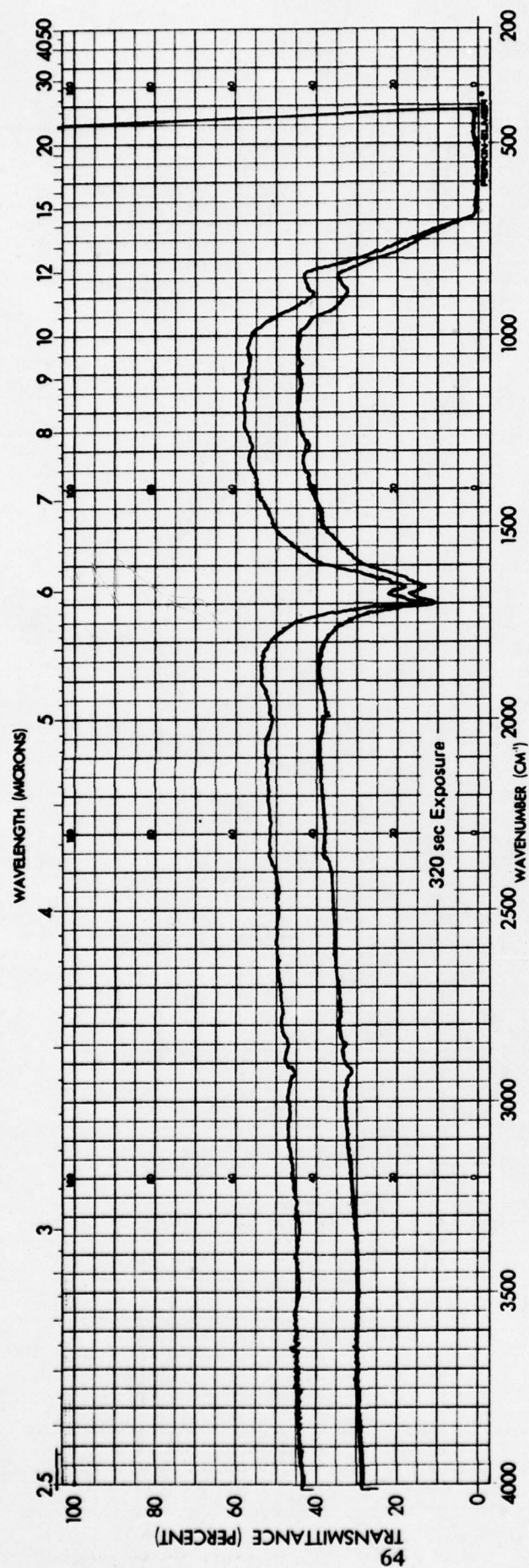


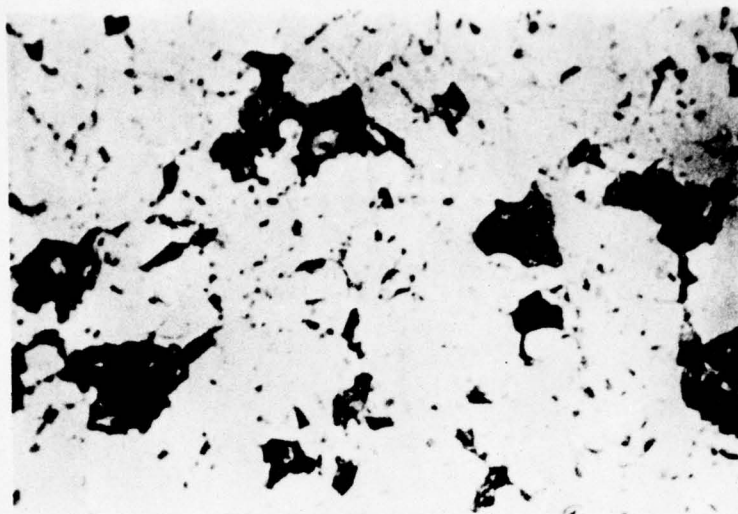
Figure 29. Effects of Rain Erosion on Spectral Transmittance of Zinc Sulfide between 2.5 and 25 Microns
(Concluded)

TABLE 5

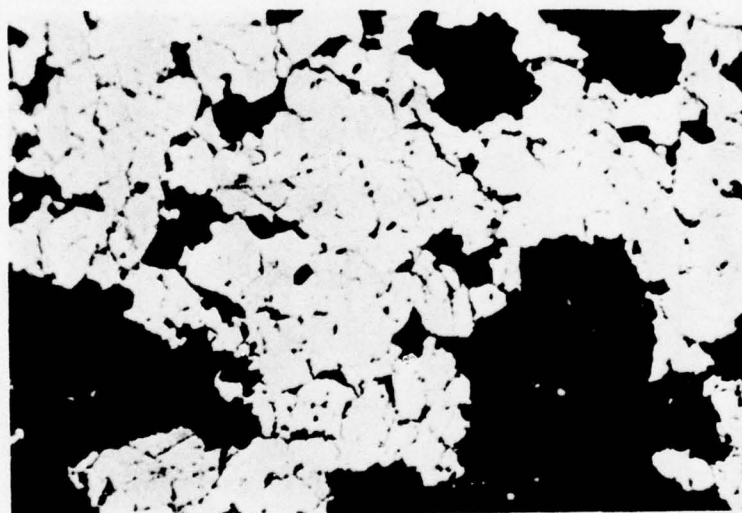
LOSS IN TRANSMITTANCE VERSUS EXPOSURE TIME IN
STANDARD RAINFIELD (1 IN./HR.) AT 730 FPS

Material	Cumulative Exposure (sec)	2 Microns		5 Microns		7 Microns		10 Microns	
		Trans. (%)	Loss (a) (%)	Trans. (%)	Loss (a) (%)	Trans. (%)	Loss (a) (%)	Trans. (%)	Loss (a) (%)
ZnSe	0	74	0	74	0	75	0	75	0
	20	40	46	56	24	58	23	60	20
	30	14	81	30	59	32	57	34	55
GaAs	0	55	0	54	0	59	0	60	0
	20	41	25	50	8	56	5	58	3
	40	26	53	44	18	50	15	52	13
ZnS	0	74	0	65	0	67	0	70	0
	20	72	3	69	+6	70	+4	72	+3
	40	68	8	70	+8	72	+7	73	+4
	80	63	15	72	+11	72	+7	73	+4
	160	54	27	72	+11	72	+7	73	+4
	240	41	45	56	14	59	12	63	10
	320	29	51	45	31	47	30	50	29

(a) Loss is percent change in transmission from initial value at 0 sec. exposure.
+ indicates apparent gain in transmission.

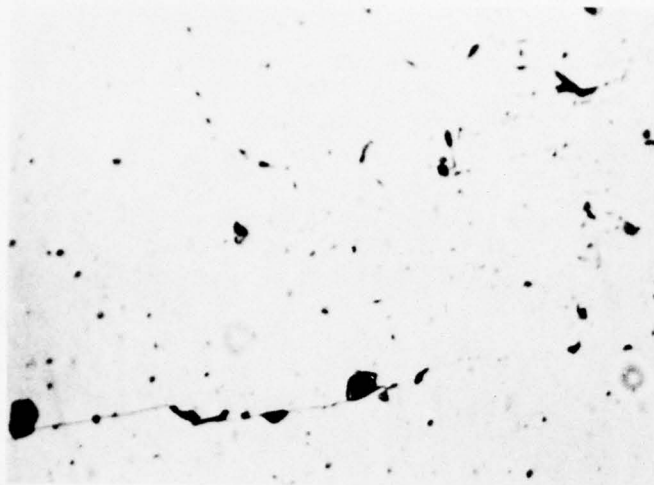


20 sec. Exposure

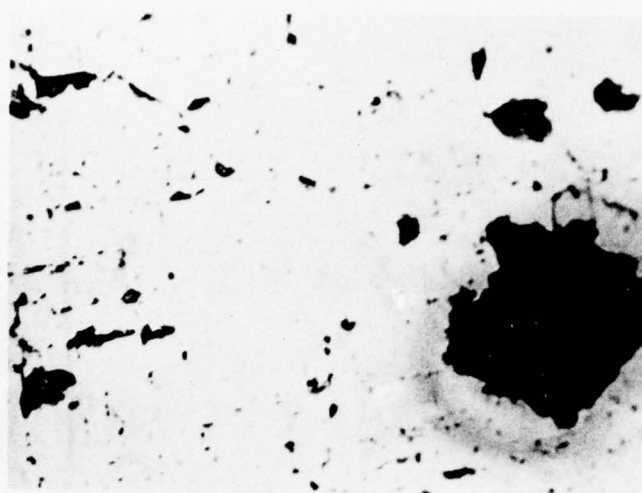


30 sec. Exposure

Figure 30. Surface Erosion of Zinc Selenide Exposed to Standard Rainfield
(1 inch/hour, 1.8 mm Drops) at 730 fps. Mag. 125X



20 sec. Exposure



40 sec. Exposure

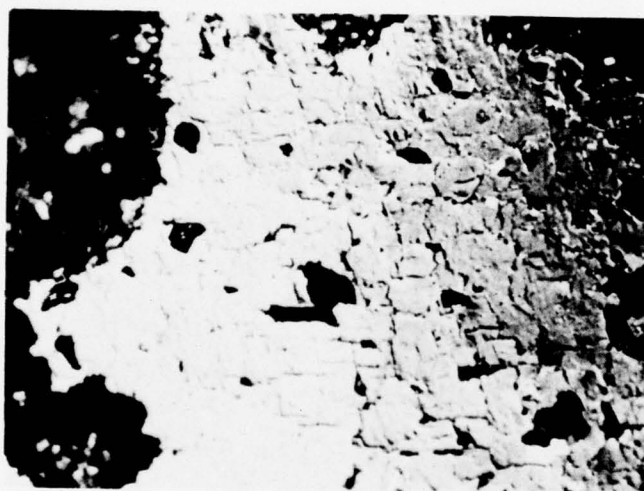
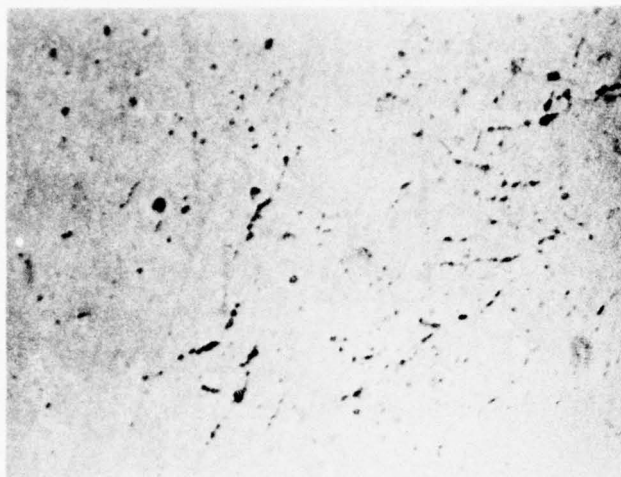
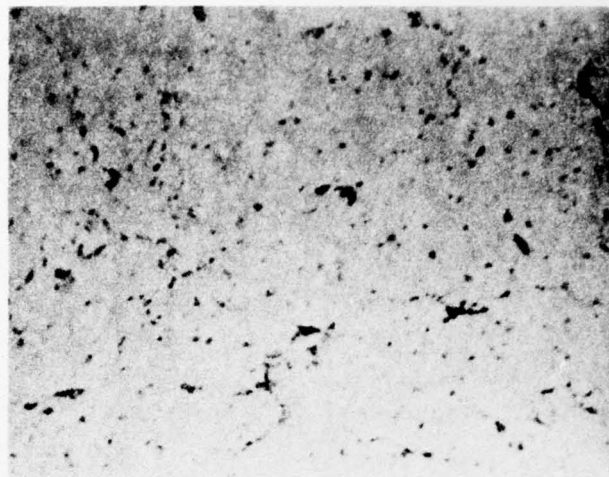


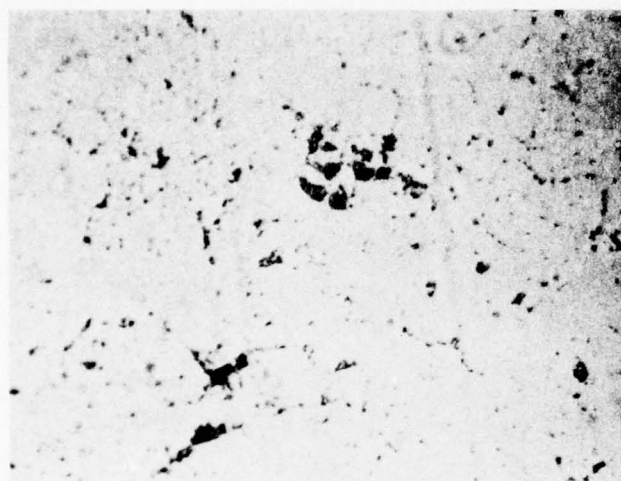
Figure 31. Surface Erosion of Gallium Arsenide Exposed to Standard Rainfield
(1 inch/hour, 1.8 mm Drops) at 730 fps. Mag. 125X



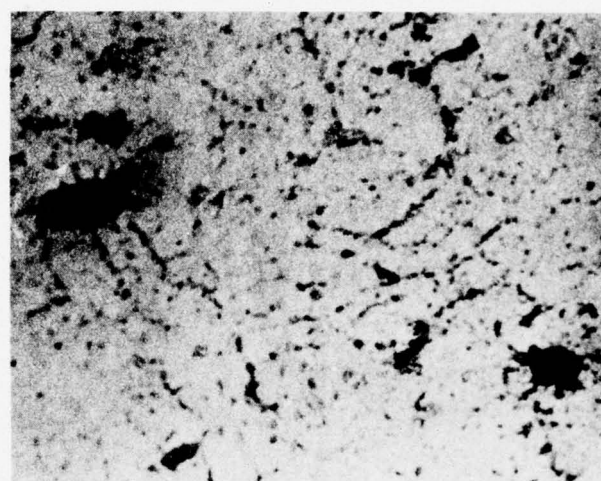
20 sec. Exposure



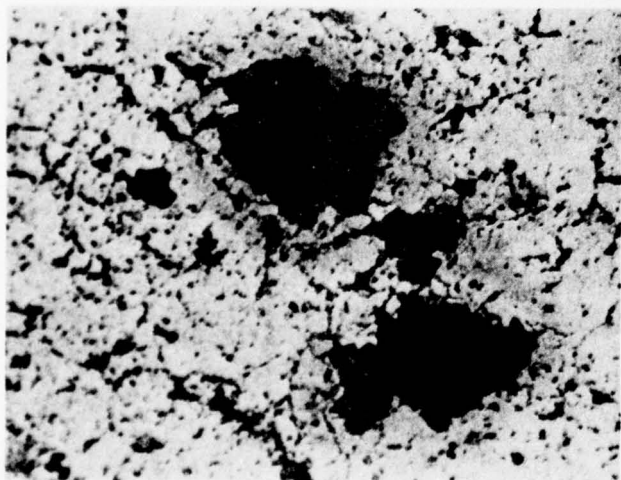
40 sec. Exposure



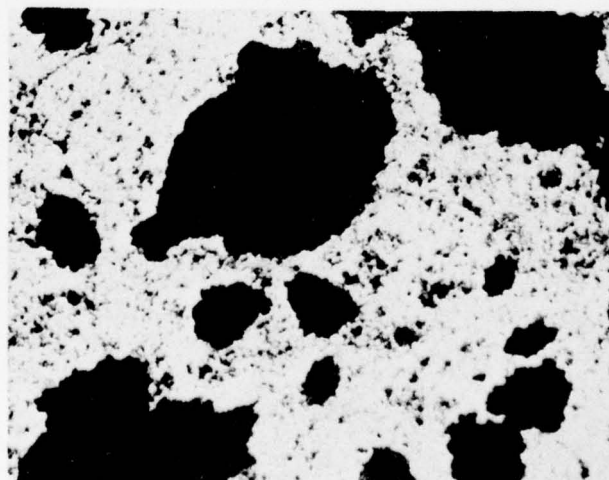
80 sec. Exposure



160 sec. Exposure



240 sec. Exposure



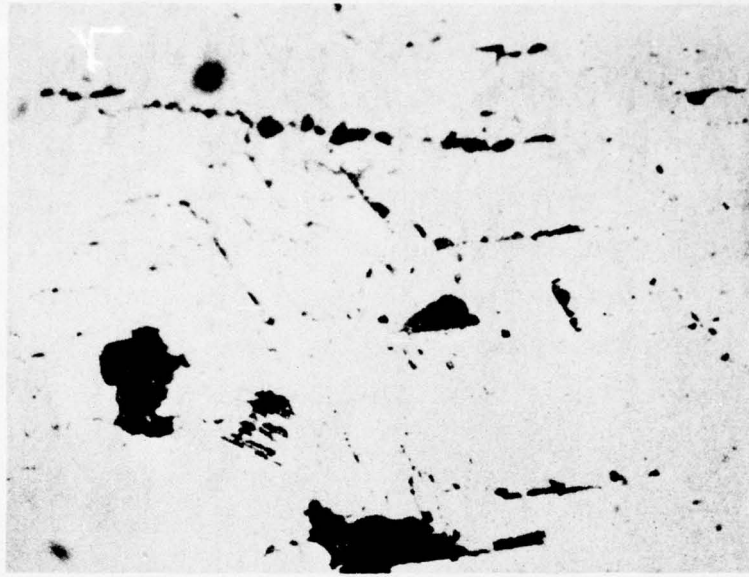
320 sec. Exposure

Figure 32. Surface Erosion of Zinc Sulfide Exposed to Standard Rainfield
(1 inch/hour, 1.8 mm Drops) at 730 fps. Mag. 125X

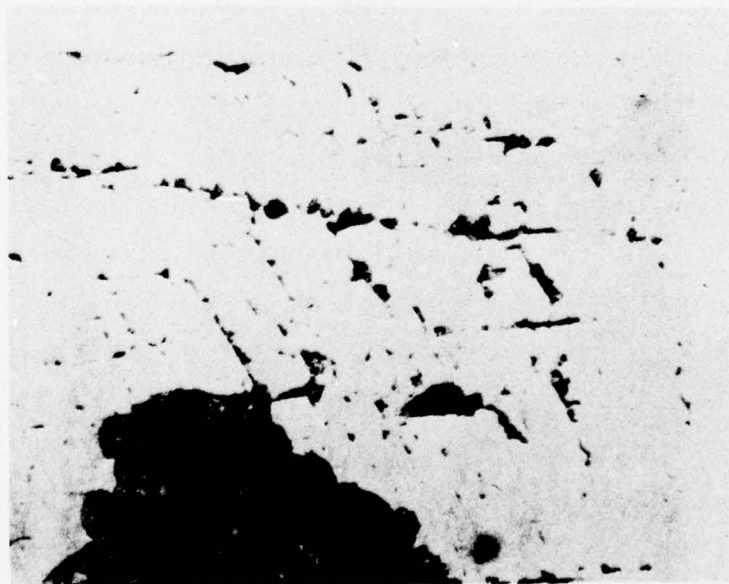
formed and started to grow on zinc selenide in 20 seconds, on gallium arsenide in 40 seconds, and on zinc sulfide in 240 seconds. Reference to Figures 27, 28 and 29 show that these times correspond to the points at which transmittance in the 2.5 to 25 micron range begins to decrease significantly. These pits, rather than surface or subsurface cracking, appear to be the primary cause of transmittance loss at the longer wavelengths. By the time the surface pits had begun to grow, the transmittance loss at wavelengths between 0.5 and 2.1 microns had already decreased by approximately 50%. Thus, subsurface damage prior to nucleation and growth of the large surface pits appear to be a major contributor to transmittance loss at the shorter wavelengths.

The progress of surface damage with exposure time at a selected site is illustrated in Figure 33 for gallium arsenide and in Figure 34 for zinc sulfide. The progress of damage can best be followed for zinc sulfide because of the greater number of exposure times. Overlapping impacts create regions of high crack density as shown by the micrographs in Figure 34 for 20, 40 and 80 seconds exposure. These regions of high crack density represent structural defects in the material which will increase the intensity of stresses generated by subsequent impacts. Relatively large pieces of material will then be chipped away to nucleate pits at these regions upon the impact of subsequent drops. Nucleation of pits is apparent in the micrograph after 160 seconds exposure. The depth of several of these small pits was estimated to be .030 to .060 mm based on the microscope travel required to change focus from the edges to the bottoms of the pits.

A pit, once nucleated, grows rapidly with continued exposure to the rain environment as illustrated by the micrograph after 240 seconds exposure. Many of the pits are quite deep by 320 seconds, often appearing to be deeper than they are wide. Similar deep pits were present on the zinc selenide specimen after 30 seconds exposure and on the gallium arsenide specimen after

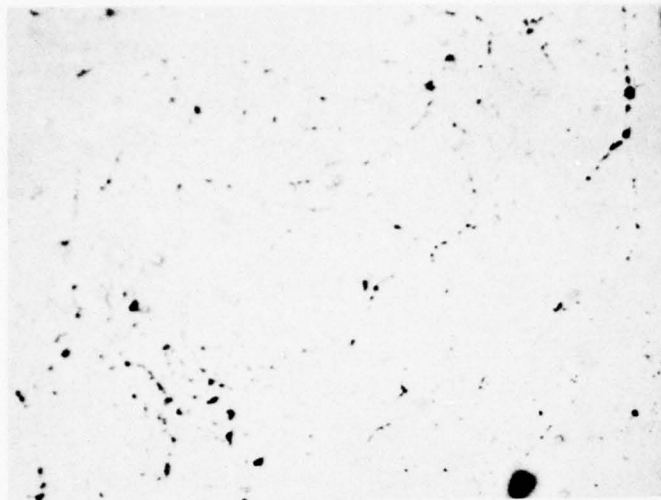


20 sec. Exposure

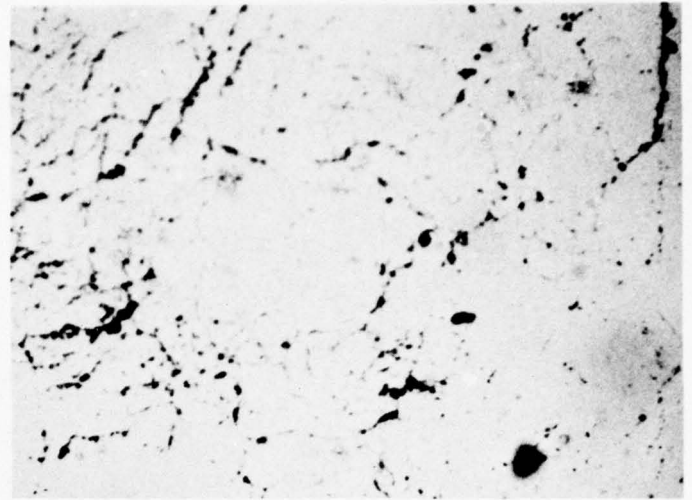


40 sec. Exposure

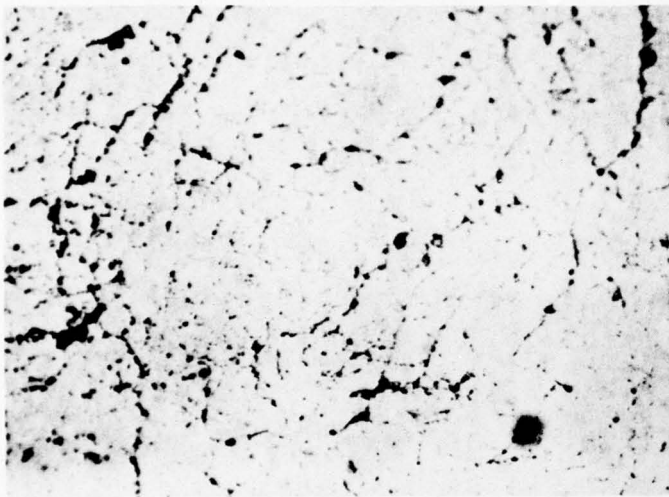
Figure 33. Progress of Damage at a Selected Site on Gallium Arsenide Exposed to Standard Rainfield (1 inch/hour, 1.8 mm Drops) at 730 fps. Mag. 250X



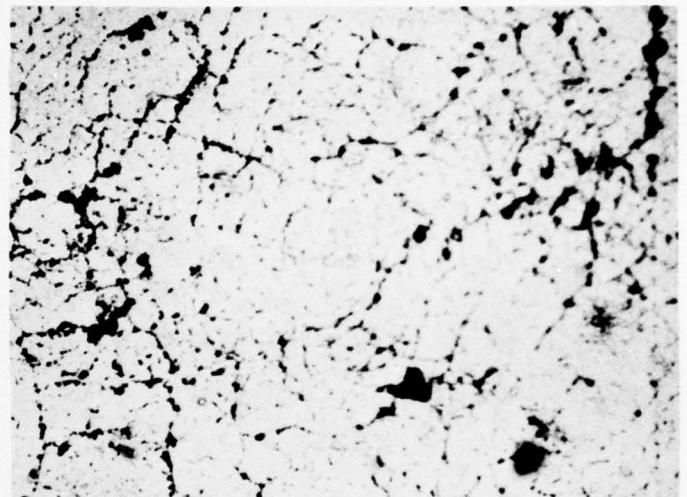
20 sec. Exposure



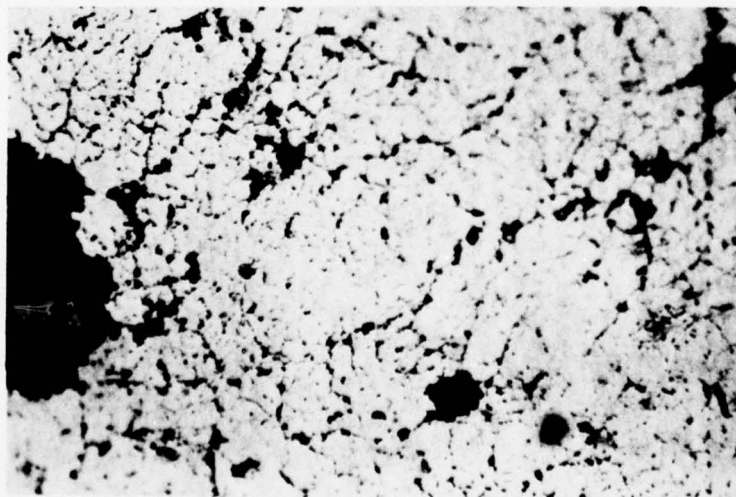
40 sec. Exposure



80 sec. Exposure



160 sec. Exposure



240 sec. Exposure

Figure 34. Progress of Damage at a Selected Site on Zinc Sulfide Exposed to Standard Rainfield (1 inch/hour, 1.8 mm Drops) at 730 fps. Mag. 135X

60 seconds exposure. It is probable that a second mechanism described by Morris⁽⁴⁾ contributes significantly to erosion once pits have been nucleated. This mechanism is the formation of a high velocity water jet when a drop impacts a pre-existing pit. This jet, with velocity four times greater than the initial drop velocity, will intensify damage at the bottom of the pit.

It is interesting to relate the progress of erosion in the rainfield to the estimated rate of drop impact. To cover one square inch of surface of the specimens with overlapping ring fractures in a hexagonal, close-packed array would require 940 impacts for zinc selenide and gallium arsenide and 1400 impacts for zinc sulfide. These numbers are based on the assumption that the distance between centers of impacts in the hexagonal array is the sum of the inner and outer radii of the ring fractures listed in Table 1 for single 2.0 mm diameter drop impact at 730 fps. The standard rainfield in the AFML/Bell erosion facility provides an impact rate of 56 drops per square inch per second at 730 fps.⁽³⁾ Thus, to cover the surface of the specimens with overlapping impacts requires 17 seconds for zinc selenide and gallium arsenide and 25 seconds for zinc sulfide. These times are based on the ideal condition that the drops impact to form a complete hexagonal, close-packed array of ring fractures before subsequent drops impact on the overlapping array already created. These times are in reasonable agreement with the results of the microscopic analyses as illustrated by Figures 30 through 34.

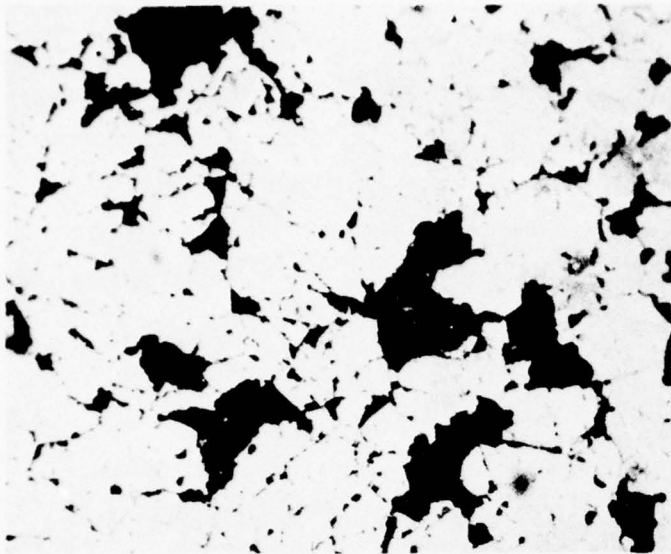
Pits are nucleated on zinc sulfide between 80 and 160 seconds based on Figure 34. Within this time range, each initial triplet impact site undergoes two to five additional sets of triplet drop impacts. Thus, an additional six to fifteen drops must impact an initial triplet overlap area before significant material removal occurs under the ideal distribution of impact sites assumed for this analysis. Actually, more than six to fifteen additional impacts are probably required because of the random distribution of impacts on the zinc sulfide specimen exposed to the rainfield in the AFML/Bell facility. Areas where

pits were nucleated between 80 and 160 seconds probably had received multiple impacts before the entire surface was covered by a single layer of overlapping ring fractures. The fact that a rather large number of overlapping impacts are required to nucleate a pit on zinc sulfide in the rainfield correlates with the results of the overlapping single drop impact experiments where overlapping single drop impact sites revealed only limited synergism.

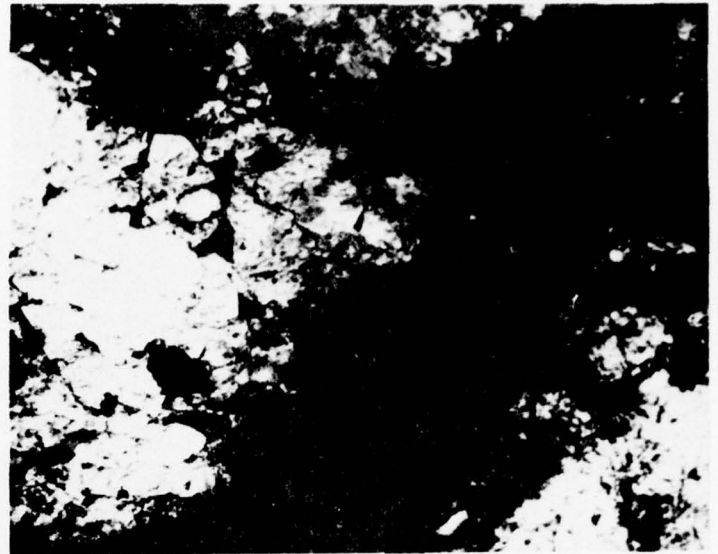
By the ideal analysis of overlapping impact in the rainfield described above, pits on zinc selenide formed after 20 seconds exposure would have been initiated by at least one additional drop impact at an overlapping triplet impact site. Similarly, pits on gallium arsenide formed after 40 seconds exposure would have been initiated by at least four additional drop impacts at an overlapping triplet impact site.

It was pointed out earlier in this section that the loss in transmittance at the longer wavelengths (2.5 to 25 microns) did not start until the nucleation and growth of large surface pits had occurred; however, by that time transmittance at the shorter wavelengths (0.5 to 2.1 micron) had already decreased drastically. This decrease in transmittance at the shorter wavelengths was assumed to be caused by extensive subsurface damage which precedes pit nucleation and growth. Figure 35 compares the surface and subsurface damage of selected areas of zinc selenide after 30 seconds of exposure and zinc sulfide after 320 seconds of exposure. Obviously, extensive subsurface damage precedes the growth of a pit in both materials.

Electron micrographs representative of various stages of erosion in the rainfield for zinc selenide, gallium arsenide, and zinc sulfide are presented in Figures 36, 37 and 38, respectively. The extensive damage of zinc selenide from multiple impacts after only 20 seconds of exposure is quite apparent in Figure 36. Cleavage steps can be seen at the bottom of the large pit shown in the lower two micrographs of this figure. The

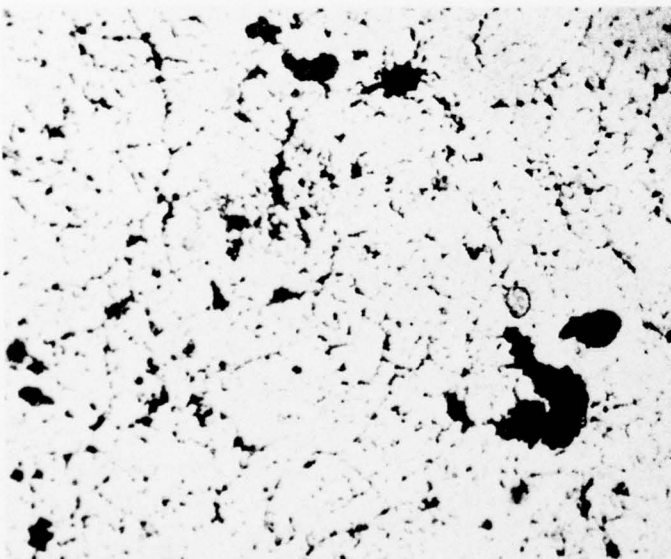


Reflected Light

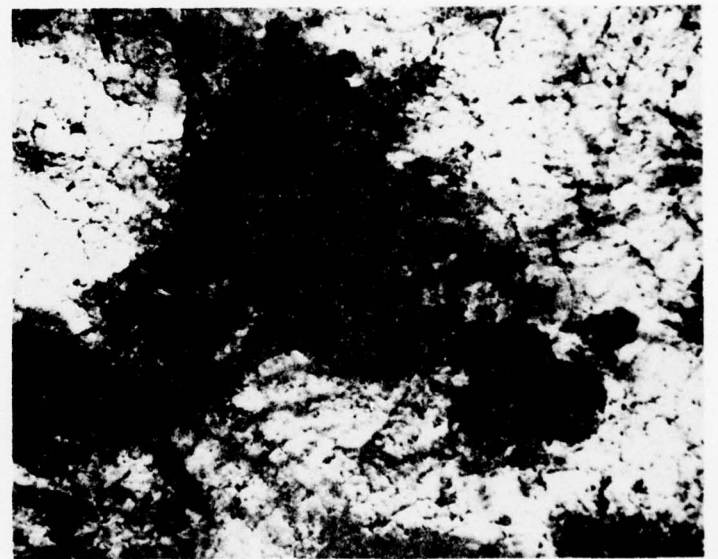


Transmitted Light

a. Zinc Selenide After 30 sec Exposure



Reflected Light



Transmitted Light

b. Zinc Sulfide After 320 sec Exposure

Figure 35. Subsurface Damage After Exposure to Standard Rainfield (1 inch/hour, 1.8 mm Drops) at 730 fps Mag. 135X

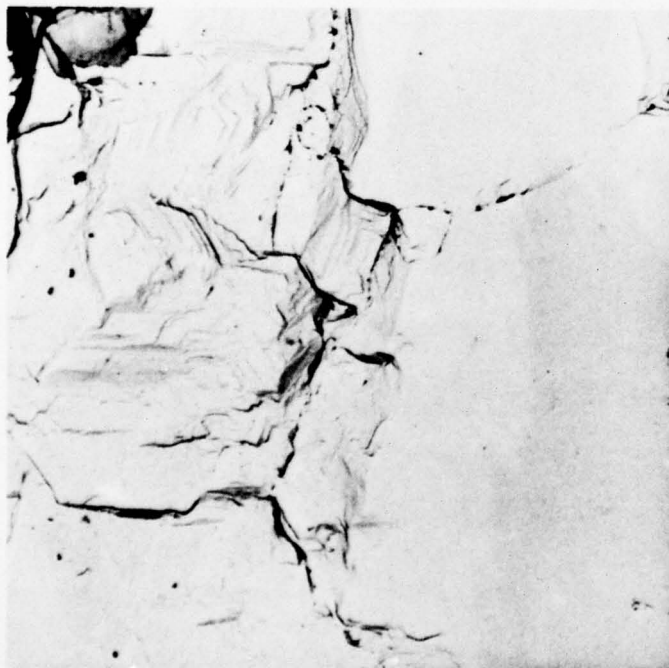


2000X

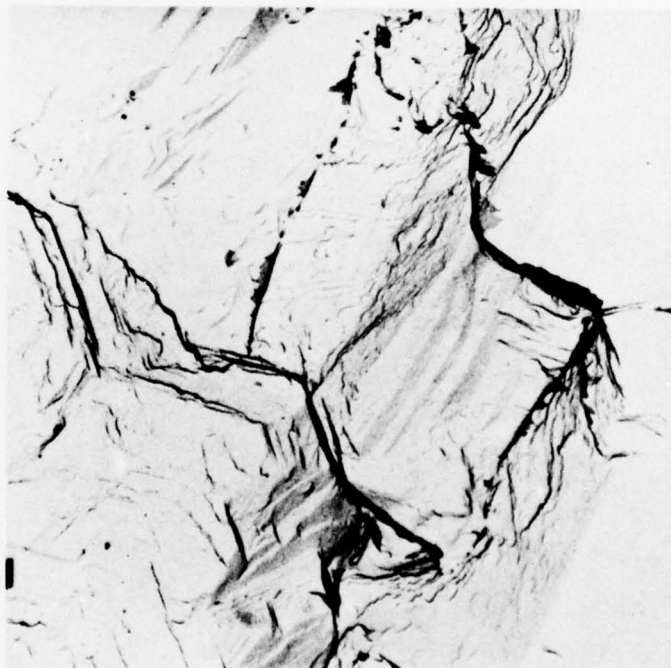


2000X

a. Intersecting Ring Fractures



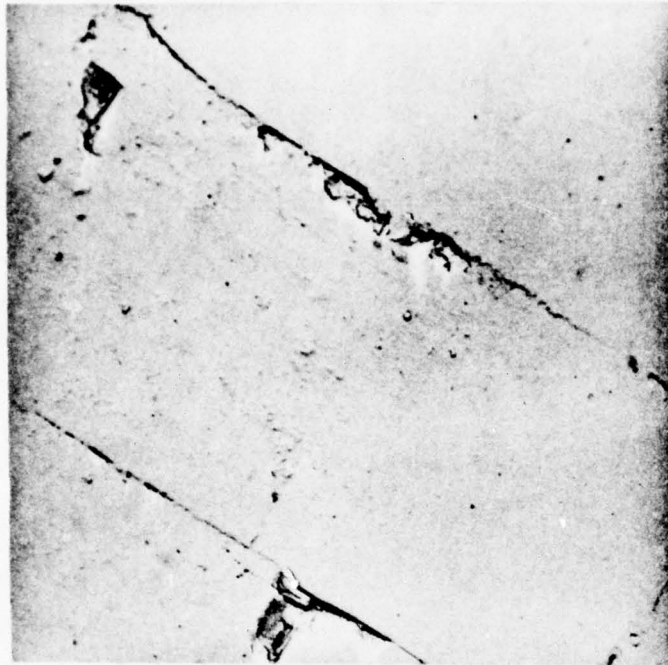
2000X



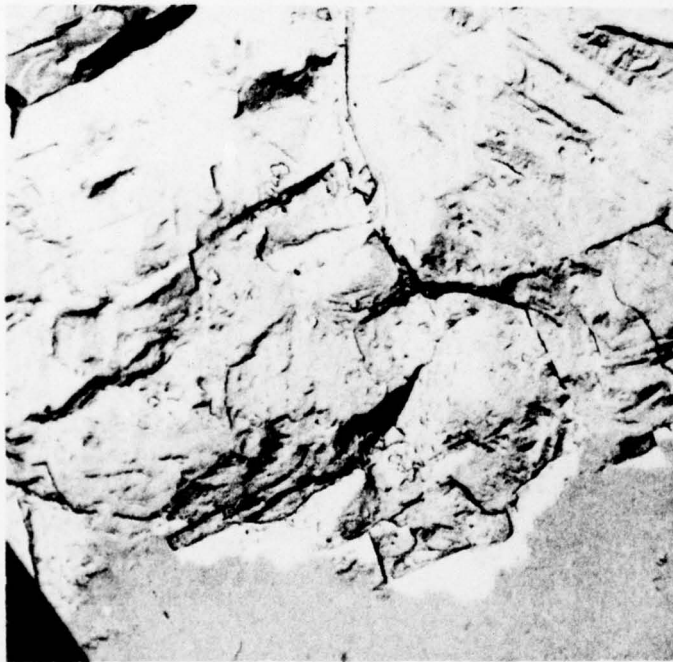
8000X

b. Features of Large Pit

Figure 36. Electron Micrographs of Typical Damage on Zinc Selenide Exposed for 20 seconds to the Standard Rainfield (1 inch/hour, 1.8 mm Drops) at 730 fps.



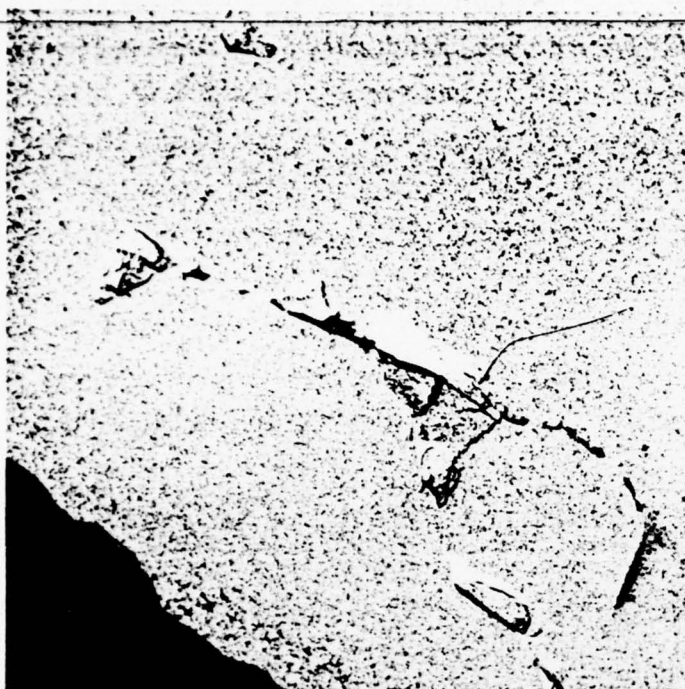
a. 20 sec. Exposure



b. 40 sec. Exposure

c. 60 sec. Exposure

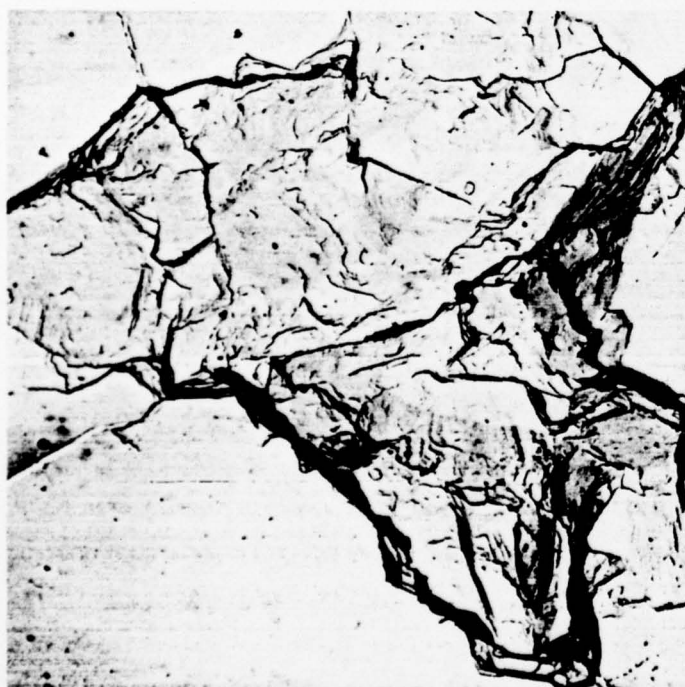
Figure 37. Electron Micrographs of Typical Damage on Gallium Arsenide Exposed to the Standard Rainfield (1 inch/hour, 1.8 mm Drops) at 730 fps. Mag. 2000X



a. 20 sec. Exposure



b. 40 sec. Exposure



c. 80 sec. Exposure



d. 160 sec. Exposure

Figure 38. Electron Micrographs of Typical Damage on Zinc Sulfide Exposed to the Standard Rainfield (1 inch/hour, 1.8 mm Drops) at 730 fps. Mag. 2000X

64-25-70 10135 DEPC

surface of this pit appears similar to the fracture surfaces of CVD zinc selenide specimens loaded as double cantilever beams.(5) Examination of the pits revealed no evidence supporting the theory proposed in Section II.C.2 that much of the subsurface damage generated by a single drop impact on zinc selenide consists of intergranular extension of the surface cracks along grain boundaries which are approximately parallel to the specimen surface. The multiple impacts required for pit nucleation and growth may generate so much additional transgranular fracture as to obliterate any evidence of an initial intergranular failure mode.

Damage to gallium arsenide after 20 seconds of exposure, as shown in Figure 37a, is not nearly so extensive as that on zinc selenide after 20 seconds. Figure 37b shows the cleavage steps at the bottom of one of the large pits which were present after 40 seconds. Figure 37c, after 60 seconds of exposure, shows the deepest crack found on gallium arsenide during the electron microscopic examination. The depth of this crack is approximately 0.008 mm (0.0003") based on the length of the shadow cast on the replica.

The limited cracking of zinc sulfide after 20 seconds in the rainfield (Figure 38a) is quite similar to that of the single drop impact sites (Figure 4d). After 40 seconds (Figure 38b), enhanced damage at intersecting ring fractures becomes apparent. Cleavage in the relatively small pit nucleated after 80 seconds can be seen in Figure 38c. Figure 38d, after 160 seconds of exposure, shows the deepest crack found during the electron microscopic examination of the replicas obtained from the zinc sulfide specimen exposed to the rainfield. The depth of this crack is approximately 0.01 mm (0.0004") based on the length of the shadow cast on the replica.

This series of experiments in the rainfield provided a considerable amount of information on the operative erosion mechanisms and the correlation between erosion damage and losses in transmittance. For zinc sulfide, several drops must impact

at a given location before any significant amount of material is removed by pit nucleation and growth. Transmittance for the shorter wavelengths (0.5 to 2.1 microns) begins to decrease with the subsurface damage from the first drop impact and continues to decrease almost linearly as the amount of subsurface damage increases with additional impacts. Transmittance for the longer wavelengths (2.5 to 25 microns) does not decrease during this initial incubation stage while the concentration of subsurface defects increases. Once pits have nucleated and started to grow in lateral area, transmittance starts to decrease for the longer wavelengths. This decrease appears to be almost directly proportional to the percentage of total pitted area.

Zinc selenide and gallium arsenide eroded too rapidly in the rainfield to provide a sufficient number of exposures for a complete analysis of the relationship between transmittance and erosion damage. It is likely that the relationship for these two materials is similar to that described above for zinc sulfide, although fewer overlapping impacts would be required to nucleate a pit.

The overlapping single drop experiments demonstrated the fact that two, or even three, overlapping drops do not cause pit nucleation. This correlates with the results from the rainfield experiments. Based on an ideal assumption of the surface distribution of drop impact sites produced by the rainfield, a total of at least nine to eighteen drops must impact the same area on zinc sulfide to nucleate a pit. Thus, additional overlapping single drop experiments are required to completely define the incubation stage from damage by a single impact to the point where significant material removal takes place.

F. Protective Layers

It is obvious that zinc selenide has poor resistance to rain erosion and will require some form of protection. One method of improving the performance of zinc selenide is to apply an outer protective layer of a more erosion resistant material

such as zinc sulfide. To investigate the behavior of protective layers, bilayered specimens consisting of outer layers of zinc sulfide bonded to zinc selenide were impacted at 730 fps with single drops of 2.0 mm diameter. The zinc sulfide layers of 0.25, 0.50 and 1.0 mm thickness were bonded to polished zinc selenide substrates with lens cement so that the layers could be separated subsequent to impact to examine the nature of the damage on the zinc selenide.

Each of the three bilayered specimens was exposed for five minutes to impact by 2.0 mm diameter single drops at 730 fps. PMMA specimens were also exposed for five minutes immediately before and after the bilayered specimens. These PMMA control specimens were to verify the location of the single drop generator and to record the single drop impact rate. The number of impact sites on each of the specimens is tabulated in Table 6. Considering the variability of the drop formation rate of the single drop generator, these data indicate a one-to-one correspondence between drop impact and ring fracture on the bilayered specimens.

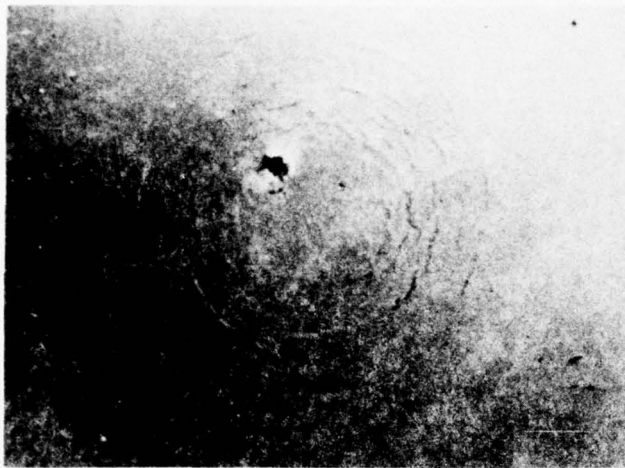
The impacted bilayered specimens were examined initially before the zinc sulfide protective layers were removed. Overall appearances of the typical ring fractures on the three different zinc sulfide layers are shown in Figure 39. Ring fractures on zinc sulfide are difficult to examine by optical microscopy and Nomarski interference contrast was used with reflected light to enhance the topography in the micrographs in Figure 39. Light transmitted through the specimen from the back face of the zinc selenide substrate proved to be effective for delineating the ring fractures as shown in Figures 40, 41 and 42.

Examination of Figures 39 thru 42 shows that the ring fractures on the 0.50 and 1.0 mm layers are similar in appearance and also similar to the ring fractures formed on bulk zinc sulfide by 2.0 mm diameter drops impacting at 730 fps. The ring fractures on the 0.25 mm zinc sulfide layer are somewhat larger

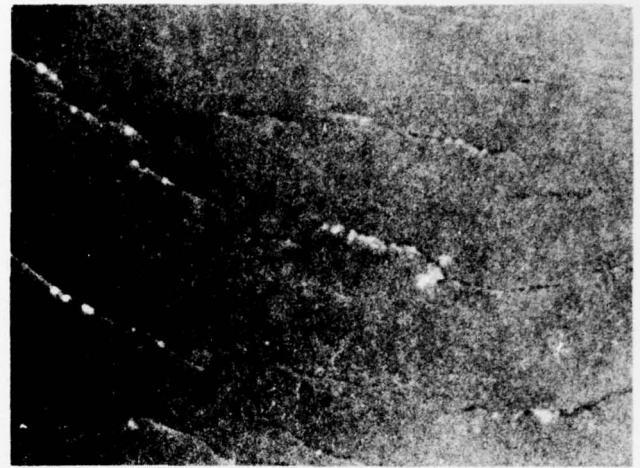
TABLE 6
 NUMBER OF IMPACT SITES OBTAINED DURING
 FIVE-MINUTES EXPOSURE TO
 SINGLE DROP IMPACT AT 730 FPS

<u>Specimen</u> ^(a)	<u>Impact Sites After 5 Minutes Exposure</u>
PMMA, Before Test	36
.25 mm ZnS/ZnSe	23
.50 mm ZnS/ZnSe	24
1.00 mm ZnS/ZnSe	16
PMMA, After Test	20

(a) Specimens listed in order of exposure.

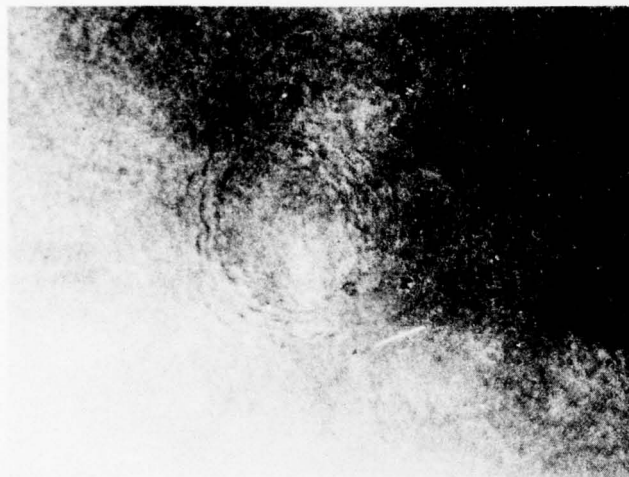


45X

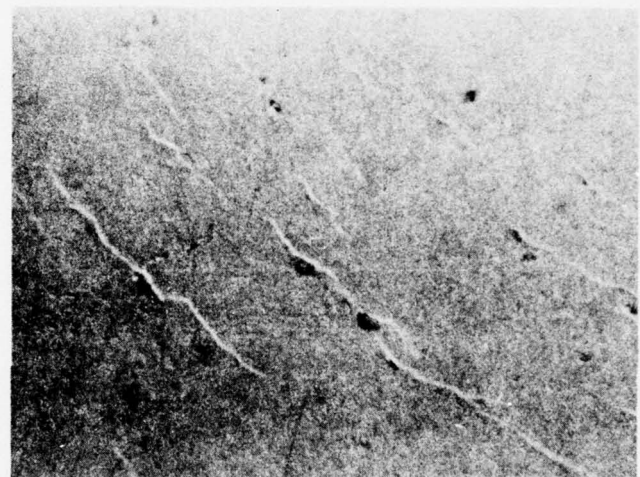


625X

a. 0.25 mm Zinc Sulfide Layer

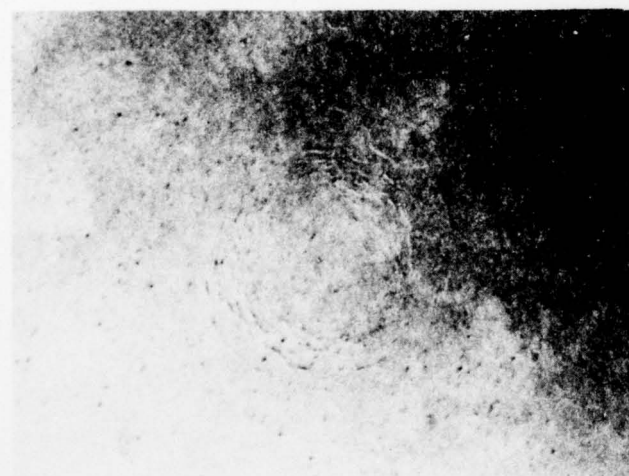


45X

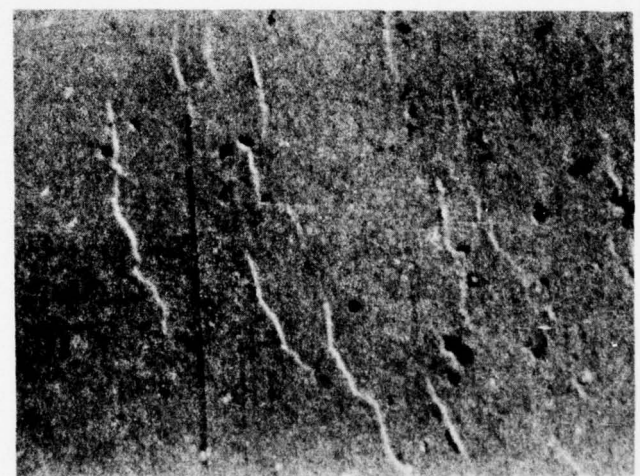


470X

b. 0.50 mm Zinc Sulfide Layer



45X



470X

c. 1.0 mm Zinc Sulfide Layer

Figure 39. Sites of 2.0 mm Single Drop Impact at 730 fps on Zinc Sulfide Protective Layers Bonded to Zinc Selenide Substrate

AD-A046 702

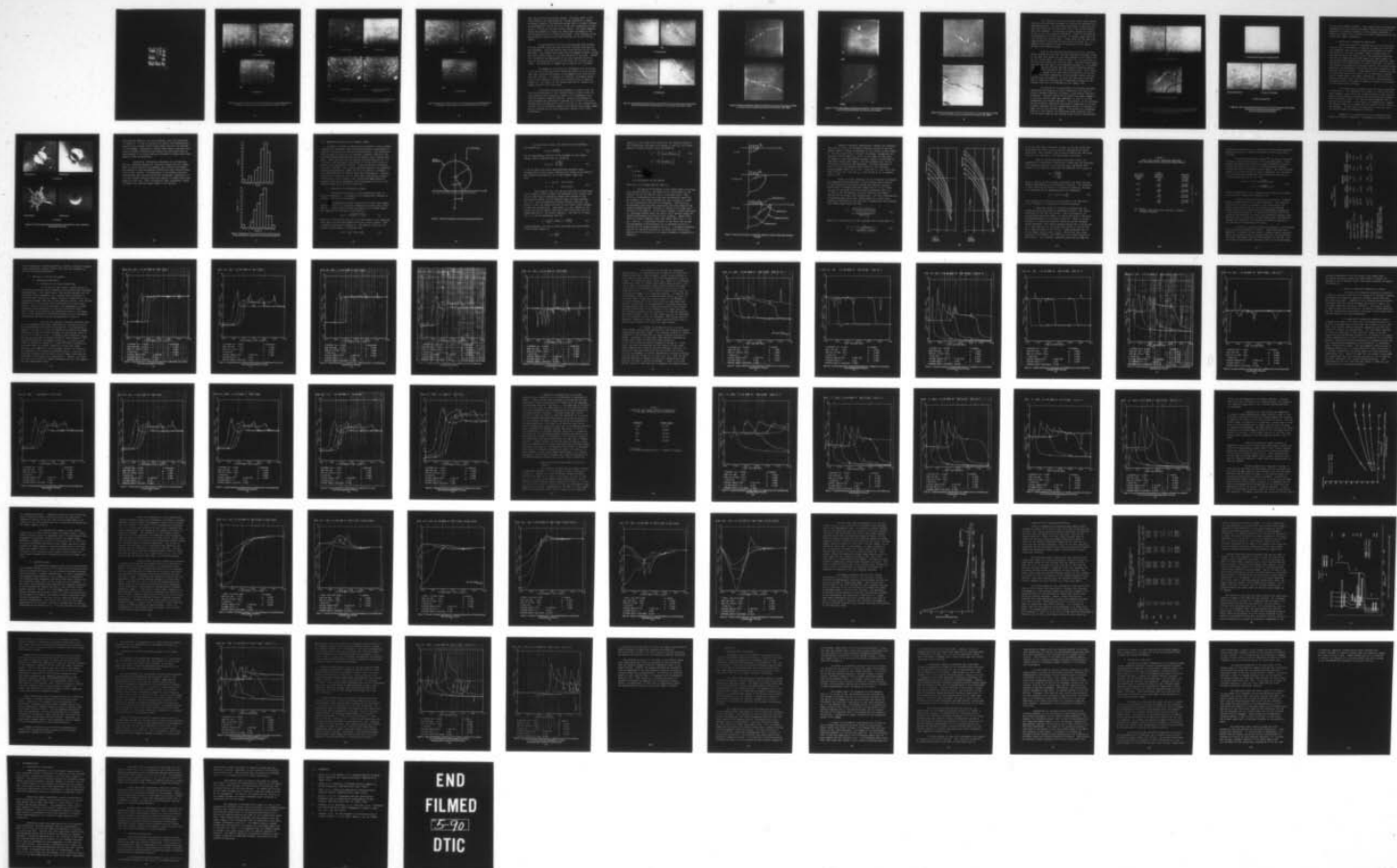
EXPLORATORY DEVELOPMENT OF RAIN EROSION RESISTANT
INFRARED WINDOW MATERIALS(U) BELL AEROSPACE TEXTRON
BUFFALO N Y J V HACKWORTH ET AL MAY 77 AFML-TR-77-84
F33615-76-C-5125

2/2

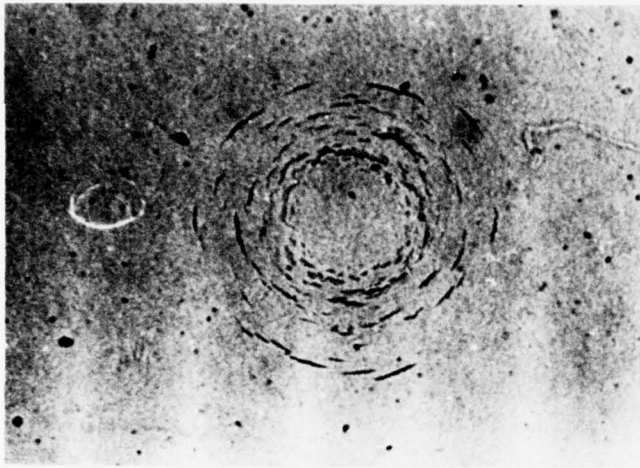
UNCLASSIFIED

F/G 9/3

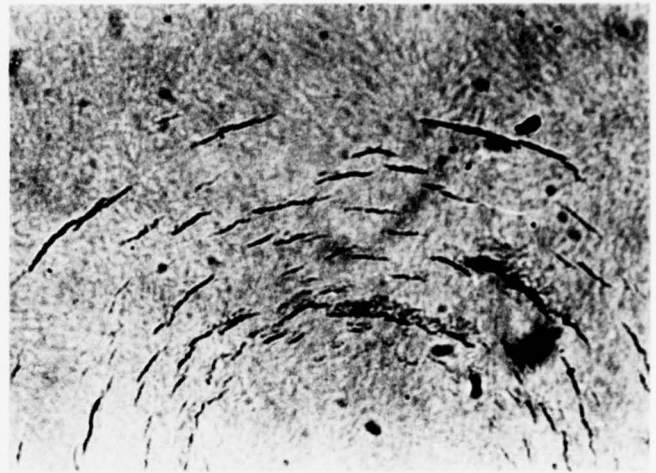
NL







35X



105X

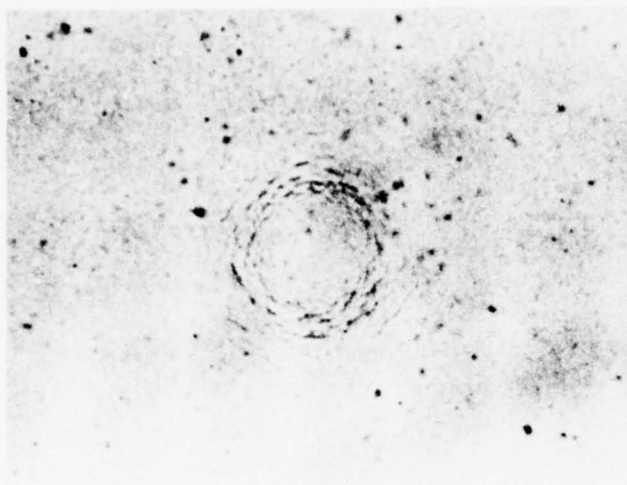
a. Transmitted Light



150X

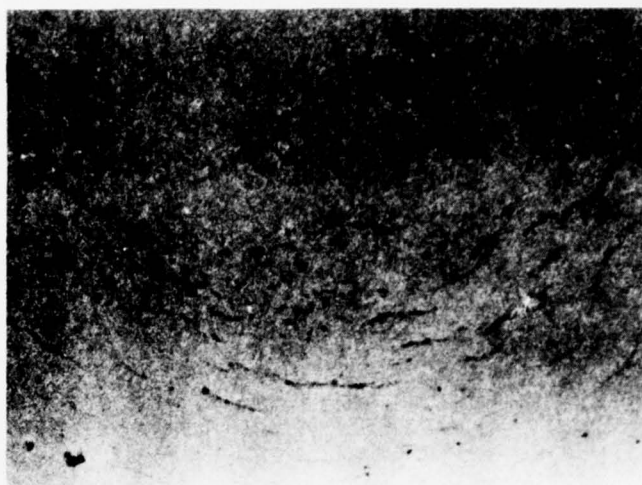
b. Reflected Light

Figure 40. Impact Site on Front Surface of 0.25 mm Thick Layer of Zinc Sulfide Bonded to Zinc Selenide. Surface Impacted by 2.0 mm Single Water Drops at 730 fps.



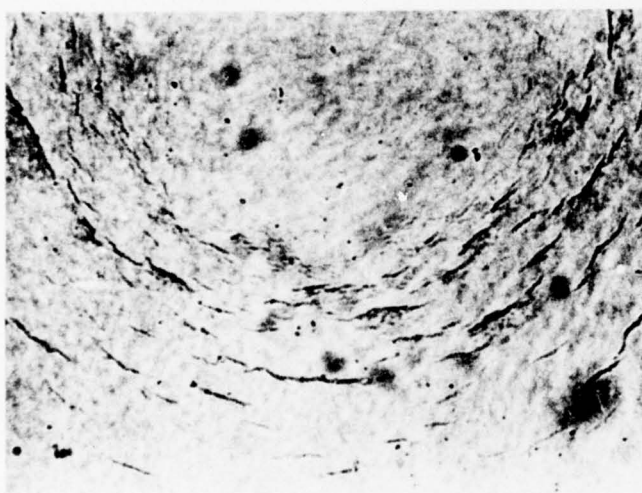
35X

a. Transmitted Light



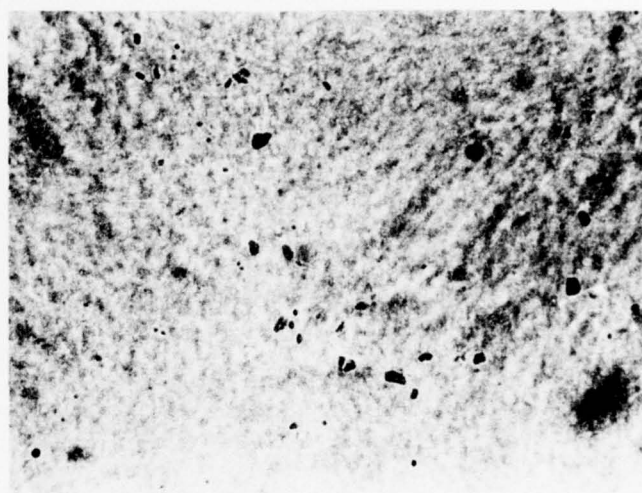
105X

b. Reflected Light



105X

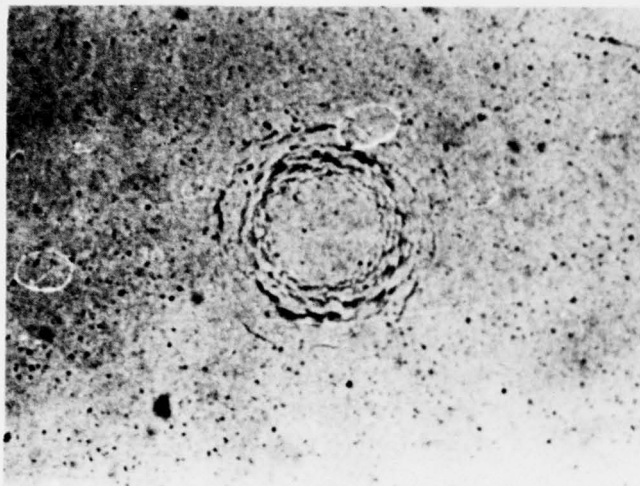
c. Transmitted Light



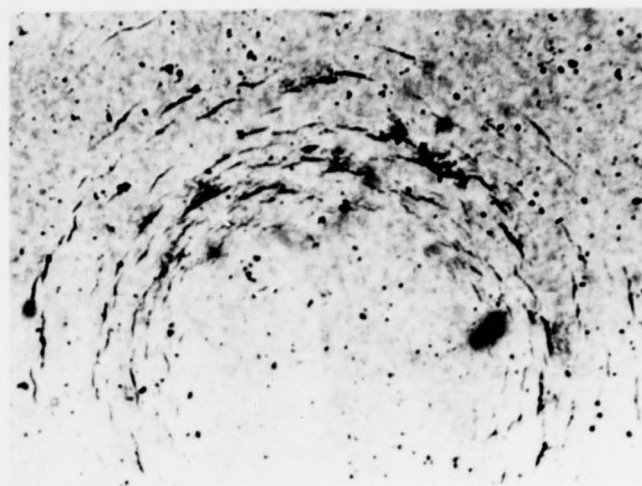
105X

d. Repeat of c, but Focused on
Zn Se Substrate

Figure 41. Impact Site on Front Surface of 0.50 mm Thick Layer of Zinc Sulfide Bonded to Zinc Selenide. Surface Impacted by 2.0 mm Single Water Drops at 730 fps.



35X



105X

a. Transmitted Light



105X

b. Reflected Light

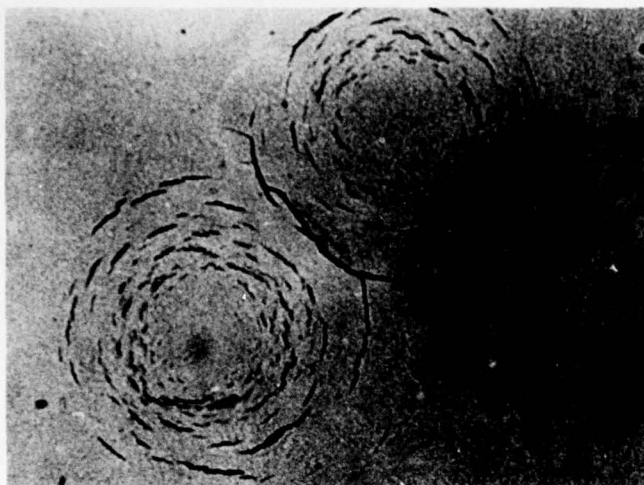
Figure 42. Impact Site on Front Surface of 1.0 mm Thick Layer of Zinc Sulfide Bonded to Zinc Selenide. Surface Impacted by 2.0 mm Single Water Drops at 730 fps.

than those on the two thicker layers. The inner radii of the ring fractures are approximately 0.20 mm regardless of layer thickness; however, the fractures extend out to a radial distance of approximately 0.50 mm on the 0.25 mm layer compared to a distance of 0.40 mm on the two thicker layers. The higher magnification micrographs in Figure 39, show slight chipping of the ring fractures on the 0.25 mm thick layer. This chipping is not particularly evident on the ring fractures on the two thicker layers.

It was possible to focus the microscope down through the zinc sulfide layer and onto the zinc selenide substrate at the interface. This was done at each ring fracture on all three specimens. No evidence was found that the damage extended through the zinc sulfide layers to the zinc selenide in any case. Figure 41d illustrates the appearance of the zinc selenide directly below a ring fracture on the 0.50 mm thick zinc sulfide outer layer. No indication of damage can be seen at the interface.

The damage at the sites of overlapping ring fractures on the zinc sulfide protective layers was found to be no greater than that exhibited previously by overlapping ring fractures on bulk zinc sulfide. An example of a doublet overlapping impact site on the thinnest (0.25 mm) zinc sulfide layer is shown in Figure 43. The impact of the second drop did not enhance the damage caused by the first drop.

An electron microscopic analysis of impact sites on the three thicknesses of zinc sulfide layers verified that the ring fractures were similar to those on the homogeneous zinc sulfide specimens impacted earlier. Electron micrographs of ring fractures are presented in Figures 44, 45 and 46 for zinc sulfide layer thicknesses of 0.25, 0.50 and 1.0 mm, respectively. Contrary to the conclusion based on the optical microscopic examination, chipping of the ring fractures occurred on all three thicknesses.

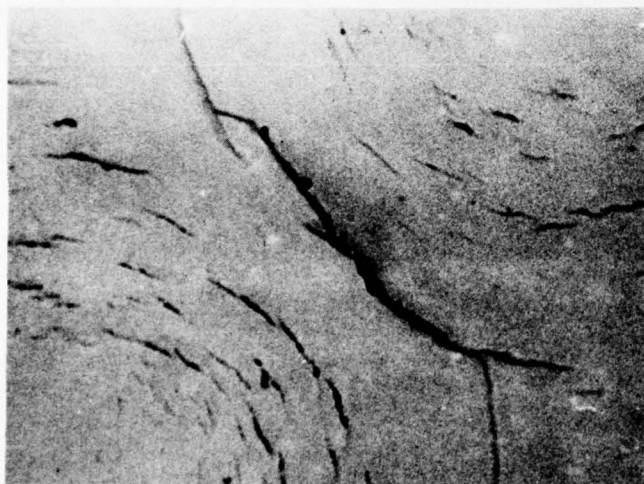


35X

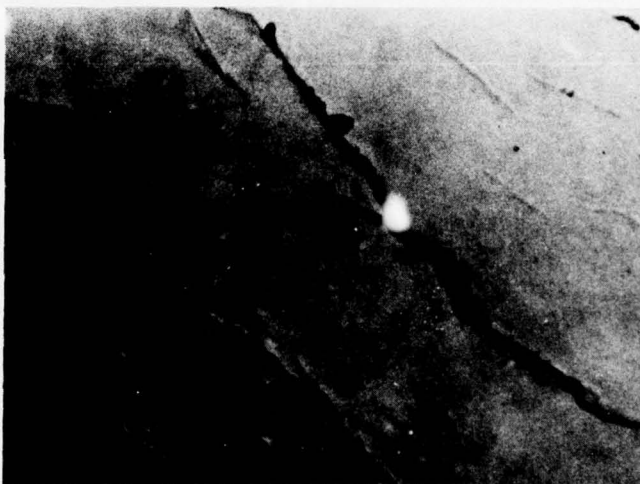


105X

a. Transmitted Light



105X



180X

b. Reflected Light

Figure 43. Overlapping Doublet Impact Sites on Front Surface of 0.25 mm Thick Layer of Zinc Sulfide Bonded to Zinc Selenide. Surface Impacted by 2.0 mm Single Water Drops at 730 fps.

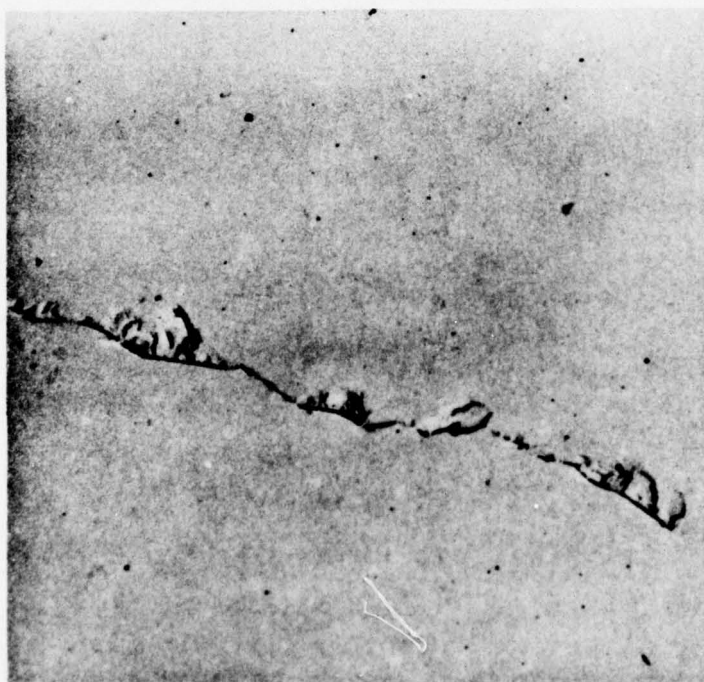
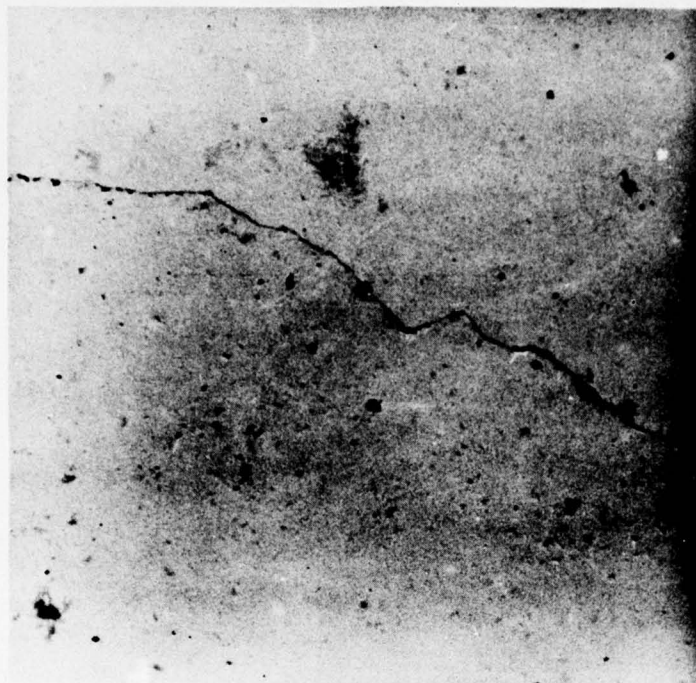
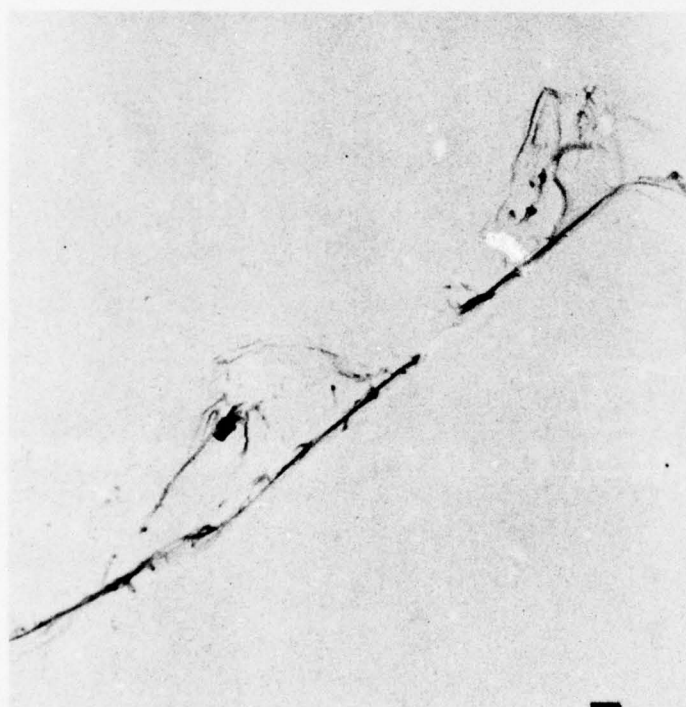


Figure 44. Electron Micrographs of Ring Fractures Formed by 2.0 mm Drop Impact at 730 fps. on 0.25 mm Thick Zinc Sulfide Layer Bonded to Zinc Selenide. Mag. 2000X



4500X



10,000X

Figure 45. Electron Micrographs of Ring Fractures Formed by 2.0 mm Drop Impact at 730 fps. on 0.50 mm Thick Zinc Sulfide Layer Bonded to Zinc Selenide

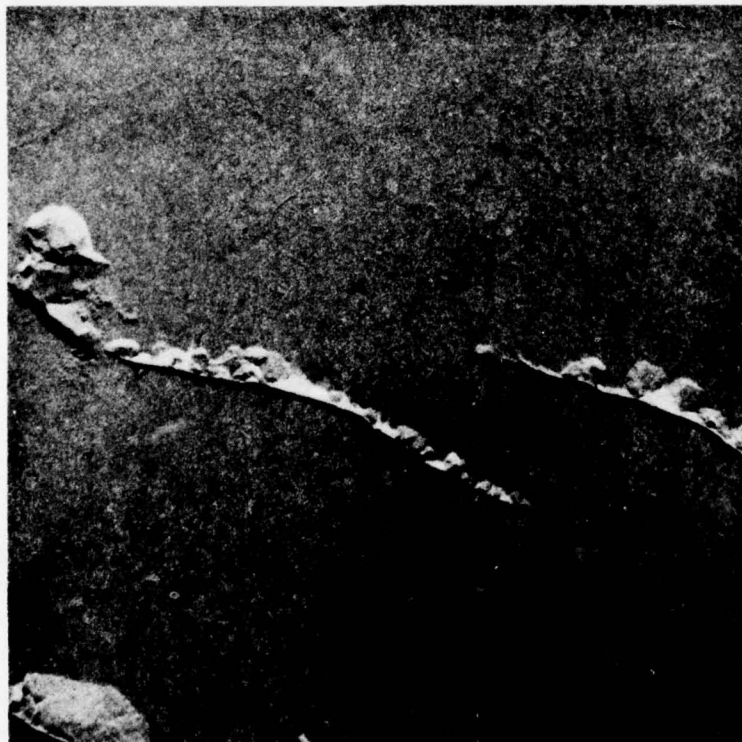
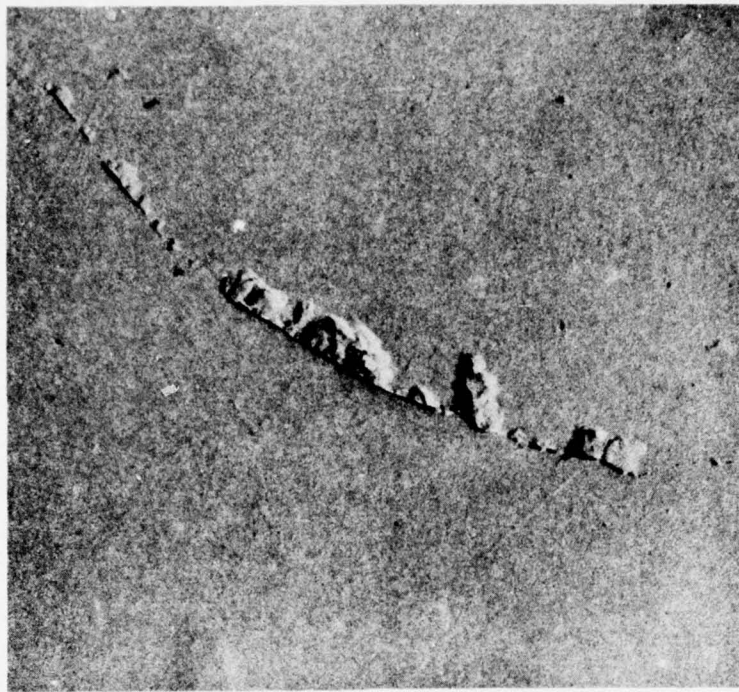
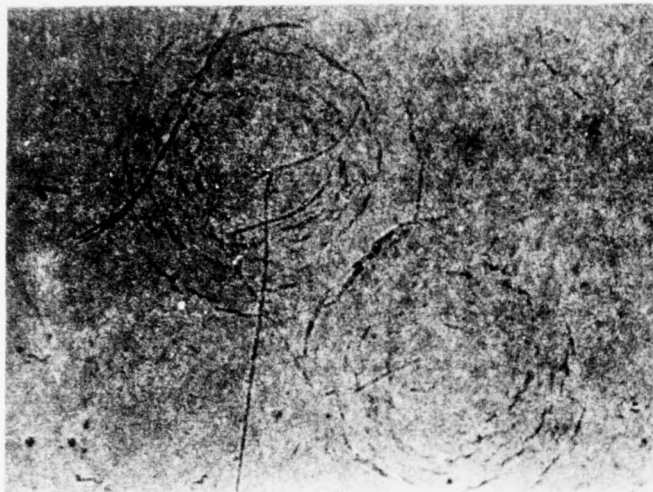


Figure 46. Electron Micrographs of Ring Fractures Formed by 2.0 mm Drop Impact at 730 fps. on 1.0 mm Thick Zinc Sulfide Layer Bonded to Zinc Selenide. Mag. 2000X

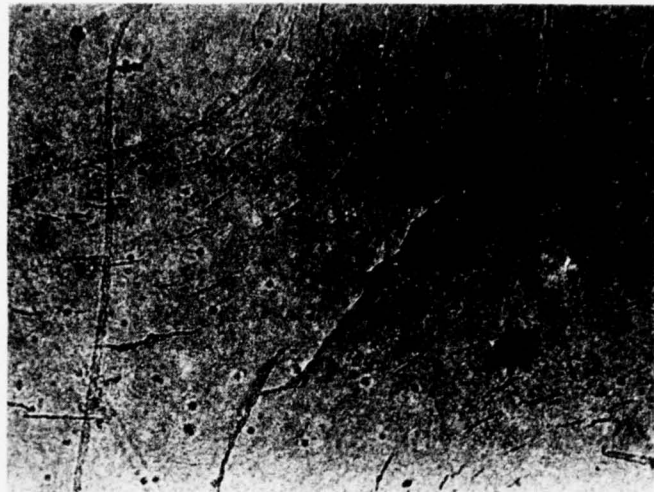
The 0.25 and 0.50 mm zinc sulfide layers were removed from the zinc selenide substrates by boiling the specimens in a decementing agent. The protected front faces of the zinc selenide substrates and the back faces of the zinc sulfide layers were then examined. No evidence of impact damage was found on either of the zinc selenide substrates. Figure 47 illustrates the appearance, from the back face, of typical impact sites on the 0.25 mm zinc sulfide layer. These sites are the same overlapping doublet shown from the front face in Figure 43. It is apparent from Figure 47b that the fractures did not extend through the protective layer.

None of the fractures on either of the zinc sulfide layers removed from the zinc sulfide substrates extended through to the back face except for one crack adjacent to an impact site on the 0.25 mm layer. As shown in Figure 48, this crack was on the back face rather than the front face. This particular impact site was near one edge of the bilayered specimen: it is probable that the crack on the back face was caused by handling during decementing and removal of the zinc sulfide layer. This conclusion is reinforced by the fact that this crack was not noticed during the initial examination of the specimen before the zinc sulfide layer was removed. It could not have been overlooked when the optical microscope was focused down through the zinc sulfide layer onto the interface at each impact site.

The results of this evaluation of bilayered specimens demonstrate the promise of using a relatively thin layer of erosion resistant material to protect a less erosion resistant substrate. The basic nature of the water drop impact damage on a thin zinc sulfide layer was comparable to that on a thick, homogeneous zinc sulfide specimen. The presence of the interface and the different mechanical and physical properties of the zinc selenide substrate did not significantly affect the response to impact of the zinc sulfide layer. As discussed in a subsequent section of this report, the analytical model predicted that a 0.25 mm thick layer of zinc sulfide would prevent ring failures

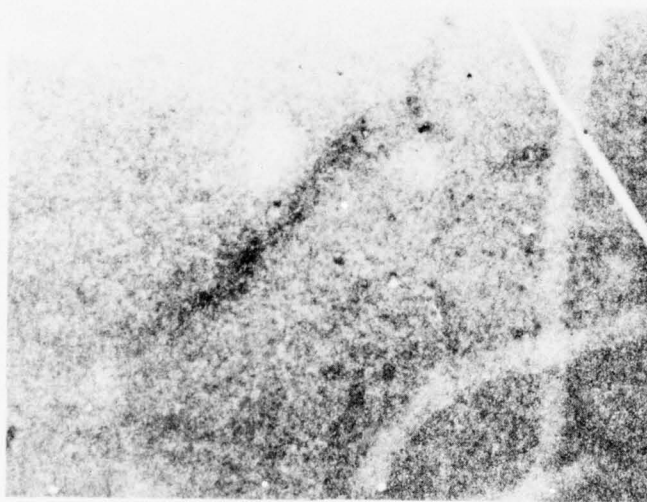


35X



105X

a. Transmitted Light Focused on Front Surface



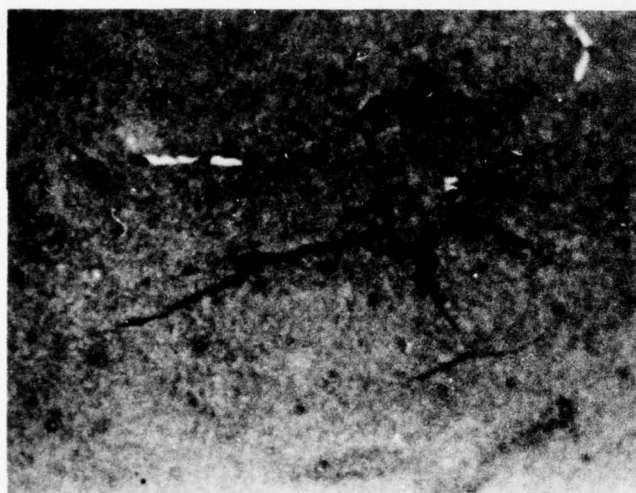
105X

b. Reflected Light Focused on Back Surface

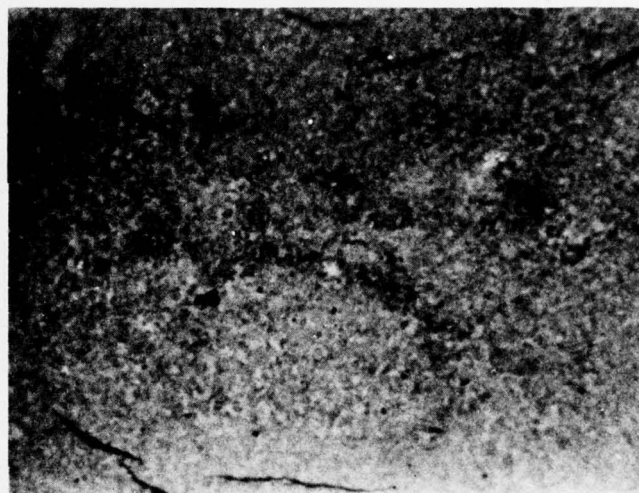
Figure 47. Overlapping Doublet Impact Sites on 0.25 mm Thick Layer of Zinc Sulfide (Same Sites as Figure 43) Viewed from the Back Surface after Removal of the Layer from the Zinc Selenide Substrate



a. Transmitted Light Focused on Front Surface, Mag 35X



Focused on Back Surface



Focused on Front Surface

b. Reflected Light, Mag 105X

Figure 48. Crack on Back Surface Near Impact Site on 0.25 mm Thick Layer of Zinc Sulfide Viewed from the Back Surface after Removal of the Layer from the Zinc Selenide Substrate

in the zinc selenide substrate. The results from the microscopic examination of the bilayered specimens confirm this prediction. Exposure of bilayered specimens to the standard rainfield is planned in future work to verify the benefits demonstrated in the single drop impact experiments.

G. Quasistatic Indentation Evaluations

Adler and Hooker⁽¹⁾ evaluated the use of the Hertzian fracture test to determine the fracture strength and ring fracture diameters for a series of glasses and attempted to relate the results to the case of dynamic impact of glass beads on borosilicate glass and fused silica. The underlying reasoning was that the impacting particles sample very small domains of the surface being impacted and that quasistatic loading by small spheres would be representative of these conditions. As part of this present investigation of erosion behavior of infrared window materials, the quasistatic indentation test was evaluated on zinc selenide and zinc sulfide. It was hoped that a correlation could be established between the results of the quasistatic loading and the single water drop impact experiments. The relatively simple indentation test could then be used to evaluate methods to improve erosion resistance of materials without the necessity of additional erosion testing.

The experimental arrangement was the same as described in Reference 1. The specimens were loaded by a 407 micron diameter sapphire sphere while the contact area was viewed from the opposite side through a microscope focused through the specimen onto the loaded surface. The load was slowly applied until a fracture was observed. At this point, the loading was stopped, the fracture load was recorded, and the diameter of the fracture was measured. The test was then repeated at a new area until the desired number of readings was obtained.

Examples of the fractures on zinc selenide and zinc sulfide are shown in Figure 49. Histograms of fracture loads

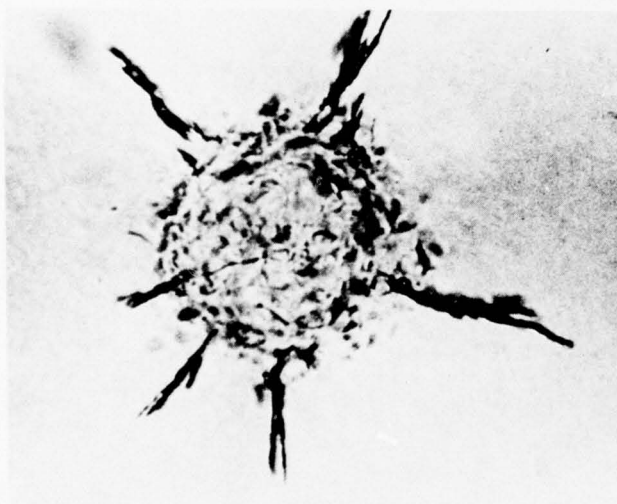


Transmitted Light

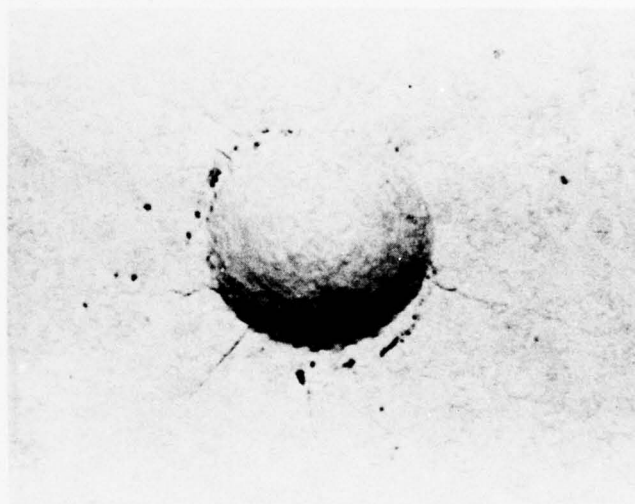


Reflected Light

a. Zinc Selenide



Transmitted Light



Reflected Light

b. Zinc Sulfide

Figure 49. Typical Fractures Produced by Quasistatic Loads Applied by a $407\text{ }\mu\text{m}$ Diameter Al_2O_3 Sphere. Mag. $290\times$

and fracture diameters for zinc selenide, only, are presented in Figure 50. It was so difficult to detect the fractures produced on zinc sulfide that reliable data could not be obtained for histograms. Quasistatic loading under these conditions produces a surface indentation and radial cracking which bear no relationship to the ring fractures produced by single water drop impact on the two materials.

Quasistatic indentation evaluation of the materials was not continued because the fractures formed were not comparable to those formed by the dynamic case of water drop impact and because of the experimental difficulties with fracture detection in zinc sulfide. Interestingly, a few similar spherical indentations were noticed during the microscopic examination of the zinc sulfide specimen which was exposed to single water drop impact at 1120 fps. These indentations were undoubtedly caused by impact with residual glass beads in the facility.

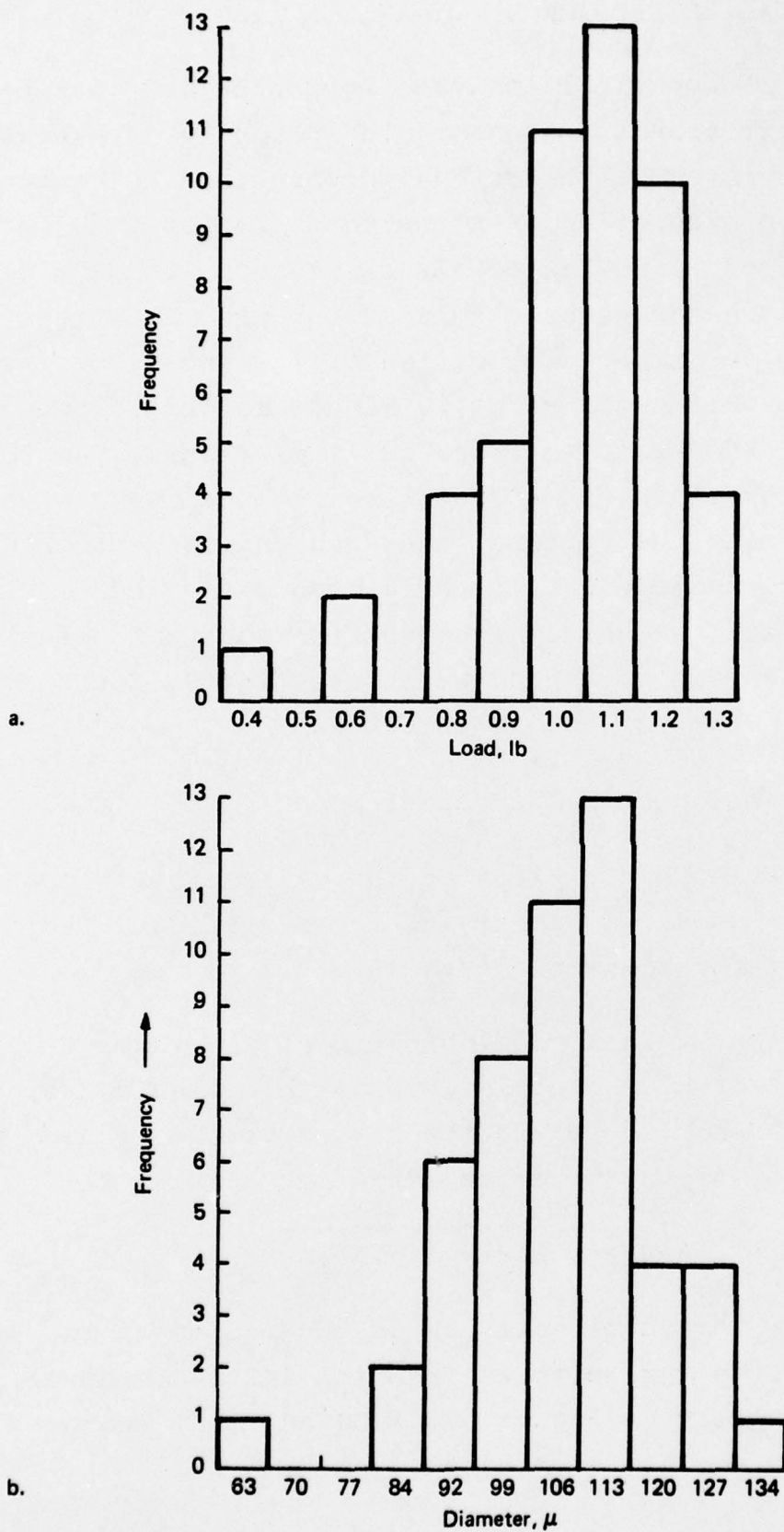


Figure 50. Histograms of Fracture Loads and Fracture Diameters for Zinc Selenide Quasistatically Loaded with 407 μm Diameter Al_2O_3 Spheres

III. THEORETICAL PREDICTION OF DYNAMIC STRESS

A number of numerical analyses were obtained to aid in understanding the experiment data and guide planning of experiments to support or disprove the theoretical predictions. The analytical task focused on prediction of transient stresses induced in the selected infrared window materials by impacts with a single rain drop. These stresses were calculated for drop diameters of 0.7, 2.0 and 2.5 mm and impact velocities of 730 and 1120 ft/sec to parallel the experimental effort. Window materials considered were zinc selenide, zinc sulfide, gallium arsenide, and germanium. Polymethylmethacrylate (PMMA) was also included as a standard for characterizing the various rain drop environments. Computer studies were conducted for all three drop sizes and both impact velocities on zinc selenide, zinc sulfide and PMMA materials. Gallium arsenide and germanium were investigated for the 2.0 mm diameter drop, only, at both velocities.

A. Description of Mathematical Model

A detailed description of the mathematical model is given in Reference 1. A summary of the significant features is presented below for completeness.

The mathematical model chosen for the water drop impact process is that of a completely compressible liquid drop colliding with a rigid surface where the radius of the loaded region as a function of time can be described by

$$a(t) = \sqrt{2RV_0t - (V_0t)^2} \quad (1)$$

where V_0 is the impact velocity, R is the radius of the spherical drop, and t is the time elapsed from the initial contact. This is shown pictorially in Figure 51. The angle ϕ , known as the lateral outflow angle, is computed from

$$\phi(t) = \sin^{-1} [a(t)/R] \quad (2)$$

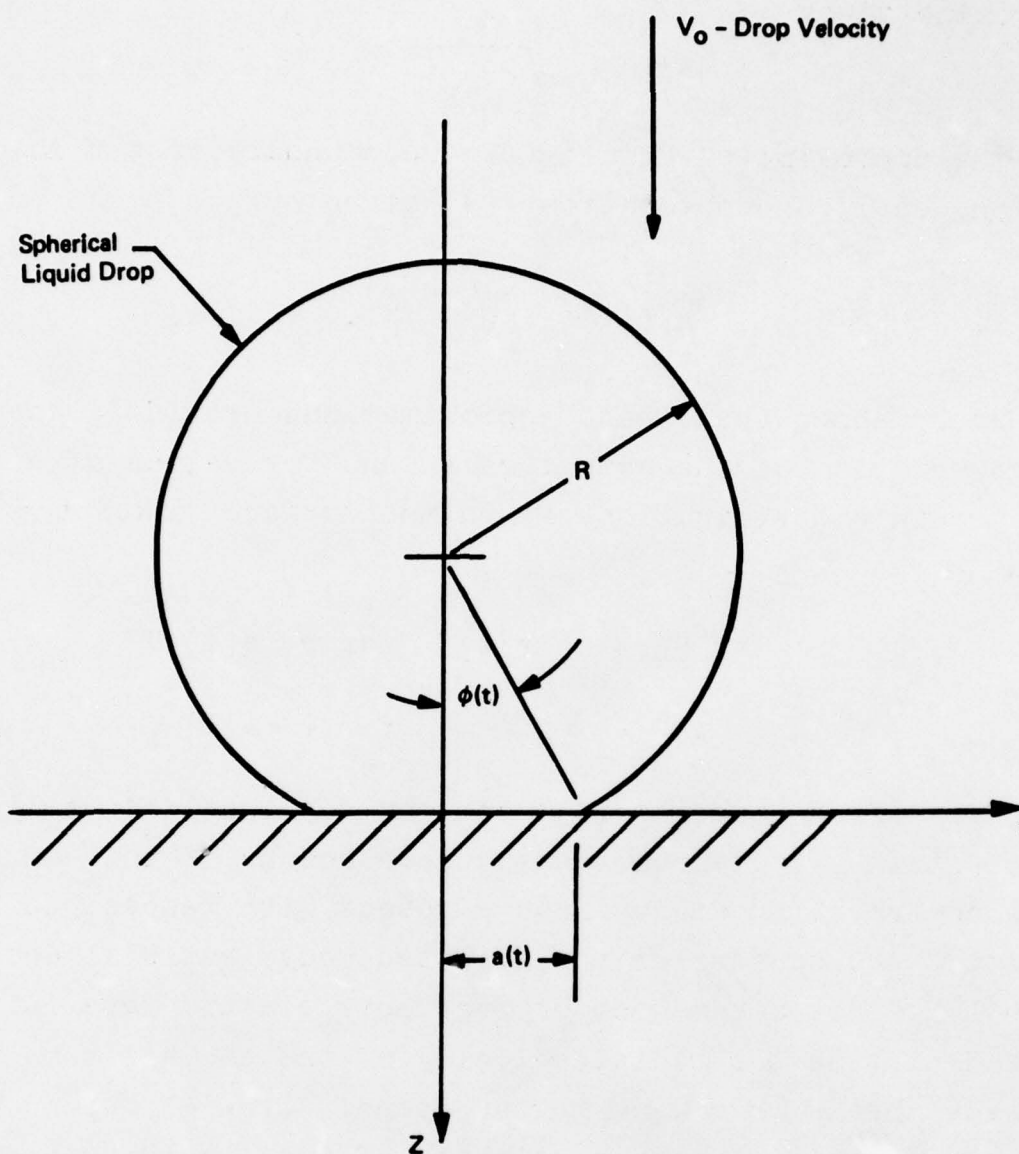


Figure 51. Perfectly Compressible Liquid Drop Impacting a Solid Surface

For very short times, the radius can be accurately approximated by

$$a(t) \approx \sqrt{2RV_0 t} \quad (3)$$

and the approximate velocity of the boundary of the loaded region, easily computed from (3), given by

$$\dot{a}(t) \approx \sqrt{\frac{RV_0}{2t}}. \quad (4)$$

It can be shown that these approximations provide a good representation of the actual relations for values of $a(t)/R \leq 0.5$. The pressure distribution, P , on the surface takes the form

$$\begin{aligned} P &= p(r, t) & \text{for } r \leq a(t) \\ P &= 0 & \text{for } r > a(t) \end{aligned} \quad (5)$$

From Equation (4), one can see that when a liquid drop first strikes a plane surface, the boundary of the contact area will be traveling at supersonic speeds with respect to the elastic wave speeds for the impacted body, but will decrease with $t^{-\frac{1}{2}}$. For a homogeneous isotropic elastic material, the period of time the radial velocity of the contact zone boundary exceeds the dilatational wave speed, C_1 , will depend on the radius and initial impact velocity of the liquid drop and the compressibility of the elastic material. The time τ_1 at which $\dot{a}(t) = C_1$ can be determined from (4).

$$\tau_1 = \left(\frac{k}{2C_1}\right)^2, \text{ where } k = \sqrt{2RV_0} \quad (6)$$

Correspondingly, the time at which the shear wave moves ahead of the loaded region is

$$\tau_2 = \left(\frac{k}{2C_2}\right)^2 \quad (7)$$

where C_2 is the shear wave velocity in the impacted material. The dilatational and shear wave speeds, C_1 and C_2 , for a homogeneous isotropic elastic solid are given by

$$C_1^2 = \left(\frac{E}{\rho} \right) \left[\frac{1-\nu}{(1+\nu)(1-2\nu)} \right] \quad (8)$$

$$C_2^2 = \left(\frac{E}{\rho} \right) \left[\frac{1}{2(1+\nu)} \right] \quad (9)$$

where

E is Young's modulus

ν is Poisson's ratio

ρ is the density of the medium

Note that C_1 is always greater than C_2 .

As long as the boundary of the loaded region is moving at a velocity $\dot{a}(t) \geq C_1$, the radius of the disturbance on the surface will be the same as that of the loaded area. When $\dot{a}(t) < C_1$, disturbances resulting from dilatational waves will move ahead of the loaded boundary and will continue to travel at the dilatational velocity of the medium. When $\dot{a}(t) < C_2$, disturbances resulting from shear waves will move ahead of the loaded boundary and will continue to travel at the shear wave velocity of the medium. In an elastic medium, a third type wave, C_R , (Rayleigh surface wave) can exist, which travels along the surface penetrating the interior only slightly. These waves travel at speeds slightly lower than shear waves (for $\nu = 0.3$ $C_R = .928 C_2$). A conclusion similar to the above can be made for propagation of disturbances due to Rayleigh waves as a function of the loaded boundary velocity. A schematic presentation of the relative location of the three wave fronts as a function of the velocity of the loaded boundary is presented in Figure 52.

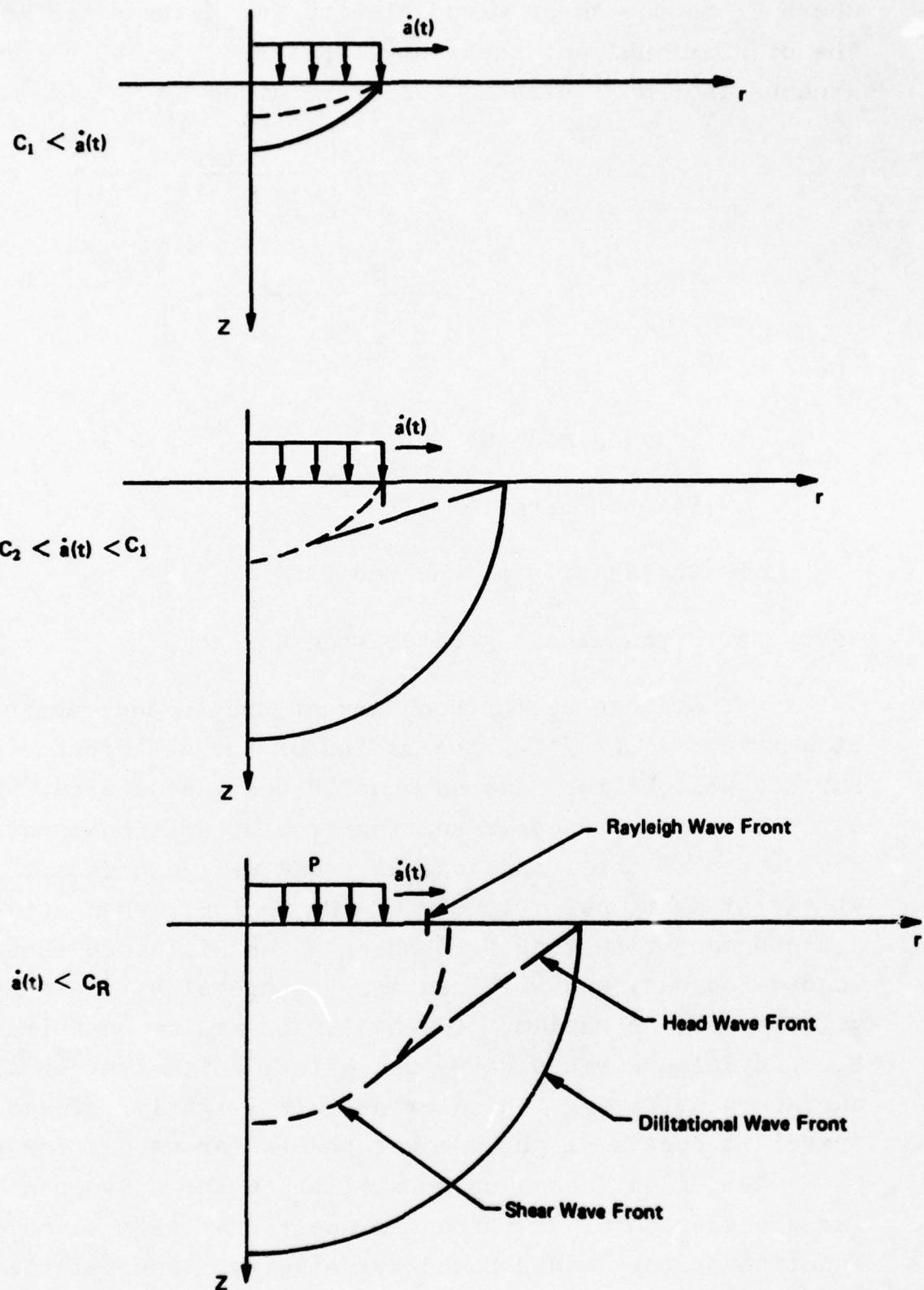


Figure 52. Wave Front Locations in a Semi-Infinite Median for Various Loaded Region Boundary Velocities

Based on available experimental evidence and analyses, the point at which the interface pressure created by the drop impact starts to decay is dependent on the lateral outflow angle ϕ . For the velocities of interest this angle, designated the critical contact angle ϕ_{2C} , falls in the range $10^\circ \leq \phi_{2C} \leq 25^\circ$. In Figure 53, the relationship between lateral outflow angle ϕ , time after liquid drop impact, and drop diameter for the two velocities of interest are presented. For drop diameters of 0.5 to 2.5 mm, the maximum time duration of the collision process ranges from 0.12 to 0.60 μ sec for $V_0 = 730$ ft/sec and from 0.07 to 0.35 μ sec for $V_0 = 1120$ ft/sec if it is assumed that $\phi = 25^\circ$.

There is little unanimity in the literature concerning the magnitude and distribution of the pressure which develops at the liquid/solid interface during the collision process. Predictions of maximum pressures range from 0.7 to 3.0 times $\rho_w C_w V_0$ for the drop velocities being considered, where ρ_w , C_w , and V_0 are the density, acoustic velocity, and impact velocity of the liquid drop respectively. For this investigation, a one-dimensional shock wave relationship for a water drop striking a deformable solid was used to approximate this pressure. This relationship takes the form

$$p_w = \frac{\rho_w (U_w [V_0 - V_w] + V_0) V_0}{1 + \frac{\rho_w (U_w [V_0 - V_w] + V_0)}{\rho_s U_s [V_w]}} \quad (10)$$

where V_w is the velocity of the interface and is described by

$$V_w = \frac{V_0}{1 + \frac{\rho_s U_s [V_w]}{\rho_w (U_w [V_0 - V_w] + V_0)}} \quad (11)$$

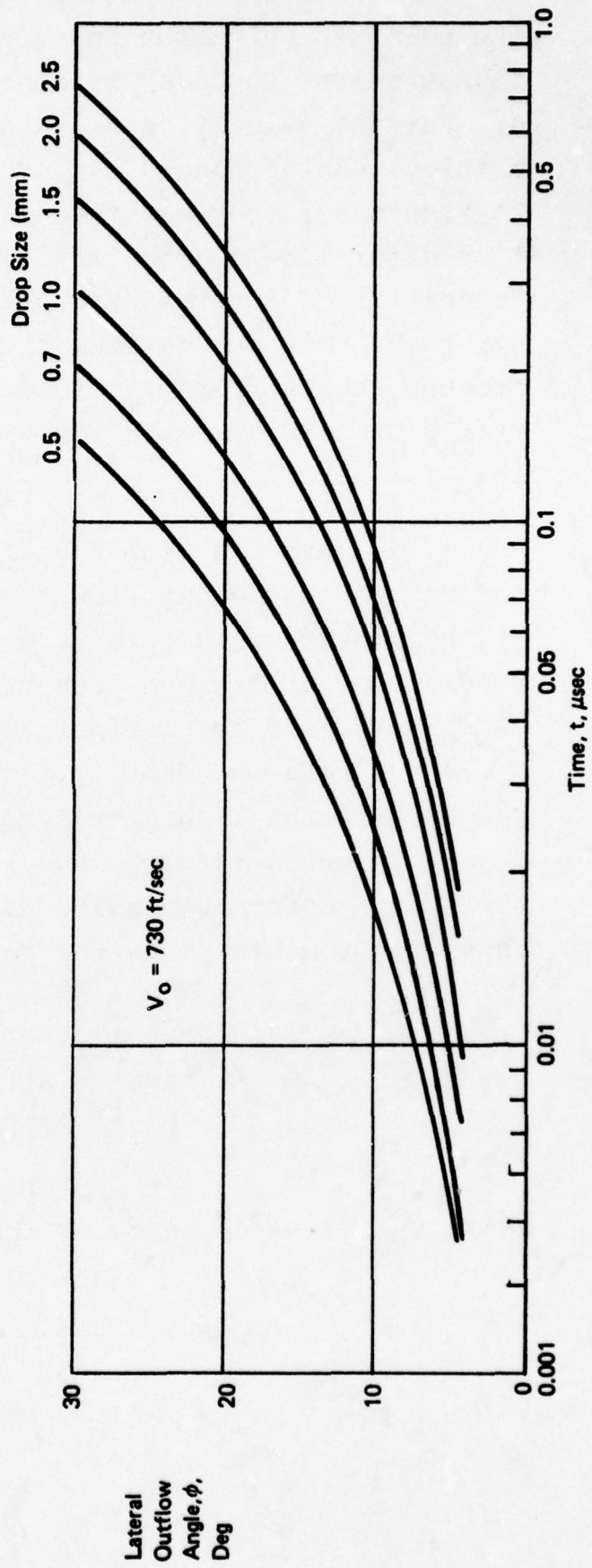
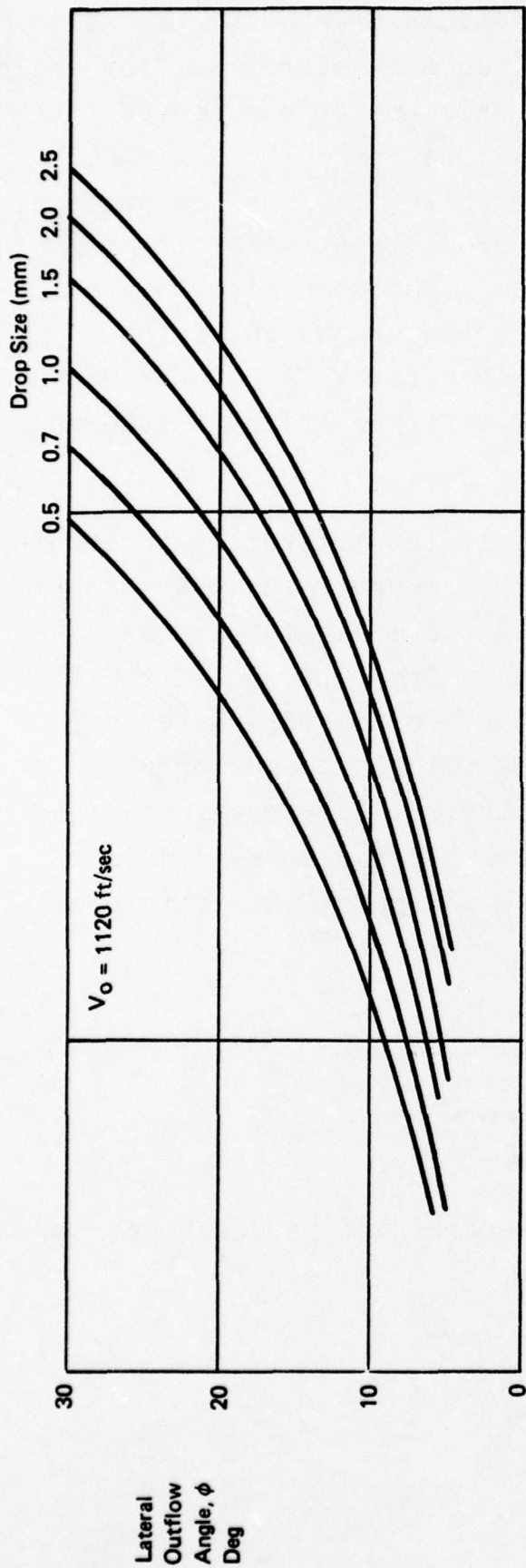


Figure 53. Lateral Outflow Angle as a Function of Time and Drop Size for Drop Velocities of 730 and 1120 ft/sec

V_o is the drop impact velocity, ρ_w and ρ_s are the liquid and solid densities, and U_w and U_s are the representative shock velocities. The notation $U []$ is used to denote that the shock velocity is a function of the particulate velocities.

When the water drop impact velocity is small in comparison to the acoustic velocities of water and the substrate, the respective particle velocities are also negligible with respect to the acoustic velocities and Equation (10) reduces to

$$p_w = \frac{\rho_w C_w V_o}{1 + \frac{\rho_w C_w}{\rho_s C_s}} \quad (12)$$

where C_w and C_s are the acoustic velocities for water and substrate, respectively, at zero particle velocity. The variation of shock velocity of water as a function of particle velocity V is known and can be approximated by the expression

$$U_w = C_w + 2V - 0.1 \left(\frac{V}{C_w} \right) V \quad (13)$$

Thus, knowing the variation of shock velocity for the solid one can compute the liquid/solid interface pressure.

Predicted values of interfacial pressure for the materials being evaluated are presented in Table 7 for impact velocities of 730 and 1120 ft/sec. With the exception of polymethylmethacrylate (PMMA), the shock velocity in the solid was assumed equal to its acoustic velocity. There is little variation in predicted pressures among the actual candidate window materials, with values ranging from 61,700 to 64,200 psi for a drop velocity of 730 ft/sec and 107,600 to 112,700 psi for a drop velocity of 1120 ft/sec. These pressures are 1.3 to 1.5 times $\rho_w C_w V_o$ where $\rho_w C_w V_o = 48,140$ psi for a drop velocity of 730 ft/sec, and 73,850 psi for a drop velocity of 1120 ft/sec. The interface pressures predicted for PMMA are

TABLE 7
WATER DROP IMPACT PRESSURES PREDICTED
FROM ONE-DIMENSIONAL SHOCK WAVE RELATIONSHIP

<u>Substrate Material</u>	<u>Drop Velocity (ft/sec)</u>	<u>Pressure (psi)</u>	
PMMA	730	41,300	
	1120	69,400	
ZnSe	730	62,200	} (a)
	1120	108,600	
ZnS	730	61,700	
	1120	107,600	
GaAs	730	63,100	
	1120	110,300	
Ge	730	64,200	
	1120	112,700	

(a) Assumes substrate shock velocity is equal to acoustic velocity.

significantly lower than those predicted for the window materials, primarily because the density and acoustic velocity are lower for PMMA.

A method developed by Blowers ⁽⁶⁾ was used to calculate stresses in the substrate due to the liquid drop impact. This analysis determines the transient stress distribution within an elastic half-space subjected to a uniform pressure loading p distributed over an expanding circular region. The time dependent radius of the loaded region is given by Equation (3), consistent with the idealized compressible water drop model resulting in a pressure distribution of the form

$$\begin{aligned} p(r,t) &= P_0 \text{ for } r \leq \sqrt{2RV_0 t} \approx a(t) \\ &= 0 \text{ for } r > \sqrt{2RV_0 t} \approx a(t) \end{aligned} \quad (14)$$

where the magnitude of P_0 is assumed to be constant with respect to time and is computed from Equation (10).

Blower's method is available in the form of a computer program TURBAN having a plot output capability. The numerical calculations provide the stresses at all points within the elastic half-space except in the vicinity of the Rayleigh surface wave near the surface where a nonremovable singularity in the equations prevails. To overcome this difficulty in the numerical calculations, the results are generally computed a few microns below the surface of the half-space where the calculated stresses are reasonably well-behaved including the regions in the vicinity of the Rayleigh wave front.

A summary of material properties employed in the analyses which follows is presented in Table 8. These data taken from suppliers' literature include density, Young's modulus, Poisson's ratio, and ultimate tensile strength along with the dilatational and shear wave speeds computed from Equations (8) and (9). For the actual window material candidates there is little difference

TABLE 8
MATERIAL PROPERTIES

Property	Polymethyl- methacrylate	Material		
		Zinc Selenide	Zinc Sulfide	Gallium Arsenide
Density (lbs/in ³)	.0428	.1903	.1473	.1920
Young's Modulus (10 ⁶ psi)	1.305(a)	9.75	10.8	12.3
Poisson's Ratio	.325(a)	.3	.3	.31
Dilatational Wave Speed C ₁ (10 ⁴ ft/sec)	.905(a)	1.360	1.627	1.544
Shear Wave Speed C ₂ (10 ⁴ ft/sec)	.461(a)	.727	.870	.810
Strength (10 ³ psi)	10.5(b)	8.5(c)	16.0(c)	20.0(c)
				10.5(c)

(a) High frequency data
(b) Ultimate tensile strength
(c) Ultimate flexural strength

in the elastically related properties; however, ultimate strengths vary considerably, ranging from 8.5 ksi for zinc selenide to 20.0 ksi for gallium arsenide.

B. Analysis of Single Drop Impacts

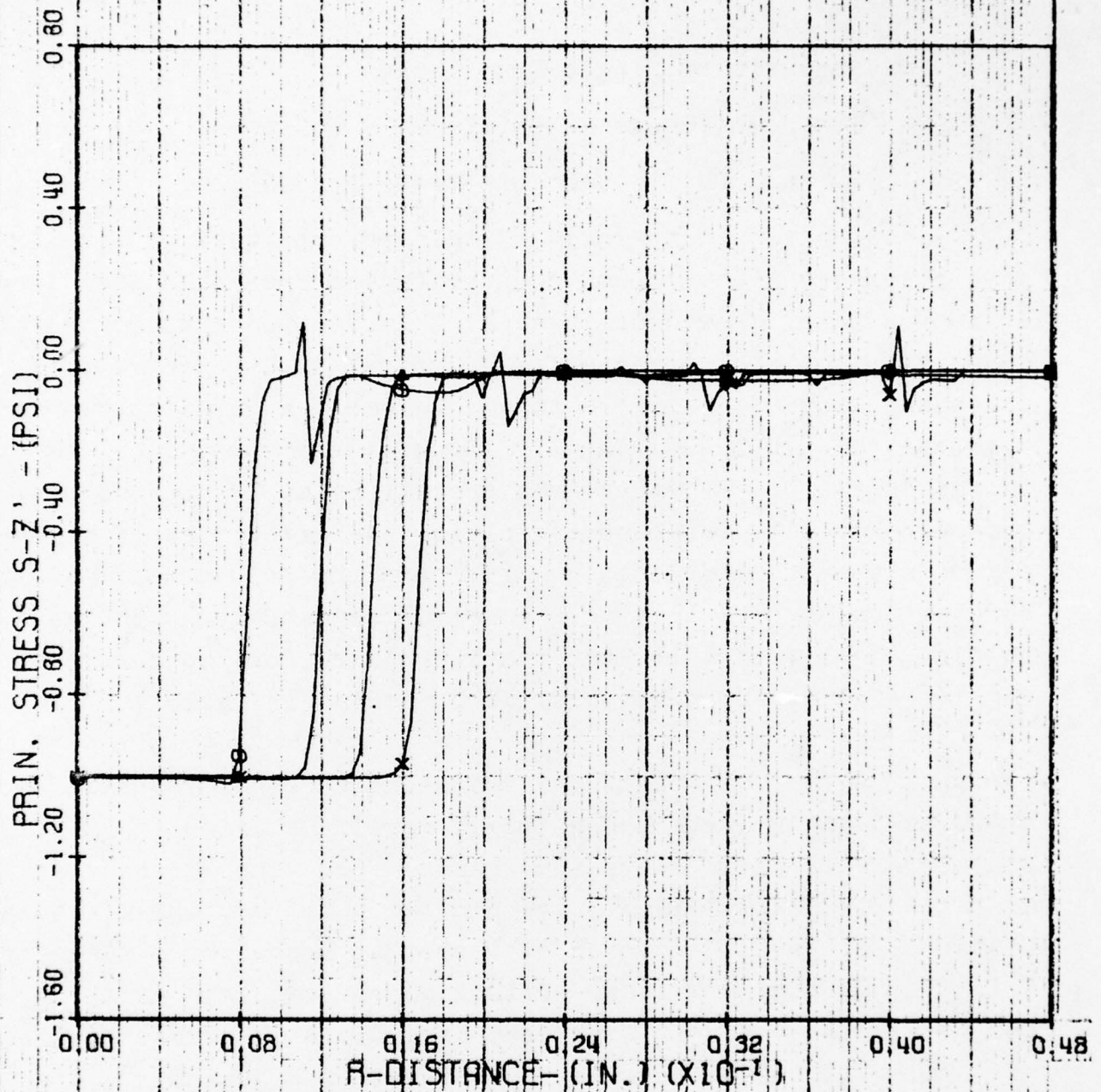
1. Homogeneous Materials

a. Description of Stress Predictions

In the body of this report, various plots of particular transient stress components are presented and discussed as appropriate. For completeness, this section presents all the transient stress components for a typical window material at one water drop size and one impact velocity as predicted by the mathematical model described in the previous section. Zinc sulfide impacted by a 2.0 mm water drop travelling at 730 ft/sec was chosen. For all of the stress plots, the magnitudes of stress components were normalized to unity and the actual stress can be found by multiplying the normalized stress by the magnitude of the liquid/solid interface pressure for the corresponding material and drop velocity as presented in Table 7.

Plots of the transient stresses resulting from a 2.0 mm diameter water drop impacting zinc sulfide at 730 ft/sec are presented in Figures 54 through 58. The stresses at a depth $z = 0.5$ mils ($12.7 \mu\text{m}$) are plotted as a function of radial distance, R , from the center of impact at preselected times of 0.1, 0.2, 0.3 and $0.4 \mu\text{sec}$. Principal stress components $(\sigma_{zz})_p$ and $(\sigma_{rr})_p$ are shown in Figures 54 and 55, and stresses in the original cylindrical coordinate system σ_{zz} , σ_{rr} , and σ_{rz} are shown in Figures 56 through 58. Since the stress calculations were made near the surface, resulting in near zero shear stresses, the behavior of the principal stresses is similar to the stresses in the original coordinate system. Plots of the principal stresses were an output for all impact cases and are included in this section for completeness. However, they were not used for the study of impact phenomenon and for the comparison with experimental data.

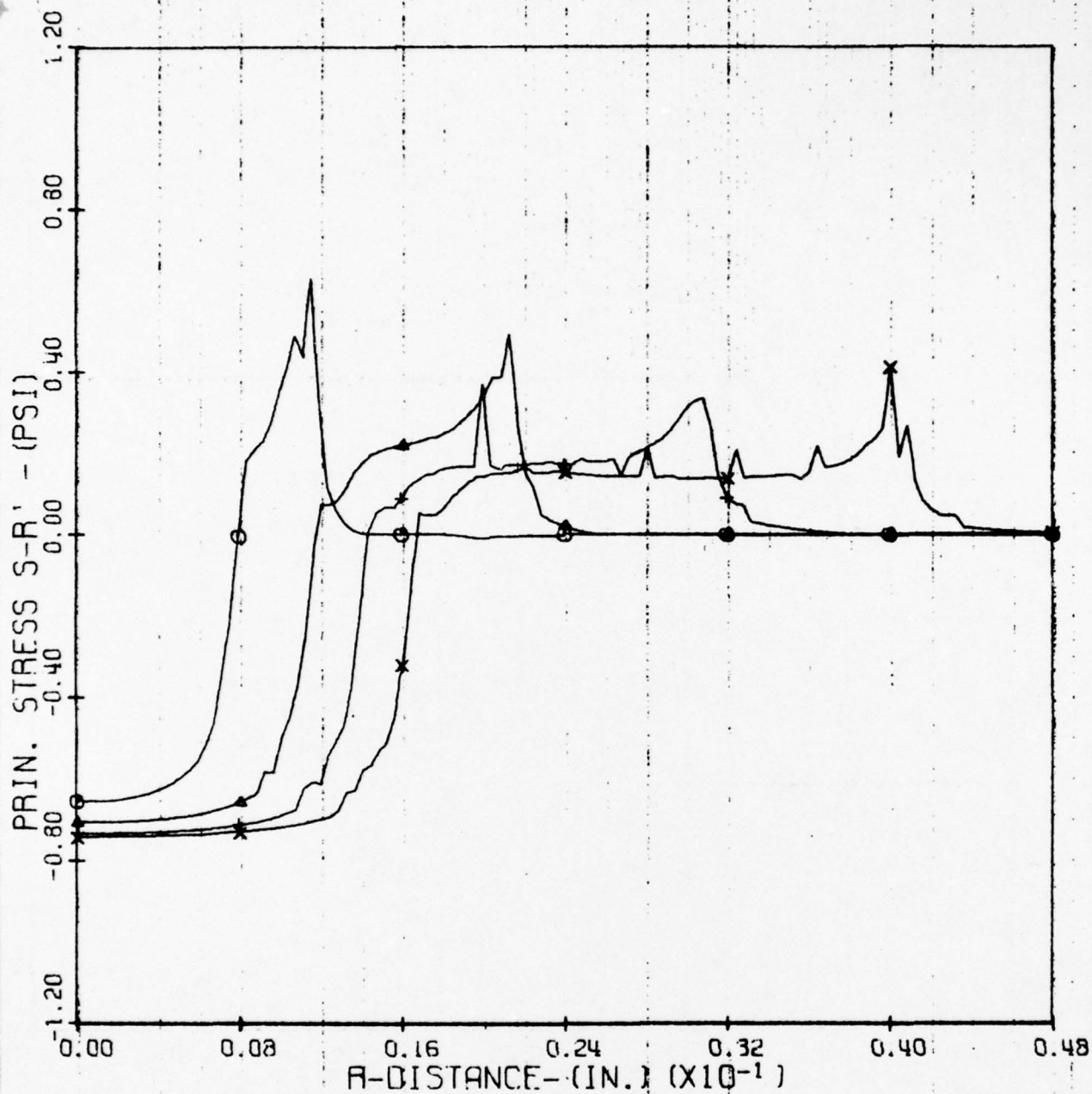
CASE 103 ZNS - 2.0 MM DROP AT 730 FT/SEC



Z-CONSTANT- (IN.)	0.0005	T- (MICRO-SEC)	
DROP SIZE- (MM)	2.00	○	0.1000
DROP VEL- (FT/SEC)	730.0	▲	0.2000
P. ZERO- (PSI)	-1.0	+	0.3000
MATERIAL MODULUS- (PSI)	10.800×10^6	×	0.4000
POISSONS RATIO- (-)	0.300		
MATERIAL DENSITY- (LB/IN ³)	0.1473		

Figure 54. Temporal Distribution of Principal Axial Stress (at $Z = 0.0005$ Inches) for a 2.0 mm Water Drop Impacting ZnS at 730 ft/sec

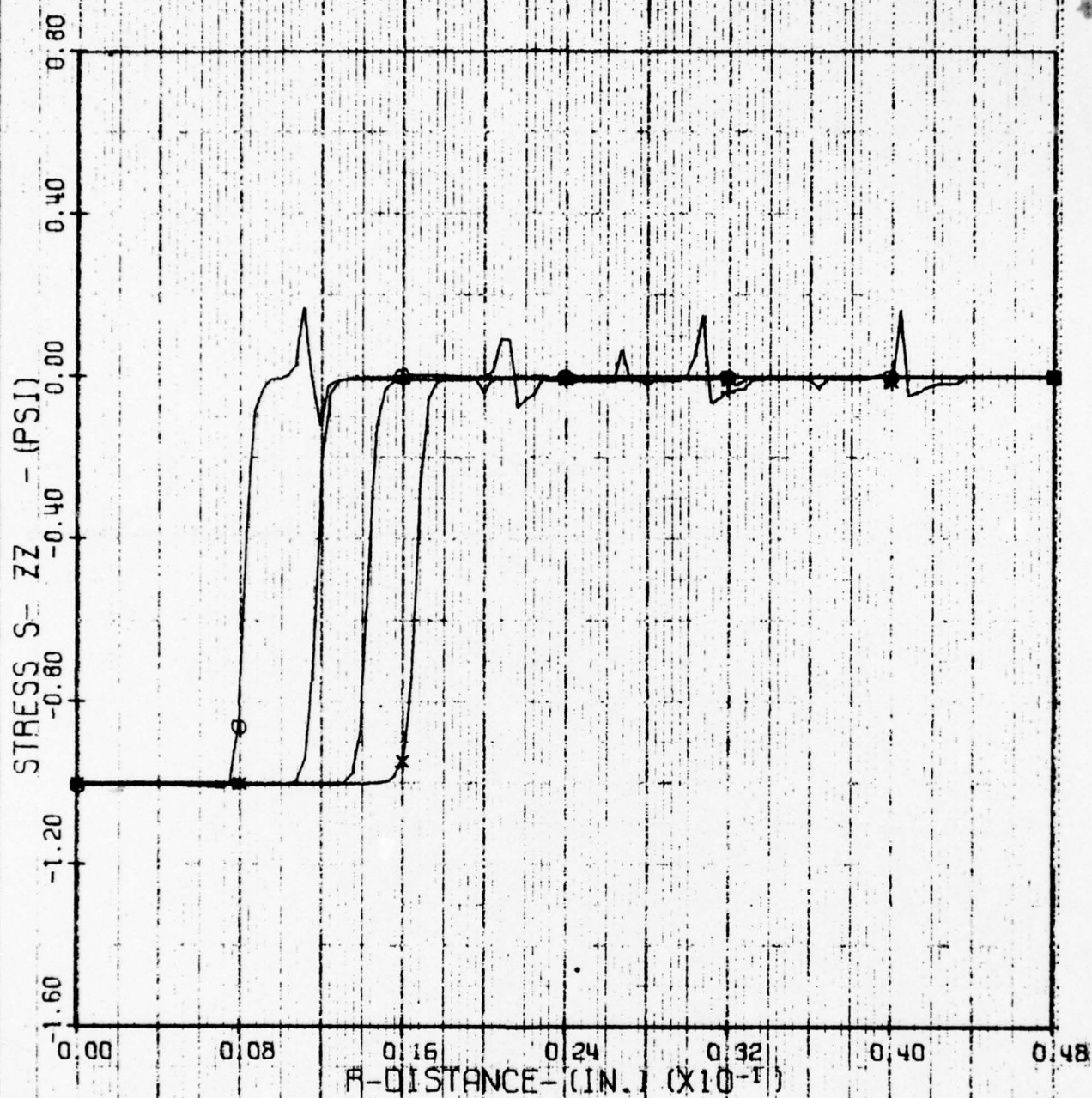
CASE 103 ZNS - 2.0 MM DROP AT 730 FT/SEC



Z-CONSTANT - (IN.)	0.0005	T - (MICRO-SEC)	
DROP SIZE - (MM)	2.00	○	0.1000
DROP VEL - (FT/SEC)	730.0	▲	0.2000
P ZERO - (PSI)	-1.0	+	0.3000
MATERIAL MODULUS - (PSI)	10.800 X10 ⁶	x	0.4000
POISSONS RATIO - (---)	0.300		
MATERIAL DENSITY - (LB/IN**3)	0.1473		

Figure 55. Temporal Distribution of Principal Radial Stress (at Z = 0.0005 inches) for a 2.0 mm Water Drop Impacting ZnS at 730 ft/sec

CASE 103 ZNS - 2.0 MM DROP AT 730 FT/SEC



Z-CONSTANT- (IN.)	0.0005	T- (MICRO-SEC)	
DROP SIZE- (MM)	2.00	○	0.1000
DROP VEL- (FT/SEC)	730.0	△	0.2000
P ZERO- (PSI)	-1.0	+	0.3000
MATERIAL MODULUS- (PSI)	10.800×10^6	x	0.4000
POISSONS RATIO- (---)	0.300		
MATERIAL DENSITY- (LB/IN ³)	0.1473		

Figure 56. Temporal Distribution of Axial Stress (at Z = 0.0005 inches) for a 2.0 mm Water Drop Impacting ZnS at 730 ft/sec

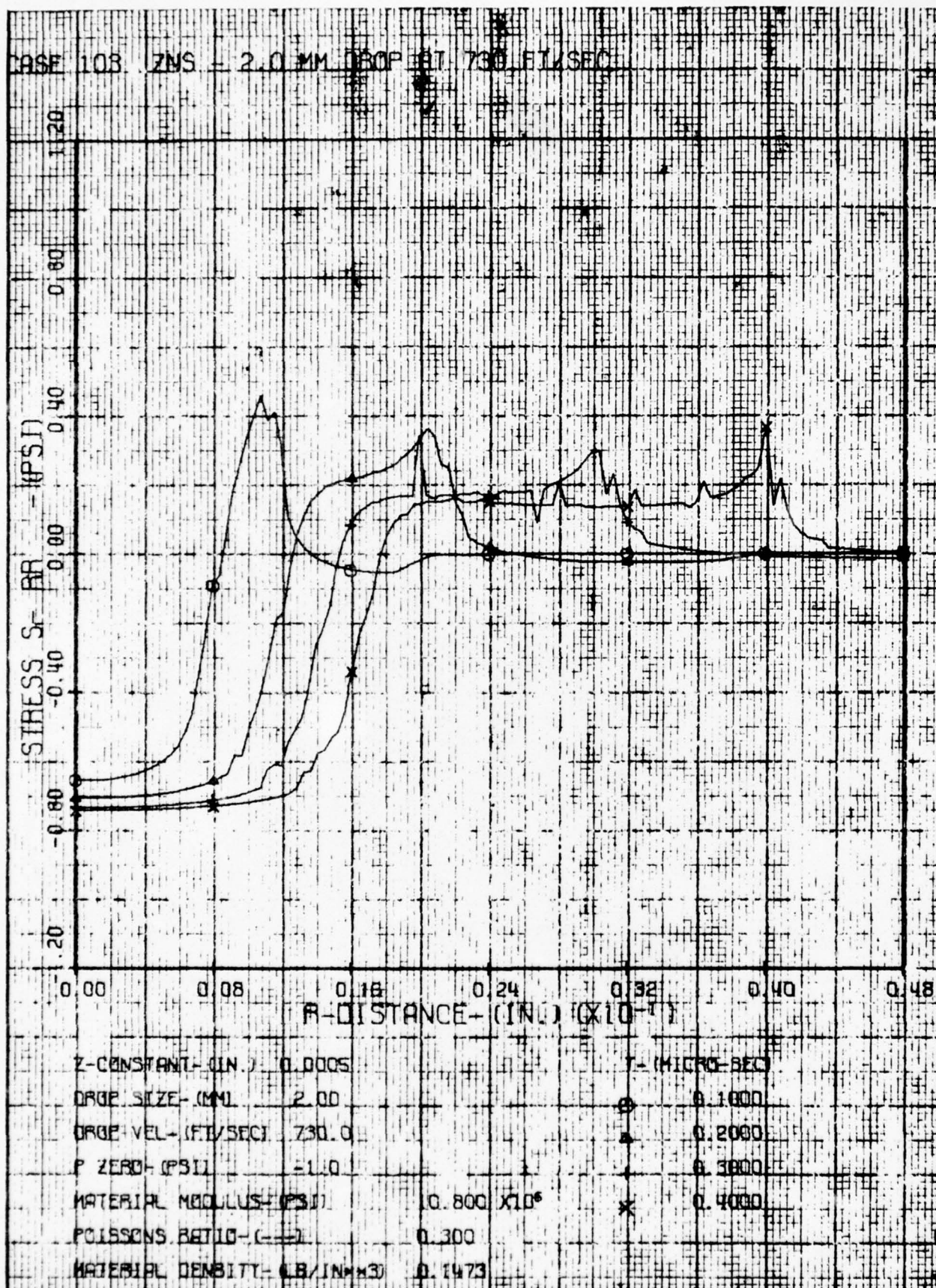
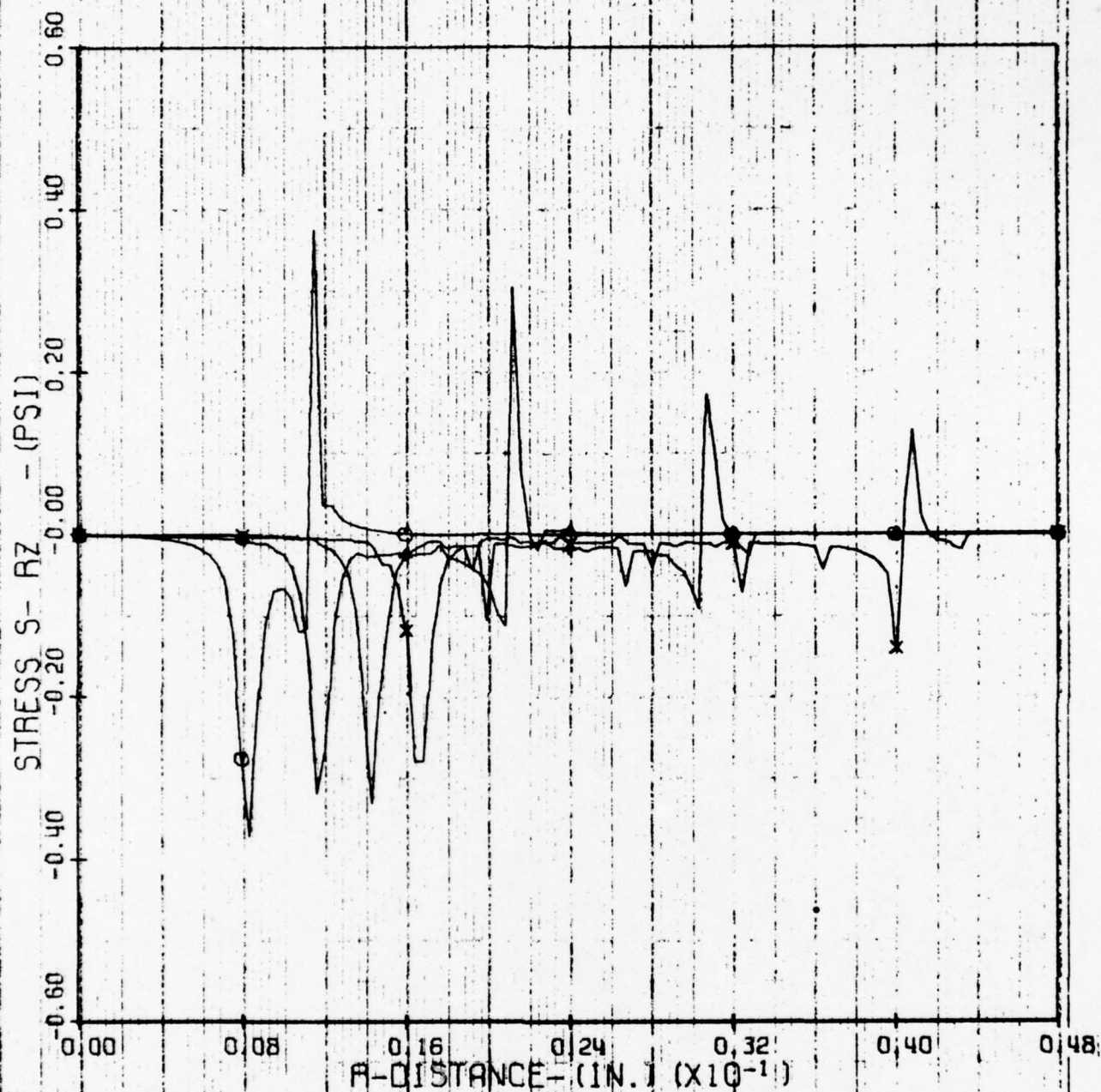


Figure 57. Temporal Distribution of Radial Stress (at $Z = 0.0005$ in.) for a 2.0 mm Water Drop Impacting ZnS at 730 ft/sec

CASE 103 ZNS - 2.0 MM DROP AT 730 FT/SEC



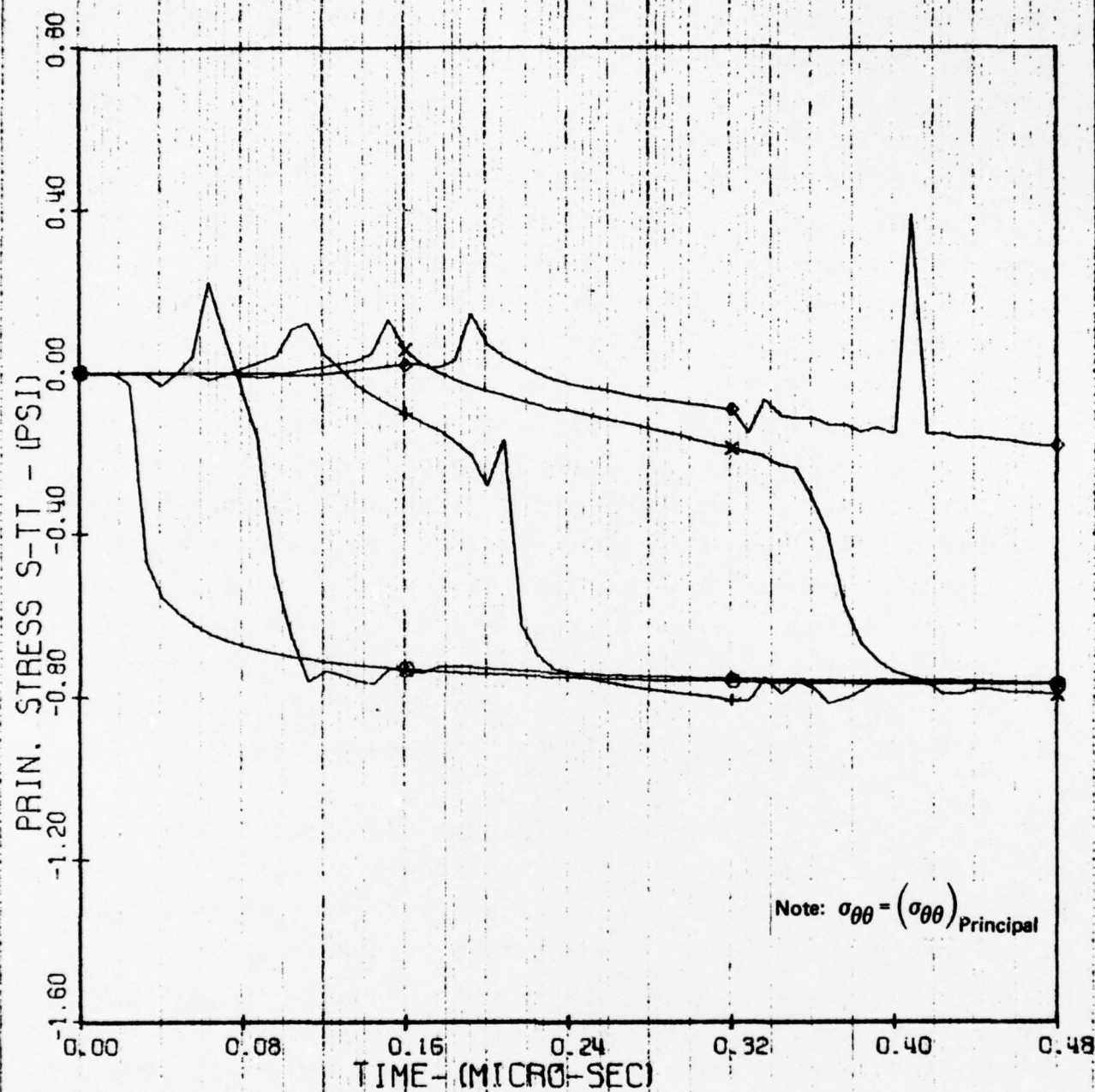
Z-CONSTANT- (IN.)	0.0005	T- (MICRO-SEC)	
DROP SIZE- (MM)	2.00	○	0.1000
DROP VEL- (FT/SEC)	730.0	●	0.2000
P ZERO- (PSI)	-1.0	+	0.3000
MATERIAL MODULUS- (PSI)	10.800×10^6	*	0.4000
POISSONS RATIO- (---)	0.300		
MATERIAL DENSITY- (LB/IN ³)	0.1473		

Figure 58. Temporal Distribution of Shear Stress (at $Z = 0.0005$ inches) for a 2.0 mm Water Drop Impacting ZnS at 730 ft/sec

From Figure 56 we see that the normalized axial stress σ_{zz} is compressive with a value of -1.0 under the loaded region and is zero elsewhere, except in the vicinity of the shear wave front where a small tensile/compressive spike is noted. The normalized radial stress σ_{rr} , Figure 57, is generally compressive under the loaded region with a value of about -.07, but it takes on significant tensile values outside the loaded region with a tensile spike occurring in the vicinity of the shear wave front. It is these tensile stresses which cause the ring fracture damage in the impacted material. As expected near the material surface, the normalized shear stress σ_{rz} shown in Figure 58 takes on near zero values except at the boundary of the loaded region and in the vicinity of the shear wave front. However, the validity of the magnitude of the spikes predicted are questionable due to the sharp discontinuity in the assumed pressure distribution at the boundary of the loaded area and the numerical instability that exists in the shear and Rayleigh wave front regions. Plots of hoop stress $\sigma_{\theta\theta}$ were not developed for this case and thus are not presented. This stress would be primarily compressive under the loaded region and would take on small tensile values just outside the load boundary.

In Figures 54 through 58, plots of stress versus radial location were presented for zinc sulfide at various preselected times after impact. The transient effects at various locations in the material are not easily assessed from such a format. Therefore, the same basic data has been replotted as stress versus time at preselected radial locations in the zinc sulfide as shown in Figures 59 through 64. These plots show both the magnitude and the duration of the stress levels experienced at various discrete material locations. It should be noted that these plots are for a depth of 0.2 mils (5.1 μm) as compared to the plots presented in Figures 54 through 58 which were for a depth of 0.5 mils (12.7 μm). When the program was modified to change the continuous variable which was plotted, the depth z was also decreased. A depth of 0.2 mils was as close as it was practical to approach the surface without

CASE 110 ZNS 2.0 MM DROP AT 730 FT/SEC (SIG VS T)



Z-CONSTANT - (IN.) 0.0002

DROP SIZE - (MM) 2.00

DROP VEL - (FT/SEC) 730.0

P ZERO - (PSI) -1.0

MATERIAL MODULUS - (PSI) 10.800×10^6

POISSONS RATIO - (-) 0.300

MATERIAL DENSITY - (LB/IN³) 0.1473

R - (INCHES)

○ 0.0040

△ 0.0080

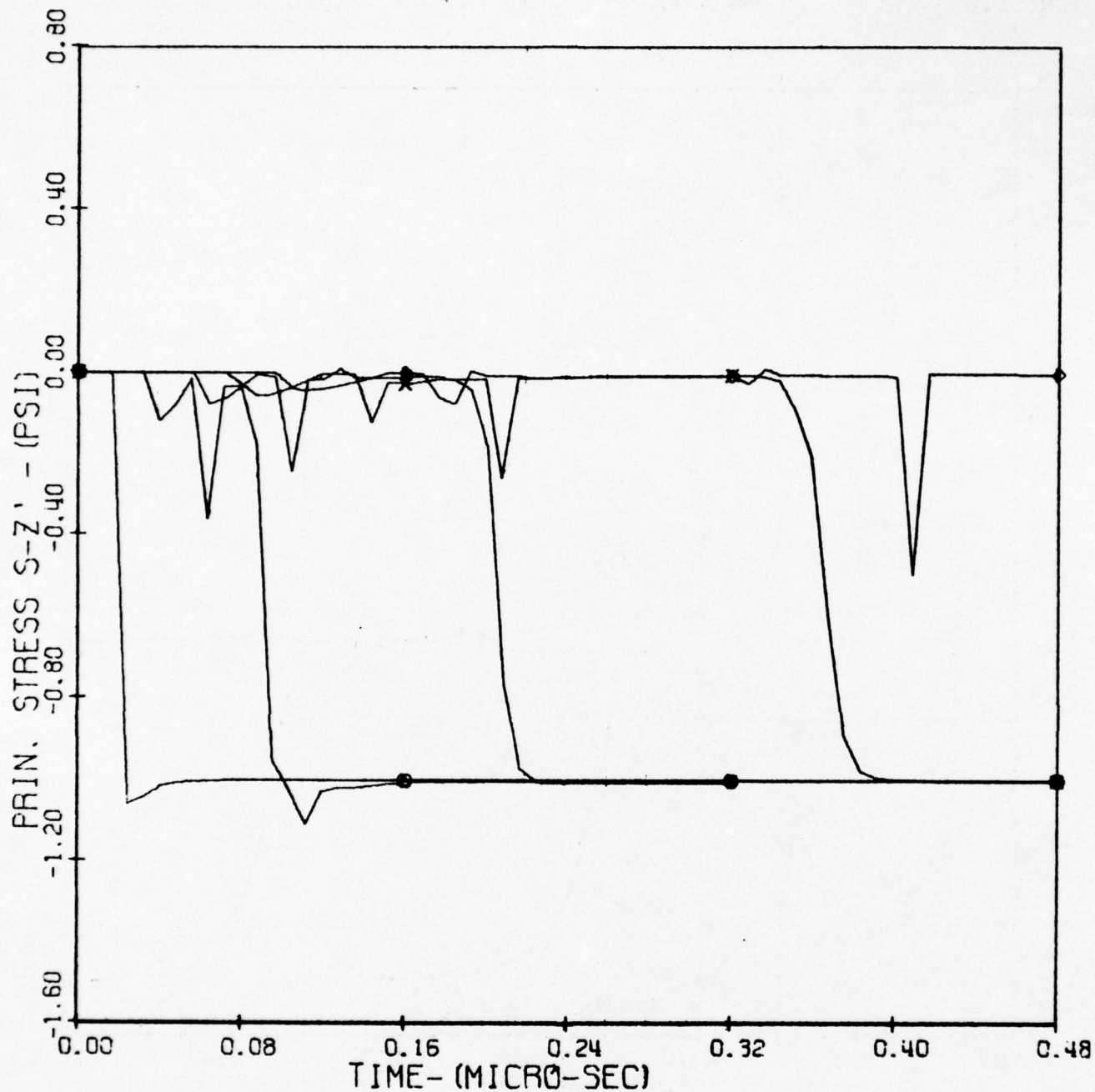
+ 0.0120

x 0.0160

◇ 0.0200

Figure 59. Temporal Distribution of Hoop Stress (at Z = 0.0002 in.) for 2.0 mm Water Drop Impacting ZnS at 730 ft/sec

CASE 110 ZNS 2.0 MM DROP AT 730 FT/SEC (SIG VS T)



Z-CONSTANT- (IN.) 0.0002

DROP SIZE- (MM) 2.00

DROP VEL- (FT/SEC) 730.0

P ZERO- (PSI) -1.0

MATERIAL MODULUS- (PSI) 10.800×10^6

POISSONS RATIO- (---) 0.300

MATERIAL DENSITY- (LB/IN**3) 0.1473

R- (INCHES)

○ 0.0040

▲ 0.0080

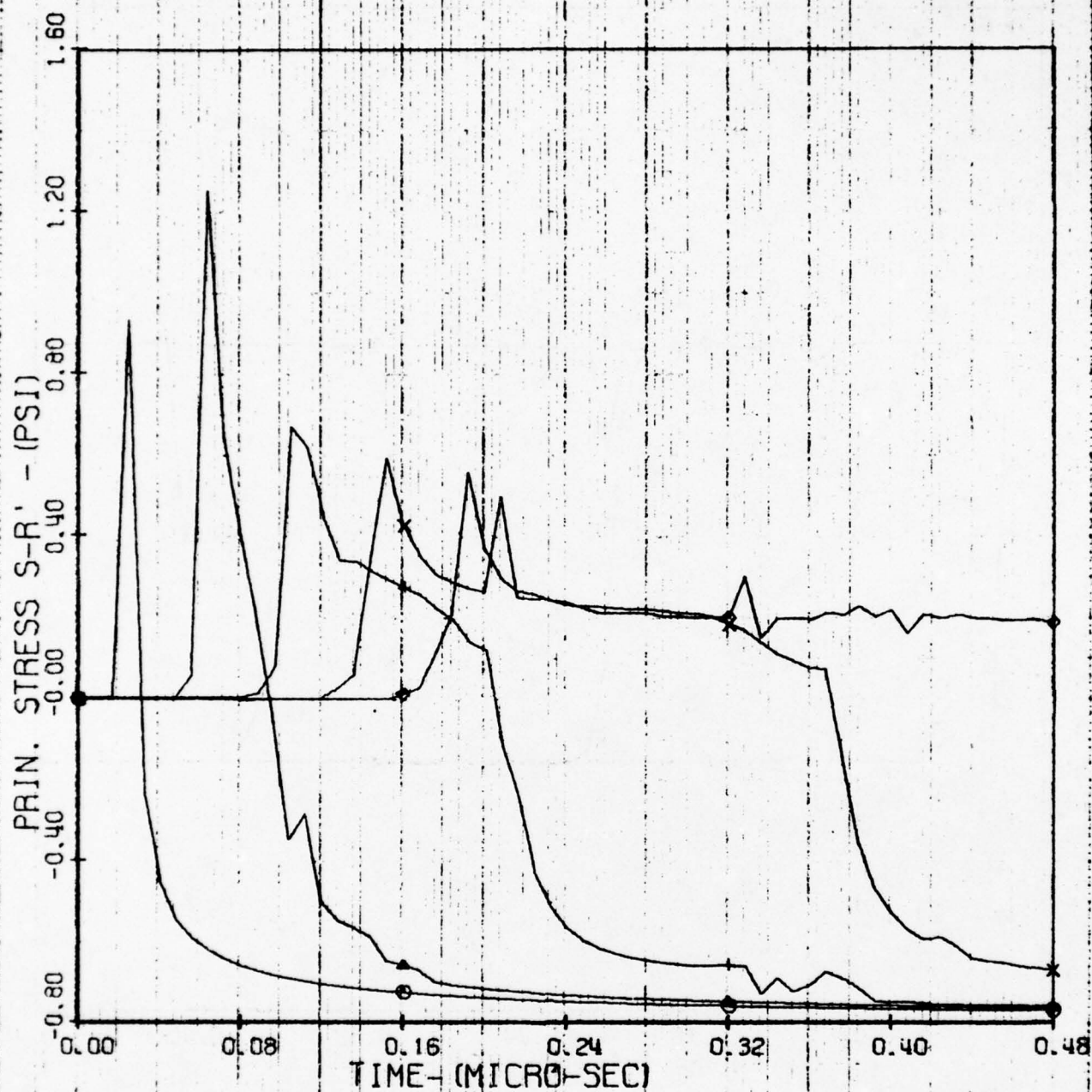
+ 0.0120

x 0.0160

◇ 0.0200

Figure 60. Temporal Distribution of Principal Axial Stress (at $Z = 0.0002$) for a 2.0 mm Water Drop Impacting ZnS at 730 ft/sec

CASE 110 ZNS 2.0 MM DROP AT 730 FT/SEC (SIG VS T)



Z-CONSTANT - (IN.) 0.0002

DROP SIZE - (MM) 2.00

DROP VEL - (FT/SEC) 730.0

P ZERO - (PSI) -1.0

MATERIAL MODULUS - (PSI) 10.800×10^6

POISSONS RATIO - (---) 0.300

MATERIAL DENSITY - (LB/IN**3) 0.1473

R - (INCHES)

○ 0.0040

▲ 0.0080

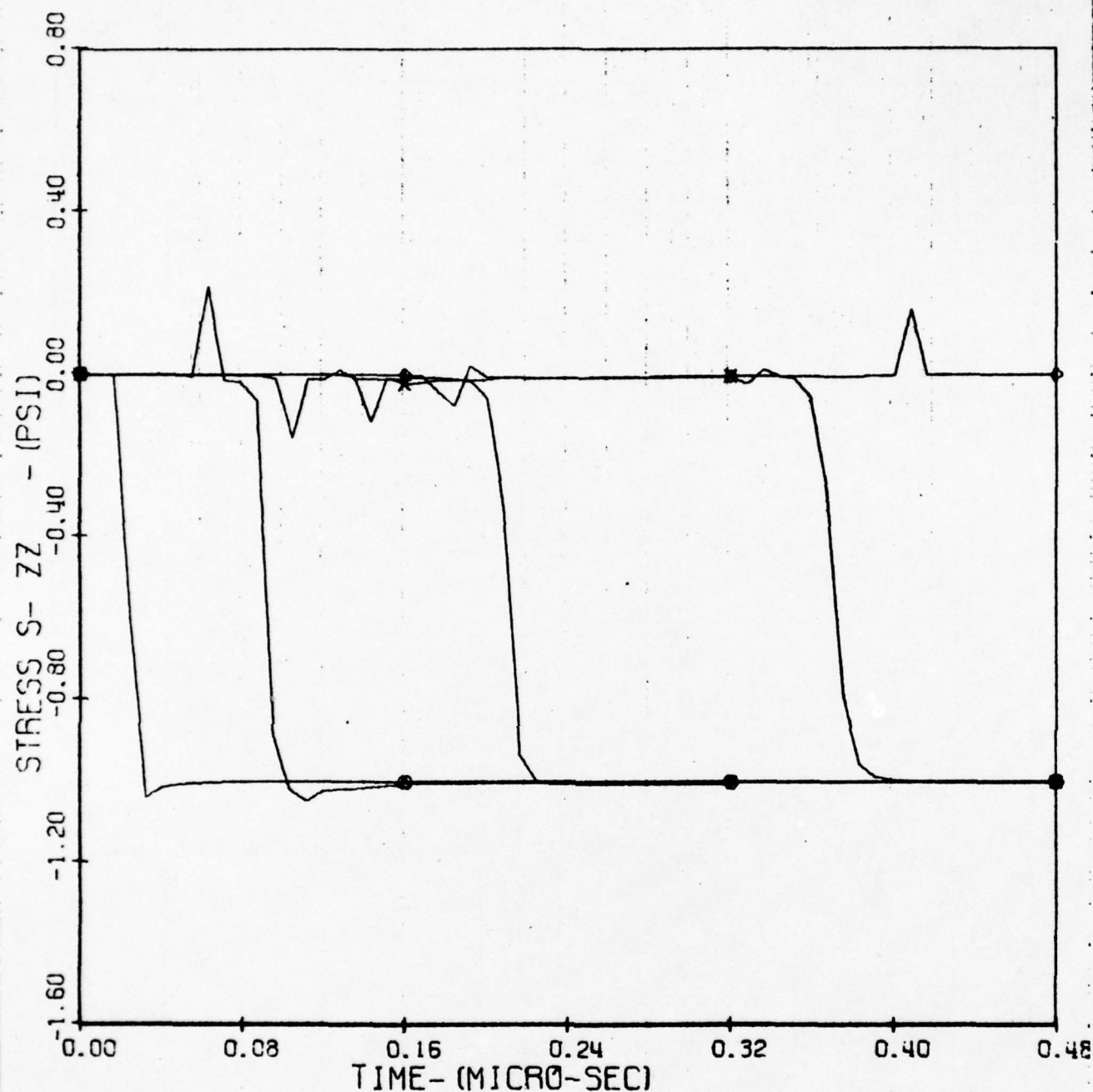
⊕ 0.0120

× 0.0160

◇ 0.0200

Figure 61. Temporal Distribution of Principal Radial Stress (at Z = 0.0002 in.) for a 2.0 mm Water Drop Impact ZnS at 730 ft/sec

CASE 110 ZNS 2.0 MM DROP AT 730 FT/SEC (SIG VS T)



Z-CONSTANT- (IN.) 0.0002

DROP SIZE- (MM) 2.00

DROP VEL- (FT/SEC) 730.0

P ZERO- (PSI) -1.0

MATERIAL MODULUS- (PSI) 10.800×10^6

POISSONS RATIO- (---) 0.300

MATERIAL DENSITY- (LB/IN**3) 0.1473

R- (INCHES)

○ 0.0040

▲ 0.0080

+ 0.0120

x 0.0160

◇ 0.0200

Figure 62. Temporal Distribution of Axial Stress (at Z = 0.0002 in.) for a 2.0 mm Water Drop Impacting ZnS at 730 ft/sec

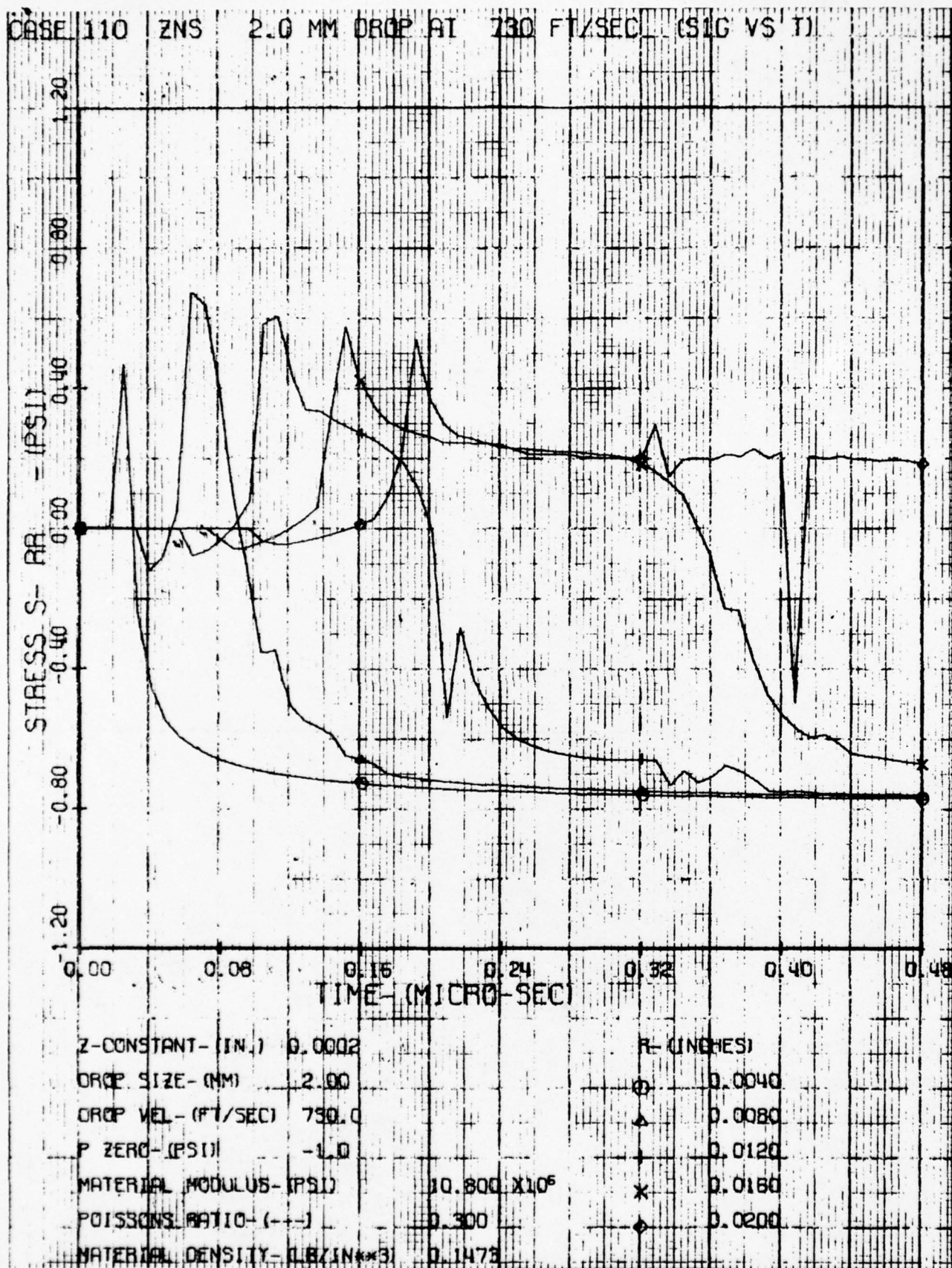
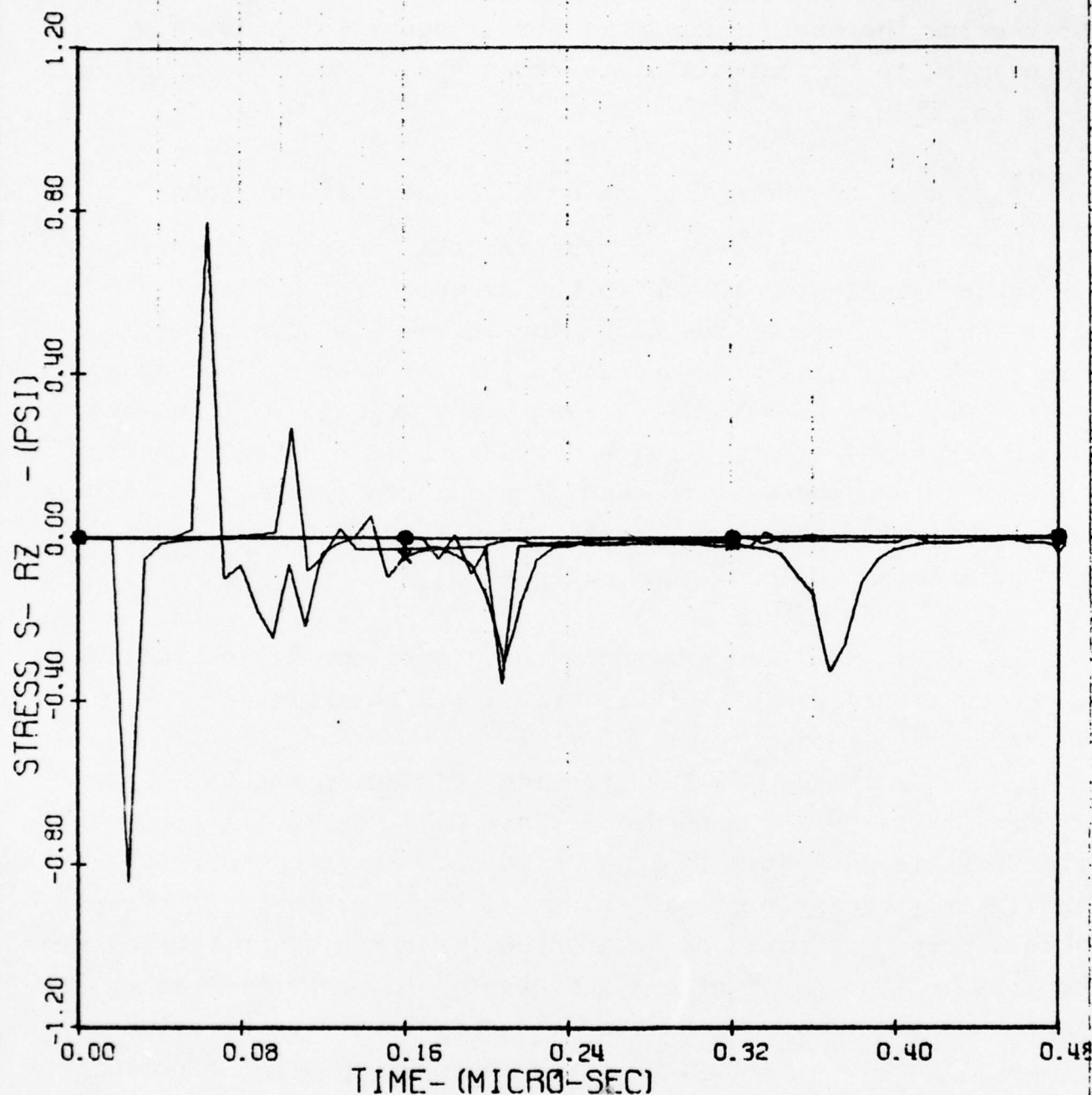


Figure 63. Temporal Distribution of Radial Stress (at $Z = 0.0002$ in.) for a 2.0 mm Water Drop Impacting ZnS at 730 ft/sec

CASE 110 ZNS 2.0 MM DROP AT 730 FT/SEC (SIG VS T)



Z-CONSTANT- (IN.) 0.0002

DROP SIZE- (MM) 2.00

DROP VEL- (FT/SEC) 730.0

P ZERO- (PSI) -1.0

MATERIAL MODULUS- (PSI) 10.800×10^6

POISSONS RATIO- (---) 0.300

MATERIAL DENSITY- (LB/IN**3) 0.1473

R- (INCHES)

○ 0.0040

▲ 0.0080

+ 0.0120

x 0.0160

◇ 0.0200

Figure 64. Temporal Distribution of Shear Stress (at Z = 0.0002) in,) for a 2.0 mm Water Drop Impacting ZnS at 730 ft/sec

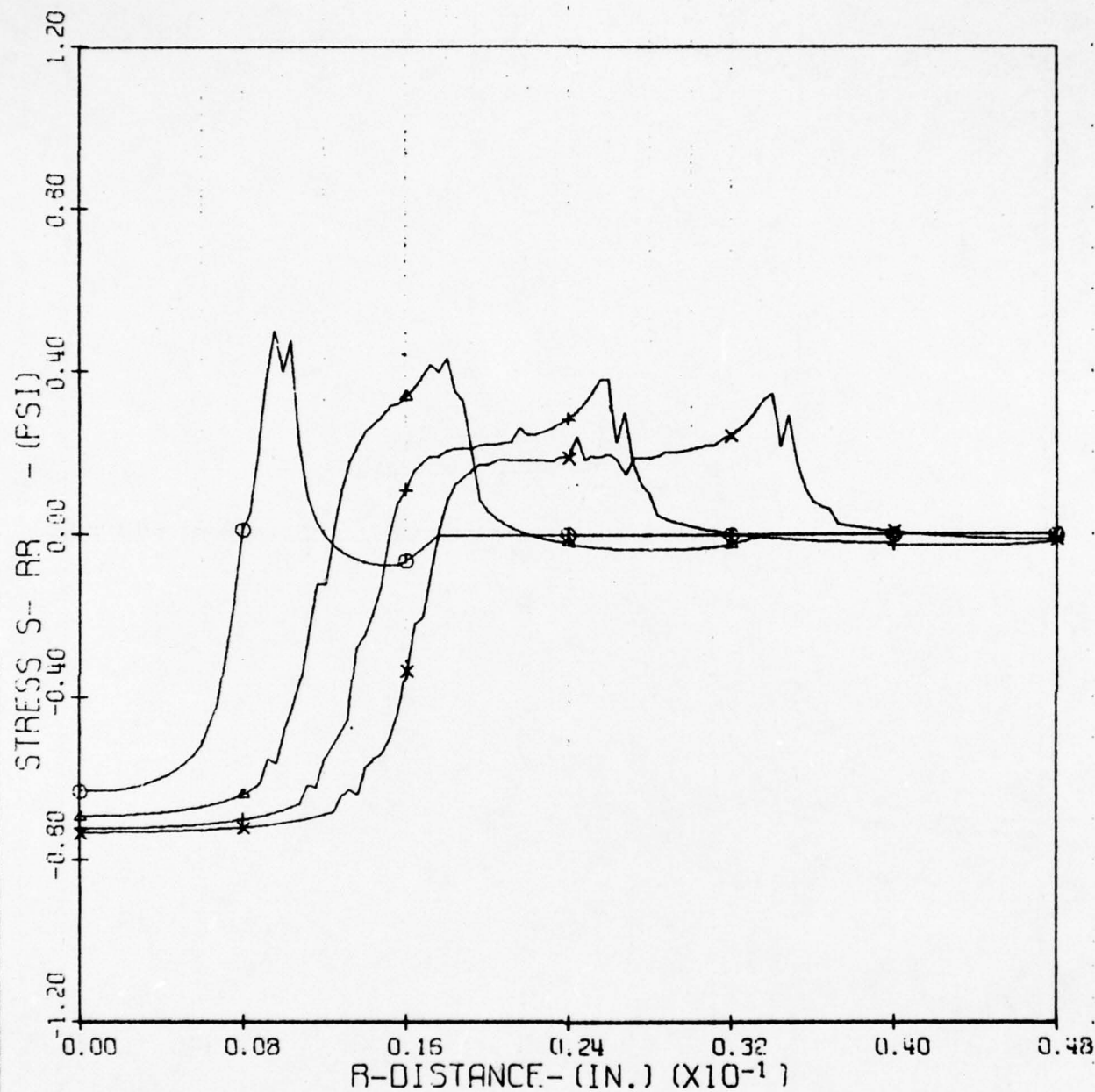
excessive computation time and noise in the output data. Decreasing the depth caused the stress peaks in Figures 59 through 64 to be somewhat higher than those presented in Figures 54 through 58.

b. Effect of Material Properties on Stress

A review of the material properties presented in Table 8 indicates that with the exception of ultimate strength, differences in properties among the infrared window materials are relatively small. Compared to the infrared window materials evaluated, PMMA has similar strength and Poisson's ratio, but its other properties are quite different. The elastic modulus of PMMA is about one-tenth that of the group of window materials and the density about one-fourth, resulting in wave speeds about one-half those in the window materials.

A comparison of predicted normalized radial stresses at a depth of 0.5 mils ($12.7\ \mu\text{m}$) resulting from a 2.0 mm water drop impacting at 730 ft/sec can be made for zinc selenide, zinc sulfide, gallium arsenide, germanium and PMMA from Figures 65 through 69, respectively. Only the radial component of stress is presented in these figures. Based on current analytical and experimental evidence, it is primarily the radial stress component which is felt to be instrumental in the failure process. Although there are differences in properties among the four infrared window materials, the differences in normalized radial stresses are slight. The only apparent effects noted in comparing Figures 65, 66, 67, and 68 are the small differences in distance traveled by the stress peaks in a given material at a particular time. Figure 69 shows that the radial stress peaks at a particular time have traveled only half as far in PMMA as they have traveled in the infrared window materials. This corresponds to the fact that the wave speeds in PMMA are only one-half those in the window materials.

CASE 3A ZNSE - 2.0MM DROP AT 730 FT/SFC



Z-CONSTANT- (IN.) 0.0005

DROP SIZE- (MM) 2.00

DROP VEL- (FT/SEC) 730.0

P ZERO- (PSI) -1.0

MATERIAL MODULUS- (PSI) 9.750×10^6

POISSONS RATIO- (---) 0.300

MATERIAL DENSITY- (LB/IN**3) 0.1900

T- (MICRO-SEC)

○ 0.1000

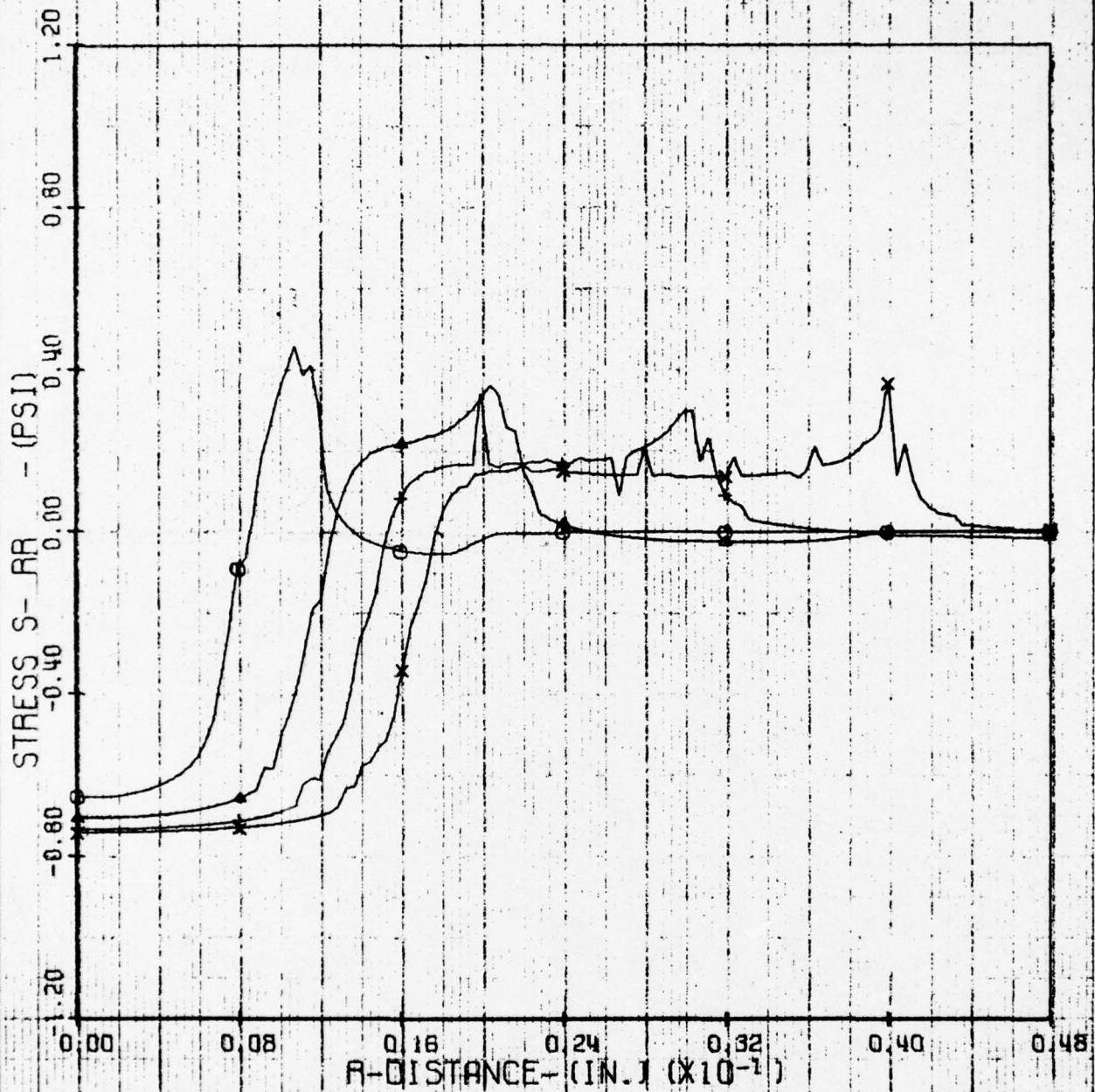
△ 0.2000

+ 0.3000

x 0.4000

Figure 65. Temporal Distribution of Radial Stress (at Z = 0.0005 in.) for a 2.0 mm Water Drop Impacting ZnSe at 730 ft/sec

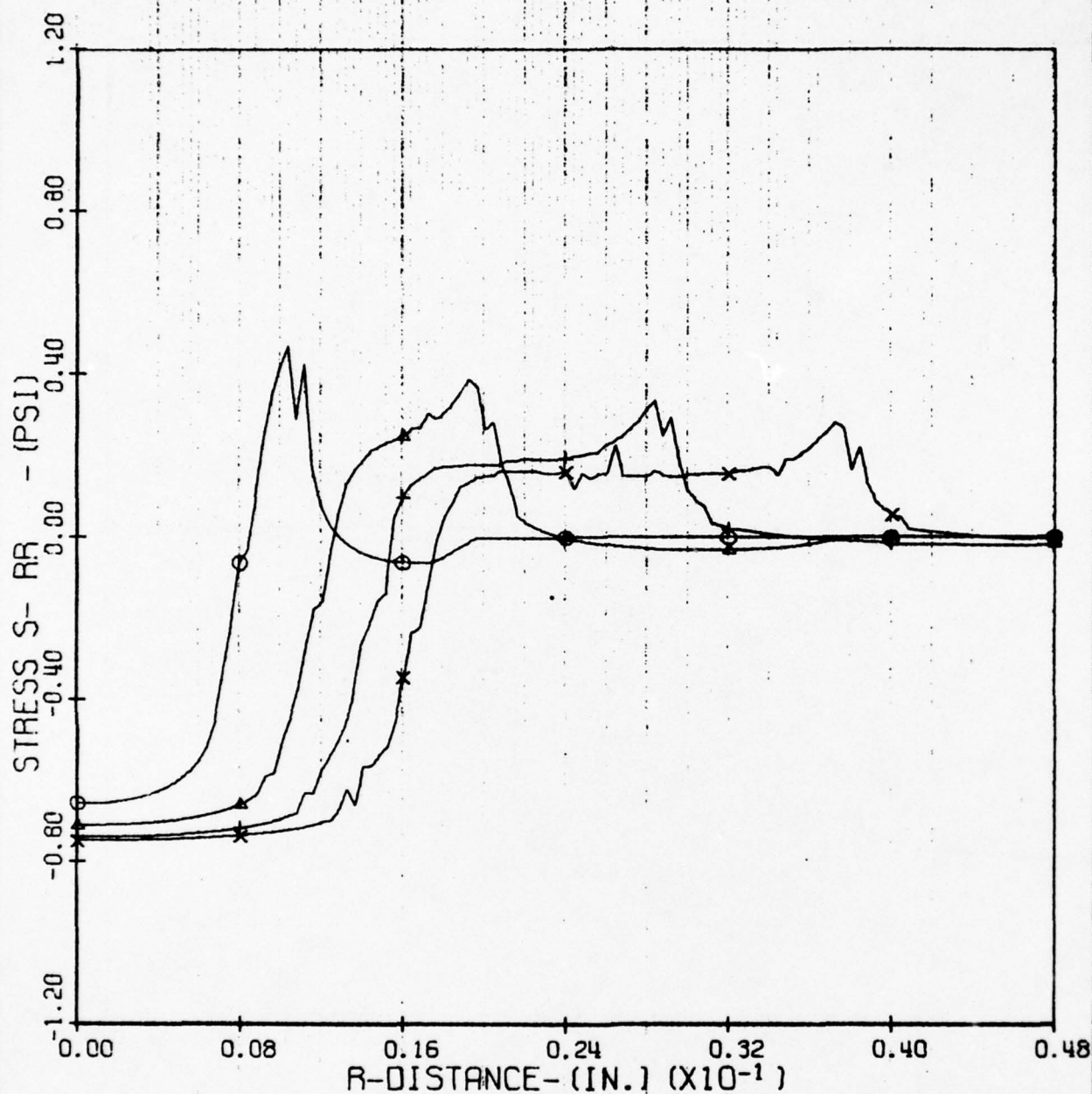
CASE 103 ZNS - 2.0 MM DROP AT 730 FT/SEC



Z-CONSTANT- (IN.)	0.0005	T- (MICRO-SEC)	
DROP SIZE- (MM)	2.00	○	0.1000
DROP VEL- (FT/SEC)	730.0	△	0.2000
P ZERO- (PSI)	-1.0	+	0.3000
MATERIAL MODULUS- (PSI)	10.800×10^6	×	0.4000
POISSONS RATIO- (-)	0.300		
MATERIAL DENSITY- (LB/IN $\times 3$)	0.1473		

Figure 66. Temporal Distribution of Radial Stress (at Z = 0.0005 in.) for a 2.0 mm Water Drop Impacting ZnS at 730 ft/sec

CASE 303 GAAS - 2.0 MM DROP AT 730 FT/SEC



Z-CONSTANT- (IN.) 0.0005

DROP SIZE- (MM) 2.00

DROP VEL- (FT/SEC) 730.0

P ZERO- (PSI) -1.0

MATERIAL MODULUS- (PSI) 12.300×10^5

POISSONS RATIO- (---) 0.310

MATERIAL DENSITY- (LB/IN³) 0.1920

T- (MICRO-SEC)

○ 0.1000

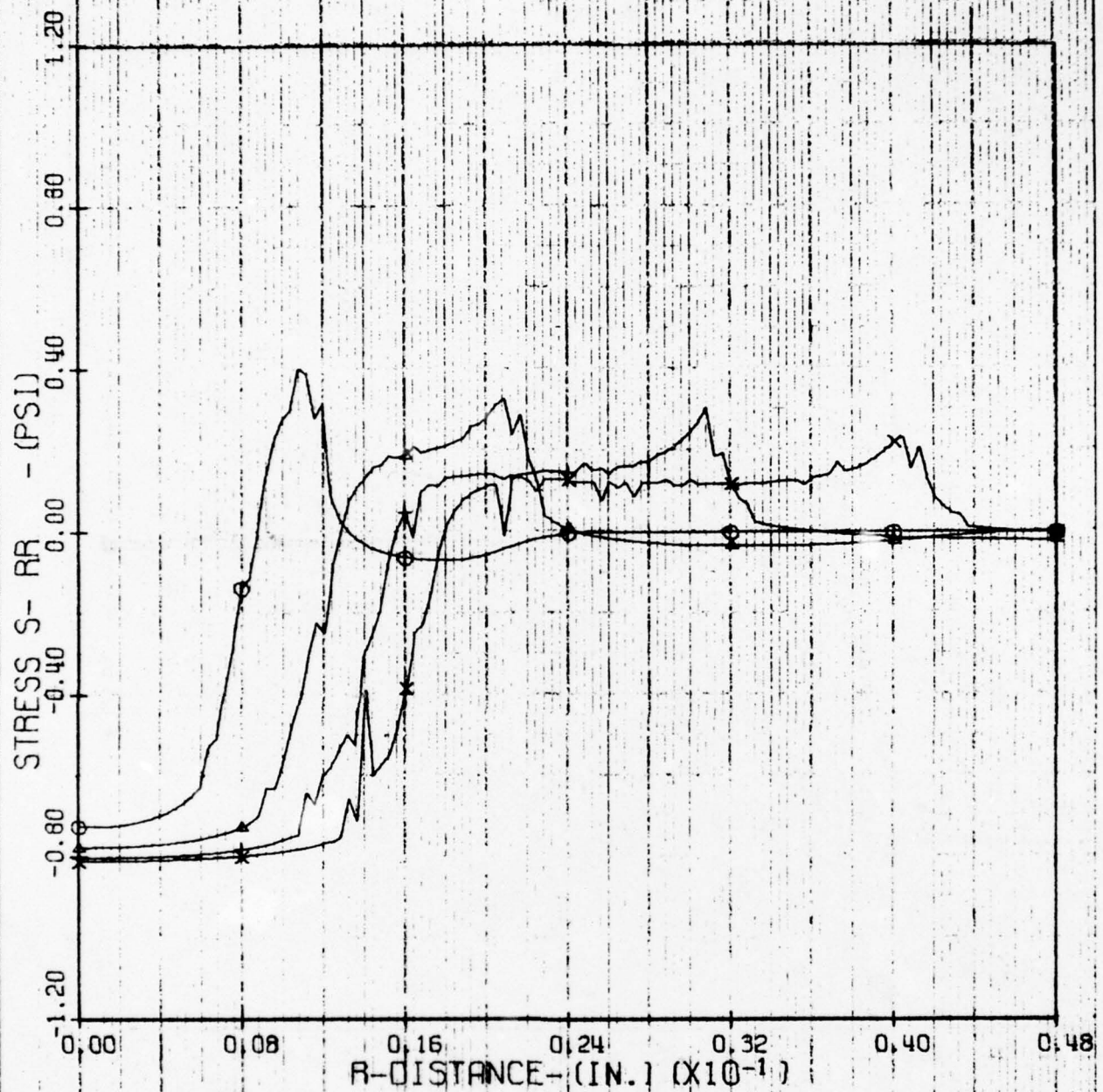
△ 0.2000

+ 0.3000

x 0.4000

Figure 67. Temporal Distribution of Radial Stress (at Z = 0.0005 in.) for a 2.0 mm Water Drop Impacting GaAs at 730 ft/sec

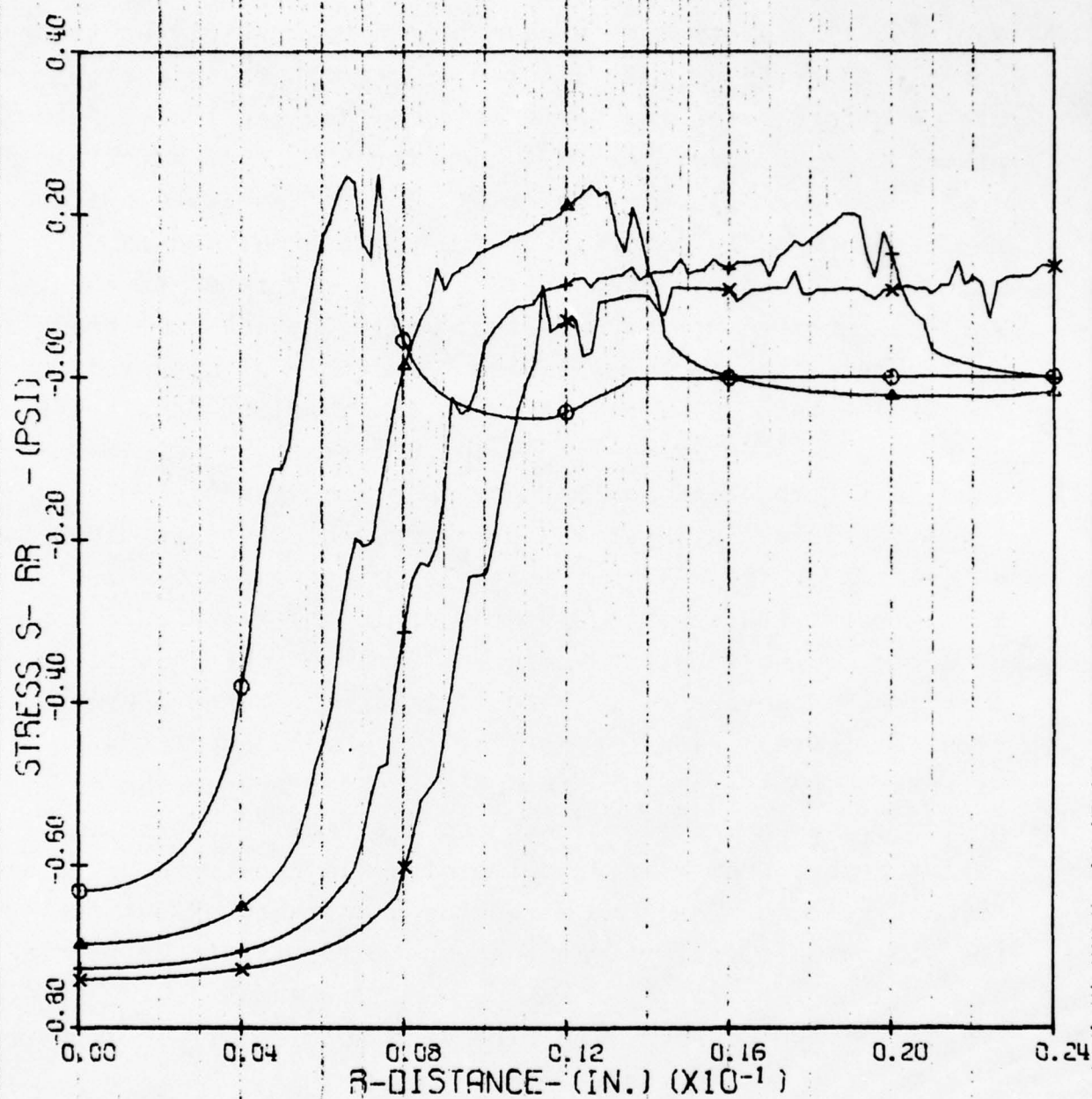
CASE 403 GE - 2.0 MM DROP AT 730 FT/SEC



Z-CONSTANT - (IN.)	0.0005	T - (MICRO-SEC)	
DROP SIZE - (MM)	2.00	○	0.1000
DROP VEL - (FT/SEC)	730.0	△	0.2000
P ZERO - (PSI)	-1.0	+	0.3000
MATERIAL MODULUS - (PSI)	14.900×10^6	×	0.4000
POISSONS RATIO - (---)	0.370		
MATERIAL DENSITY - (LB/IN ³)	0.1925		

Figure 68. Temporal Distribution of Radial Stress (at Z = 0.0005 in.) for a 2.0 mm Water Drop Impacting Ge at 730 ft/sec

CASE 203 PMMA - 2.0 DROP AT 730 FT/SEC



Z-CONSTANT - (IN.) 0.0005

DROP SIZE - (MM) 0.70

DROP VEL - (FT/SEC) 730.0

P ZERO - (PSI) -1.0

MATERIAL MODULUS - (PSI) 1.305×10^6

POISSONS RATIO - (---) 0.325

MATERIAL DENSITY - (LB/IN³) 0.0428

T - (MICRO-SEC)

○ 0.1000

△ 0.2000

+ 0.3000

× 0.4000

Figure 69. Temporal Distribution of Radial Stress (at Z = 0.0005 in.) for a 2.0 mm Water Drop Impacting PMMA at 730 ft/sec.

A summary of the magnitudes of the peak radial tensile stresses for the five materials is presented in Table 9. These stresses were obtained by multiplying the peak normalized stresses from Figures 65 through 69 by the appropriate interface pressures from Table 7. The magnitude of the peak stress is much lower for PMMA than for the other materials due to a lower normalized value combined with the lower pressure at the drop/substrate interface. The peak normalized tensile stresses in PMMA are about one half the magnitude of the values for the infrared window materials while the pressure produced at the interface for PMMA is about two-thirds that produced for the window materials, resulting in the absolute peak tensile stress in PMMA being about one-third that in the window materials. Thus, differences in maximum stresses are directly related to the differences in interface pressure, which are in themselves a function of the substrate material stiffness and density, and also directly related to differences in the transient response of a particular substrate material for the same type of loading function. However, within the limited range of property variations associated with the stiffer and more dense infrared window materials considered in this analysis, differences in interface pressure and in transient response are small. The ability to resist damage from rain drop impact would appear to be related primarily to the fracture strengths and fracture toughnesses of the window materials rather than to their elastic properties.

c. Effect of Drop Size and Impact Velocity on Stresses

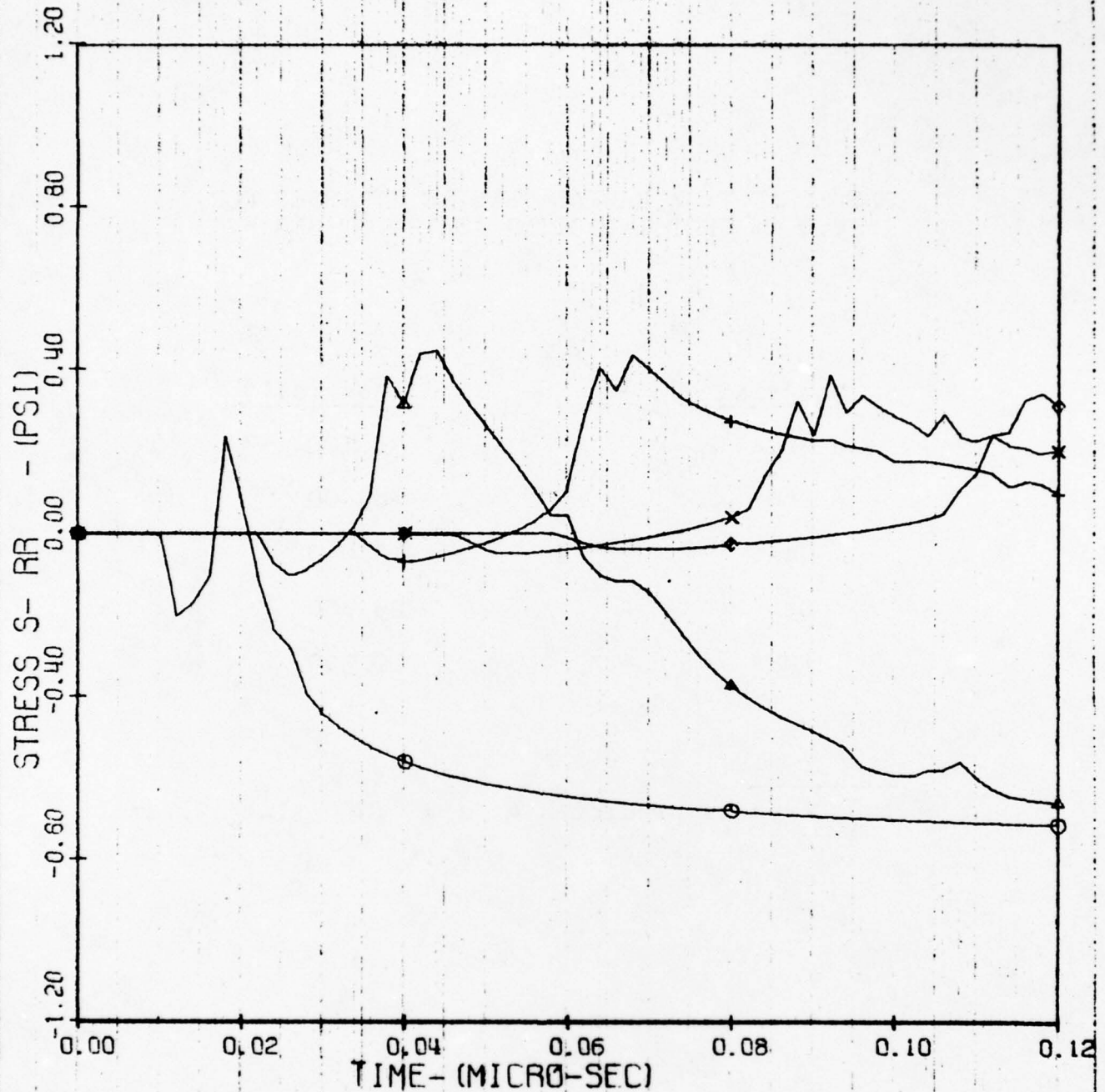
The influence of drop size and impact velocity on predicted stresses in zinc selenide is shown in Figures 70 through 74. Figures 70, 71, and 72 present normalized radial stresses at a depth of 0.2 mils ($5.1 \mu\text{m}$) as a function of time for 0.7, 2.0, and 2.5 mm diameter drops impacting at 730 fps. Figures 73 and 74 present radial stresses at a depth of 0.2 mils ($5.1 \mu\text{m}$) as a function of time for 0.7 and 2.0 mm diameter drops impacting at 1120 fps. Examination of the data in these figures permits an assessment of the roles of drop size and impacting

TABLE 9
 PREDICTED PEAK RADIAL TENSILE STRESSES FOR
 2.0 mm DROP IMPACTING AT 730 FT/SEC (a)

<u>Material</u>	<u>Stress (psi)</u>
ZnSe	31,100
ZnS	28,400
GaAs	29,000
Ge	25,700
PMMA	10,300

(a) Stresses predicted at $z = 0.0005$ in ($12.7\mu\text{m}$)

CASE 10 ZNSE 0.7 MM DROP AT 730 FT/SEC (SIG VS T)



Z-CONSTANT- (IN.) 0.0002

DROP SIZE- (MM) 0.70

DROP VEL- (FT/SEC) 730.0

P ZERO- (PSI) -1.0

MATERIAL MODULUS- (PSI) 9.750×10^6

POISSONS RATIO- (-+-) 0.300

MATERIAL DENSITY- (LB/IN³) 0.1900

R- (INCHES)

○ 0.0020

▲ 0.0040

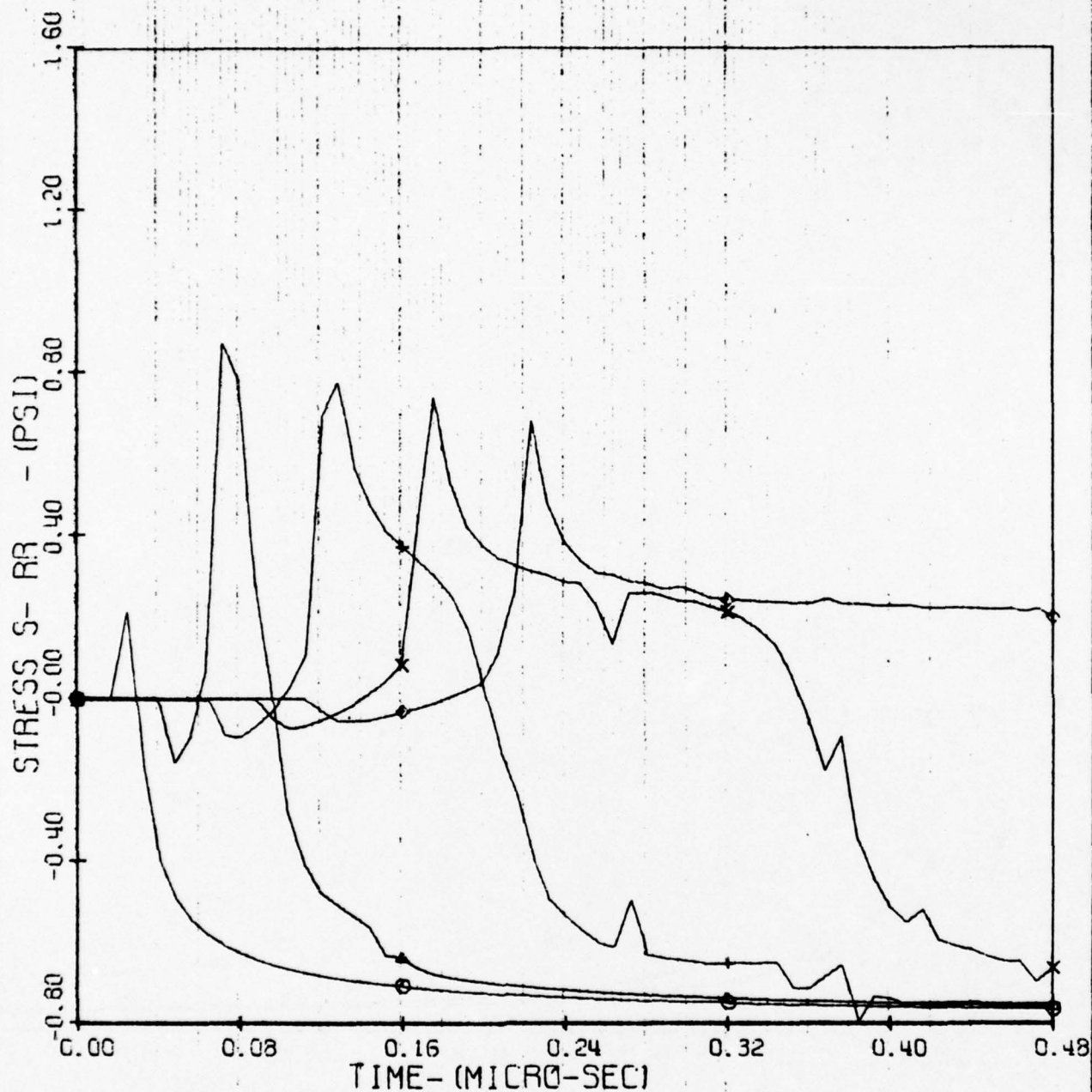
+ 0.0060

x 0.0080

◇ 0.0100

Figure 70. Temporal Distribution of Radial Stress (at Z = 0.0002 in.) for a 0.7 mm Water Drop Impacting ZnSe at 730 ft/sec

CASE 11 ZNSE, 2.0 MM DROP AT 730 FT/SEC (SIG VS T)



Z-CONSTANT- (IN.) 0.0002

DROP SIZE- (MM) 2.00

DROP VEL- (FT/SEC) 730.0

P ZERO- (PSI) -1.0

MATERIAL MODULUS- (PSI) 9.750×10^6

POISSONS RATIO- (---) 0.300

MATERIAL DENSITY- (LB/IN³) 0.1900

R- (INCHES)

○ 0.0040

▲ 0.0080

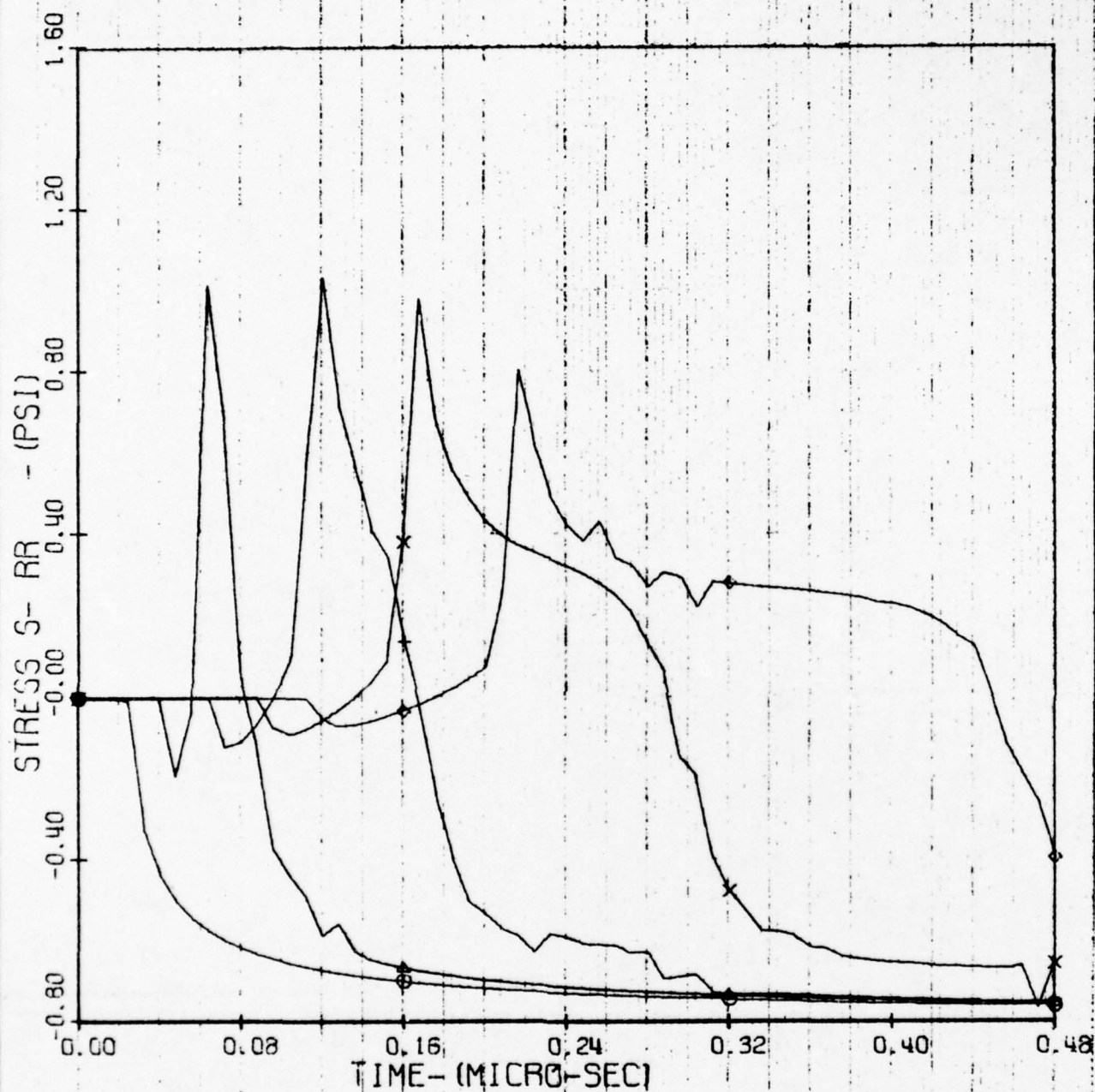
+ 0.0120

x 0.0160

◇ 0.0200

Figure 71. Temporal Distribution of Radial Stress (at Z = 0.0002 in.) for a 2.0 mm Water Drop Impacting ZnSe at 730 ft/sec

CASE 12 ZNSE 2.5 MM DROP AT 730 FT/SEC (SIG VS T)



Z-CONSTANT - (IN.) 0.0002

DROP SIZE - (MM) 2.50

DROP VEL - (FT/SEC) 730.0

P ZERO - (PSI) -1.0

MATERIAL MODULUS - (PSI) 9.750×10^6

POISSONS RATIO - (---) 0.300

MATERIAL DENSITY - (LB/IN³) 0.1900

R - (INCHES)

○ 0.0040

△ 0.0080

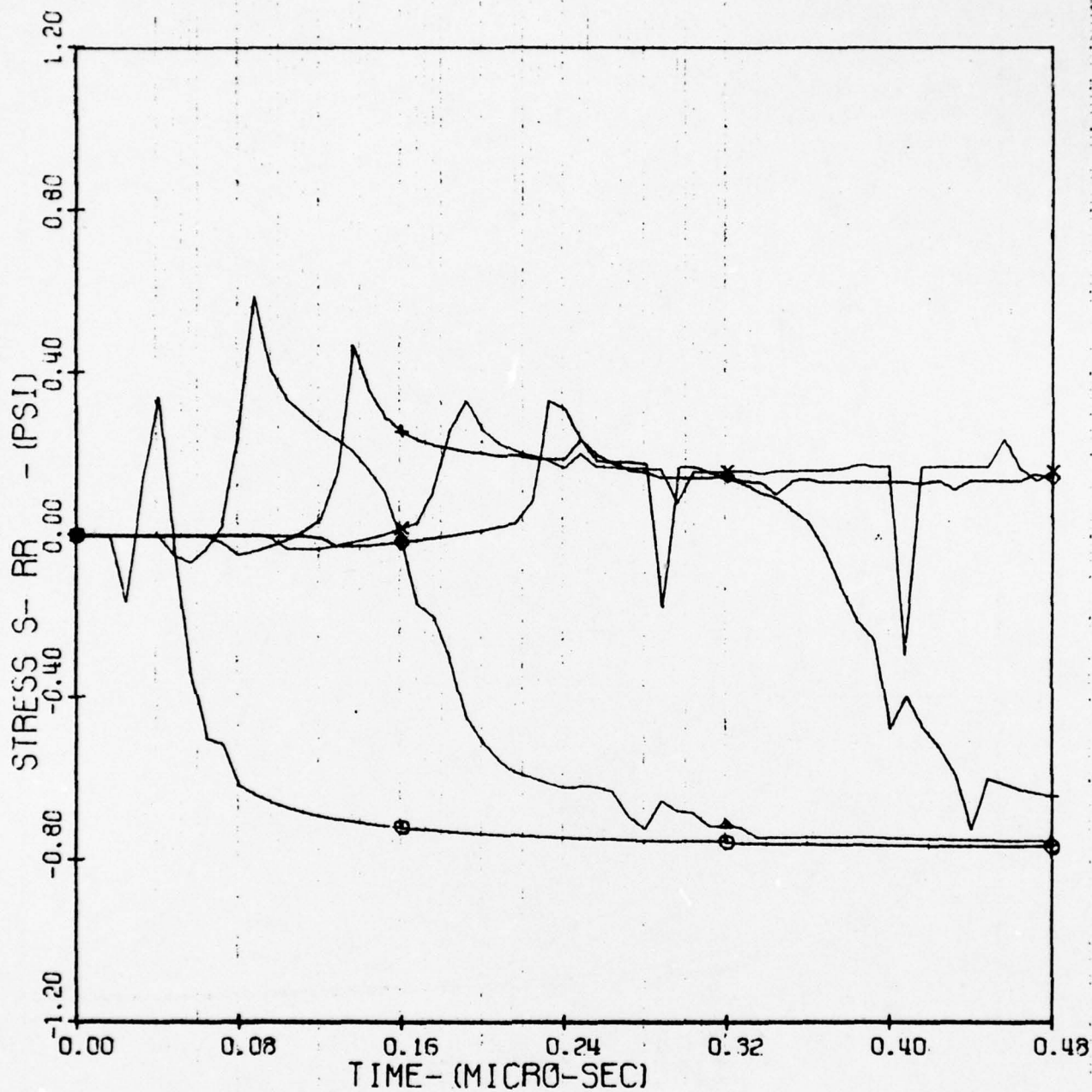
+ 0.0120

x 0.0160

◇ 0.0200

Figure 72. Temporal Distribution of Radial Stress (at Z = 0.0002 in.) for a 2.5 mm Water Drop Impacting ZnSe at 730 ft/sec

CASE 22 ZNSE 0.7 MM DROP AT 1120 FT/SEC (SIG VS T)



Z-CONSTANT - (IN.) 0.0002

DROP SIZE - (MM) 0.70

DROP VEL - (FT/SEC) 1120.0

P ZERO - (PSI) -1.0

MATERIAL MODULUS - (PSI) 9.750×10^6

POISSONS RATIO - (---) 0.300

MATERIAL DENSITY - (LB/IN³) 0.1900

R - (INCHES)

○ 0.0040

△ 0.0080

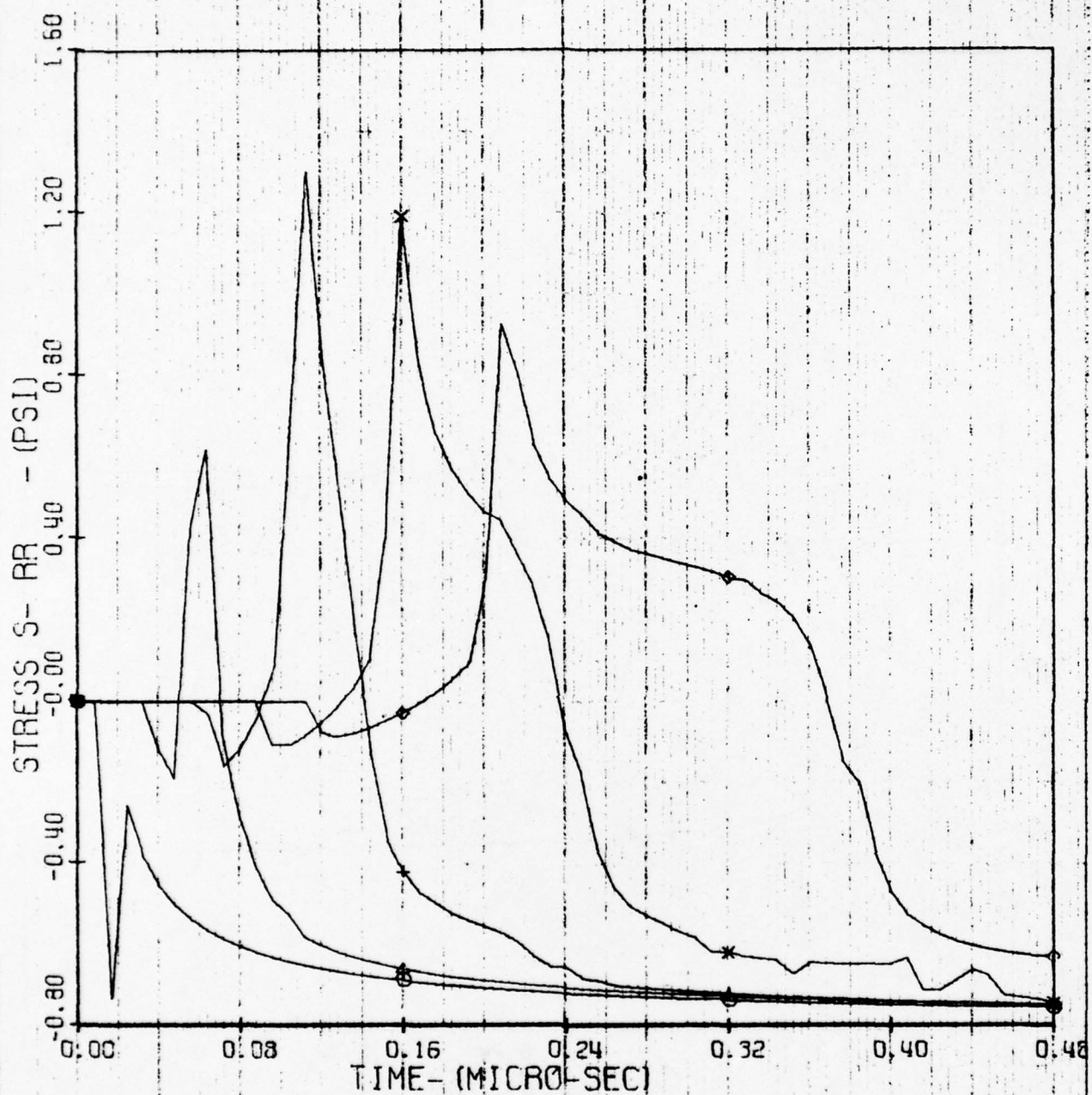
+ 0.0120

× 0.0160

◇ 0.0200

Figure 73. Temporal Distribution of Radial Stress (at $Z = 0.0002$ in. and $0.004 < R < 0.020$ in.) for 0.7 mm Water Drop Impacting ZnSe at 1120 ft/sec

CASE 20 ZNSE 2.0 MM DROP AT 1120 FT/SEC (SIG VS T)



Z-CONSTANT- (IN.) 0.0002

DROP SIZE- (MM) 2.00

DROP VEL- (FT/SEC) 1120.0

P ZERO- (PSI) -1.0

MATERIAL MODULUS- (PSI) 9.750×10^6

POISSONS RATIO- (---) 0.300

MATERIAL DENSITY- (LB/IN**3) 0.1900

R- (INCHES)

○ 0.0040

△ 0.0080

+ 0.0120

× 0.0160

◇ 0.0200

Figure 74. Temporal Distribution of Radial Stress (at $Z = 0.0002$ in. and $0.004 < R < 0.020$ in.) for a 2.0 mm Water Drop Impacting ZnSe at 1120 ft/sec

velocity on the magnitude of the radial stresses. Although this discussion is limited to a single material, zinc selenide, the trends are applicable to zinc sulfide, gallium arsenide, and germanium.

Highlights of these figures are summarized in Figure 75 where peak absolute radial tensile stress in zinc selenide is plotted as a function of drop diameter and velocity at depths of 0.2 mils ($5.1\ \mu\text{m}$) and 0.5 mils ($12.7\ \mu\text{m}$). From the results shown in Figure 75 it is possible to relate peak tensile stress to drop diameter and to impact velocity over the range of variables investigated. The peak radial stress at both depths increases as the drop diameter raised to the 0.55 power when the velocity is 730 fps. At the higher velocity of 1120 fps, peak radial stress increases as the drop diameter raised to the 0.7 power.

When the influence of impact velocity is examined at the 0.5 mil ($12.7\ \mu\text{m}$) depth peak radial stresses are found to be approximately proportional to the velocity squared. Nearer the surface at the 0.2 mil ($5.1\ \mu\text{m}$) depth the exponent for velocity is slightly higher than 2. These relationships between peak stress and impact velocity agree reasonably well with the relative energies of impact which are proportional to velocity squared.

Further comparison of Figures 70 through 74 shows that as both drop size and impact velocity increase, not only does the peak tensile stress increase, but also the radial distance from the center of impact to the location where the stresses become positive (tensile) increases. Specifically, considering a radial location 4.0 mils ($0.10\ \text{mm}$) from the impact center for the 730 fps impact velocity, it is apparent that as drop size increases both the magnitude of the stress and time duration for which the stress is positive decrease. In fact, for the 2.5 mm drop no positive state of stress is predicted at this location. A similar conclusion can be reached for the effect

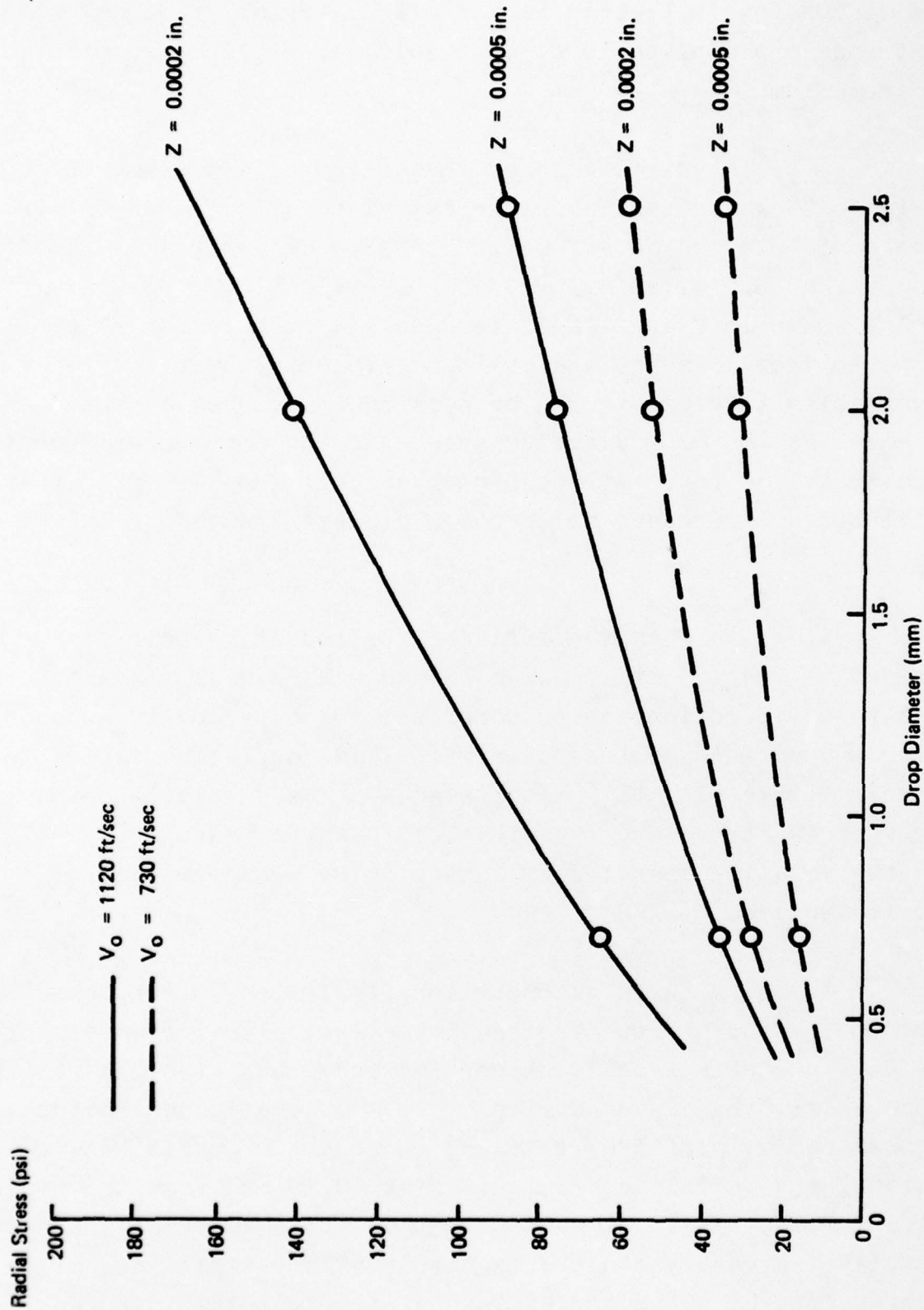


Figure 75. Variation of Peak Radial Stress in ZnSe (at $Z = 0.0002$ and 0.0005 inches) With Drop Size and Impacting Velocity

of increasing velocity. Comparing results for the 2.0 mm drop size at identical radial locations for the two velocities (Figures 71 and 74), it is seen that both the magnitude of the stress and the time duration when it is positive are smaller for the higher impact velocity.

For a particular instant of time, tensile stresses do not exist directly under the loaded region. Radial tensile stresses cannot be generated until the disturbances have propagated a sufficient distance outside the loaded region. Referring to Equations (6) and (7) in Section III.A., the time at which disturbances generated by drop impact are able to move outside the loaded region is directly proportional to the drop radius and impact velocity. Thus, the distance from the center of impact to the location where a radial tensile stress can exist should increase with increasing drop size and impact velocity.

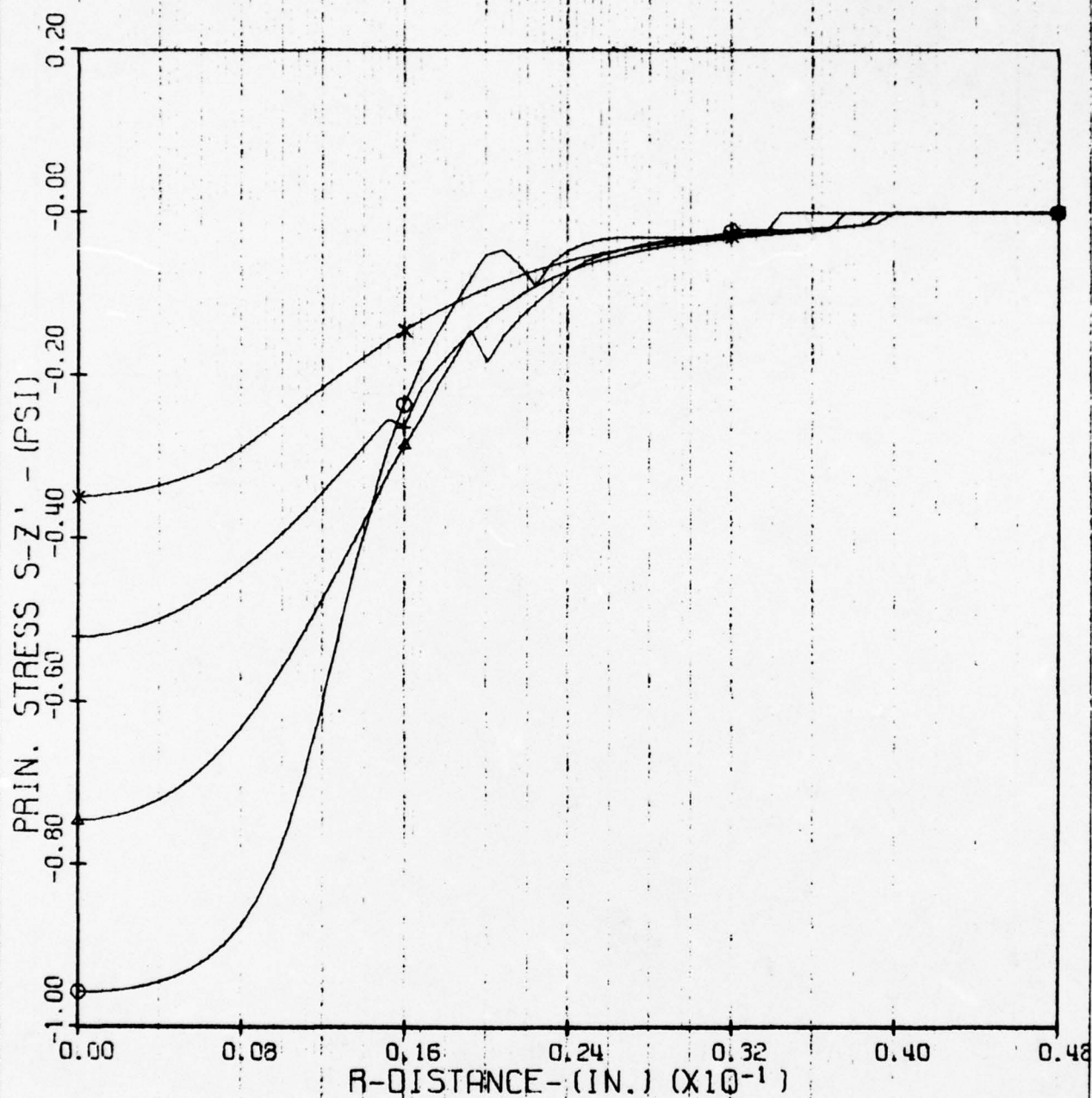
2. Layered Systems

One hardening procedure under current consideration for infrared windows is the use of a more erosion resistant material as a protective layer on a less erosion resistant material which has better infrared transmittance. In this configuration, the pressure pulse imparted to the surface of the laminate by the impacting drop propagates spherical waves which transmit to the substrate forces which are not normal to the interface. In this case, the governing field equations and boundary conditions at the interface are complex and pose a very difficult mathematical problem. While it is a formidable task to solve the coupled mathematical problem, Blowers' ⁽⁶⁾ method for predicting the stresses in an elastic half-space affords a reasonable quantitative evaluation of the local stress conditions within the layered configuration. This method will yield a first order approximation of the actual stresses, provided that the elastic properties do not differ too much from one material to the other.

Trends to be expected in a zinc sulfide/zinc selenide bilayered system were estimated on the basis of stresses computed at various depths in homogeneous slabs of zinc sulfide and zinc selenide. From results of the experimental investigation, zinc sulfide was chosen as the most likely candidate for use as a protective layer because of its superior resistance to liquid drop impacts. The similarity in the transient stress response of the two materials, as evidenced by prior analyses, suggested that the behavior of a thin layer of zinc sulfide over zinc selenide might be inferred from interpolation between results for the two materials considered separately. This series of analyses was conducted for a 2.0 mm water drop impacting zinc sulfide and zinc selenide at a velocity of 730 fps. Stresses were calculated as functions of radial distance from the center of impact at depths of 5, 10, 15 and 20 mils (0.13, 0.25, 0.38 and 0.51 mm) for selected times from 0 to 0.48 microseconds.

Typical results for zinc sulfide are presented in Figures 76 through 81 which depict stress as a function of radial position for various depths at 0.2 microseconds after impact. Both principal stresses and stresses in the coordinate axes are presented with the exception of the hoop stress where the principal and coordinate stresses are identical and only one plot is shown. Examination of the plots indicates that the magnitudes of all stresses decrease rapidly as a function of depth. At a depth of 5 mils (0.13 mm) the maximum principal radial stress is only about 6000 psi based on the normalized stress from Figure 77 multiplied by the appropriate interface pressure in Table 7. This stress is quite small compared to a peak predicted value of 78,000 psi calculated at a depth of 0.1 mils (2.5 μ m). However, large shear stresses, about 20,000 psi, at the 5 mil (0.13 mm) depth may influence interface strength requirements. Generally, the shear stress tends to peak at a distance between 0.2 and 5.0 mils (0.005 and 0.13 mm) below the surface, decreasing rapidly at greater depths. Thus, the requirement for high interface shear strength could be offset by utilizing a thicker outer layer.

CASE 109 - ZNS 2.0 MM DROP AT 730 FT/SEC (THICK STUDY)



T-CONST. - (MIC-SEC) 0.2000

DROP SIZE - (MM) 2.00

DROP VEL - (FT/SEC) 730.0

P ZERO - (PSI) -1.0

MATERIAL MODULUS - (PSI) 10.800×10^6

POISSONS RATIO - (---) 0.300

MATERIAL DENSITY - (LB/IN³) 0.1473

Z - (INCHES)

○ 0.0050

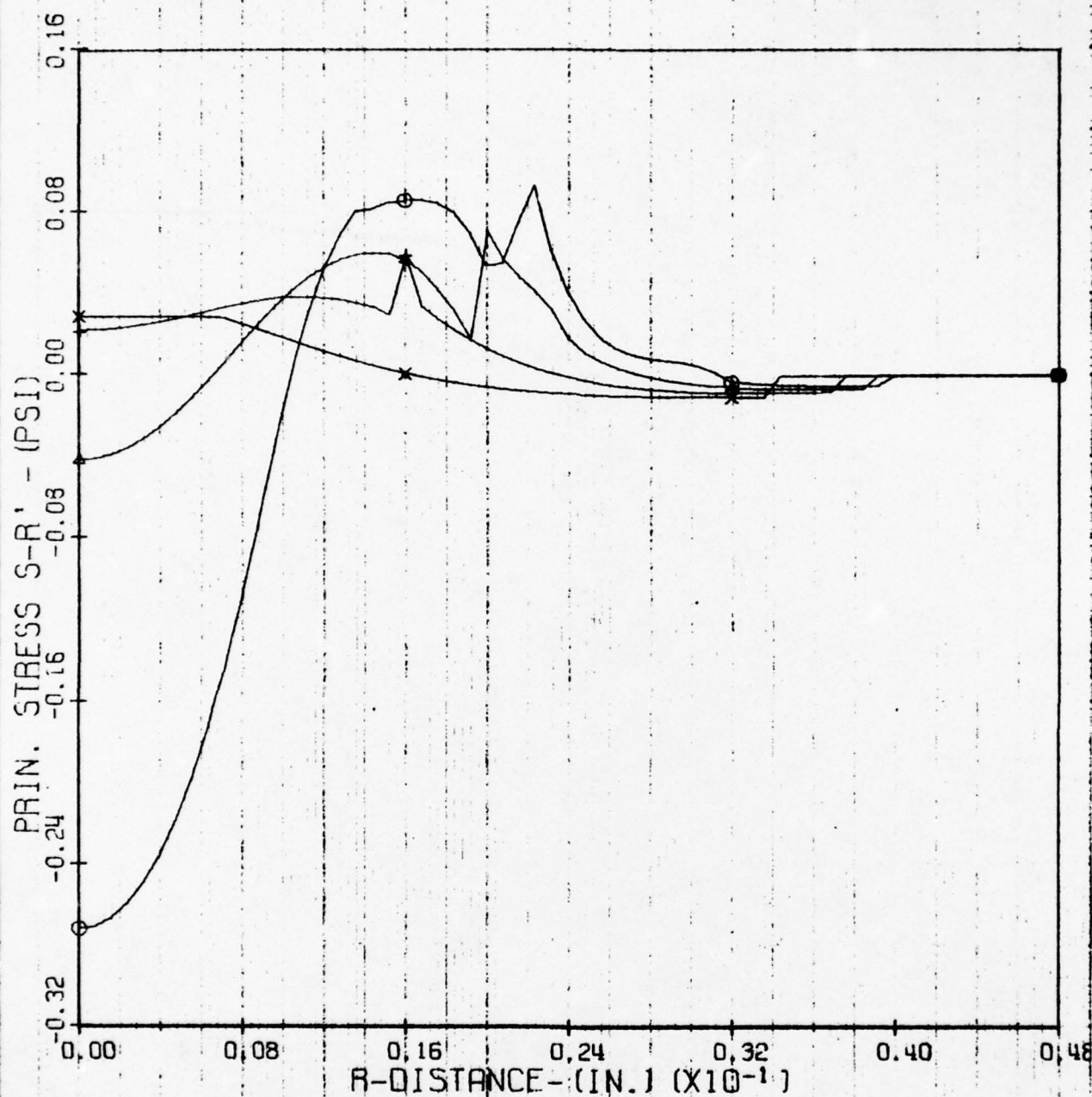
▲ 0.0100

⊕ 0.0150

× 0.0200

Figure 76. Variation of Principal Axial Stress ($t = 0.2 \mu\text{sec}$) with Depth for a 2.0 mm Water Drop Impacting ZnS at 730 ft/sec

CASE 109 - ZNS 2.0 MM DROP AT 730 FT/SEC (THICK STUDY)



T-CONST. - (MIC-SEC) 0.2000

DROP SIZE - (MM) 2.00

DROP VEL - (FT/SEC) 730.0

P ZERO - (PSI) -1.0

MATERIAL MODULUS - (PSI) 10.800×10^6

POISSONS RATIO - (---) 0.300

MATERIAL DENSITY - (LB/IN³) 0.1473

Z - (INCHES)

○ 0.0050

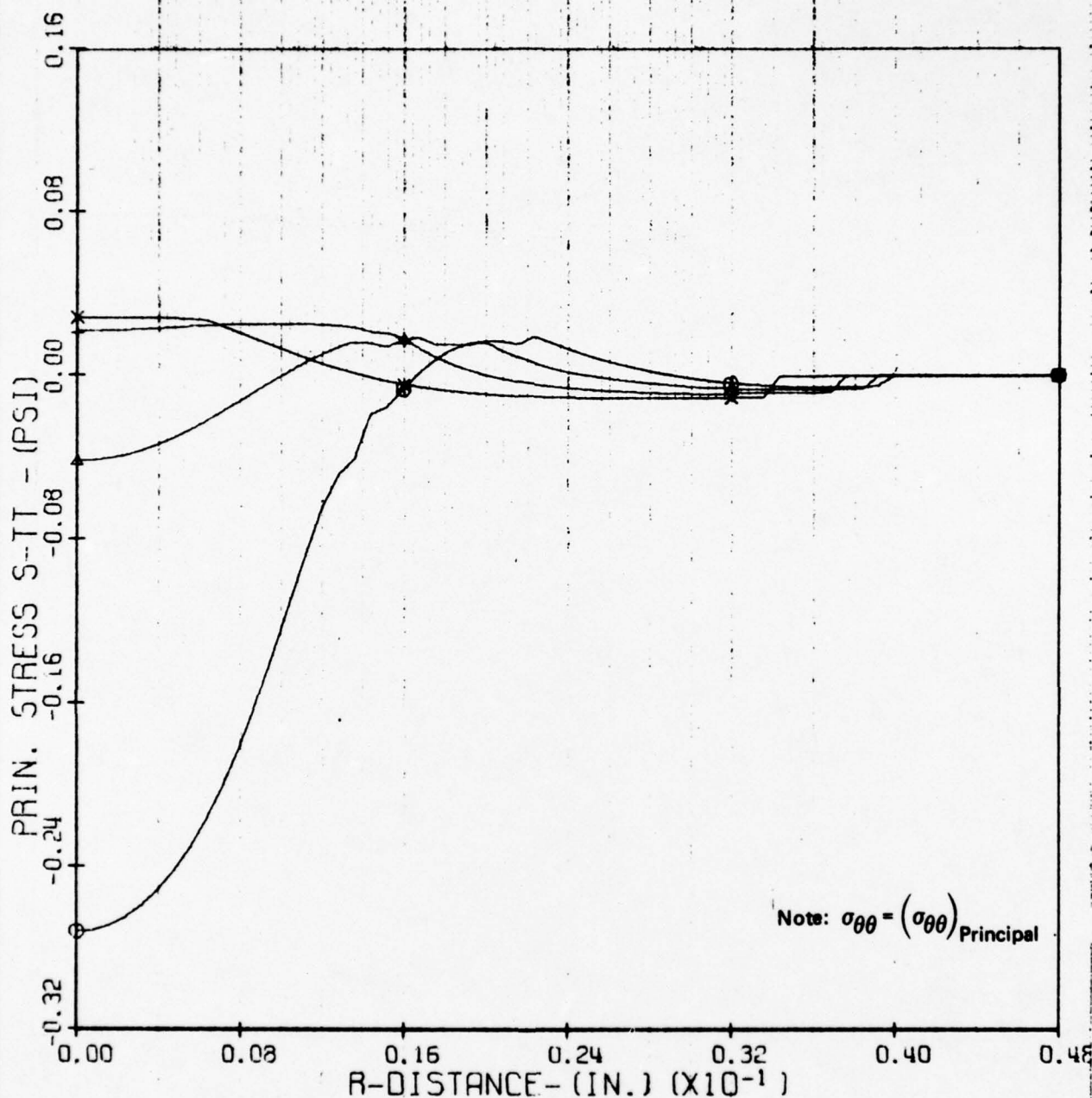
▲ 0.0100

+ 0.0150

× 0.0200

Figure 77. Variation of Principal Radial Stress ($t = 0.2 \mu\text{sec}$) with Depth for a 2.0 mm Water Drop Impacting ZnS at 730 ft/sec

CASE 109 + ZNS: 2.0 MM DROP AT 730 FT/SEC (THICK STUDY)



T-CONST. - (MIC-SEC) 0.2000

DROP SIZE - (MM) 2.00

DROP VEL - (FT/SEC) 730.0

P ZERO - (PSI) -1.0

MATERIAL MODULUS - (PSI) 10.800×10^6

POISSONS RATIO - (---) 0.300

MATERIAL DENSITY - (LB/IN**3) 0.1473

Z - (INCHES)

○ 0.0050

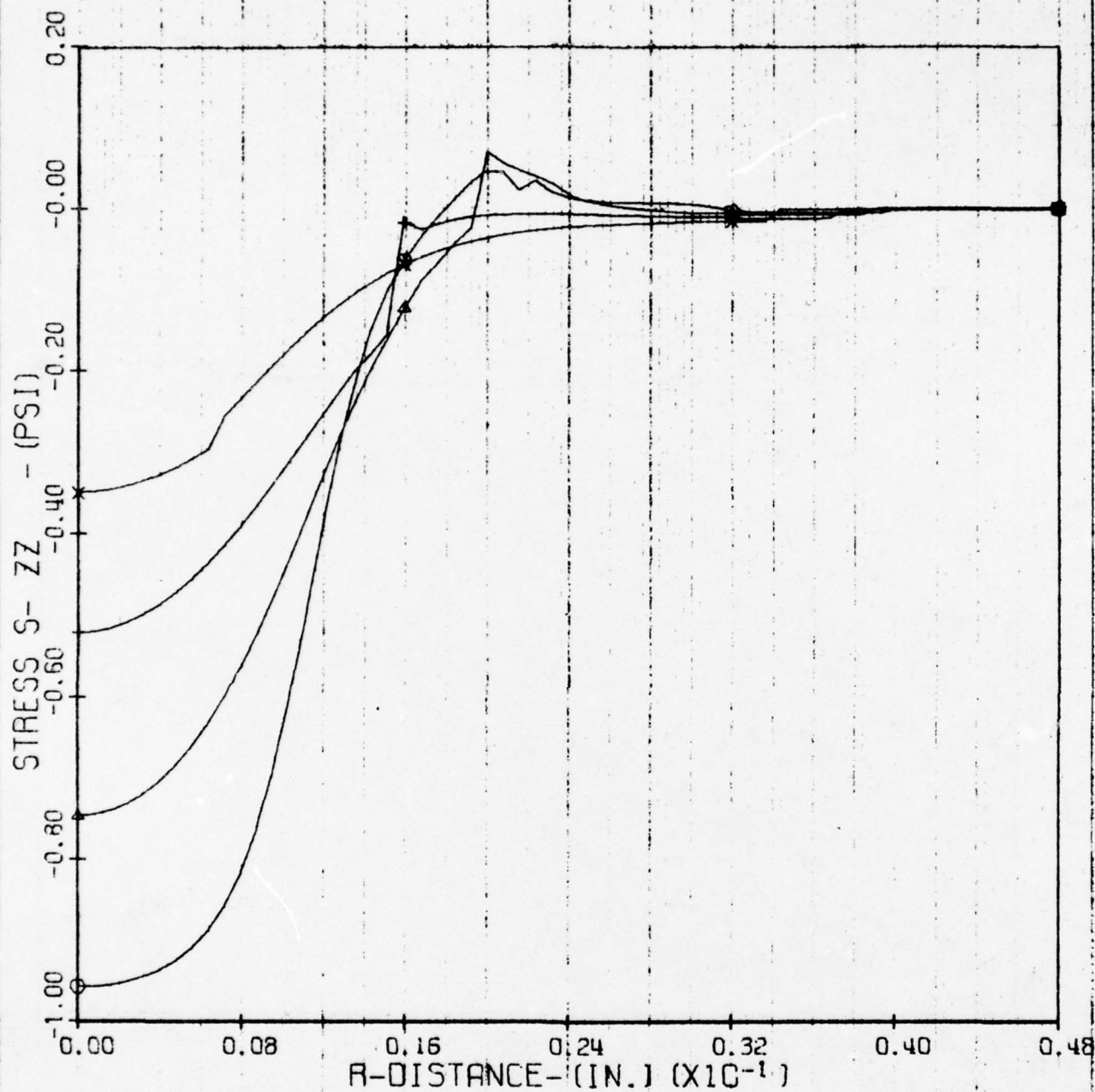
▲ 0.0100

+

x 0.0200

Figure 78. Variation of Principal Hoop Stress (at $t = 02. \mu\text{sec}$) with Depth for a 2.0 mm Water Drop Impacting ZnS at 730/ft/sec

CASE 109 - ZNS 2.0 MM DROP AT 730 FT/SEC (THICK STUDY)



T-CONST. - (MIC-SEC) 0.2000

DROP SIZE - (MM) 2.00

DROP VEL - (FT/SEC) 730.0

P ZERO - (PSI) -1.0

MATERIAL MODULUS - (PSI) 10.800×10^6

POISSONS RATIO - (---) 0.300

MATERIAL DENSITY - (LB/IN**3) 0.1473

Z - (INCHES)

○ 0.0050

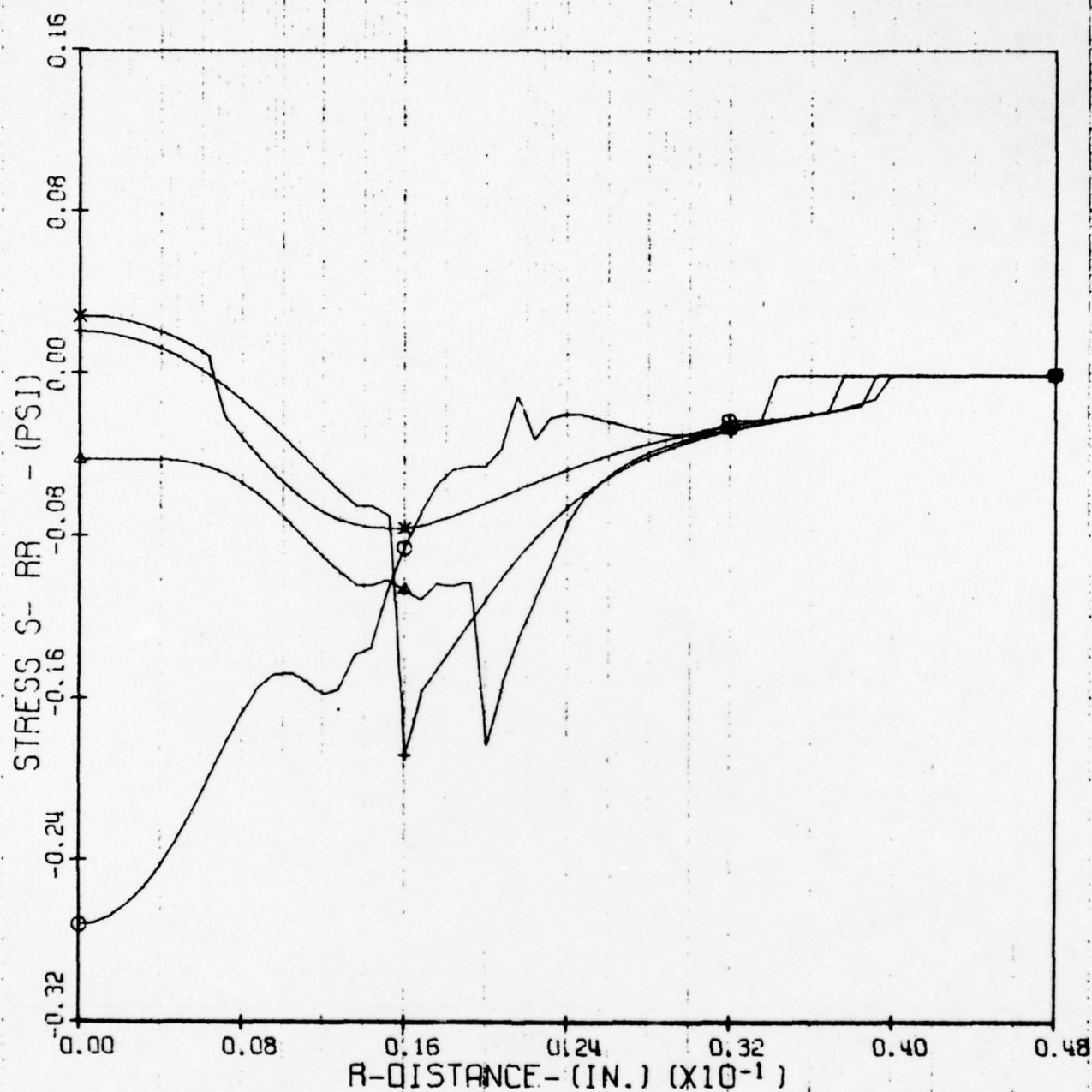
△ 0.0100

+ 0.0150

× 0.0200

Figure 79. Variation of Axial Stress (at $t = 0.2 \mu\text{sec}$) with Depth for a 2.0 Water Drop Impacting ZnS at 730 ft/sec)

CASE 109 - ZNS 2.0 MM DROP AT 730 FT/SEC (THICK STUDY)



T-CONST. - (MIC-SEC) 0.2000

DROP SIZE - (MM) 2.00

DROP VEL - (FT/SEC) 730.0

P ZERO - (PSI) -1.0

MATERIAL MODULUS - (PSI) 10.800×10^6

POISSONS RATIO - (---) 0.300

MATERIAL DENSITY - (LB/IN³) 0.1473

Z - (INCHES)

○ 0.0050

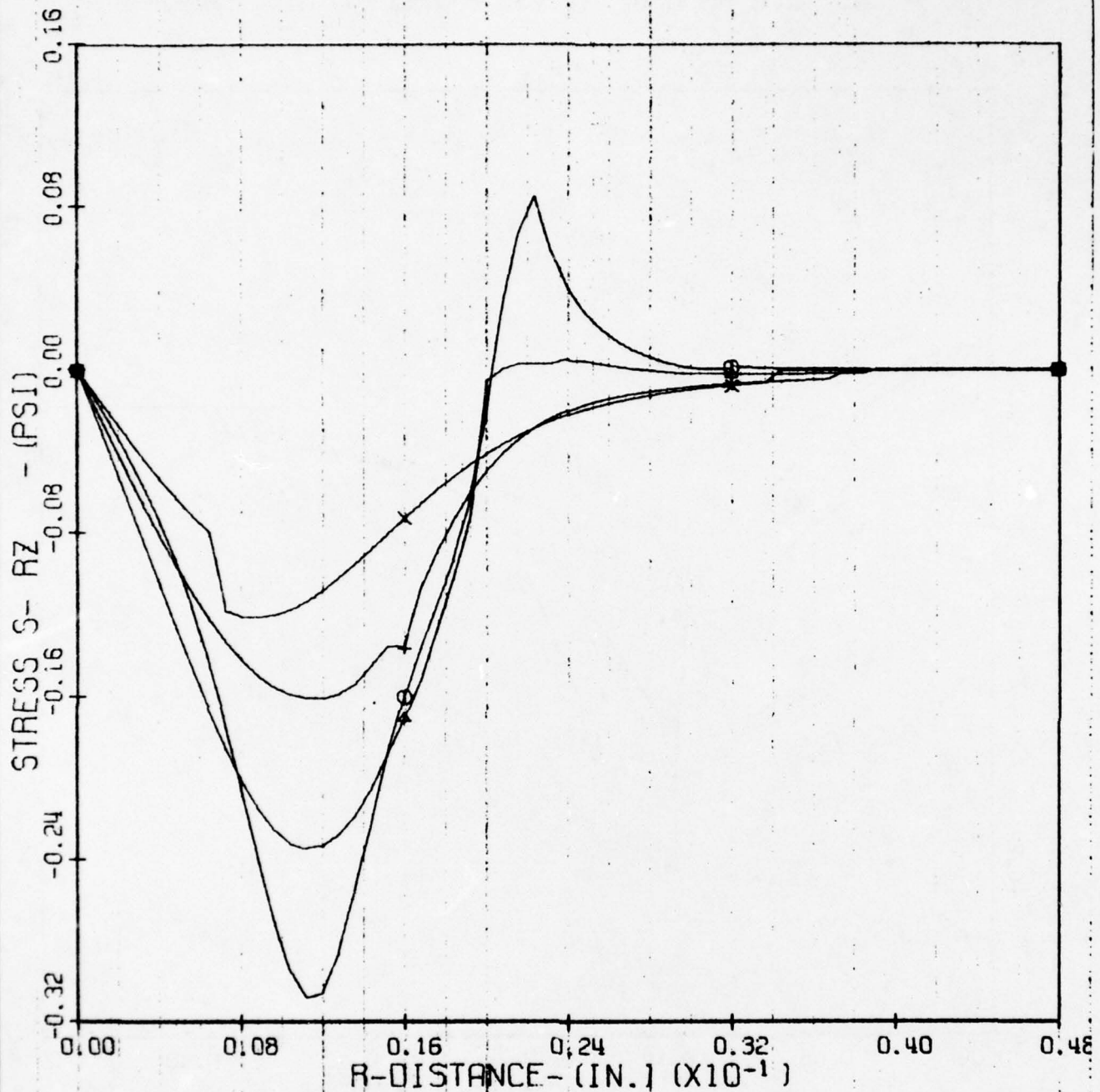
▲ 0.0100

⊕ 0.0150

× 0.0200

Figure 80. Variation of Radial Stress (at $t = 0.2 \mu\text{sec}$) with Depth for a 2.0 mm Water Drop Impacting ZnS at 730 ft/sec

CASE 109 - ZNS 2.0 MM DROP AT 730 FT/SEC (THICK STUDY)



T-CONST. - (MIC-SEC) 0.2000

DROP SIZE - (MM) 2.00

DROP VEL - (FT/SEC) 730.0

P ZERO - (PSI) -1.0

MATERIAL MODULUS - (PSI) 10.800×10^6

POISSONS RATIO - (---) 0.300

MATERIAL DENSITY - (LB/IN³) 0.1473

Z - (INCHES)

○ 0.0050

△ 0.0100

+ 0.0150

× 0.0200

Figure 81. Variation of Shear Stress (at $t = 0.2 \mu\text{sec}$) with Depth for a 2.0 mm Water Drop Impacting ZnS at 730 ft/sec

For the outer layer thicknesses of 10, 20, and 40 mils (0.25, 0.50, 1.0 mm) of zinc sulfide on zinc selenide used in the experimental work, the analytical results indicate that no ring fractures should be observed in the zinc selenide substrate. Even accounting for the fact that shear strength might be higher than the measured flexural strength, the low value of flexural strength for zinc selenide suggests a strong possibility of an interface shear failure of the 10 mil (0.25 mm) sample, possible failure of the 20 mil (0.50 mm) sample, but no failure of the 40 mil (1.0 mm) sample. If shear strength is not a limitation, the outer zinc sulfide layer could be even thinner than 10 mils (0.25 mm) as shown by Figure 82. This figure relates the maximum principal radial tensile stress to layer depth for zinc selenide for depths less than 6 mils (0.15 mm) at 0.1 microseconds after impact. The curve for zinc sulfide is practically identical and therefore not shown. The curve in Figure 82 shows that a zinc sulfide layer thickness as low as 5 mils (0.13 mm) might be sufficient to prevent the formation of fracture in the zinc selenide substrate.

The analysis predicts that the zinc sulfide thicknesses of 10, 20 and 40 mils (0.25, 0.51 and 1.02 mm) selected for experimental evaluation should prevent fracture of the zinc selenide by single drop impact. Not only are the stress levels in the zinc selenide too low to generate fracture, but the thickness of the zinc sulfide is too great for cracks to propagate from it into the zinc selenide. The prediction of absence of ring fractures in the zinc selenide was verified by the experimental work described in Section II.F. Single drop impact experiments with zinc sulfide layers less than 10 mils (0.25 mm) thick to establish the threshold for damage on the zinc selenide substrate would provide additional verification of the analytical model.

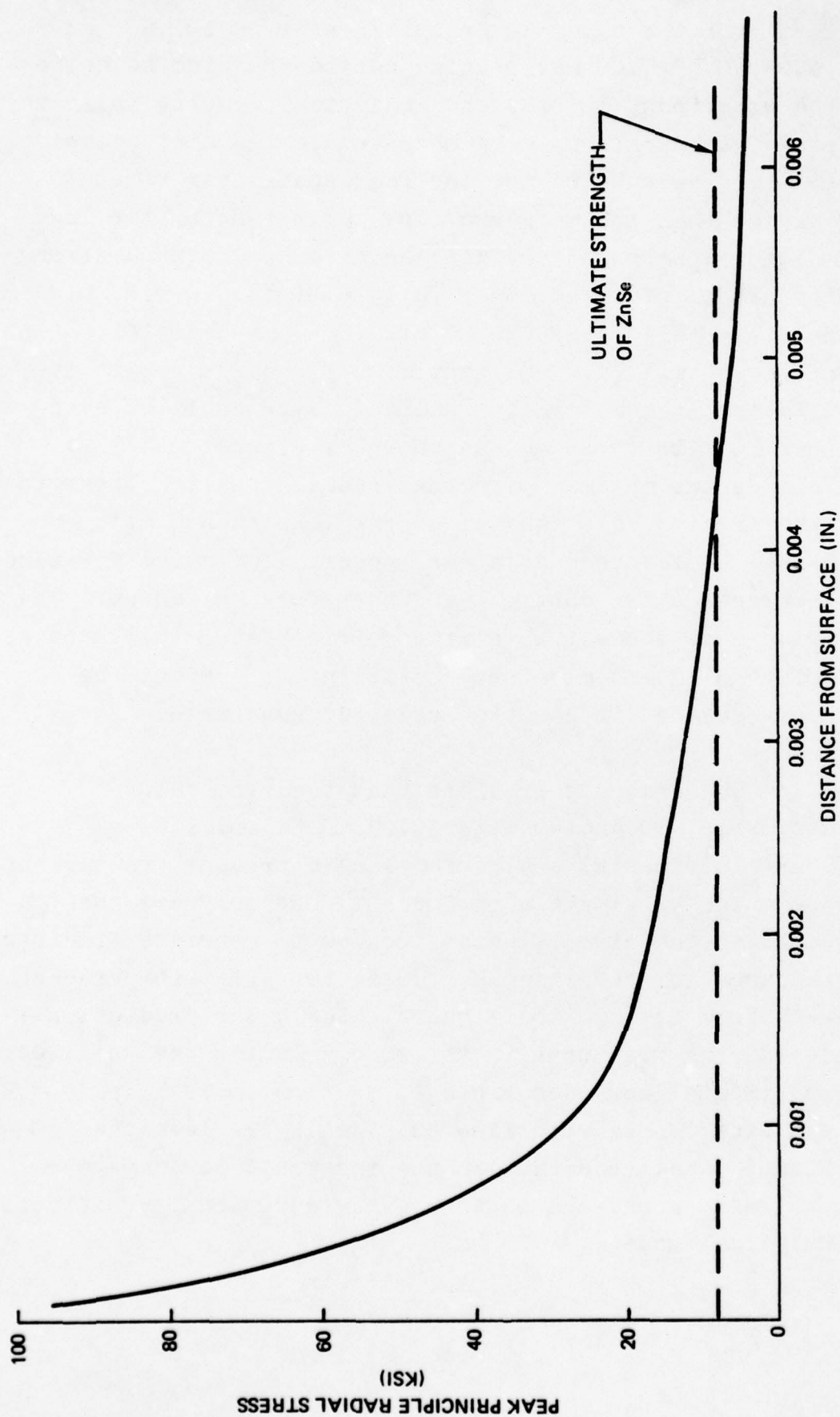


Figure 82. Variation of Peak Principle Radial Stress (at $t = 0.1 \mu\text{sec}$) With Depth for a 2.0 mm Water Drop Impacting ZnSe at 730 ft/sec

C. Comparison with Experimental Results

Table 10 summarizes the predicted peak radial tensile stresses at depths of 0.5 and 0.2 mils (12.7 and 5.1 μm) for zinc selenide, zinc sulfide, gallium arsenide, germanium, and PMMA for all drop sizes and impact velocities analyzed. Even at the greater depth of 0.5 mils (12.7 μm), these stresses equal or exceed the material ultimate strengths presented in Table 8. Closer to the surface, predicted stresses are at least two or more times the material strengths. Thus, for the five materials considered and for the range of drop sizes and velocities investigated, the mathematical model predicts that material failures should have occurred.

The analytical model predicts that ring fracture from single drop impact is a surface phenomenon. Figure 82 shows the peak radial stress in zinc selenide falls off rapidly below a depth of 1 mil (25 μm) and by 4 mils (100 μm) is less than the reported fracture strength. Figure 82 is for zinc selenide, but an almost identical curve is predicted for zinc sulfide. The stress drops below the reported fracture strength of zinc sulfide at a depth of only 2 mils because of the higher strength of zinc sulfide. These data indicate that zinc selenide should be more severely damaged than zinc sulfide by a single drop impact.

The greater damage to zinc selenide was borne out by the results of the single drop experiments. However, zinc selenide was damaged to a much greater degree than was zinc sulfide to be explained merely by the difference in depth where stress falls below the fracture strength. Figure 1 shows that the zinc selenide has a high percentage of grains with diameters as large as 4 mils (100 μm). These diameters are of the order of the depth of significant peak radial stresses. It is logical to expect that the ring fractures would penetrate to at least this depth. The largest grains in the zinc sulfide, on the other hand, have diameters of about 0.4 mils (10 μm). Ring fractures would have to penetrate across five or more grains within the layer where the

TABLE 10.

PREDICTED PEAK RADIAL TENSILE STRESSES FOR
730 AND 1120 FT/SEC WATER DROP
IMPACTS

Material	Drop Diameter (mm)	Stress (psi) at $z=0.0005$ in.			Stress (psi) at $z=0.0002$ in.		
		$V_o = 730$ fps	$V_o = 1120$ fps	$V_o = 730$ fps	$V_o = 1120$ fps	$V_o = 730$ fps	$V_o = 1120$ fps
ZnSe	0.7	14,900	34,800	27,370	67,330		
	2.0	31,100	76,000	53,490	141,180		
	2.5	34,832	89,000	64,070	-----		
ZnS	0.7	11,400	30,000	-----	-----		
	2.0	28,400	68,900	41,340	109,750		
	2.5	33,300	-----	-----	-----		
GaAs	0.7	-----	-----	-----	-----		
	2.0	29,000	66,200	54,270	-----		
	2.5	-----	-----	-----	-----		
Ge	0.7	-----	-----	-----	-----		
	2.0	25,700	65,400	-----	-----		
	2.5	-----	-----	-----	-----		
PMMA	0.7	-----	-----	22,300	48,580		
	2.0	10,300	17,350	47,080	90,220		
	2.5	-----	-----	51,630	-----		

stress is above the fracture strength. It is not likely that the ring fractures will extend that deep because extra energy is required for the fractures to cross grain boundaries and propagate in neighboring grains at different crystallographic orientations. It appears probable that the fracture domains for a single drop impact extends to a depth comparable to one grain diameter, i.e., 4 mils (100 μm) for zinc selenide and 0.4 mils (10 μm) for zinc sulfide. This fracture domain for zinc sulfide corresponds to the depth of the deepest crack found during the electron microscopic examination of the zinc sulfide specimen progressively eroded in the rainfield (Figure 38d).

The experimentally measured annular ring fracture radii in Tables 2 and 4 are compared in Figure 83 with the theoretical lateral outflow angles and drop radii. Strictly speaking, the radii for PMMA shown in Figure 83 are for the indented annulus. For the range of variables investigated there appears to be no direct relationship between the location of the ring fracture zone and the theoretical outflow angle. For the 2.0 and 2.5 mm water drops impacting at 730 fps, the major extent of ring cracking occurred at locations where the theoretical lateral outflow angles were 10 to 25 degrees. For the 0.7 mm drops impacting at 730 fps, most of the ring cracking extended well beyond the region where the lateral outflow angle was 25 degrees. At the higher velocity of 1120 fps, most of the ring cracking also extended beyond the region where the lateral outflow angle was 25 degrees.

The effects of drop size and impact velocity are shown quite clearly in Figure 78 for PMMA and zinc selenide. At a constant impact velocity of 730 fps, it is apparent that the size of the ring fracture zone and the inner radius of the zone tend to increase with increasing drop size. At a constant drop size of 2.0 μm , it is apparent that the ring fracture zone and the inner radius of the zone also increase with increasing velocity. These trends are consistent with the results presented in the section on the effect of drop size and impact velocity, III.B.1.c. Further examination of Figure 83 indicates a dependency of the

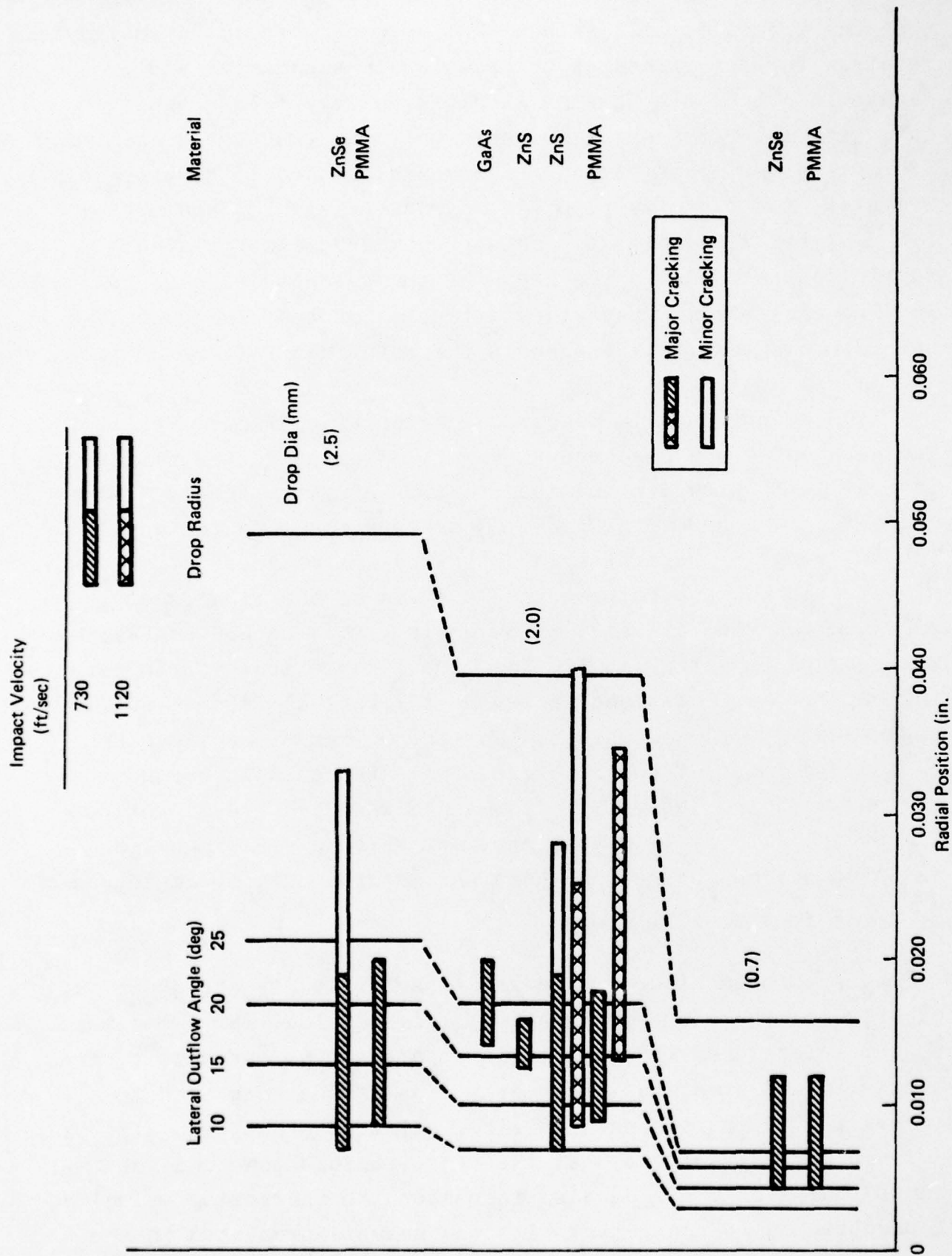


Figure 83. Comparison of Ring Crack Fracture Radii to Theoretical Lateral Outflow Angle

annular width of the fracture zone on the material ultimate tensile strength. Although not completely evident for 0.7 mm drop impact results, the remaining experimental data indicate an apparent trend of decreasing width of fracture zone with increasing material strength.

Examination of the stress plots presented in the various sections for the various materials shows that the stresses in the region between the center of impact and the first ring of cracks is of sufficient magnitude to exceed the ultimate strengths of the materials. However, the wave forms are sharp triangular spikes. The fact that failure does not occur in this region suggests that the very high strain rates (10^5 to 10^6 in/in/sec, equivalent to about 10^{12} to 10^{13} psi/sec) associated with the initial portion of the transient loading result in an effective material strength considerably greater than that measured with flexural tests. The experimental results show that failure is not observed until a radial location is reached where the computed stress waveform begins to broaden (i.e. longer time duration of the positive radial stress) suggesting a rate sensitivity for material strength.

These observations might be explained also by consideration of the amount of material subjected to a particular stress level. Inasmuch as the strength of brittle materials is statistical in nature, one would expect a higher stress level to be sustained by a smaller volume (or area) of material than by a larger volume (or area). For the parameters associated with the experiments, it would be surprising if the strength evidenced by the smaller volume would be more than twice that of the larger volume where failure occurred. Therefore, the statistical strength aspect, while important, does not appear to be the dominant aspect of the observed behavior.

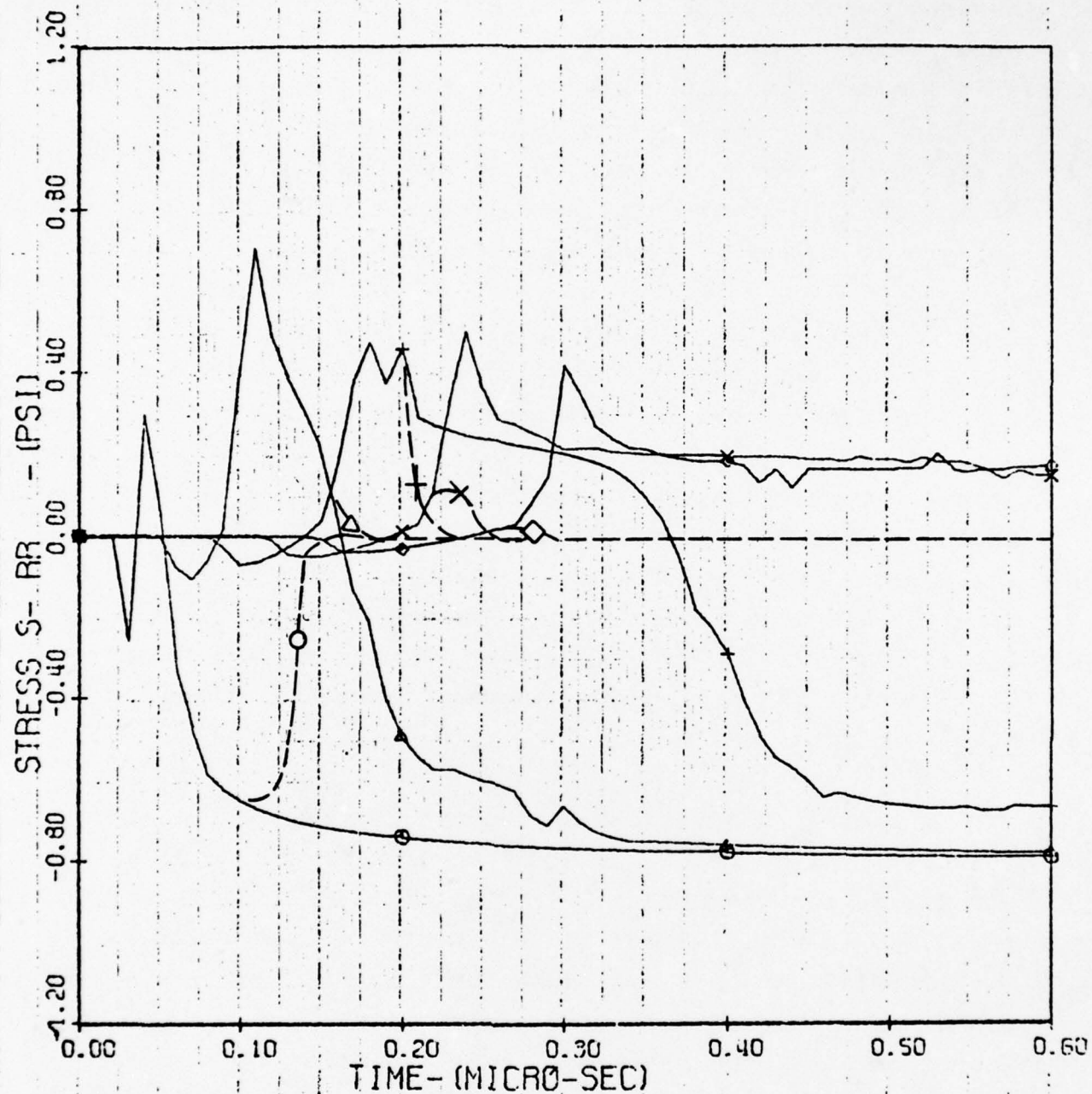
A degree of caution must be used in interpreting the results from the analytic model because of the following assumptions inherent in the model:

1. The substrate is homogeneous (i.e., defect free and without provisions for any redistribution of stresses as a result of local material failures.
2. A uniform and constant interface pressure in the loaded regions.
3. The radius of the loaded area increases at $t^{\frac{1}{2}}$. Since there are no provisions in the model for load removal as there would be in the actual liquid drop impact process, an alternate method was used to correlate experimentally measured fracture zones with the analytical stress predictions.

It can be assumed that the passage of stress waves generated by the drop impact disturbance past any radial position will have a similar time duration as the loading. Empirical and theoretical data show that when the lateral outflow angle ϕ reaches 25 degrees, the pressure at the drop/substrate interface has decreased to nearly zero. An estimate of load duration can therefore be made from the time taken to reach this critical lateral outflow angle. Referring to Figure 53, load durations of 0.096 μsec for 0.7 mm drops and 0.275 μsec for 2.0 mm drops impacting at 1120 fps are obtained for a critical lateral outflow angle $\phi = 25$ degrees. These loading durations served as the basis for modifying the predicted stress curves for impact at 1120 fps to provide for decay of the stress. A similar procedure was not attempted for 730 fps impact cases because curves were not available at sufficiently large radial distances to encompass the outer radii of the fractured zones.

Figure 84 presents the radial stresses resulting from 0.7 mm drop impacting PMMA at 1120 fps with the dashed lines representing the decay of the stress at each radial position approximately 0.096 μsec from the time the disturbance is first felt. At a radial position of $r = 0.004$ in. (0.10 μm), a tensile spike having a duration less than 0.02 μsec is predicted. The stress then becomes highly negative because the region of loading very

CASE 222 PMMA 0.7 MM DROP AT 1120 FT/SEC (SIG VS T)



Z-CONSTANT- (IN.) 0.0002

DROP SIZE- (MM) 0.70

DROP VEL- (FT/SEC) 1120.0

P ZERO- (PSI) -1.0

MATERIAL MODULUS- (PSI) 1.305×10^6

POISSONS RATIO- (---) 0.325

MATERIAL DENSITY- (LB/IN³) 0.0428

R- (INCHES)

○ 0.0040

△ 0.0080

+ 0.0120

× 0.0160

◇ 0.0200

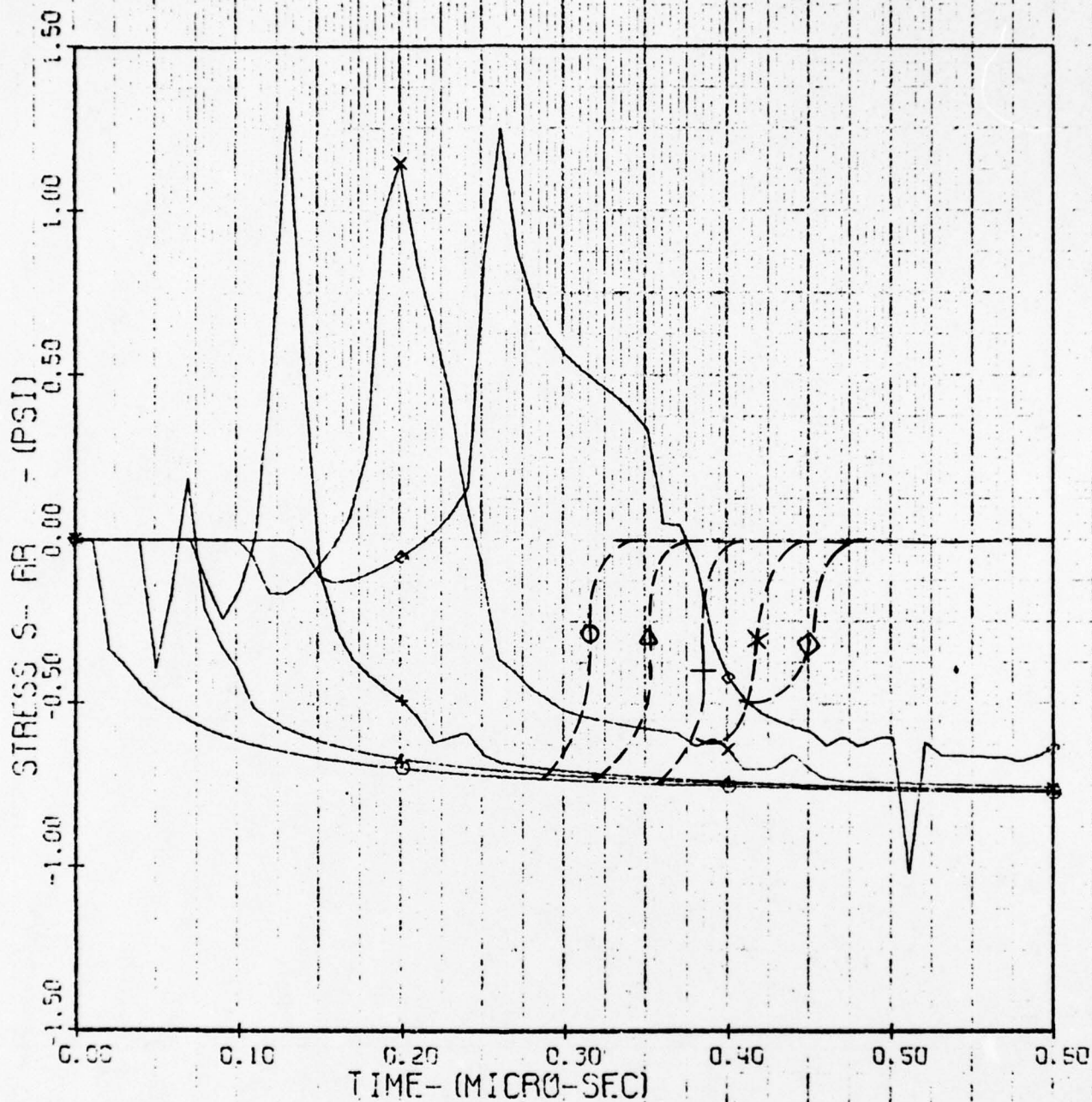
Figure 84. Temporal Distribution of Radial Stress (at $Z = 0.0002$ in. and $0.004 < R < 0.020$ in.) for a 0.7 mm Water Drop Impacting PMMA at 1120 ft/sec, with Pressure Pulse Limited to $0.096 \mu\text{sec}$ Duration

quickly moves over this location. A material failure would not be expected to result from this short duration tensile loading. At a radial location of $r = 0.008$ inch (0.20 mm), the magnitude of the peak tensile stress has increased and, more importantly, the time duration of the tensile stress has increased to 0.07 μ sec. For $r \geq 0.016$ inch (0.406 mm) the magnitude and duration of the tensile stress becomes very small indicating that material failure is unlikely beyond this position.

Similar modified results for a 2.0 mm drop impacting PMMA at 1120 fps are presented in Figure 85 and 86 where the stress at each radial location is assumed to decay to zero 0.275 μ sec after the disturbance is first felt. These curves show that tensile stresses having a significant time duration occur between radial location $r = 0.012$ inch (0.305 mm) and $r = 0.040$ inch (1.02 mm). These values agree reasonably well with the experimental data for 2.0 mm drop impact on PMMA presented in Table 4 and Figure 83, where the average inner ring fracture radius was 0.013 inch (0.33 mm) and the average outer radius was 0.035 inch (0.88 mm).

A similar analysis was conducted for ZnSe for an impact velocity of 1120 fps. For a 0.7 mm drop impact on ZnSe, the annular region where tensile radial stresses occur lies between $r = 0.004$ inch (0.102 mm) and $r = 0.016$ inch (0.406 mm). No experimental data are available for comparison since impact with 0.7 mm drop was not performed at 1120 fps. For a 2.0 mm drop impact on ZnSe, the predicted inner radius of the annular region lies between $r = 0.004$ inch (0.102 mm) and $r = 0.008$ inch (0.203 mm). However, at $r = 0.004$ inch the predicted time duration of positive stress is only about 0.02 μ sec, probably too short to cause fracture. The computer analyses are limited to radial locations up to 0.040 inch (1.01 mm) resulting in insufficient data to predict the outer radius of the annular region for zinc selenide. From Table 4, the measured average annular region where damage occurred on ZnSe for 2.0 mm drop impacts at 1120 fps was from $r = 0.008$ inch (0.203 mm) to

CASE 220 PMMA 2.0 MM DROP AT 1120 FT/SEC (SIG. VS T)



Z-CONSTANT- (IN.) 0.0002

DROP SIZE- (MM) 2.00

DROP VEL- (FT/SEC) 1120.0

P ZERO- (PSI) -1.0

MATERIAL MODULUS- (PSI) 1.305×10^6

POISSONS RATIO- (---) 0.325

MATERIAL DENSITY- (LB/IN**3) 0.0423

R- (INCHES)

○ 0.0040

△ 0.0080

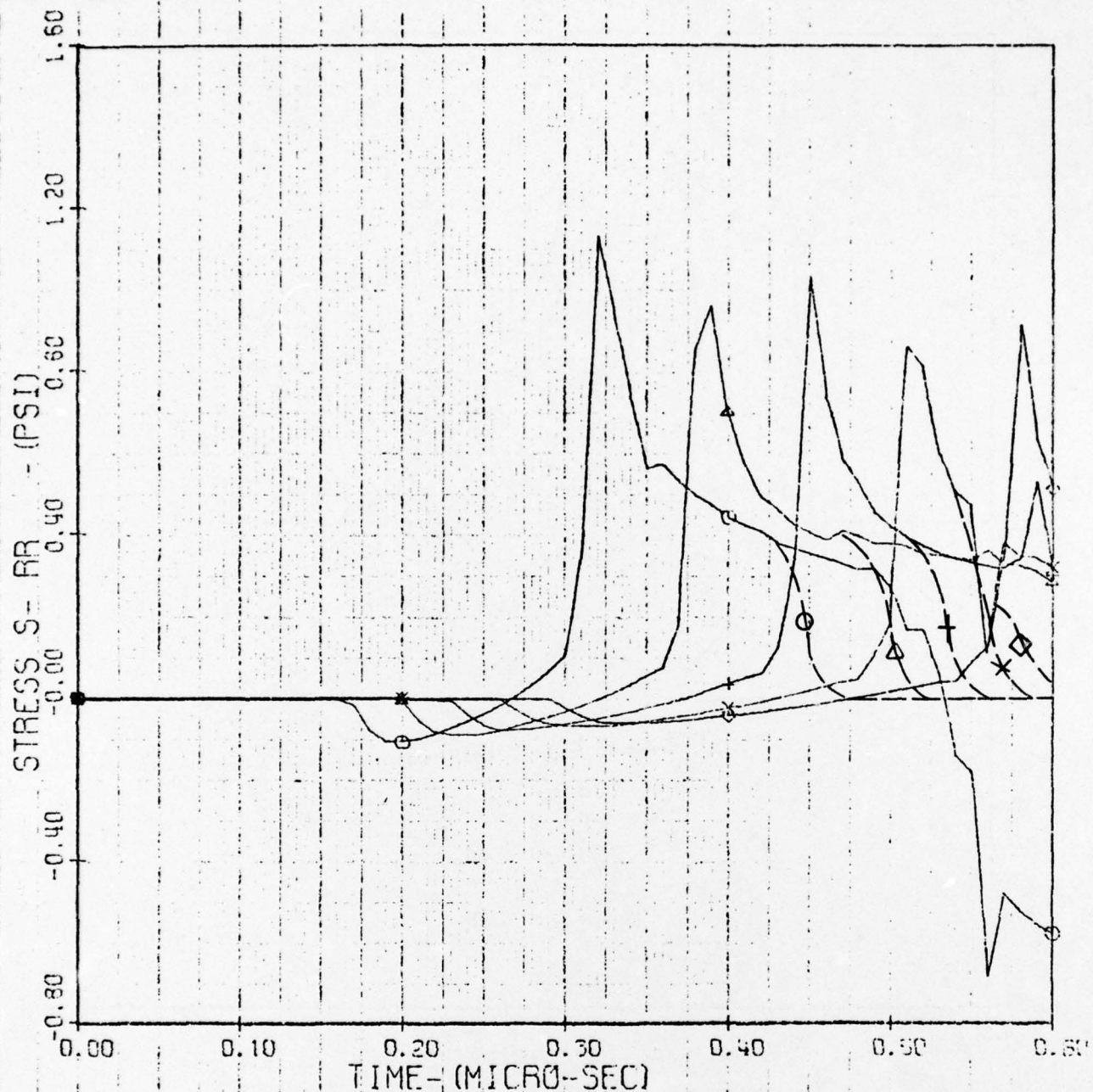
+ 0.0120

x 0.0160

◇ 0.0200

Figure 85. Temporal Distribution of Radial Stress (at $Z = 0.0002$ in. and $0.004 < R < 0.020$ in.) for a 2.0 mm Water Drop Impacting PMMA at 1120 ft/sec, with Pressure Pulse Limited to $0.275 \mu\text{sec}$ Duration

CASE 221 PMMA 2.0 MM DROP AT 1120 FT/SEC (SIG VS T)



Z-CONSTANT- (IN.)	0.0002	R- (INCHES)	
DROP SIZE- (MM)	2.00	○	0.0240
DROP VEL- (FT/SEC)	1120.0	△	0.0280
P ZERO- (PSI)	-1.0	+	0.0320
MATERIAL MODULUS- (PSI)	1.305×10^7	x	0.0360
POISSONS RATIO- (---)	0.325	◊	0.0400
MATERIAL DENSITY- (LB/IN ³)	0.0423		

Figure 86. Temporal Distribution of Radial Stress (at $Z = 0.0002$ in. and $0.024 \leq R \leq 0.040$ in.) for a 2.0 mm Water Drop Impacting PMMA at 1120 ft/sec, with Pressure Pulse Limited to $0.275 \mu\text{sec}$ Duration

$r = 0.040$ inch (1.01 mm) which is within the region where positive radial stresses of significant duration are predicted.

Conclusions for 0.7 and 2.0 mm drop impacts on ZnS are basically the same as for ZnSe due to the similarity in material properties.

The predicted locations of the radii of the annular damage sites agree quite well with the experimental data indicating that the computer program provides a reasonable model of the impact process. However, the program requires the assumption that the magnitude of the drop/substrate interface pressure is constant during the loading process. In reality, the pressure starts at zero, quickly rises to a maximum, and then gradually decays to zero. This variation of pressure with time will certainly influence the magnitude of the predicted tensile stress. In particular, it would tend to significantly reduce the stress levels at points far from the center of impact.

IV. CONCLUSIONS

A. Experimental Investigation

Experience with the installation and operation of a single drop generator demonstrated that it is possible to investigate in a controlled manner the incubation state of rain erosion of infrared window materials in the AFML/Bell rain erosion facility. Drops with a preselected diameter ranging from 0.7 to 2.5 mm can be obtained with the single drop generator. The drops remain intact and do not distort at specimen velocities up to 1120 fps, the highest velocity investigated.

The single drop experiments provided valuable information on the response of zinc selenide, zinc sulfide and gallium arsenide to rain drop impact. The impact of a single water drop at 730 fps produced a distinct and characteristic annulus of ring fractures on all three materials. The ranking of the three materials with respect to increasing resistance to damage by a single 2.0 mm diameter drop impact at 730 fps was zinc selenide, gallium arsenide, and zinc sulfide. Resistance to damage was not related to hardness or fracture strength both of which increase in the order zinc selenide, zinc sulfide, and gallium arsenide.

The characteristics of the ring fractures formed by 2.0 mm diameter water drop impact at 730 fps were quite different for each material. The fractures on zinc selenide were predominantly transgranular with some intergranular fracture near the inner radius of the damaged annulus. Dislocations were also generated near the inner radius. Extensive subsurface damage was also present at single drop impact sites. This subsurface damage was associated with surface cracks which changed direction as they propagated below the surface. The ring fractures on zinc sulfide were completely transgranular with no evidence of dislocation generation. The fractures were quite shallow and subsurface damage was absent. The fractures on gallium arsenide differed from those on zinc selenide and zinc sulfide because of

the extremely large grain size of the gallium arsenide. A typical grain was several times larger than a single drop impact site. The ring fractures on gallium arsenide displayed distinctive crystallographic orientation, probably $\{110\}$ cleavage. Subsurface damage could not be assessed since gallium arsenide is not optically transparent.

No surface or subsurface defects which would influence the response of the material to single drop impact were found on any of the zinc selenide or zinc sulfide specimens. The surface of the gallium arsenide specimens, although visually a mirror finish, contained scratches which nucleated additional damage when a drop impacted nearby. The primary cracking of gallium arsenide resulted from stresses exceeding the cleavage strength; however, much secondary cracking was associated with the presence of small precipitates within the matrix of the grains.

The primary effect of increasing the drop diameter from 0.7 to 2.0 and 2.5 mm, as determined on zinc selenide at 730 fps, was to increase the size of the annular fractured area. The nature of the damage did not vary with drop size except for noticeably less subsurface penetration of the cracks generated by a 0.7 mm diameter drop. The primary effect of increasing the impact velocity from 730 fps to 1120 fps, as determined on zinc selenide impacted with 2.0 mm diameter drops, was to increase the size of the fractured area by increasing the outer radius of the annulus. Increasing the impact velocity did not change the nature of the damage.

A second 2.0 mm diameter drop impacting at 730 fps so as to overlap the ring fracture area formed by a prior drop impact caused very little increase in the damage from the first impact for all three materials. The damage in the overlapping fractures appeared to be essentially additive. For zinc selenide, even a third drop impacting on the overlapping damage from two prior impacts did not nucleate a pit. No overlapping impact sites from three drops were formed on zinc sulfide or gallium arsenide,

so no definite conclusion can be made. However, it can be assumed that more than three drops impacting the same area would be required to nucleate a pit on these two materials because their resistance to damage from a single drop impact was greater than that of zinc selenide.

A reasonably complete correlation was established between the progress of erosion of the infrared window materials in a rainfield at 730 fps and the loss of transmittance, based on the results for zinc sulfide. Transmittance at short wavelengths (0.5 to 2.1 microns) decreased almost linearly with time of exposure for all three materials indicating a dependence of transmittance loss on the extent of subsurface damage. However, zinc sulfide exhibited a definite incubation period somewhat greater than 160 seconds before loss of transmittance at long wavelengths (2.5 to 25 microns). After an exposure of 160 seconds, surface pits had nucleated and started to grow. The extensive development of subsurface damage during the incubation stage prior to pit nucleation did not reduce transmittance at the longer wavelengths. Once pits were nucleated, the rate of loss of transmittance at the longer wavelengths was approximately proportional to the growth rate of the total cross-sectional area of the pits.

Zinc selenide and gallium arsenide eroded at too rapid a rate in the standard rainfield to permit the number of observations required to characterize the incubation period. However, both materials did show a decrease in the rate of transmittance loss with exposure time as the wavelength increased. The relationships between the progress of erosion damage and the loss of infrared transmittance for zinc selenide and gallium arsenide are probably similar to those described above for zinc sulfide, except on a shorter time scale with fewer overlapping drops required to nucleate pits.

It should require at least nine overlapping drop impacts to nucleate a pit on zinc sulfide. This conclusion is based on (1) ideal calculations of the rate of drop impact and the

distribution of impact sites on a specimen exposed to the standard rainfield at 730 fps and (2) experimental observations that pits have nucleated on zinc sulfide after an exposure of 160 seconds. This estimate of the number of overlapping impacts required for pit nucleation appears reasonable considering the limited effect of overlapping impacts observed in the single drop experiments.

An outer layer of erosion resistant material is a promising method to protect a less erosion resistant substrate as demonstrated by the behavior of zinc sulfide layers of various thicknesses (0.25, 0.50 and 1.0 mm) bonded to zinc selenide. Single and overlapping doublet ring fractures formed by impact with 2.0 mm drops at 730 fps did not propagate through even the thinnest (0.25 mm) zinc sulfide layer and the underlying zinc selenide surface was undamaged. Essentially, the zinc sulfide layers responded to drop impact in a manner similar to bulk zinc sulfide. Although a thin layer of zinc sulfide should protect the zinc selenide in the incubation stage of erosion, the thickness of the protective layer might be limited by the rate of deepening of the surface pits after the incubation stage has been completed. Experiments in the rainfield are required to verify this.

Lengthening the incubation period before pits are nucleated appears to be a good method to significantly improve the overall performance of the infrared window materials. For example, the incubation period, with no loss in transmittance at the longer wavelength range of 2.5 to 25 microns, extended for approximately one-half of the useful life of zinc sulfide in the rainfield experiments. The length of the incubation period is controlled by the manner in which the surface layer of the material responds to drop impact. Techniques to increase the incubation period include surface hardening and the formation of a surface layer with residual compressive stresses. Additionally, the superior erosion resistance of the very fine grained zinc

sulfide with respect to coarse grained zinc selenide suggests that a reduction in the grain size of the zinc selenide would increase its erosion resistance.

B. Theoretical Predictions

The analytical model evaluated in this program provided insight regarding transient stresses generated within infrared window materials impacted by a water drop. Computed radial tensile stresses for all cases investigated, including various drop sizes (0.7, 2.0, and 2.5 mm diameter) and impact velocities (730 and 1120 fps), exceeded the typical fracture strengths reported for the infrared window materials, zinc selenide, zinc sulfide, gallium arsenide, and germanium. Although there are some differences in properties among the four infrared window materials investigated, the differences in magnitudes of predicted radial stresses were slight at identical drop sizes and impact velocities. Small differences were also predicted for the distance traveled by the stress peak in each material at a particular time after impact.

The effects of drop size and impact velocity on radial stress were calculated for single drop impact on zinc selenide. The magnitude of the maximum value of the radial stress increased as an exponential function of drop diameter with the exponents being 0.55 and 0.7 at impact velocities of 730 and 1120 fps, respectively. The magnitude of the maximum value of the radial stress was also predicted to increase as a function of the velocity squared. An increase in drop size or impact velocity also increased the distance from the center of impact to the location at which the radial stress became positive (tensile) and at which the highest positive value of the stress occurred.

The analytical model showed ring fracture to be a surface phenomenon with a rapid fall off in radial tensile stress predicted at depths below 1 mil (25 μm). The stresses were below the reported fracture strengths of zinc selenide and zinc sulfide by depths of 4 mils (100 μm) and 2 mils (50 μm), respectively.

These differences in depths do not explain the much greater single drop impact damage suffered by zinc selenide as compared to zinc sulfide. It is concluded that the difference in damage probably resulted from an order of magnitude difference in grain diameters, with zinc selenide having the larger grain size.

The predicted locations of the inner radii of the annular areas of ring fractures agreed quite well with the experimental data indicating that the computer program provided a reasonable model of the drop impact process. However, the radial distance to which the damage extended could not be predicted accurately because the analytical model allowed the stress waves to proceed indefinitely with time. A technique for allowing the interface pressure to vary with time should provide a more accurate simulation of material behavior.

The analytical model was used to predict the response to drop impact of a bilayered construction having an erosion resistant zinc sulfide layer on a zinc selenide substrate. The results predicted that zinc sulfide thicknesses as low as 10 mils (0.25 μm) should prevent fracture of the zinc selenide. This prediction was verified by the experimentation in which ring fractures formed by 2.0 mm drops impacting a bilayered specimen with a 10 mil thick outer layer of zinc sulfide at 730 fps did not penetrate the zinc sulfide layer and the zinc selenide substrate was not damaged. Shear stresses which peaked at a distance between 0.2 and 5.0 mils (0.005 and 0.13 mm) below the surface might limit the minimum thickness of the protective layer.

The analytical model contains assumptions which inherently limit the accuracy of the stress predictions. These include the following: (1) the substrate is homogeneous (i.e., defect free and without provisions for any redistribution of stresses as a result of local material failures); (2) a uniform and constant interface pressure in the loaded region; and (3) the radius of the loaded area increases as $t^{\frac{1}{2}}$ for all time.

In addition, numerical instabilities create problems when attempts are made to compute stresses near the surface at depths less than 0.2 mils ($5\text{ }\mu\text{m}$). These limitations can be corrected to improve the accuracy of the stress predictions as described in the recommendations presented in the next section.

V. RECOMMENDATIONS

A. Experimental Investigation

Impacting specimens with single water drops proved to be an excellent method to determine the behavior of zinc selenide, zinc sulfide, and gallium arsenide in the very early stage of erosion. The behavior of a material during this incubation stage, before significant material removal, appears to provide a key to the overall behavior of the material in a rainfield environment. Thus, the results from single drop experiments can be expected to contribute significantly to the development of improved materials and these experiments should be continued as recommended below.

Single drop impact experiments should be performed at lower velocities to establish the threshold velocity for detectable damage from a single drop impact on zinc selenide, zinc sulfide, and gallium arsenide. Such experiments would provide data required to refine the predictive capabilities of the analytical models. Additional overlapping single drop experiments should be performed on these three materials to provide better understanding of the incubation stage leading to pit nucleation.

Additional single drop experiments with the bilayered zinc sulfide/zinc selenide specimens are also recommended in which the 0.25 mm zinc sulfide layers are reduced in thickness to 0.13 mm and less. Results from these experiments would verify the analytical method used to predict the behavior of layered specimens. Bilayered specimens with 0.25, 0.50, and 1.0 mm thick zinc sulfide layers should be exposed to the standard rainfield at 730 fps for increments of time comparable to those used for bulk zinc sulfide. This series of experiments will relate the performance of the bilayered specimens and the bulk zinc sulfide with respect to erosion rate and loss of transmittance. The results will also verify the performance of the protective layers which has now been demonstrated in single drop impact experiments.

Experiments in the rainfield to investigate the progress of erosion and loss of transmittance with exposure time should be performed on zinc selenide and gallium arsenide with the rainfall rate reduced to 0.5 in./hr. or less. The standard rainfield with a rainfall rate of 1 in./hr. was too erosive to permit a sufficiently large number of exposure periods to characterize the incubation stage of erosion for these two materials.

Single drop impact experiments should be extended to investigate the behavior of infrared window materials in addition to the three materials evaluated in this program. Examples of such additional materials include magnesium fluoride, spinel, silicon, and sapphire. Single drop experiments should also be performed to evaluate the behavior of antireflectant coatings applied to infrared window materials.

Studies should be undertaken to assess techniques for reducing the grain size of zinc selenide. Such a reduction in grain size should significantly improve the erosion resistance of zinc selenide by decreasing the depth of penetration of the ring fractures and reducing the extent of subsurface damage. In addition, techniques should be evaluated for producing compressive surface layers on zinc selenide and zinc sulfide. Such layers should increase the incubation stage of erosion and, thus, the overall performance of these materials.

B. Theoretical Predictions

The analytical model has provided insight into the transient stress distribution produced in a homogeneous elastic solid by an impacting spherical liquid drop. The accuracy of any mathematical model is dependent on the assumptions made and it is felt that a number of improvements can be made to provide a more realistic representation of liquid drop impact phenomenon and increase the analytical accuracy.

An investigation should be made into the reasons for the numerical instability that exists in the TURBAN computer

program when attempts are made to compute stresses near the material's surface, especially in the vicinity of the Rayleigh surface wave front. This problem might be solved by a reformulation of the integrals which are solved numerically.

Improvements should be made in the model for liquid drop impact to account for compressibility effects in the liquid. The current model assumes the liquid drop to be perfectly compressible during the collision process. The radius and velocity of the loaded boundary as a function of time are computed based on this assumption. In reality, the radius and the velocity of the loaded boundary are largely dependent upon the degree of compressibility of the liquid.

The variation in pressure with respect to time at the liquid/solid interface should also be included in the TURBAN program. Recently, more sophisticated analytical methods have provided a very accurate description of the pressure distribution, as a function of spatial position and time, at the liquid/solid interface. These results have indicated that the pressure over the loaded region is not uniform and that the magnitude at any point changes considerably with time. The TURBAN computer program assumes that the pressure is uniform over the loaded region and is constant with time. It is suggested that the TURBAN program be updated to at least account for the timewise variation in pressure. The spatial variation in pressure, expected to have a lesser influence on predicted stresses, should also be considered if practical.

VI. REFERENCES

1. Adler, W. F. and Hooker, S. V., Characterization of Transparent Materials for Erosion Resistance, AFML-TR-76-16 (March 1976).
2. Adler, W. F., Analysis of Multiple Particle Impacts on Brittle Materials, AFML-TR-74-210 (Sept. 1974).
3. Adler, W. F., Analytical Modeling of Liquid and Solid Particle Erosion, AFML-TR-73-174 (Sept. 1973).
4. Morris, J. W. Jr., Supersonic Rain and Sand Erosion Research; Part II- Mechanistic Investigation of Rain Erosion, AFML-TR-69-287, Part II, (Sept. 1969).
5. Freiman, S. W., Mecholsky, J. J., and Rice, R. W., "Influence of Microstructure on Crack Propagation in ZnSe," J. Amer. Cer. Soc., 58, 406 (1975).
6. Blowers, R. W., "On the Response of an Elastic Solid to Droplet Impact", J. Inst. Math. Applics., 5, 167 (1969).

**END
FILMED**

DATE: **5-90**

DTIC